PMT Studies and Loop Antenna Development for the LZ Dark Matter Search

Theresa M A Fruth

Oriel College

University of Oxford

A thesis submitted for the degree of

Doctor of Philosophy

Trinity 2019

Für meine Omas. Zwei starke Frauen.

Acknowledgements

The past four years have been an incredible journey. I have learnt and grown as a human and as a physicist. Many people have accompanied me throughout this time. I am grateful to all of them and would like to mention a few here.

I would like to thank my supervisor Professor Hans Kraus for the opportunity to do this DPhil. His guidance and support throughout the years has been invaluable.

I thoroughly enjoy being part of the LZ collaboration. There are many people who have inspired me. I would especially like to thank my colleagues in the Oxford LZ group and the wider LZ UK community. Amy, Andrew, Alfredo, FengTing, Jim, Junsong, Kathryn, Umit and many others - thank you for your company, advice and support. I have had the pleasure of spending time at Imperial College and SLAC and would like to thank the groups there for always being welcoming! I have learnt a lot from Brais, Tomasz and Alden and enjoyed working with them very much. I am grateful to Professor Henrique Araújo for the opportunities and encouragement he has given me.

I would also like to thank the administrative and technical staff at Oxford Physics who were always incredibly helpful - even for last minute requests.

I could not have done this DPhil without the unwavering support of my family and friends. Especially, my parents and sister who have always stood behind me!

Abstract

The nature of dark matter remains one of the biggest mysteries of the universe. Extensions to the Standard Model of particle physics provide potential candidates for dark matter. Such dark matter particles can be searched for using direct detection experiments. LUX-ZEPLIN (LZ) is a next-generation search for dark matter currently under construction at SURF, South Dakota. LZ employs a two-phase, liquid xenon time projection chamber (LXe TPC). A dark matter particle would scatter off a xenon nucleus, which causes scintillation and electroluminescence light signals. The light is detected by Photomultiplier Tubes (PMTs) on the top and bottom of the detector. The sensitivity projection for a 1000 live day run with 5.6 tonne fiducial mass is $1.6 \times 10^{-48}\,\mathrm{cm}^2$ for a $40\,\mathrm{GeV}/c^2$ mass WIMP at 90% confidence level.

The first part of this thesis is concerned with the precise modelling of PMT properties and their impact on detector performance. To optimize sensitivity to WIMP masses of less than 10 GeV, it is essential to understand the single photon PMT response in detail. A simulation model, including undersized PMT pulses, is developed based on data taken with spare LZ PMTs. Variation in the PMT single photon response impacts detection efficiencies, energy resolution and position reconstruction. The improved PMT simulation is used to assess the impact of PMT failures on LZ signal detection efficiency, signal to background discrimination and ultimately LZ sensitivity.

High voltage discharges, accompanied by sparks, are a potential danger to the PMTs and a known problem in liquid noble gas detectors. The second part of this thesis discusses the development of the first dedicated high voltage discharge monitoring sensor in a LXe TPC. The loop antenna provides useful information about the electromagnetic environment of the detector and monitors for such discharges.

Statement of Originality

I declare that the work presented in this thesis is my own. Any work that is not my own is referenced appropriately. Specific contributions by collaborators to each chapter are listed below.

Chapter 1 gives an overview of the current status of dark matter evidence, theory and experiments.

Chapter 2 focuses on dark matter detection with liquid xenon and the LZ detector building on literature and work done by the LZ collaboration.

Chapter 3 is concerned with the development of a realistic PMT simulation. The PMT simulation is part of the Detector Electronics Response Simulation package developed by Cees Carles, a previous Oxford graduate student. My contribution is the development and implementation of an extended PMT model accounting for undersized PMT signals and noise and assessing the impact of these effects. The extended model is based on LZ spare PMT data I took in collaboration with Brais López Paredes at Imperial College London.

Chapter 4 assesses the effect of PMT loss on LZ data analysis and sensitivity. The data was generated using LZ simulation and data reduction tools developed by the collaboration. The analysis of the data is my own work.

Chapter 5 is concerned with the development of the loop antenna. The prototype sensor presented was designed by Junsong Lin, a previous Oxford graduate student. I have characterized and tested the antenna in detail, developing methods to extract meaningful information from its data in a detector environment. Using these results, I developed a new and improved design and an adaptive triggering algorithm to ensure reliable sensor operation in LZ. The LZ test stand at which the loop antenna

was tested was developed, built and run by collaborators at SLAC. I controlled the loop antenna data taking remotely from Oxford. The germanium-screening, ICP-MS and radon emanation results presented were provided by collaborators at South Dakota School of Mines, University College London and Lawrence-Berkeley National Laboratory. The loop antenna readout board described in the chapter was designed and programmed by Hans Kraus. The loop antenna data onsite was recorded with assistance from Umit Utku and Brais López Paredes.

Theresa Fruth

Contents

List of Figures

Introduction

With the emergence of the standard model of particle physics in the past century and the discovery of the Higgs boson in 2012, particle physics provides a thorough understanding of the most fundamental constituents of the universe. However, a large part of the universe is still unknown to us. The majority of mass in the universe is made of dark matter. There are many different theories on what dark matter could be. One of the most promising candidates is the weakly interacting massive particle. Such a particle could be detected with earth-based direct detection experiments.

The LUX-ZEPLIN (LZ) experiment is a next-generation direct detection experiment using a liquid xenon time-projection chamber. It is currently under construction, and data-taking is due to start in 2020. If a weakly interacting massive particle interacts in the detector, it causes the emission of scintillation light and ionization. The scintillation light is detected by Photomultiplier Tubes (PMTs) on top and bottom of the detector. An electric field is applied to the detector to extract ionization electrons to a gas phase on top of the detector. The electrons are accelerated in the gas phase and produce electroluminescence light, which again is detected by PMTs. To achieve a very low energy threshold and be sensitive to WIMP masses of less than 10 GeV, it is essential to have an optimum performance of the light detectors and understand their response in detail. The work presented in this thesis focuses on the precise understanding and modelling of the PMT response to single photons, including signal-induced noise and the impact of PMT properties and potential PMT

failures on the detector performance. One potential danger to the PMTs are sparks accompanying high voltage discharges. Such discharges have been a problem in previous noble liquid TPCs. A sensor was developed to monitor the detector for such discharges and periods of field instability.

In **Chapter 1**, observational evidence for dark matter is discussed, and its particle nature is motivated. Different dark matter searches are introduced, and the current best experimental limits are presented.

Chapter 2 introduces the LZ detector. It starts by looking at liquid xenon as a detector medium and the signatures of particle interactions in it. Subsequently, the LZ detector design, calibrations, backgrounds and projected physics reach are discussed.

In **Chapter 3** the PMT Singe Photon Response is discussed. A model is presented drawing on literature and previous measurements of the LZ PMTs. This model is used to interpret high gain PMT data taken at Imperial College. 6 spare LZ PMTs are powered to higher gains than in LZ to study the contribution of undersized signal pulses to the PMT single photon response. Results from these tests and analytic calculations are used to develop an extended PMT model for the Detector Electronics Simulation. This simulation is part of the official LZ simulation chain used to generate mock data. It is shown that variations in the PMT response impact detection efficiency, energy resolution and position reconstruction and are therefore important to consider when preparing for analysis of real LZ data.

Chapter 4 assesses the effect of potential PMT failures on LZ data analysis and sensitivity. Experience from previous experiments has shown that a fraction of PMTs tends to fail during long-term operation. The impact of losing PMTs on light collection efficiency, fiducialization and signal to background discrimination is studied using GEANT4 Simulations and the PMT simulation discussed in Chapter 3. It is shown that more than 4% failed PMTs can have a severe effect on LZ sensitivity and

that the location of failed PMTs matters.

Chapter 5 is concerned with the development of the loop antenna, a sensor monitoring the detector for changes in the EM environment. The sensitivity and cleanliness considerations going into the design and construction of the loop antenna are described. The main focus is the characterization of the antenna and the extraction of useful information in a noisy detector environment. The prototype antenna was tested at the LZ test stand at SLAC. Results from this test led to a redesign of the antenna and the development of an adaptive triggering algorithm. Eight antennae are installed in LZ and have already provided useful information during construction by monitoring the cleanroom, in which the LZ detector is being assembled, for static discharges.

Chapter 6 is a summary of the work in this thesis and an outlook of how this work could be extended in the future.

Chapter 1

Dark Matter

The observation of the night sky is one of the oldest scientific endeavours. The idea that some of the things in the universe are *dark*, as in non-accessible to the human eye (yet) was a common one throughout that history [1]. Over the past centuries, advances in technologies have allowed astronomers and astrophysicists to push the boundaries of the unseen back further and further. Recently the first image of a black hole was captured [2]. Even with these advances, a significant fraction of the universe remains *dark*. The current best cosmological model of the universe requires about 26% of its mass density to be made of a new form of matter - dark matter. The following chapter reviews evidence for dark matter, its candidates and experimental searches, focusing on direct detection.

1.1 Evidence for dark matter

1.1.1 Galactic scale

One of the oldest pieces of evidence for dark matter is the behaviour of rotational velocities of stars in a galaxy as a function of their distance to the galactic centre. According to Newtonian dynamics, the velocity of objects as a function of distance

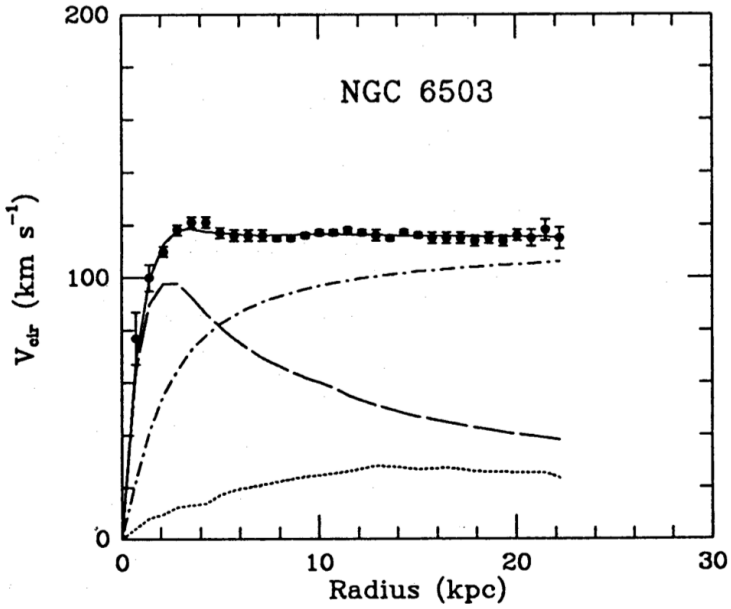

Figure 1.1: Galactic rotational curve indicating the observed data and the contributions from the optical disk (dashed line), gas (dotted line) and the dark matter halo (dash-dotted line). Image taken from [7].

from the galactic centre r behaves as

$$v(r) = \sqrt{\frac{GM(r)}{r}}, \tag{1.1}$$

where $M(r) = 4\pi \int \rho(r) r^2 dr$. As most of the visible matter of the galaxy is contained in the centre of the galaxy, it is expected that the mass density profile of the galaxy, $\rho(r)$ would fall as $\frac{1}{\sqrt{r}}$ beyond its luminous centre. However, it is observed that rotational curves become flat at large distances from the galactic centre. This suggests the existence of a invisible halo with $\rho(r) \propto \frac{1}{r^2}$ at large radii. The distribution of visible and dark matter and the rotational velocity at different radii is illustrated in Fig. 1.1. This phenomenon was first observed in the 1970s by Vera Rubin and collaborators [3] and is still a topic of ongoing research. Low Surface Brightness (LSB) galaxies, which have a dominating dark matter component throughout the galaxy, are investigated to get a better understanding of the dark matter distribution in galaxies [4, 5, 6].

Figure 1.2: The bullet cluster with pink indicating the interstellar gas and purple showing the area of greatest gravitational potential as found by gravitational lensing. Image cedit: X-ray: NASA/CXC/M.Markevitch et al. Optical: NASA/STScI; Magellan/U.Arizona/D.Clowe et al. Lensing Map: NASA/STScI; ESO WFI; Magellan/U.Arizona/D.Clowe et al.

1.1.2 Galaxy cluster scale

In the 1930s Fritz Zwicky noticed a discrepancy between the mass of the Coma galaxy cluster inferred from velocity dispersions of the galaxies in the cluster and the observed amount of stellar material in the cluster. The virial theorem relates the total kinetic energy of the galaxy cluster to the total gravitational potential energy of the cluster. Applying this theorem to the measured velocity dispersions and combining it with optical observations of the cluster, Zwicky estimated the mass-to-light ratio of the galaxies to be 400 solar masses per solar luminosity. This unexpectedly large ratio led Zwicky to propose that dark, non-luminous matter could provide mass leading to higher orbital velocities [8].

One of the most famous pieces of evidence for dark matter is the bullet cluster, as seen in Fig. 1.2. It resulted from the collision of two galaxies. Galaxies consist mostly of inter-cluster plasma. This plasma experiences ram pressure during the collision, while the luminous matter of the galaxies behaves almost as collision-less particles. During the collision, the galaxies spatially decouple from plasma. The location of the

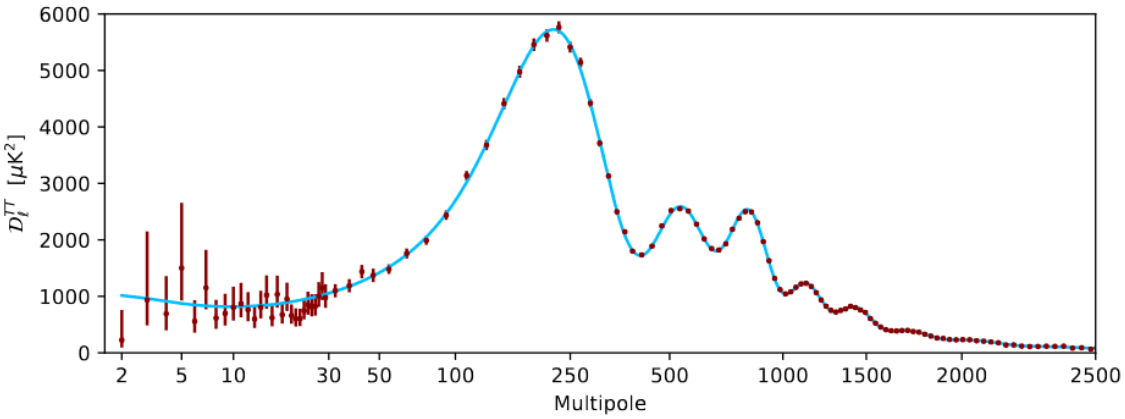

Figure 1.3: Angular power spectrum of temperature fluctuations in the Cosmic Microwave Background as measured by Planck [10]. Credit: ESA and the Planck Collaboration.

intergalactic plasma can be mapped as it is X-ray emitting. The luminous parts of the galaxies have moved ahead of their respective plasma clouds, which remain closer to the point of impact. Using weak gravitational lensing, the gravitational potential can be observed. The gravitational potential is located near the brightest point of the cluster, rather than coincide with the X-ray concentration. Therefore, most of the mass of the galaxy must be provided by dark matter which interacts gravitationally but can pass through the point of collision without interacting [9].

1.1.3 Cosmological scale

The cosmic microwave background (CMB) is remnant radiation from the early days of the universe. The photons in the CMB last interacted when the universe was only 300,000 years old. Since then the photons have travelled through space freely. Before the decoupling, small gravitational wells had already begun to form. Due to the interplay of radiation pressure from photons and gravitational compression of the photon-baryon fluid, the fluid underwent acoustic oscillation. This oscillation can still be observed today as small temperature variations in the blackbody spectrum of the CMB. These anisotropies in the CMB contain information about cosmological

parameters.

Fig. 1.3 shows the power spectrum of the temperature fluctuations as a function of the angular size of the pattern. It is often referred to as the CMB power spectrum and allows measurement of these parameters. The location of the first peak indicates the flat geometry of the universe and the total energy density. The locations and heights of peaks 2 and 3 give information about the baryon density and therefore indirectly about the dark matter density in the universe [11]. The latest measurements of these parameters are from the Planck satellite, which scanned the skies in the microwave and sub-millimetre spectrum from 2009 to 2013. It measured the baryon density, $\Omega_b = 0.0024 \pm 0.0001$ and the dark matter density, $\Omega_c = 0.120 \pm 0.001$ [10, 12]. The CMB spectrum is well described by the Lambda Cold Dark Matter Model of Cosmology (ΛCDM) which has emerged as the Standard Model of Cosmology over the past decades. This model requires the existence of non-baryonic, non-relativistic (cold) particles making up the dark matter in the universe [11].

Large scale structures observed in the universe today also provide evidence for the ΛCDM model. Galaxies and galaxy clusters have formed from small fluctuations in density. Non-baryonic dark matter plays a vital role in structure formation, as it does not interact electromagnetically and thus already started to cluster in gravitational wells during periods in which baryonic matter was still coupled to radiation. However, relativistic dark matter particles can escape the gravitational potential of over-densities and therefore damp the density fluctuations. If dark matter particles would have remained relativistic until the matter and radiation equality in the universe was reached, density fluctuations up to the mass scale of large super-clusters would have been erased. As large scale structures exist today, dark matter particles must have become non-relativistic much earlier [14].

The linear matter power spectrum quantifies the clustering and distribution of galaxies and galaxy clusters. In Fig. 1.4, it can be seen that observations from large

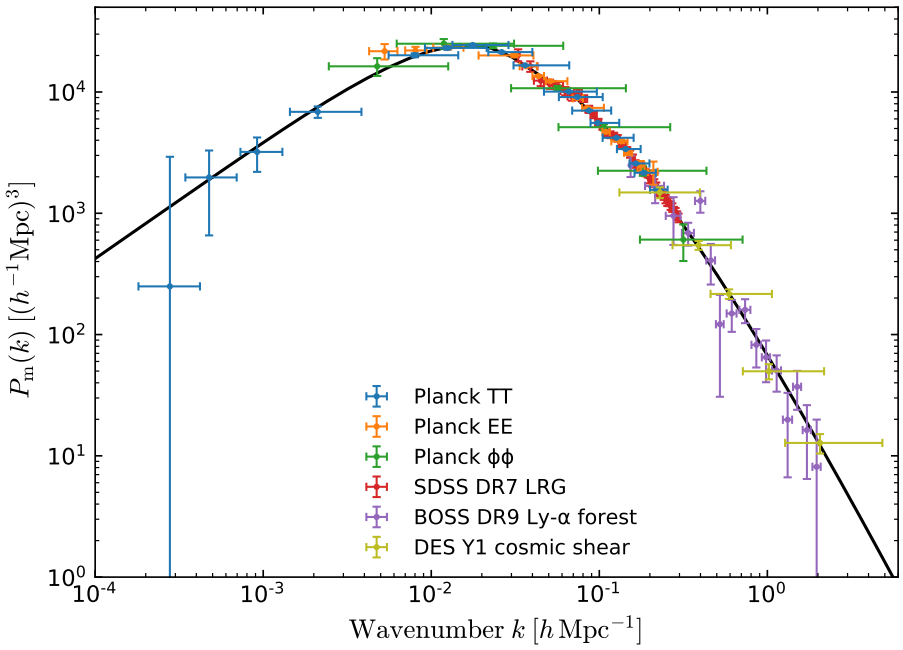

Figure 1.4: The linear matter power spectrum P(k) vs wavenumber extrapolated to z=0. The data from a range of cosmological measurements is best fit by the ΛCDM [13]. Credit: ESA and the Planck Collaboration.

scale surveys such as the Sloan Digital Sky Survey (SDSS) [15] and the measurements by the Planck observatory [10] are in good agreement with the theoretical prediction for structure formation with cold dark matter. A more detailed method of comparing theory to observation are n-body simulations. These simulations take the CMB measurements as input and predict how the structure of the universe developed over time using non-linear gravitational clustering processes [16, 17]. N-body simulations have been an essential tool in showing how the initial conditions measured in the CMB spectrum could have led to a cosmological structure as is observed today.

1.2 Dark matter candidates

1.2.1 Non-baryonic dark matter

The current best understanding of the cosmos, summarised by the ΛCDM model, requires the existence of non-baryonic cold dark matter. Extensions to the Standard Model of particle physics provide candidates for dark matter particles. Discrepancies in particle physics motivate many of these extensions, which provide natural candidates for Dark Matter. The essential requirements for a dark matter candidate particle are that it is stable, long-lived and does not interact electromagnetically or strongly.

1.2.1.1 Neutrinos

An early candidate for dark matter was the standard model neutrino. As stable, long-lived and weakly-interacting particles, they seemed like a good choice to constitute dark matter. However, N-body simulations have shown that the relativistic neutrinos, cannot account for structure formation [18]. Another candidate is a new neutrino species. Sterile neutrinos are postulated to only interact with SM particles via a small mixing angle to standard model neutrinos. Depending on their mass, sterile neutrinos could constitute the dark matter in the universe [19].

1.2.1.2 WIMPs

A collection of possible new particles, which could constitute dark matter, are Weakly-Interacting Massive Particles (WIMPs). The particles in this group are stable, weakly interacting, long-lived, massive and non-relativistic in the early universe. WIMPs are well motivated from cosmology as they could provide the right abundance of dark matter in the universe. It is assumed that dark matter was in thermal equilibrium with the baryonic matter in the early stages of the universe. As the universe expanded and

cooled, the reaction rates fell below the level required for thermal equilibrium. What remained was the relic abundance of dark matter observed today. An annihilation cross-section of the order of the weak scale would result in a dark matter energy density consistent with that observed by cosmological measurements [20].

Extensions to the standard model of particle physics have been developed to solve remaining problems in particle physics, like the hierarchy problem and gauge coupling unification. Some of them naturally provide suitable candidates for WIMPs. A popular theory is supersymmetry, which introduces a bosonic supersymmetric partner with the same quantum numbers for every standard model fermion. Supersymmetry offers a wide range of electrically neutral and weakly interacting particles [21]. Other theories which provide WIMP candidates are the little Higgs model and universal extra dimension theories [22, 23].

The strong case for WIMPs from both cosmology and particle physics has motivated many WIMP searches in the GeV mass range in the past decades. Such experiments have already excluded a vast amount of parameter space. The lack of observation of non-standard model particles at the LHC has also constrained many models. Current and future searches are focusing on closing the remaining parameter space and moving towards exploring sub-GeV WIMP masses. Experimental efforts are discussed in more detail in Section 1.3.

1.2.1.3 Axions

Axions are Goldstone bosons postulated by Peccei and Quinn as a solution to the strong CP problem [24]. Axions of a mass range 10^{-6} to 10^{-2} eV produced in the early universe and stable on cosmological timescales could provide the correct dark matter abundance [25]. Searches for axions and axion dark matter are ongoing. The ADMX collaboration uses the expected axion-photon coupling to look for axion dark matter using a microwave cavity experiment. A strong magnetic field is applied to

a cavity. Axions are expected to convert into monochromatic microwave photons which can be detected using an antenna [26, 27]. The CASPEr collaboration is looking for a time-varying nuclear dipole moment (CASPEr-Electric) and nuclear spin precession (CASPEr-Wind) induced by axions using nuclear magnetic resonance [28]. Other direct detection experiments primarily dedicated to WIMP searches have placed limits on axio-electric coupling [29, 30, 31].

1.2.2 MACHOs and primordial black holes

Massive astrophysical compact halo objects (MACHOs) contribute to the non-luminous mass in the universe. Examples for these objects are faint stars, substellar objects and star remnants. Microlensing searches have shown that MACHOs contribute to the mass of galactic halos but cannot explain more than $20 - 25\%$ of the galactic halo mass [32, 33]. Another contributor to dark matter could be primordial black holes. Such black holes could have been produced before Big Bang nucleosynthesis. They can have masses below the sensitivity of microlensing surveys, which has made it challenging to look for them. Different experimental efforts have shown that such objects only contribute a small fraction to the mass of galaxies. In 2016 LIGO measured gravitational waves of two merging black holes, both around 30 solar masses [34]. Black holes of this mass range are difficult to produce through stellar evolution. Therefore, this observation suggests that LIGO might have discovered a new population of black holes, which could have formed in the early universe. Such primordial black holes could constitute at least a fraction of dark matter [35]. Interferometers like LIGO and LISA will allow a better estimate of the density of black holes with tens of solar-masses over the next couple of years.

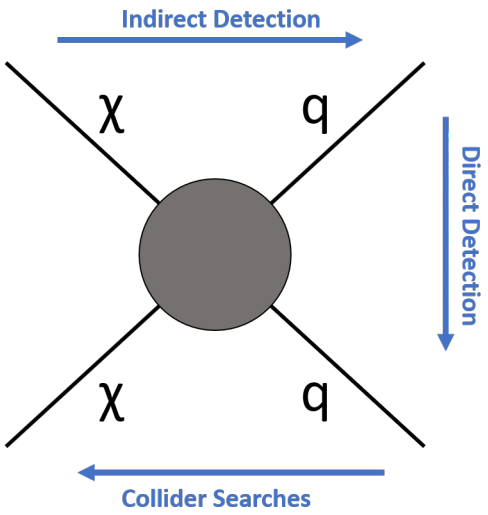

Figure 1.5: Feynman diagram depicting three interactions used to search for particle dark matter. The dark matter candidate particle is denoted as χ, and a Standard Model particle as q.

1.3 WIMP searches

1.3.1 Overview

Fig. 1.5 illustrates three complementary methods of looking for particle dark matter and specifically WIMPs. In dense regions of the universe, dark matter particles can annihilate to produce standard model particles. Astrophysical searches for pair-production of neutrinos, electron-positron pairs and photons are indirect tests for WIMP annihilation. Places to look for these signatures are places where a high density of dark matter is expected, like the centre of galaxies, dwarf galaxies and galaxy clusters [36].

If dark matter particles lie within the mass range of accessible energies at the LHC, they could be pair-produced in collisions of standard model particles. Dark matter particles would not induce a signal in the LHC detectors as they do not interact electromagnetically. An imbalance in the sum of energies of final state to initial state particles would indicate the existence of such particles. However, the LHC experiments cannot measure the lifetime or astrophysical abundance of the particle.

Additional experimental evidence from direct or indirect detection experiments would be required to determine whether the discovered particle is the astrophysical dark matter [37, 38].

Weakly-interacting dark matter particles (e.g. WIMPs) from our galaxy's dark matter halo are expected to scatter off atomic nuclei. Underground direct detection experiments are looking for signatures of such interactions. Direct detection is discussed in detail in the next section.

1.3.2 Direct detection concept

Direct detection searches rely on the assumption that a dark matter particle can scatter elastically of an atomic nucleus. As WIMPs are heavy particles, the scattering process can best be described as non-relativistic two-body scattering [39].

An important assumption which impacts the rate of interaction is the distribution of dark matter in the Earth's neighbourhood. To calculate the expected scattering rate of dark matter in the detector, the local dark matter density, the velocity of the WIMPs in the halo and the relative motion of the Earth with respect to that halo need to be known. The dark matter distribution in galaxies is typically quantified using rotation curves. As the Earth lies within the Milky Way, it is hard to get a precise estimate of the local dark matter distribution. A standard isothermal Gaussian halo model with a Maxwellian velocity distribution is assumed. The following assumptions are used in this chapter and for any sensitivity estimates presented in this thesis. The local dark matter density is $\rho = 0.3\,\mathrm{GeV/cm^2}$, the local circular velocity of the sun around the center of the galaxy is $v_0 = 220\,\mathrm{km/s}$, the local galactic escape velocity is $v_{esc} = 544\,\mathrm{km/s}$ and the mean velocity of the earth relative to the dark matter halo is $v_{earth} = 245\,\mathrm{km/s}$. The astrophysical uncertainties are well illustrated by recent calculations suggesting a local dark matter density between 0.2 and $0.6\,\mathrm{GeV/cm^3}$ [40].

Another important parameter when calculating the WIMP-nucleus interaction

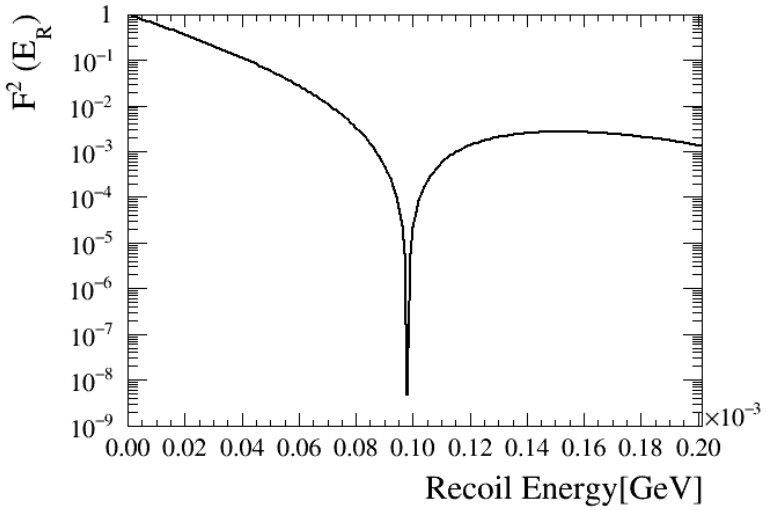

Figure 1.6: Nuclear Form Factor for ^{131}Xe.

rate is the cross-section, σ. The zero momentum spin-independent cross-section, σ_0 describes the coherent interaction with the whole nucleus,

$$\sigma_0 = A^2 \left(\frac{\mu_N}{\mu_n} \right)^2 \sigma_n, \tag{1.2}$$

where A is the atomic number of the target nucleus, σ_n is the scalar WIMP-nucleon cross-section, μ_N and μ_n are the WIMP-nuclear, and WIMP-nucleon reduced masses. The scattering rates are larger for heavier nuclei due to the A^2 dependence of σ_0.

At higher momentum transfers, the nucleus cannot be approximated as homogeneous sphere anymore. The form factor has to be included in the calculation to account for this [41]:

$$F_{SI}^2(q) = \frac{3j_1(qr_n)}{qr_n}^2 e^{-q^2 s^2}. \tag{1.3}$$

$j_1(x)$ is a first order spherical Bessel function. For ^{131}Xe, the effective nuclear radius is $R = 1.2A^{1/3}\,\mathrm{fm}$ and the skin thickness is $s = 1\,\mathrm{fm}$, giving $r_n = \sqrt{R^2 - 5s^2}$. The momentum transfer is calculated as $q = \sqrt{2m_N E_R}$. The resulting form factor is shown in Fig. 1.6.

The differential recoil rate is given by:

$$\frac{dR}{dE_R} = F^2(q)\frac{\rho_0\sigma_0}{2m_W\mu_N^2}\int_{v_{min}}\frac{f(v)}{v}dv, \tag{1.4}$$

where the velocity of WIMPs in the halo and the relative earth motion is parameterized as $f(v)$. The lower integration limit v_{min} is determined by the lowest WIMP speed causing a recoil of energy E_R. The solution to the velocity integral is given by:

$$\int_{v_{min}}\frac{f(v)}{v} = \begin{cases} \frac{1}{v_0 y} & z < y, x < |y-z| \\ \frac{1}{N_{esc}v_0 y}[erf(x+y) - erf(x-y) - \frac{4}{\sqrt{\pi}}ye^{(-z^2)}] & z > y, x > |y-z| \\ \frac{1}{2N_{esc}v_0 y}[erf(z) - erf(x-y) - \frac{2}{\sqrt{\pi}}(y+z-x)e^{(-z^2)}] & x > |y-z|, x < |y+z| \\ 0 & y+z < x, \end{cases} \tag{1.5}$$

using $x = \frac{v_{min}}{v_0}$, $y = \frac{v_{earth}}{v_0}$, $z = \frac{v_{esc}}{v_0}$ and $N_{esc} = erf(z) - \frac{2ze^{-z^2}}{\sqrt{\pi}}$ [42].

The minimum WIMP mass detectable and the uncertainty on the scattering rate for small WIMP masses is dependent on the WIMP escape velocity. At masses above 6 GeV, the dominant uncertainty on the rate comes from the local dark matter density [43]. From Equ. 1.3 and 1.4, it can be seen that the rate also depends on the mass of the WIMP and the target nucleus. Fig. 1.7a shows a comparison of the event rate of a 40 GeV WIMP with a cross-section of $10^{-46}\,\mathrm{cm}^2$ for different target materials. It can be seen that compared to lighter target nuclei, xenon has a higher interaction rate. Fig. 1.7b shows the event rate for varying WIMP masses and ^{131}Xe as target nuclei. ^{131}Xe is an excellent target material for WIMPs in the tens of GeV WIMP mass region.

Detector thresholds and efficiencies have to be taken into account to estimate the rate of events in a detector. Experiments need to be sensitive to a wide range of

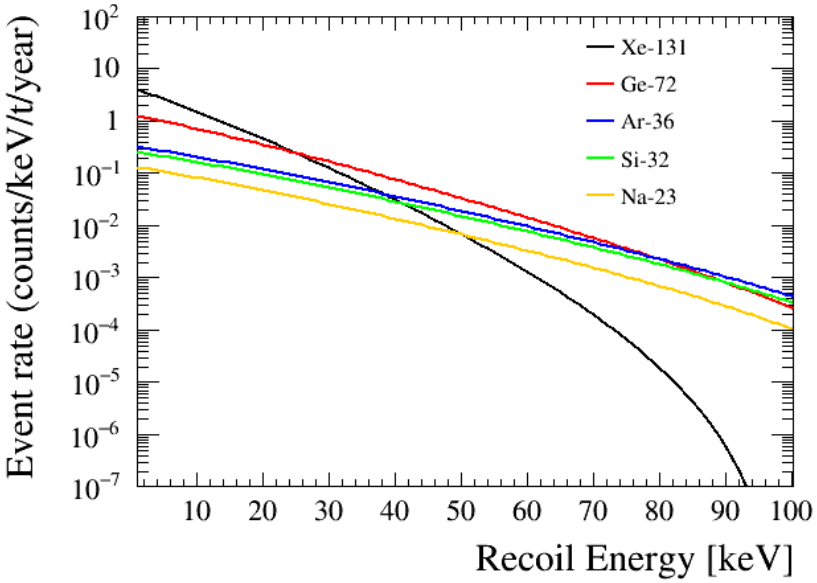

(a)

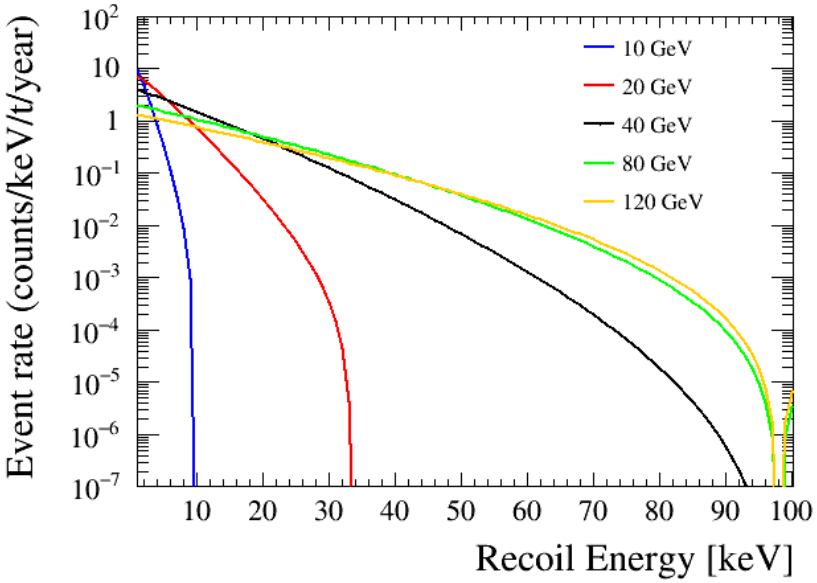

(b)

Figure 1.7: Comparison of differential event rates for (a) a 40 GeV WIMP with cross section of $1 \times 10^{-46}\text{cm}^2$ interacting with different target materials and (b) a range of WIMP masses with cross section of $1 \times 10^{-46}\text{cm}^2$ interacting with ^{131}Xe.

nuclear recoil energies, reduce backgrounds and maximise exposure by having a large detector to increase the chance of detecting a WIMP.

1.3.3 Detector technologies overview and status

1.3.3.1 Detector requirements

The energy deposited by a nuclear recoil in a target material typically produces three detectable signatures: scintillation light, ionisation and heat (phonons). Since direct detection of dark matter was first proposed in the 1980s [39], many different experimental concepts have been developed using different target materials and detecting different signals. The current best experimental limits are displayed in Fig. 1.8 and the corresponding experiments and techniques are discussed in the following sections.

A challenge all of these experiments have had to face is the reduction of backgrounds from cosmogenic radiation and trace radioactivity in the detector components themselves. Nuclear recoils can be caused by neutrons and daughter nuclei from radioactive decays. Radiation from radioactive decays can cause electron recoils in the detector. To be able to search for rare events like a dark matter particle scattering off a target nucleus, background rates have to be reduced significantly. Dark Matter direct detection experiments, thus, typically take place in underground laboratories to avoid cosmogenic backgrounds. Screening and material selection play an important role in minimising the trace radioactivity in the detector. Additionally, various experimental techniques have been developed to distinguish between electron (background) and nuclear (signal) recoils. Backgrounds and background reduction strategies for the LUX-ZEPLIN experiment are discussed in-depth Section 2.5.

Other important design drivers for dark matter direct detection experiments are the increase of detector volume to maximise exposure and pushing to lower energy thresholds. Different experiments have addressed these concerns with different approaches. The following is not a complete list of current and past experiments but

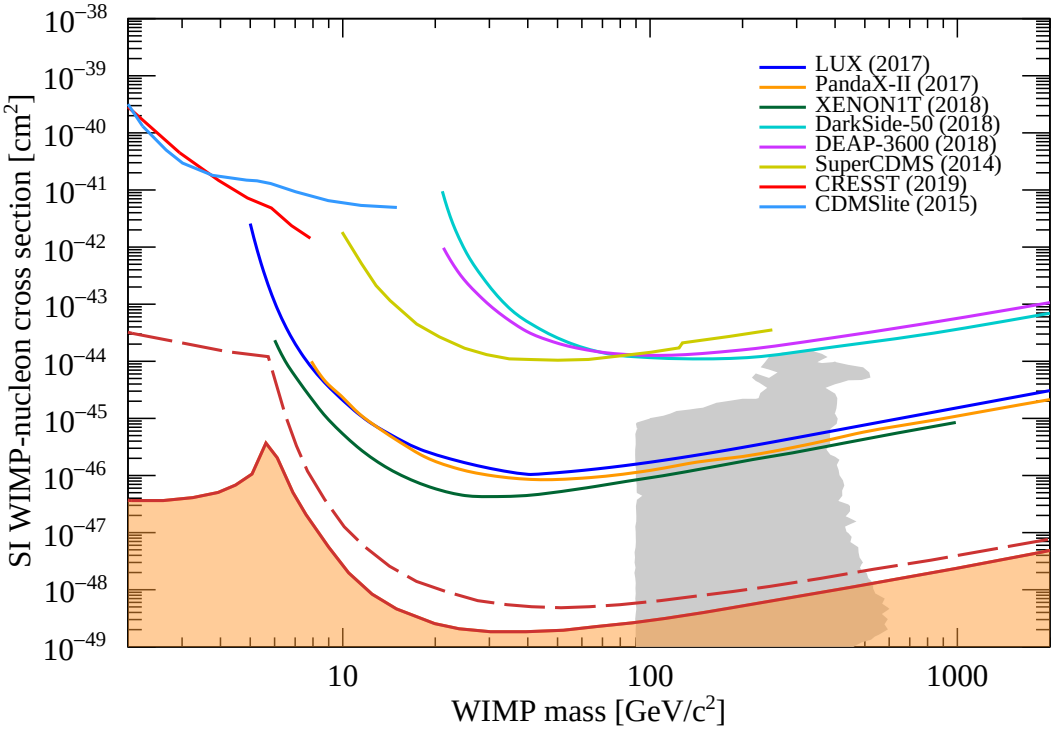

Figure 1.8: Current best experimental limits from different direct detection experiments. The limits displayed here are for LUX [44], PandaX-II, Xenon 1T [45], DarkSide, DEAP-3600, SuperCDMS [46] and CRESST [47].

highlights different detector technologies and strategies.

1.3.3.2 Annual modulation

One way of avoiding background discrimination is to look for annual modulation of the recorded signal instead. While most radioactive backgrounds in the detector are expected to be unchanged throughout the year, the WIMP-nucleon interaction rate would vary over the course of a year [48]. The DAMA/LIBRA experiment uses thallium-doped sodium iodide (NaI(TI)) scintillating crystals equipped with photomultiplier tubes to look for annual modulation. They have been detecting an annual modulation in their data at 12σ and are claiming that this is due to dark matter interactions [49, 50]. However, their claimed discovery is incompatible with limits set by other direct detection experiments with different target materials. For a model-

independent test of the DAMA/LIBRA discovery claim, new NaI experiments like COSINE-100, and ANAIS will be running over the next years. Both experiments have recently published their first results, which are both still consistent with a null hypothesis. Longer exposure is needed to confirm or refute DAMA/LIBRA's discovery claim [51, 52]. The SABRE experiment is planning twin NaI detectors in Australia and Italy to minimise the susceptibility to systematic seasonal effects [53].

1.3.3.3 Cryogenic solid-state detectors

The first experiments to achieve event-by-event discrimination between nuclear recoils (signal) and electron recoils (background) were cryogenic solid-state detectors. The distinction is achieved by looking at the ratio of two different channel readouts, ionisation and phonon energy (EDELWEISS, CDMS) and scintillation and phonon energy (CRESST). For these experiments relying on crystals as target materials, scaling up to higher masses and therefore higher exposure is very challenging. SuperCDMS in the Soudan Mine (USA) uses the interleaved Z-sensitive ionisation photon technique (iZIP) to detect both ionisation and phonons from their cryogenic germanium detectors. An electric field is applied to the detector modules to extract the electron to the detector surface. Phonon sensors are located on the faces of the detectors. In 2018, SuperCDMS, published their latest limits with an exposure of 1690 kg-days, an upper limit of $1.4 \times 10^{-44}\,\mathrm{cm}^2$ is set on the WIMP-nucleon spin-independent cross section [46]. The CDMSlite experiment applied even higher voltages to the CDMS detector modules, allowing to convert the ionisation signal to phonons and therefore lower the threshold to 56 eV and publish the best limits between 1.6 to 5.5 GeV [54]. CRESST uses $CaWO_4$ crystals as detector modules and transition-edge sensors (TES) to read out the phonon signal. The scintillation light is detected using silicon calorimeters, which in turn are also read out by TES. With CRESST-III, the collaboration has moved their focus completely onto the mass region of a few GeV WIMPs. The 2019

results from CRESST-III show an energy threshold of 30.1 eV for one of their detector modules, which allows them to put limits down to 0.16 GeV, providing the leading limits below 1 GeV [47].

1.3.3.4 Noble liquid detectors

In the $10 - 100\,\mathrm{GeV/c^2}$ mass range, the most sensitive detectors use the noble liquids argon and xenon. Similarly to cryogenic solid-state experiments, both argon and xenon allow discrimination between nuclear and electron recoils looking at scintillation and ionisation signals. While the discrimination achieved is not quite as good as for cryogenic solid-state experiments, these liquids can be purified more easily, and the detectors can be scaled up relatively straightforwardly. Using a two-phase time-projection chamber configuration, these experiments offer excellent vertex reconstruction and enable fiducialization, which reduces backgrounds considerably. The scintillation light signal (S1) is detected with photomultiplier tubes (PMTs) at the bottom and top of the detector. An electric drift field is applied to the detector to transport the ionisation charge to a gas phase region where it induces electroluminescence light which is detected by the PMTs. Due to the A^2 term in Equ. 1.4, xenon has a higher WIMP-nucleus interaction cross-section than argon. There are no long-lived radioisotopes in natural xenon. Odd-neutron isotopes allow sensitivity to spin-dependent cross-sections. Argon is cheaper than xenon, has a higher ionisation yield and better ER-NR discrimination using pulse-shape discrimination. Unfortunately, naturally occurring argon contains the radioisotope ^{39}Ar [55].

DEAP-3600 is a single-phase argon detector based at SNOLAB in Canada. It consists of a single-liquid phase containing 1 ton of LAr, surrounded by Photomultiplier Tubes detecting scintillation light. ER-NR discrimination can be achieved using the scintillation pulse shape. For 4.44 days of data, DEAP-3600 has published a limit of $1.2 \times 10^{-44}\mathrm{cm}^2$ for a WIMP mass of 100 GeV and is still collecting more data [56].

DarkSide-50 is a two-phase argon TPC using low-radioactivity argon from underground sources. They recently published a limit of $1.14 \times 10^{-44}\text{cm}^2$ for an exposure of 16660 kg-days [57]. For the next generation, several smaller collaborations are joining together to build DarkSide-20k, still pursuing a TPC but moving to silicon photo-sensors which are more efficient and radio-pure [58].

The current best spin-independent WIMP-nucleon limits are held by two-phase xenon time-projection chambers. The LUX experiment ran in the Davis Cavern at SURF, South Dakota from 2013 to 2015. The combined results over the entire exposure of 3.35×10^4 kg-days had a minimum cross section of $1.1 \times 10^{-46}\,\text{cm}^2$ at $30\,\text{GeV/c}^2$ [59]. The Chinese PandaX-II experiment had a 54 ton-day exposure and reached $8.6 \times 10^{-47}\,\text{cm}^2$ at $40\,\text{GeV/c}^2$. The best results are from Xenon1T in the Italian Gran Sasso Laboratory. With 1 t-year exposure, they set a limit of $4.1 \times 10^{-47}\,\text{cm}^2$ at $30\,\text{GeV/c}^2$ [45]. While the PandaX collaboration is moving towards a neutrinoless double beta decay search with PandaX-III, LUX-ZEPLIN and XenonNT are second generation LXe TPCs going up to 7 ton fiducial volume. They are currently under construction.

More recently, it has been suggested that liquid noble gas experiments can extend their sensitivity towards sub-GeV masses using the Migdal effect and bremsstrahlung in inelastic scattering. The atomic electrons around a recoiling nucleus only follow the nucleus with some delay which causes ionisation and excitation of the recoiling atom. This ionisation and excitation provide additional energy deposited in the detector, producing a measurable signal [60]. Nuclear bremsstrahlung describes the emission of a photon from a recoiling atomic nucleus [61]. For low-mass dark matter particles, both effects lead to an electron recoil event of higher energy than the corresponding nuclear recoil. LUX has extended their limit down to 0.4 GeV by taking advantage of these effects [62]. It has been shown that considering the Migdal effect, second-generation two-phase xenon time-projection chambers like LZ could be sensitive down

to a mass of 0.1 GeV [63].

1.3.3.5 Spin-dependent searches

Liquid xenon TPCs have also set the leading limits on spin-dependent WIMP-neutron cross-sections thanks to odd-neutron isotopes. The PICO experiments at SNOlab have reached the leading limits for WIMP-proton spin-dependent cross-sections. PICO employs a bubble chamber technique, where a superheated fluid is kept just below its boiling point, and particle interactions cause bubble nucleation. The location of the bubble is determined by taking an image with a CCD camera. Backgrounds such as gammas, do not deposit enough energy for bubbles to form. The remaining backgrounds are α particles. These are louder than nuclear recoils. Therefore an acoustic signal can be used to distinguish these events [64]. PICO-2L used two litres of C_3F_8 and PICO-60 used 60 litres of CF_3I. With PICO-60 the collaboration reached the most stringent limits of $2.5 \times 10^{-41}\,\mathrm{cm}^2$ for a $25\,\mathrm{GeV/c}^2$ WIMP at 1404 kg-day exposure [65]. A next-generation detector moving to up to 500 kg of active mass is in development.

1.3.3.6 Directional detectors

Another possible way of discriminating WIMP signals from background is directionality. If the detector can measure not only the energy deposited in the detector but also the direction of the nuclear recoil, the cosmological origin of the signal can be confirmed. The DRIFT collaboration pioneered the technique of recoil tracking in low-pressure gas TPCs [66]. The international Cygnus collaboration is planning to place large low-pressure gas TPCs in several underground laboratories around the world. Cygno is the prototype detector proposed within this project and will be located in LNGS [67].

1.3.3.7 Next generation experiments

Apart from DAMA/LIBRA, no experiment is currently claiming to have seen any signs of dark matter. The biggest improvements in sensitivity are expected from next-generation LXe TPCs. LUX-ZEPLIN and XenonNT will start taking data within the next year and are promising to close most of the parameters space towards the neutrino floor for WIMP masses larger than 10 GeV. A more detailed sensitivity expectation for LUX-ZEPLIN is presented in the next chapter. Beyond these next-generation experiments, there are plans for a third-generation LXe TPC of 50 ton, called DARWIN [68]. This experiment would start to cut into the so-called neutrino floor, the ultimately irreducible background of atmospheric and solar neutrinos. Cryogenic solid-state experiments will continue to push for lower energy thresholds and to become more sensitive in the low mass region. While next-generation searches using directional detectors and bubble chambers (PICO) are planned, the dark matter community is also looking for new ideas, knowing that having many complimentary searches for dark matter is useful [69].

Chapter 2

The LUX-ZEPLIN Experiment

The LUX-ZEPLIN (LZ) experiment is a next-generation search for dark matter currently under construction at SURF, South Dakota. LZ employs a two-phase, liquid xenon time projection chamber. This chapter introduces the experimental concept of liquid xenon time projection chambers focusing on the LUX-ZEPLIN detector system. It starts by discussing particle interactions in liquid and gaseous xenon and the theory behind signal generation, before looking at the LZ detector, its calibration and backgrounds in more detail. Finally, LZ simulation, analysis tools and the sensitivity projection are presented.

2.1 LXe Time-Projection Chambers

Liquid xenon (LXe) is a very favourable detector material for WIMP direct detection searches. As shown in the previous chapter, the WIMP-xenon nucleus interaction cross-section is large for intermediate WIMP masses of O(10-100) GeV due to its high atomic number $A = 131$. Xenon does not have any long-lived radioactive isotopes, which makes it very suitable for low background searches. Naturally occurring odd-neutron isotopes of xenon allow searches for spin-dependent WIMP interactions. If a particle interacts with the atomic nucleus or electrons in LXe, scintillation photons

and ionisation electrons are emitted. As xenon is transparent to its scintillation light, a detectable signal is created. The high scintillation and ionisation yields of LXe mean that even very low energy interactions produce a measurable signal [55, 70].

These excellent properties can be optimally exploited using a two-phase LXe time-projection chamber. ZEPLIN-III [71] and Xenon10 [72] pioneered the method. The current best limits are held by Xenon1T [73], LUX [44] and PANDA-X [74]. In general, time-projection chambers (TPC) use electric fields to allow 3D event localisation. For two-phase LXe TPCs, the detector consists of a large liquid phase and a thin gas phase layer on the top of the detector as seen in Fig. 2.1. Scintillation photons produced by an interaction in the liquid volume are detected by Photomultiplier Tubes (PMT) on top and bottom of the detector. Ionisation electrons are extracted to the gas phase by a vertical electric field of several 100 V/cm. In the gas phase, they are accelerated and produce electroluminescence light, which is detected by the PMTs. Every interaction, therefore, gives both a prompt scintillation signal and a delayed, larger electroluminescence signal. Having two signals allows both 3D position reconstruction and background discrimination, as discussed in the following sections.

2.2 Particle interactions and detection

2.2.1 Particle interactions in LXe

WIMPs are massive, electrically neutral particles. They are expected to interact with the atomic nucleus of xenon and cause a nuclear recoil (NR). Nuclear recoils can also be caused by neutrons, daughter nuclei from radioactive decays and the coherent scattering of neutrinos of an atomic nucleus [76]. The majority of radioactive background radiation, like betas and gammas, preferentially interact with the atomic electrons and induce electron recoils (ER) [77].

The recoiling particle in both cases (ER and NR) scatters with neighbouring

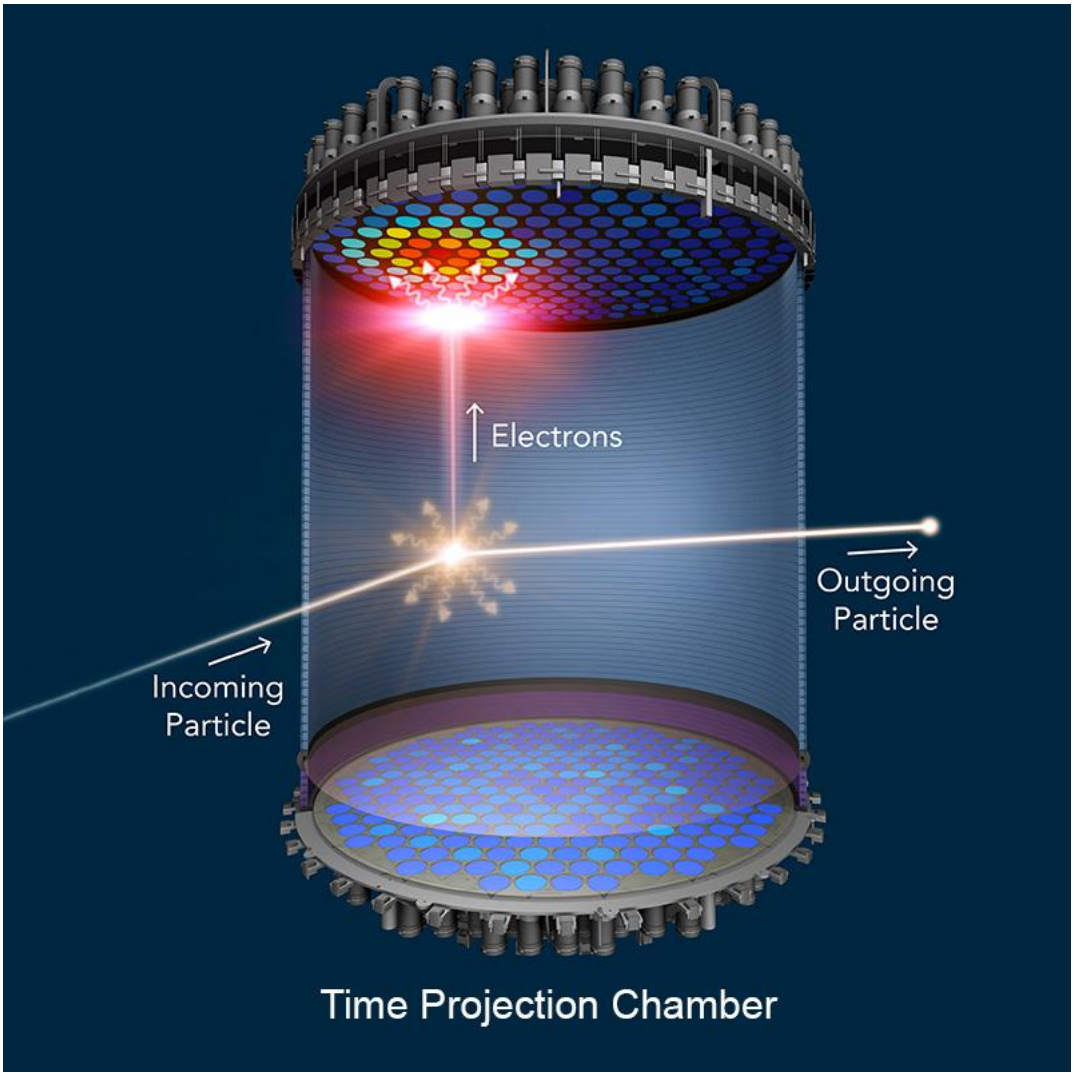

Figure 2.1: Schematic drawing of a particle interacting in the LZ time-projection chamber [75]

atomic electrons and nuclei and causes excitation and ionisation of the surrounding atoms. Recoiling electrons create well-defined tracks along which energy is deposited primarily in the form of excitation and ionisation and only some nuclear scattering. A recoiling nucleus is likely to scatter off an entire xenon atom and transfer energy to the target atom in the form of kinetic energy. This atomic motion cannot be detected in LXe TPCs. For NRs, therefore, a smaller fraction of the deposited energy goes into the electronic system and creates a measurable signal. The different signatures are further discussed in the following sections.

2.2.2 Primary scintillation - S1 signal

Through the impact of an electron or a nuclear recoil, a xenon atom reaches an excited state (Equ. 2.1- 2.2). It forms a molecular excimer (dimer) with a neighbouring atom (Equ. 2.2). It is distinguished between excited states with vibrational excitation (Equ. 2.2) and states with purely electronic excitation ($\nu = 0$) (Equ. 2.3). The excimer de-excites to the ground state under the emission of a VUV photon (Equ. 2.4).

$$e^- + Xe \rightarrow Xe^* + e^- \tag{2.1}$$

$$Xe^* + Xe \rightarrow {Xe_2}^{*,\nu} \tag{2.2}$$

$${Xe_2}^{*,\nu} + Xe \rightarrow {Xe_2}^* + Xe \tag{2.3}$$

$${Xe_2}^* \rightarrow Xe + Xe + h\nu \tag{2.4}$$

The second path to the release of scintillation photons is the recombination of ionisation electrons with di-atomic xenon ions. Di-atomic xenon ions form when xenon ions interact with neighbouring xenon atoms (Equ. 2.6). Recombination leads to an excited atomic state (Equ. 2.7). The excited atom forms a molecular excimer with a neighbouring atom (Equ. 2.8- 2.9) and decays following a similar de-excitation path as the dimer in the scintillation process. Again a VUV photon is emitted (Equ. 2.10).

$$e^- + Xe \rightarrow Xe^+ + 2\,e^- \tag{2.5}$$

$$Xe^+ + Xe + Xe \rightarrow {Xe_2}^+ + Xe \tag{2.6}$$

$$e^- + {Xe_2}^+ \rightarrow Xe^{**} + Xe \tag{2.7}$$

$$Xe^{**} + Xe \rightarrow Xe^* + Xe + \text{heat} \tag{2.8}$$

$$Xe^* + Xe + Xe \rightarrow Xe_2^* + Xe + \text{heat} \tag{2.9}$$

$${Xe_2}^* \rightarrow Xe + Xe + h\nu \tag{2.10}$$

The fraction of ionisation electrons undergoing this recombination process is dependent on the initial recoil energy, and the electric field applied [78]. The VUV scintillation light is centered around 178 nm with FWHM 14 nm. Light attenuation is due to absorption and Rayleigh scattering. Absorption is mostly due to impurities like water vapour, as self-absorption of the scintillation photons in VUV is very unlikely. It is, therefore, essential to purify the xenon to a high degree. In LZ absorption lengths between 30 and 100 m are expected. The VUV scintillation light can be detected by the PMTs located on top and bottom of the detector and is typically referred to as the S1 signal [55, 70].

2.2.3 Secondary scintillation - S2 signal

The remaining ionisation electrons are transported to the liquid surface by applying a vertical electric field. The electrons have to overcome a potential barrier at the liquid surface to escape into the gas phase. To enable this, an electric field of several kV/cm is applied between a grid just below and one just above the liquid surface [79]. In the gas phase, the electrons are further accelerated. In collisions with xenon atoms, they produce xenon excimers. When the excited atomic states relax back to the ground state, VUV photons are emitted. The light emission spectrum is similar

to the scintillation spectrum. This process is also referred to as electroluminescence [55]. The electroluminescence or S2 signal is again detected by the PMTs on top and bottom of the detector. The number of electroluminescence photons per electron depends on the applied electric field and the pressure in the gas phase. Compared to the S1 signal, the S2 signal is orders of magnitude larger and delayed due to the time it takes the electrons to drift to the liquid surface. For the LZ detector with a TPC height of 1.46 m and a drift field of 0.31 kV/cm, an electron from the bottom of the detector travels on the order of 800 µs. The hit pattern of the S2 signal on the PMTs at the top allows position reconstruction in the horizontal plane. The time delay between S1 and S2 signal adds information about the vertical position of the interaction in the detector, allowing 3D event reconstruction. Electrons diffuse on their way to the liquid surface. This diffusion limits our knowledge on the interaction position and smears the S2 signal width. In LZ, electrons from the bottom of the detector have an expected diffusion of 2.2 mm in the transverse direction and 1.4 mm longitudinally [75]. More problematic is that a fraction of ionisation electrons are lost to the capture of electrons on electro-negative impurities in the liquid, like oxygen and water atoms. The electron lifetime can be measured and used to correct the reduction in S2 signal size. However, to be able to detect even small S2s from the bottom of the detector, high xenon purity is needed.

2.2.4 Light and charge yields

As discussed in the previous sections, both ERs and NRs deposit energy in the form of ionisation, excitation and heat. The deposited energy, E can, therefore, be expressed as a function of the number of excitons, n_{ex} and electron-ion pairs, n_i [78]:

$$E = LW(n_{ex} + n_i). \tag{2.11}$$

The average energy needed to produce a single exciton or electron-ion pair has been measured to be

$$W = 13.7 \pm 0.2\,\text{eV}. \tag{2.12}$$

The factor L accounts for energy lost in the form of heat. For ERs, this fraction is negligible, and it can be assumed that all energy goes into the electronics system and contributes to a measurable signal ($L = 1$). The fraction of nuclear recoil energy transferred to electrons varies with energy and is described by the Lindhard model:

$$L = \frac{kg(\epsilon)}{1 + kg(\epsilon)}, \tag{2.13}$$

where $g(\epsilon)$ is a function that models the ratio of electronic to nuclear stopping powers. The proportionality constant k gives the relationship between the electronic stopping power and the velocity of the recoiling nucleus [80, 81]. The Lindhard model describes interactions in xenon above 2 keV well with $k = 0.17$. For low energy interactions, additional biexcitonic effects have to be taken into account [82, 44].

To express energy in terms of the measurable quantities in LXe TPCs, scintillation photons and electroluminescence from electrons, recombination and detector efficiencies have to be considered. The number of photons, n_γ and electrons, n_e after recombination can be expressed as

$$n_\gamma = n_{ex} + n_i r \tag{2.14}$$

$$n_e = n_i(1 - r), \tag{2.15}$$

where r is the fraction of ions which recombine. Recombination is anti-correlated, therefore $n_{ex} + n_i = n_\gamma + n_e$. Defining the scintillation light collection efficiency as g_1, and the light collection efficiency in gas as $g_{1,gas}$, the S1 and S2 signals (in units of detected photons) can be written in terms of n_γ and n_e:

$$S_1 = n_\gamma g_1 \tag{2.16}$$

$$S_2 = n_e \epsilon N_{ph} g_{1,gas}. \tag{2.17}$$

Here, ϵ is the electron extraction efficiency and N_{ph} is the number of electroluminescence photons per electron. Defining the overall electron detection efficiency as $g_2 = \epsilon N_{ph} g_{1,gas}$, E becomes

$$E = LW \left(\frac{S_1}{g_1} + \frac{S_2}{g_2} \right). \tag{2.18}$$

From calibrations of past LXe TPC detectors, it is known that electron and nuclear recoils differ in their light and charge yields. For ERs the ratio of excitons to electron-ion pairs is < 0.2 [83, 84]. For NRs the relative fraction of excitons is approximately 1. The recombination fraction for both processes depends on the applied electric field, particle energy and fluid density. The difference in initial exciton to ion ratio leads to a different S2/S1 ratio for ERs and NRs [85].

2.2.5 Discrimination and self-shielding

Background levels must be kept low and be well understood to be able to search for rare interactions. LXe time projection chambers have desirable properties which allow background reduction, most notably ER-NR discrimination and self-shielding.

As discussed in the previous section, ERs and NRs differ in their ratio of ionisation electrons to scintillation photons. When plotting the $\log_{10}$(S2/S1) of interactions versus S1, ERs and NRs form two distinct bands, as shown in Fig. 2.2. ER events leaking below the NR mean, extracted from a Gaussian fit, limit the ER-NR discrimination. LZ expects to achieve a 99.5% ER-NR discrimination by rejecting all events above the NR median line [86].

The large, dense, high-Z and continuous detection medium with the ability to

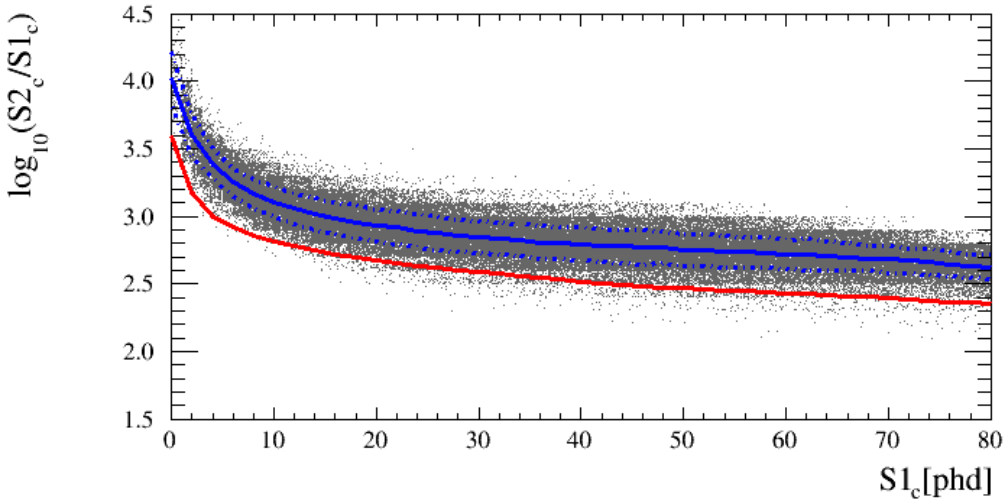

(a)

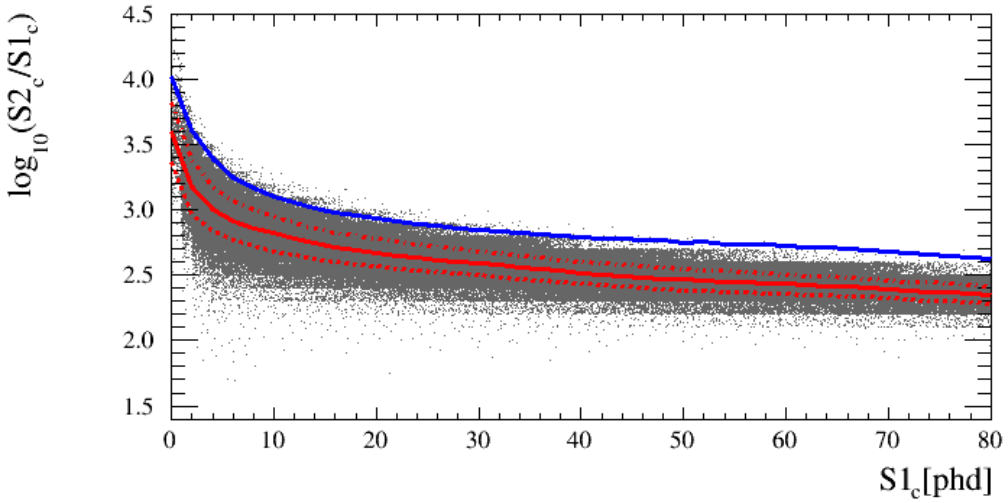

(b)

Figure 2.2: Simulated ER and NR events in LZ in $\log_{10}$(S2/S1) vs S1 parameter space show the distinct (a) ER and (b) NR bands. The Gaussian mean and standard deviation contours (dashed) are indicated in red (NR) and blue (ER). The units are photons detected (phd).

resolve interaction sites in 3D allows the definition of a fiducial volume. For the LZ detector, which is much larger than the mean interaction length of gamma-rays and neutrons, the fiducial volume is shielded by a layer of xenon on the outside.

2.3 The LUX-ZEPLIN detector

2.3.1 Overview and status

The LZ detector is 20 times larger than its predecessor LUX. While in principle, the detector concept is the same, having a much larger detector brings new challenges such as the maximisation of light collection and electron extraction efficiency in the TPC to be sensitive to even low WIMP masses. Backgrounds have to be well understood and minimised to maximise LZ sensitivity. Extensive screening campaigns were conducted to only select radiopure materials for the detector construction. Additionally, LZ is the first LXe TPC with two dedicated anti-coincidence veto detectors, as shown in Fig 2.3. The detector will be located in a large water tank 4850 feet underground in the Davis Cavern at SURF, South Dakota. It is currently being assembled, and the first physics data-taking will start in 2020.

2.3.2 TPC

The LZ detector is nested in two cryostats made from ultrapure titanium [87]. The inner cryostat (ICV) contains 10 tonnes of LXe and is vacuum insulated inside the outer cryostat (OCV). The TPC, as shown in detail in Fig. 2.4, is a cylinder with height and width of 1.46 m, containing 7 tonnes of LXe. To increase the light collection efficiency, the TPC walls are made of highly reflective PTFE. High voltage is applied to four horizontal electrode plates woven from stainless steel wires, which split the TPC into three different field regions, as shown in Fig. 2.5: Drift Field Region, Extraction Field Region and Reverse Field Region.

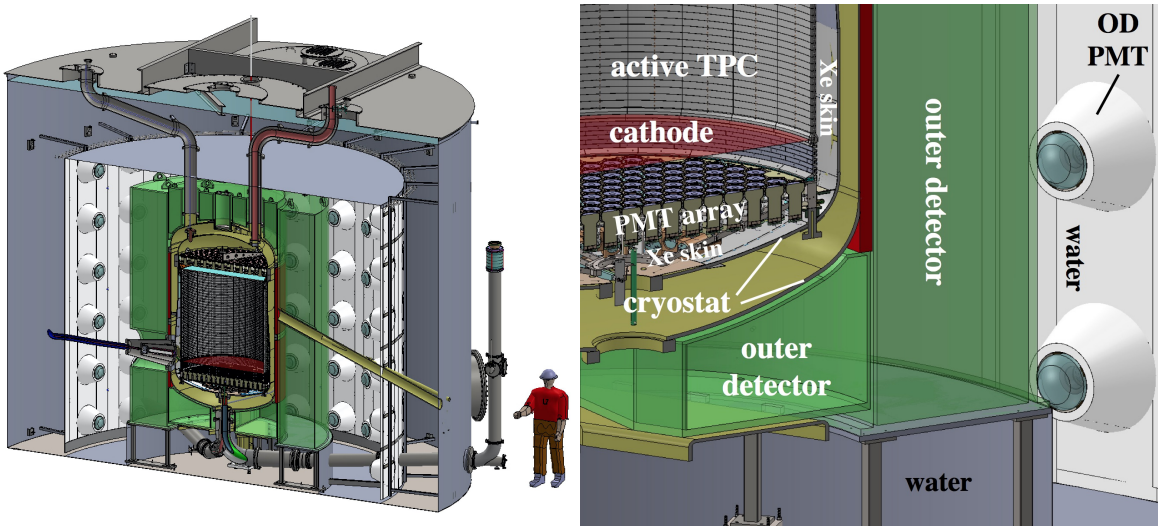

(a) (b)

Figure 2.3: (a) Schematic drawing of LZ detector, including the Outer Detector tanks (green) and their dedicated light collection system (white). The entire experiment is surrounded by a water tank system (blue-grey). (b) Zoom into lower right corner, showing the different detectors in more detail.

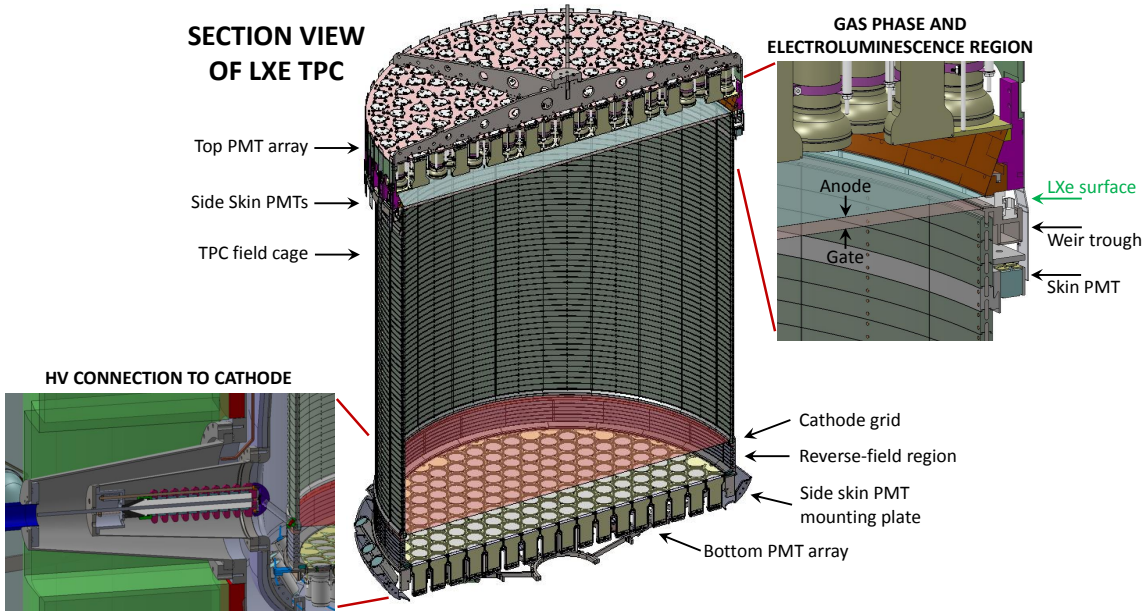

Figure 2.4: Cross-section view of LZ time-projection chamber with PMT array and high voltage delivery.

Parameter [units]	Value
TPC active height [m]	1.46
TPC inner diameter [m]	1.46
active LXe mass [kg]	7000
xenon skin thickness [cm]	4.0 - 8.0
inner cryostat diameter [m]	1.58-1.66
inner cryostat height [m]	2.59
outer cryostat diameter [m]	1.83
outer cryostat height [m]	3.04
GdLS tanks outer radius [m]	1.64
GdLS mass [t]	17.3
water tank diameter [m]	7.62
water tank height [m]	5.92
water mass [t]	228

Table 2.1: LZ detector dimensions [86]

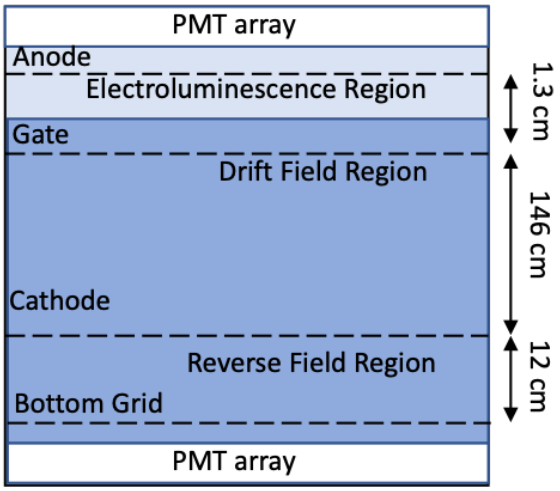

Figure 2.5: Cross-section sketch of the LZ detector indicating the grids and field regions (not to scale).

The Drift Field Region contains the active fiducial volume of the TPC. It is located between the cathode at the bottom of the detector and the gate just below the liquid surface. 57 equally spaced field-shaping rings are embedded into the TPC walls connected by resistors to grade the electric field in this region. They provide a vertical drift field to transport ionisation electrons to the liquid surface.

The extraction field and electroluminescence region are located between the gate and anode grids. The field in the region between the gate and liquid surface must be significantly higher than the drift field to increase the electron extraction probability. Due to the lower dielectric constant of the gas phase, the field in the xenon gas is about twice as strong as in liquid.

Another grid is located just below the cathode creating the reverse field region, which is needed to shield the bottom PMTs from the electric field. Ionisation electrons from interactions in the reverse field region are not extracted. Hence, events occurring in this region only have an S1 signal. All nominal voltages and fields are summarised in Table 2.2.

Grid/Field	Design Voltage
Cathode Voltage	-50 kV
Gate Voltage	-4 kV
Anode Voltage	+4 kV
Gas Region Field	10.6 kV/cm
Drift Field	0.31 kV/cm

Table 2.2: Nominal design voltages and field strengths [75].

2.3.3 PMT arrays and light collection

494 PMTs monitor the active liquid xenon region inside the TPC. The PMTs, model number R11410-22, were developed for LZ and manufactured by Hamamatsu. They were optimised for low-radioactivity and excellent performance in liquid xenon detectors. The PMTs have a high quantum efficiency (QE) to VUV light (25-30%), an excellent SPE resolution and low dark noise. With 12 dynode stages, they have a nominal gain of 5×10^6 at an operating voltage of 1500 V. They can be operated stably at liquid xenon temperatures [88]. The PMTs are installed on titanium support frames on top and bottom ends of the TPC. 241 PMTs are located on the bottom and 253 on the top array. The layout of the PMTs in the arrays was optimised for high light collection efficiency. The S1 signal, originating in the liquid phase, is preferentially detected by the bottom array PMTs which are immersed in the liquid. A high S1 light detection efficiency is needed for low-energy NR events, as well as ER-NR discrimination. The array layout of a closed packed hexagonal pattern was chosen to maximise the photocathode coverage of the TPC cross-section. The top array detects most of the S2 light and is used for the position reconstruction of events. To allow accurate position reconstruction of events from the TPC walls, which is needed for fiducialization, the outermost row of PMTs is located above the TPC wall [75].

2.3.4 Monitoring sensors

A range of sensors has been developed to monitor the TPC conditions during commissioning and operation. Capacitive level sensors monitor filling and draining of detector and the liquid surface during operation [89]. A hexapod with six displacement sensors connects the top PMT array to the ICV lid. This system is used to measure any displacement or tilt between the two as could happen due to unequal material contraction during cool-down [90]. Pt100 thermometers are distributed in both the ICV and OCV to monitor the temperature at all times. Additionally, acoustic sensors are installed on the outside of the ICV, listening for bubble formation and, therefore, providing information on the thermal environment [91]. The loop antennae system discussed in Chapter 5 is used to monitor the electrostatic environment of the detector, especially looking for high voltage discharges.

2.3.5 Xenon system

The liquid xenon temperature in the cryostat is maintained at 175 K using a thermosyphon system [92]. Electro-negative impurities in the xenon, lead to a finite electron lifetime. Due to outgassing materials, like the PTFE of the TPC walls, it is necessary to purify the xenon continuously. The goal is to suppress impurities to the level of 0.1 ppb at all times. The liquid is circulated to an external purification tower, where the liquid is evaporated. The xenon gas is then passed through a commercial getter, before being condensed back and circulated back into the detector. Separate gas flow through the purification system ensures high purity in the gas phase [75].

2.3.6 Veto detectors

LZ has two veto detectors, the Skin and the Outer Detector (OD). A WIMP which interacts in the TPC does not deposit energy in the veto, while backgrounds like

neutrons are likely to do so.

The several cm thick xenon skin between the TPC wall and the ICV and the dome skin below the bottom PMT array are instrumented with PMTs to be used as an anti-coincidence detector. In total there are 93 1-inch PMTs (Hamamatsu R8520) and 20 2-inch PMTs (Hamamatsu R8778) observing the side skin and 18 2-inch PMTs (Hamamatsu R8778) viewing the dome region. The skin region is far less sensitive than the inner TPC region, as only scintillation light is collected, and the light collection efficiency is much worse. The skin is primarily intended for the detection of internal gamma rays, but can also detect neutrons.

The Outer Detector is a near-hermetic gamma-ray and neutron anti-coincidence system. It consists of 10 acrylic tanks filled with 17 tonnes of gadolinium-loaded liquid scintillator. This region is monitored by 120 8-inch PMTs (Hamamatsu R5912), which are located in the water space outside of the transparent acrylic tanks. The liquid scintillator used is linear alkylbenzene (LAB). 0.1% neutral gadolinium is added to enhance the neutron detection [93]. Additional standard fluor and wavelength shifter are added to provide a scintillation wavelength detectable by the PMTs. If a neutron interacts in the TPC, it is likely to pass through the OD and capture on the gadolinium. A total energy of about 8 MeV is emitted as a burst of several gamma rays, which interact and create detectable signals in the LS. The OD response would happen well within the event time window frame of the TPC, therefore providing an effective coincidence veto [75].

2.3.7 DAQ

The PMT signal is shaped and amplified by the analogue front-end electronics. Each PMT is read-out by two channels with different amplification. The low gain channel amplifies the PMT pulse area by a factor of four. It is intended for high energy events. The high gain channel has a 40 times amplification and is needed for low energy

Isotope	Interacting particle	Purpose	Deployment
Tritium	beta, Q = 18.6 keV	ER band	Internal
^{83m}Kr	beta/gamma, 32.1 keV/9.4 keV	TPC (x,y,z)	Internal
^{131m}Xe	164 keV gamma	TPC (x,y,z), Xe skin	Internal
^{220}Rn	various alphas	xenon skin	Internal
AmLi	(alpha, n)	NR band	CSD
^{252}Cf	spontaneous fission	NR efficiency	CSD
^{57}Co	122 keV gamma	Xe skin threshold	CSD
^{228}Th	2.615 MeV gamma	OD energy scale	CSD
^{22}Na	back-to-back 511 keV gamma's	TPC and OD sync	CSD
^{88}Y Be	152 keV neutron	low-energy NR response	External
^{205}Bi Be	88.5 keV neutron	low-energy NR response	External
^{206}Bi Be	47 keV neutron	low-energy NR response	External
DD	2,450 keV neutron	NR light and charge yields	External
DD	272 keV neutron	NR light and charge yields	External

Table 2.3: LZ calibration sources with their deployment and calibration purpose [75]. Internal dispersed sources are gaseous sources which are in injected into the xenon circulation process. The calibration source deployment (CSD) allows the deployment of neutron and gamma sources in the region between the inner and outer cryostat. External sources are located outside the outer cryostat.

events. Subsequently, the signal is digitised at 100 MHz and 14-bit resolution with a dynamic range of 2 V. To save disk space, LZ uses a Pulse Only Digitisation (POD), i.e. pulses and only minimal baseline are digitised. An online trigger using digital filters to distinguish between S1 and S2 pulses is used for further data sparsification [94].

2.4 Calibrations

2.4.1 Overview

LZ employs a range of calibration sources to calibrate the detector response as accurately as possible. Due to self-shielding of xenon, it is necessary to employ internal calibration sources, additionally to external sources. An overview of all calibration sources and their deployment is given in Table 2.3

2.4.2 Internal dispersed sources

A range of gaseous sources is injected into the xenon circulation process. These are needed to calibrate for spatially varying detector efficiencies. The S1 light collection efficiency in the detector depends on the position of the event. Electro-negative impurities in the xenon mean that the ionisation electrons have a finite lifetime. Therefore, fewer electrons are extracted for events taking place at the bottom of the detector. The mono-energetic sources ^{83m}Kr and ^{131}Xe can be used to determine correction factors. The detector response is then corrected to the middle of the detector [95].

To calibrate the ER band, LUX pioneered the use of tritiated methane. Tritium (^{3}H) is a β^- emitter with a Q value of 18.6 keV$_{ee}$, which is very well suited to calibrate the ER band down to threshold. LUX demonstrated that purification systems could effectively remove the tritiated methane molecule without leaving any activity [96].

^{220}Rn is a source of large S1 pulses and therefore useful for the calibration of the xenon skin. Different from ^{222}Rn, ^{220}Rn has no long-lived radioactive daughters and can be introduced into the detector safely [75].

2.4.3 Calibration source deployment

The calibration source deployment system consists of 3 vertical stainless steel tubes, which are located between ICV and OCV. This system allows the deployment of neutron and gamma calibration sources. A range of neutron sources, like AmBe and AmLi, are deployed to characterise the NR band. External gamma-sources are used to calibrate for high-energy backgrounds, look at the signals near the edge of the TPC and characterise the response of the veto detectors [75].

2.4.4 External sources

A photoneutron source is used to calibrate low energy NRs, in the region in which Boron-8 neutrinos are expected to appear. Photoneutron sources use (γ, n) reactions on nuclei to produce neutrons. In LZ the photoneutron source is deployed above the outer cryostat [75].

A deuterium-deuterium neutron source is used for NR calibrations. The generator is set up outside of the water tank. It produces a mono-energetic neutron beam which can travel through conduits in the LZ water tank and OD to reach the active Xe volume. This technique was pioneered by LUX and allows an in-situ NR calibration down to low energies [82].

2.5 Backgrounds

2.5.1 Cosmogenic backgrounds

Cosmogenic backgrounds are mitigated by underground operations and the water tank which surrounds the Outer Detector. The rock overburden of 4,300 m water equivalent reduces the muon flux by a factor of 3×10^6 relative to the earth surface. The remaining muons are easily vetoed as they are likely to deposit energy in the water tank or veto detectors [97]. More problematic are neutrons produced in muon-induced electromagnetic and hadronic showers. These neutrons can generate background events in the detector. However, they are expected to scatter multiple times in the TPC or the veto detectors, while candidate events are only single scatters [98].

2.5.2 Surface contaminants

A big concern for the experiment is plate-out of dust on detector surfaces during production and construction. ^{222}Rn is present in air. Charged radon progeny can settle on surfaces exposed to air. Radon daughters, like ^{210}Po and ^{214}Pb release alpha particles in the decay chain, which results in neutron emission following an alpha-n reaction. Plate-out is therefore especially problematic for materials with large (α, n) yields such as PTFE, which is the main material of the TPC [86].

Decays of radon progeny on the TPC wall, due to energy and charge loss at the wall, have a broad energy spectrum and reach into the NR signal region in the $\log_{10}$(S2/S1) parameter space. It is therefore essential to accurately reconstruct the radial position of interactions and use fiducial cuts to eliminate such wall-events from the data. Radon daughters such as ^{210}Pb can also become mobile and enter the fiducial volume.

Dust settling on surfaces during construction has intrinsic radioactivity and radon. Dedicated cleanliness protocols are in place for the manufacture, cleaning and assembly of all detector components to reduce the radon exposure and dust on surfaces.

2.5.3 Trace radioactivity

To reduce the trace radioactivity in the detector, LZ has gone through a comprehensive screening and material selection campaign [75]. Materials were screened for the gamma-emitting isotopes ^{40}K, ^{137}Cs, ^{60}Co, ^{238}U, ^{235}U and ^{232}Th and their progeny. Events from external radioactivity and trace radioactivity in detector materials are cut using the self-shielding properties of liquid xenon. For LZ, a fiducial mass of 5.6 tonnes which are practically free of external gamma-ray or neutron backgrounds can be defined. Additionally, anti-coincidence detectors (Skin and OD) look for coincident interactions.

More problematic are radioisotopes dispersed in the xenon, which cannot be ve-

toed using self-shielding. Such contaminants come primarily from radon emanation from materials and dust from the detector surfaces. Naked beta emission from ^{214}Pb in the ^{222}Rn sub-chain is the dominant source of background for LZ [86]. Online radon reduction is only possible for small streams of gas from problematic areas such as cable conduits. It was, therefore, important to radon-emanate all detector materials for material selection and accurate background modelling [99].

Xenon naturally has trace amounts of ^{85}Kr and ^{39}Ar. These are largely removed using a specially developed purification system [75].

2.5.4 Other backgrounds

As discussed in the previous sections, the dominant backgrounds in LZ are from radon daughter decays and ^{85}Kr. There are other non-standard backgrounds which are expected to contribute. A few background events are expected due to neutrino interactions. PP-solar neutrinos are expected to induce ER events. Atmospheric neutrinos can induce coherent scatters, which cause NRs. Coherent nuclear scattering of ^{8}B solar neutrinos is an important source of very low energy NR events [86].

Multiple scatters of gamma rays where one vertex occurs in the reverse field region are referred to as gamma-X events. Only scintillation light, but no charge collection for one of the vertices, lead to a lower S2/S1 ratio than average. Events are likely to leak into the NR band.

Another non-standard background is an accidental coincidence of simultaneous dark counts on multiple PMTs. Such coincidental dark counts can combine with S2-only events to fake S1-S2 pairs. A 3-fold PMT coincidence level is imposed for S1s in event selection to keep this coincidence rate low [86].

All estimated background rates for a 1000 day run are shown in Fig. 2.6.

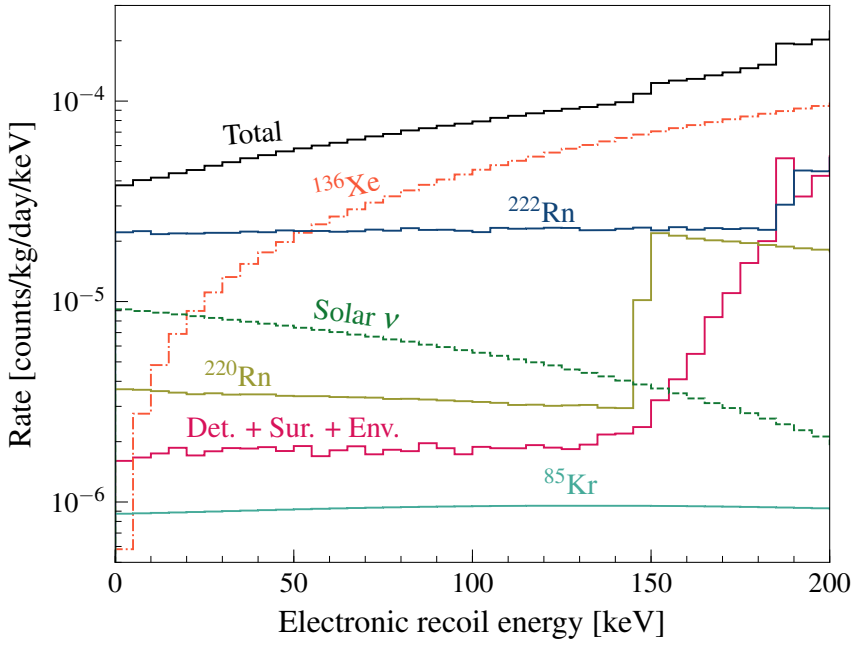

(a)

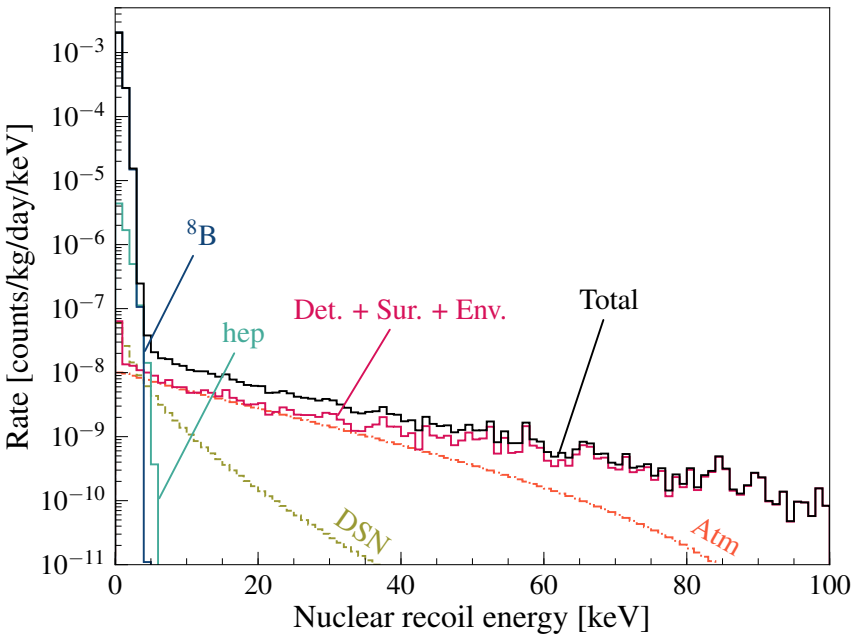

(b)

Figure 2.6: Projected single-scatter background events for a 1000 day science run which do not induce a signal in the veto detectors [86].

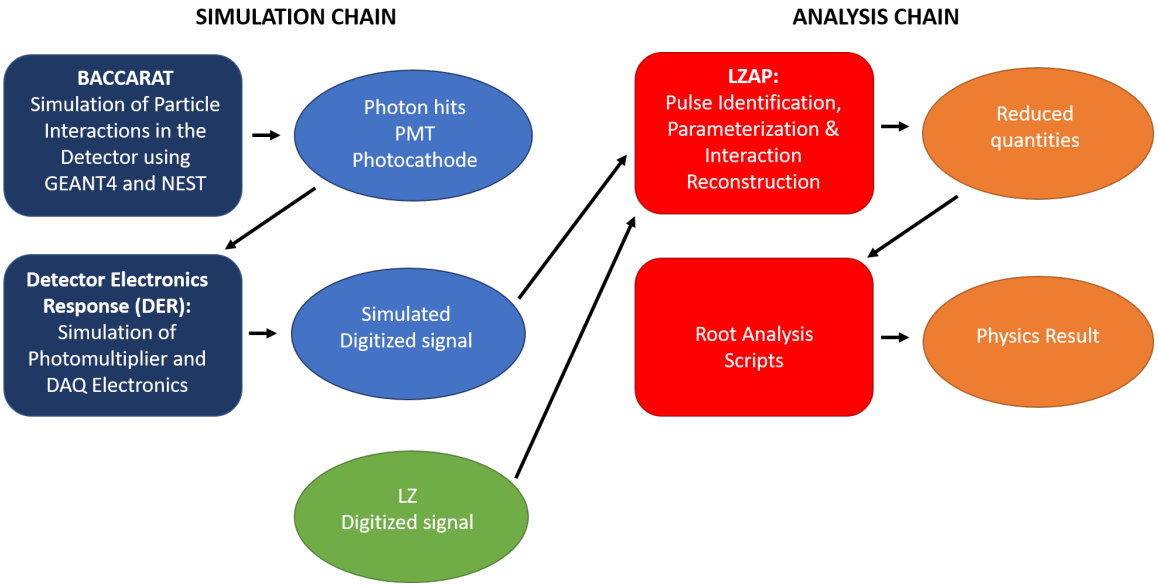

Figure 2.7: Simulation and Analysis framework overview.

2.6 LZ simulation and sensitivity projection

2.6.1 Overview

The LZ simulation tools have informed the design and construction of the experiment. They are used to evaluate the projected LZ sensitivity and train the LZ analysis framework. Fig. 2.7 shows an overview of LZ simulation and analysis tools and how they relate to the analysis of real data.

2.6.2 Simulation chain

The main LZ simulation is called BACCARAT. BACCARAT simulates particle interactions using the GEANT4 simulation package. The particle interactions and energy deposits are recorded on a geometry component basis. The Noble Element Simulation Technique (NEST) is used to convert the deposited energy into scintillation photons and ionisation electrons. NEST models the underlying microphysics using a semi-empirical collection of models verified using data from previous detector calibrations [100]. NEST is also used to simulate the drifting of ionisation electrons to the liquid

surface, their extraction to the gas phase and the production of electroluminescence light. Standard GEANT4 processes handle propagation of scintillation and electroluminescence photons until they reach a photocathode or are absorbed in a different material.

To convert PMT hits into waveforms, a second simulation package was developed. The Detector Electronics Response (DER) models the PMT response including quantum efficiency (QE) and dark noise, the front-end electronics and the digitisation of the signal. The resulting waveforms are saved in the same data structure as real LZ data to allow the training of analysis frameworks on simulation data. The PMT model developed for this part of the simulation is the topic of Chapter 3.

2.6.3 Event reconstruction and analysis

The LZap framework is used for event reconstruction of LZ simulation and real data. It finds, parameterises and classifies pulses. S1 and S2 pulses are combined into interactions. The position and energy of each interaction are reconstructed, and reduced quantities are written to file for further analysis. LZ will be using the same statistical-based x-y position reconstruction algorithm as LUX, Mercury [101]. Light response functions (LRFs) are used to predict the response of each PMT for interactions at an arbitrary distance from that PMT. These functions are directly obtained from calibration data, which minimises the reliance on simulations. Mercury uses an iterative method minimising all LRFs at the same time. For simulation studies prior to LZ data taking, Mercury employs LRFs obtained from simulation data. The S1 and S2 size is corrected for spatially varying detector efficiencies. The corrected quantities are denoted $S1_c$ and $S2_c$

After reconstructing events, several cuts are applied, starting with a single scatter cut. Secondly, a WIMP region of interest window is defined with a 3-fold coincidence in the TPC PMTs, a total corrected $S1_c$ size of less than 80 photons detected and

an uncorrected S2 signal larger than the equivalent of 5 single electrons (ensuring functional position reconstruction). Using the reconstructed position, fiducial volume cuts are applied to remove the background events near the edges of the TPC.

If there is a time-coincident signal in either of the veto detectors, the event is removed. For the Skin veto, the coincidence window is 800 µs before and after the time of the TPC S1 signal. If a signal of at least three phd is observed in this time frame, the event is vetoed. The event is also vetoed if at least 200 keV were deposited in the OD within 500 µs. These time intervals are chosen to ensure the vetoing of both prompt gammas and the delayed signals from thermal neutron capture.

2.6.4 Sensitivity projection

The LZ sensitivity is estimated using a Profile Likelihood Ratio method [102]. A frequentist background-only hypothesis test is done for each WIMP mass, finding the median 90% confidence level upper limit on the relevant WIMP-nucleon cross-section for the background-only hypothesis. The PLR package takes the signal and background probability density functions (PDFs) parameterised in $S1_c$ and $S2_c$ as input. PDFs are created using NEST. The LZ background rates are estimated by simulating the measured material radioactivity and anticipated levels of dispersed and surface radioactivity using BACCARAT and the detector parameters shown in Table 2.4. The standard analysis cuts discussed in Section 2.6.3 are applied to the event rates. For the region of interest of a 40 GeV WIMP 1195 ER counts and 1.03 NR counts are expected for 1000 live days in a 5.6 t fiducial volume. Assuming 99.5% discrimination with an NR acceptance of 50%, the ER counts reduce to 5.97 and NR to 0.52 counts. For the WIMP signal model, the standard halo model, as discussed in the previous chapter, is assumed.

The LZ projected sensitivity at 40 GeV is 1.6×10^{-48} cm^2 [86]. The sensitivity projection to SI WIMP-nucleon elastic scattering for 1000 live days and a 5.6 tonne

Detector Parameter	**Value**
g_1 [phd/ph]	0.119
$g_{1,gas}$ [phd/ph]	0.102
Single electron size [phd]	83
g_2 [phd/e]	79
PTFE-LXe reflectivity	0.977
LXe photon absorption length [m]	100
PMT efficiency at 175 nm	0.269
Single phe trigger efficiency	0.95
Single phe relative width	0.38
S1 coincidence level	3-fold
S2 electron extraction efficiency	0.95
Electron lifetime [μs]	850

Table 2.4: Projected detector parameters.

fiducial mass is displayed in Fig. 2.8. At low WIMP masses ($< 10\,\mathrm{GeV}$), the sensitivity is strongly dependent on the low energy nuclear recoil detection efficiency. Similarly, the observed rate of ^{8}B and hep solar neutrinos elastically scattering off xenon nuclei depends on the low energy threshold. The observation of neutrinos from the solar pp fusion chain belongs to a range of secondary science goals in LZ. Axion-like particles (ALPs) could interact in the detector via the axioelectric effect. An axion is absorbed, and an atomic electron is ejected, causing an ER signal with energies up to a few tens of keV$_{ee}$. Such a signal could be distinguished from the background due to its characteristic spectral shape [103]. Should a nearby supernova occur during the detector lifetime, LZ could observe neutrinos from it via coherent nuclear scattering [104]. Using xenon isotopes, LZ can conduct searches for rare processes. An example is the neutrino-less double-beta decay with ^{136}Xe [105]. The recent observation of two-neutrino double electron capture in ^{124}Xe by Xenon1T shows the feasibility of such rare process searches in LXe TPCs [106].

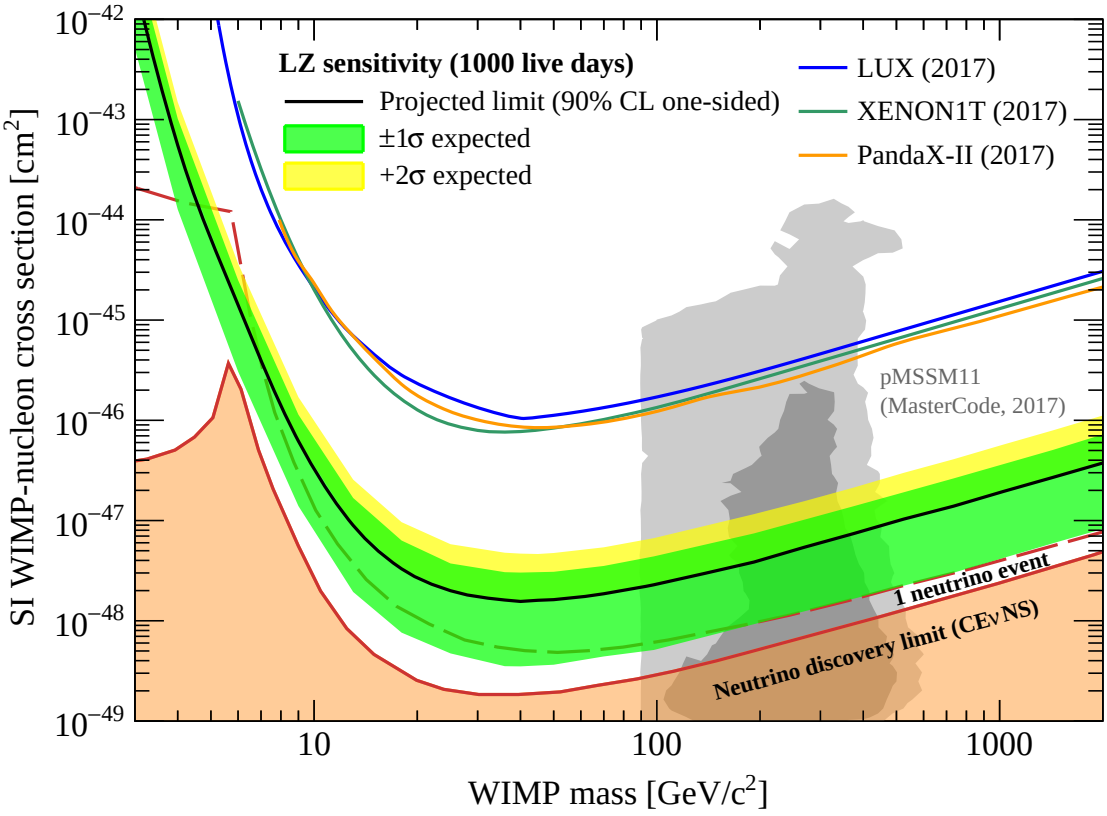

Figure 2.8: LZ sensitivity projection to SI WIMP-nucleon elastic scattering for 1000 live days and 5.6 fiducial mass compared to the LUX, XENON1T and PandaX-II results [86].

Chapter 3

PMT Single Photon Response

This chapter is concerned with the precise understanding and modelling of the LZ Photomultiplier Tube response to single photons. Including a realistic model of the PMT response in the simulation is essential for the understanding of signals in the detector and the development of sophisticated data analysis tools. In the first section, a PMT response model is introduced, which is the basis for the analysis of PMT measurements and simulation of PMT signals. Secondly, a study dedicated to characterizing pulses smaller than the regular single photoelectron response for the R11410 PMT type is presented. Building on these results, the third part of this chapter discusses improvements to the simulation of single photon signals to include different PMT dynode effects, dark counts and afterpulsing. Finally, the impact of different PMT effects on data analysis and detector performance is discussed. A possible improvement to low mass WIMP sensitivity by detecting first dynode hits is shown. LZ has four different types of PMTs in the detector. This chapter focuses mainly on the Hamamatsu R11410-22 PMTs which monitor the TPC xenon volume. The simulation of signals from PMTs monitoring the veto detectors (skin and OD) is mentioned.

3.1 Motivation

All signals in LZ are detected by PMTs; their efficiency and resolution have an important impact on the LZ detector performance. Realistic simulation data is important for the training and validation of data analysis tools prior to commissioning of the detector. The accurate modelling of the detector with all its uncertainties and variations is essential to understand uncertainties, especially if LZ should observe events in the signal region. Processes inside the PMT are probabilistic, leading to variation in gain and time response. Different dynode effects can lead to undersized signals introducing further variation in the signal spectrum. Dark counts and afterpulsing constitute backgrounds, which need to be considered in data analysis. While the smallest S2 signals in LZ are expected to consist of several hundred photons, S1 signals are much smaller. For NRs below 10 GeV less than 10 photons are detected on average. It can, therefore, be seen that understanding the single photon response precisely is essential to achieve high detection efficiency in the low energy regime. In-situ gain calibrations are done with blue LED light, rather than VUV light. Wavelength dependence of the PMT response, thus, has to be understood.

Previous studies of the R11410 PMT type, of which the LZ PMTs are a subtype, have focused on characterizing the performance in terms of quantum efficiency, gain, timing and afterpulsing [107, 108, 109, 110, 111]. Two studies have measured the probability of double photoelectron emission from the photocathode [112, 113]. It has been shown that photoconversion on the first dynode leads to a significant fraction of small pulses [114, 113]. No comprehensive studies have been performed to understand the impact of undersized signals on the response of R11410 PMTs. Undersized signals are expected to impact the detection efficiency and single photoelectron resolution in the PMTs. The characterization of such signals is the main focus of the PMT test discussed in this chapter.

While for many applications, it is sufficient to simulate the PMT response in terms

of charge and time distributions [115, 116], to prepare for LZ analysis, it is crucial to simulate realistic PMT waveforms in the time domain. As discussed in Section 2.6.2, the Detector Electronics Simulation takes the raw photon hits from the GEANT4 detector simulation and converts them into digitized waveforms stored in an output file identical to LZ DAQ data. At the beginning of this simulation-chain stands an analytic PMT model. The work presented in the following is concerned with making the analytic PMT response model as realistic as possible.

3.2 PMT response model

3.2.1 Photomultiplier tubes

A photomultiplier tube (PMT) is a vacuum tube, which contains a photocathode and a dynode chain. A photon hitting the photocathode gets converted to a photoelectron via the photoelectric effect. Voltages applied to the dynodes create electric fields inside the PMT. A focusing electric field accelerates the photoelectron onto the dynode chain. At each dynode stage, the electron gets multiplied, as indicated in Fig. 3.1. The charge is collected at the anode, from where it is read out via a load resistance. The resulting pulse has an area proportional to the charge collected at the anode.

3.2.2 Photoconversion

The efficiency of photoconversion is referred to as quantum efficiency (QE). It is typically defined as the ratio of photoelectrons emitted from the photocathode to photons incident on it. This ratio depends on several different sub-processes, which are described by Spicer's three-step model of photoemission from surfaces [117]. First, a photon is absorbed into the material of the photocathode. The absorbed photon imparts energy to an electron in the material. The energized electron diffuses through the material, losing some of its energy. If the electron reaches the surface with suffi-

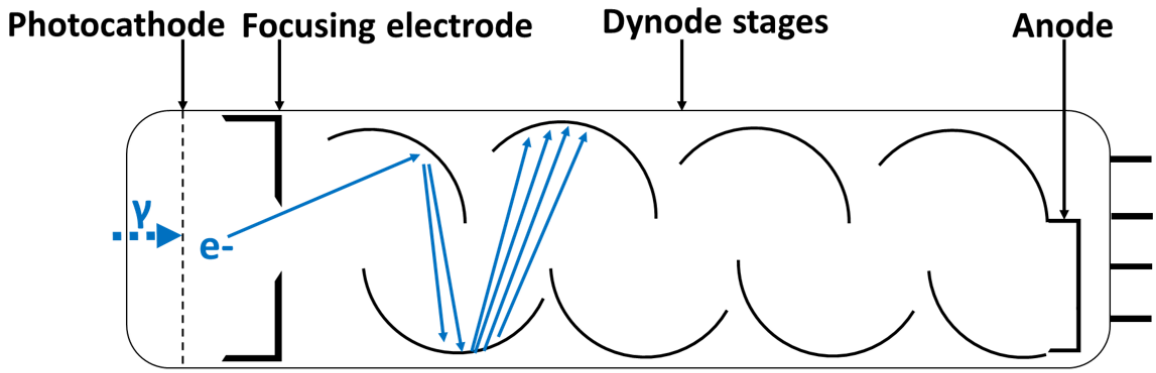

Figure 3.1: Schematic drawing of PMT showing the photoconversion on the photocathode and the mulitplication of electrons on the first few dynode stages.

cient excess energy, it can escape from it. The process can be described by a binomial distribution with probability QE of photoelectron emission. An emitted photoelectron only leads to a measurable signal if it reaches the active area of the first dynode. The collection efficiency describes the probability of this happing. Here, the QE is defined as the ratio of photons inducing a response in the PMT. Therefore, the collection efficiency is included in the QE. The QE process is wavelength-dependent, as discussed further in the context of the simulation.

3.2.3 Electron mulitplication

The multiplication gain g of a PMT is the ratio of charge collected at the anode to the charge of the photoelectron emitted from the photocathode. At later dynode stages backscattering of electrons from the dynodes is the principal cause of inefficiencies. The multiplication gain is the product of secondary emission coefficients δ_i of the dynodes [118, 116].

$$g = \Pi_{i=1}^{N} \delta_i \tag{3.1}$$

The secondary emission coefficient is a function of the kinetic energy of the incident electrons. Assuming that the electrons are emitted with zero potential energy, the

Stage	**Resistance** $[R/R_0]$	ΔV **[V]**
C - Dy1	4	324.3
Dy1 - Dy2	1.5	121.6
Dy2 - Dy3	2	162.2
Dy3 - Dy4	1	81.1
Dy4 - Dy5	1	81.1
Dy5 - Dy6	1	81.1
Dy6 - Dy7	1	81.1
Dy7 - Dy8	1	81.1
Dy8 - Dy9	1	81.1
Dy9 - Dy10	1	81.1
Dy10 - Dy11	1	81.1
Dy11 - Dy12	1.5	121.6
Dy12 - A	1.5	121.6
Total	18.5	1500

Table 3.1: R11410 base resistances and inter-dynode voltage distributions for 1500 V total voltage applied [75].

secondary emission coefficient depends on the voltage difference between the preceding and the current dynode V_i and the exponent κ, accounting for inefficiencies due to backscattering from the dynodes. κ depends on the structure and material of the dynodes [119].

$$\delta_i = a_i \times (V_i)^{\kappa} \tag{3.2}$$

The total multiplication gain therefore becomes:

$$g = \Pi_{i=1}^{N} a_i \times (V_i)^{\kappa}. \tag{3.3}$$

The bases of the LZ TPC PMTs follow the voltage distribution recommended by Hamamatsu as shown in Table 3.1. It is known that κ is typically between 0.7 and 0.8, i.e. 20 to 30% of electrons scatter off the dynodes.

In LZ, the PMTs are biased to an average multiplication gain of 3.5×10^6. The gain varies as the secondary emission is a probabilistic process. At each dynode, the

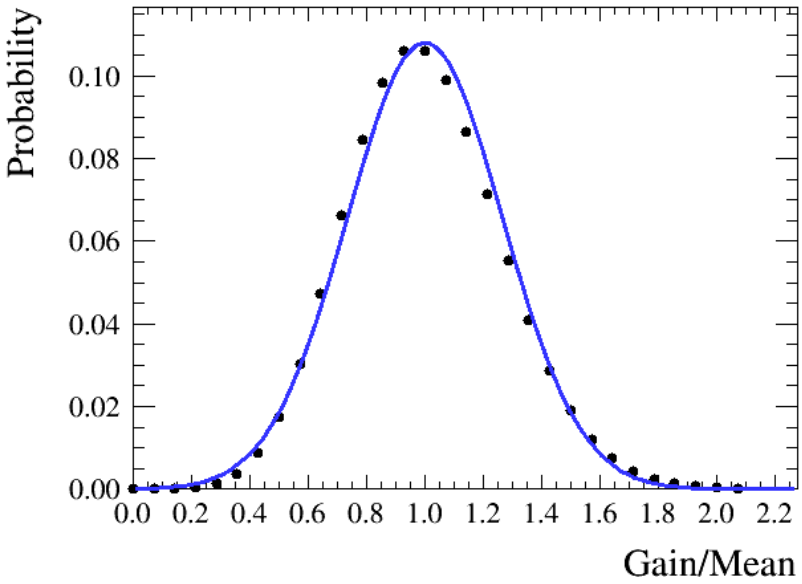

Figure 3.2: Simulated multiplication gain at first dynode using Poisson distribution with mean $\mu = 14$. A Gaussian distribution with $\sigma = \frac{\sqrt{14}}{14}$ is overlayed in blue.

multiplication can be described by a Poisson process. Fig. 3.2 shows a simulation of the multiplication of a single photoelectron (SPE) at the first dynode using a random number Poisson distribution with mean 14, which is the first dynode gain as provided by the manufacturer. It is overlayed with a Gaussian distribution with standard deviation $\frac{\sqrt{14}}{14} = 0.27$. It can be seen that the Gaussian can describe the distribution reasonably well. The standard deviation of 0.27 agrees with the measured SPE resolution, defined as $\frac{\sigma}{\mu}$, for the R11410 PMTs [111]. Thus, the multiplication at the first dynode is the dominant process for gain variation. The validity of approximating the gain distribution as Gaussian is tested further in Section 3.3.

An important parameter measuring the separation of the single photoelectron (SPE) peak in the pulse area spectrum from the baseline noise is the peak-to-valley ratio. It is calculated taking the ratio of the SPE peak height to the minimum point of the valley to its left.

3.2.4 Signal timing

The PMT response time depends on the electron path length and the average speed of the electron over its entire trajectory. The transit time is defined as the time between a photon hitting the photocathode and the time the maximum of the charge pulse arrives at the anode. The emission of the photoelectron from the photocathode is a subdominant contribution to this time. For alkali-antimonide photocathodes, the response time lies between 0.1 to 1 ps [117]. The signal from LZ PMTs is digitized at 10 ns. The photocathode response time is, therefore, negligible. The time of flight of a photoelectron to the first dynode can be calculated approximating the potential distribution between the cathode and first dynode to follow a square law,

$$V(s) = V(s_0)\left(\frac{s}{s_0}\right)^2. \tag{3.4}$$

The calculation shown here follows [119]. The acceleration of a charged particle of mass m and charge e in an electric field E is described by

$$m\frac{d^2s}{dt} = -Ee \tag{3.5}$$

Considering the conservation of energy, the change in potential equals the gain in kinetic energy:

$$\frac{1}{2}m(v^2 - v_0^2) = e(V - V_0). \tag{3.6}$$

The time of flight for an electron starting at the cathode, s=0 and travelling to the first dynode at position s_0 is given by

$$t = \int_0^{s_0} \frac{ds}{v}. \tag{3.7}$$

Using Equ. 3.4 to describe the potential distribution, Equ. 3.7 becomes

$$t = \frac{(m/2e)^{\frac{1}{2}}}{V(s_0)^{\frac{1}{2}}} s_0 \int \frac{ds}{(V_0 s^2)/V(s_0) + s^2)^{\frac{1}{2}}} \tag{3.8}$$

$$t = \frac{(m/2e)^{\frac{1}{2}}}{4(V(s_0))^{\frac{1}{2}}} s_0 \ln(4V(s_0)/V_0) \tag{3.9}$$

Every photoelectron follows a unique path through the photomultiplier. Even if two photoelectrons get emitted at precisely the same position on the photocathode, their way to the first dynode depends on their initial energy and emission angle. The transit time fluctuation observed when identical light pulses strike the same part of the photocathode is defined as time jitter. Time jitter limits the accuracy of the timing signal and is dependent on the diameter of the PMT.

The path through the multiplier also contributes to the transit time. Differences in the path taken by the individual secondary electrons mostly impact the width of the pulse. The collection of charge adds to the transit time and depends on the voltage and distance between last dynode and anode. Electro-optic modelling is needed to understand these timing contributions precisely. For the work presented here, it is sufficient to use the transit time and transit time variations provided by the manufacturer and be able to calculate the contribution of the photoelectron time of flight between the cathode and first dynode.

3.2.5 Single photon response types

A photon impinging on the photocathode can induce different types of responses in the PMT, leading to different contributions to the single photon response distribution apart from the standard single photoelectron (SPE).

Double photoelectron (DPE) VUV photons are very energetic. For a fraction of events, the excited electron in the photocathode scatters with another electron and excites it, leading to a double photoelectron emission from the photocathode. For LZ

Figure 3.3: Picture of a Hamamatsu R11410-22 PMT window, showing the focusing electrode and the first dynode. Photo credit: Matthew Kapust, Sanford Underground Research Facility.

TPC PMTs, this has been measured to make up 23% of the single photon response spectrum [112]. This is often referred to as double photoelectron effect. The two photoelectrons can be treated independently and lead to twice the area while keeping the same pulse width. This effect is wavelength dependent, and the probability for double photoelectron emission is negligible for visible light [113].

First dynode hits (FDH) A photon can be transmitted through the photocathode and create a photoelectron on the first dynode as shown in Fig. 3.5b. Fig. 3.3 shows a view of the first dynode behind the focusing grid through the PMT window. It can be seen that the dynode provides a relatively large area to light entering through the PMT window. The first dynode typically has a low work-function similar to that of the photocathode. It is, therefore, not surprising that this is a sizeable effect for LZ PMTs at VUV wavelengths, while it plays a smaller role for blue LED light [113]. In [114], a first estimate of the quantum efficiency of the first dynode is given as 10.6%.

The multiplication for these photoelectrons only starts from the second dynode

[115]. The gain is reduced by the gain of the first dynode,

$$g_{FDH} = \Pi_{i=2}^{N} \delta_i. \tag{3.10}$$

As a photon travels faster than a photoelectron, the first dynode hit pulses arrive earlier at the anode than regular pulses. The time difference corresponds to the difference in time of flight of the photoelectron from the cathode to the first dynode t_{c-d1} compared to the time the photon takes to travel the same distance. The new average transit time is

$$t_{FDH} = t_{SPE} - t_{c-d1}. \tag{3.11}$$

As first dynode hits result in much smaller pulses, these responses do not contribute to the measured QE. Taking this effect into account could allow a boost in efficiency for low energy events with S1 signals of a few photons.

Second dynode collection (SDC) In some cases, photoelectrons miss the first dynode completely or scatter off it at high speed to be directly collected on the second dynode (see Fig. 3.5c) [119]. Again the multiplication process only starts from the second dynode. However, the photoelectron reaches the second dynode at a higher speed due to the higher potential difference between the photocathode and the second dynode. Equ. 3.10 describes the gain, but with an altered second dynode emission coefficient:

$$\delta_2 = a \times (V_1 + V_2)^{\kappa} \tag{3.12}$$

Elastic and inelastic scattering (ES, IES) Photoelectrons can backscatter elastically (Fig. 3.5d) or inelastically (Fig. 3.5e) off the first dynode or the metal structures around the first dynode (see Fig. 3.3). Elastically backscattered photoelectrons de-

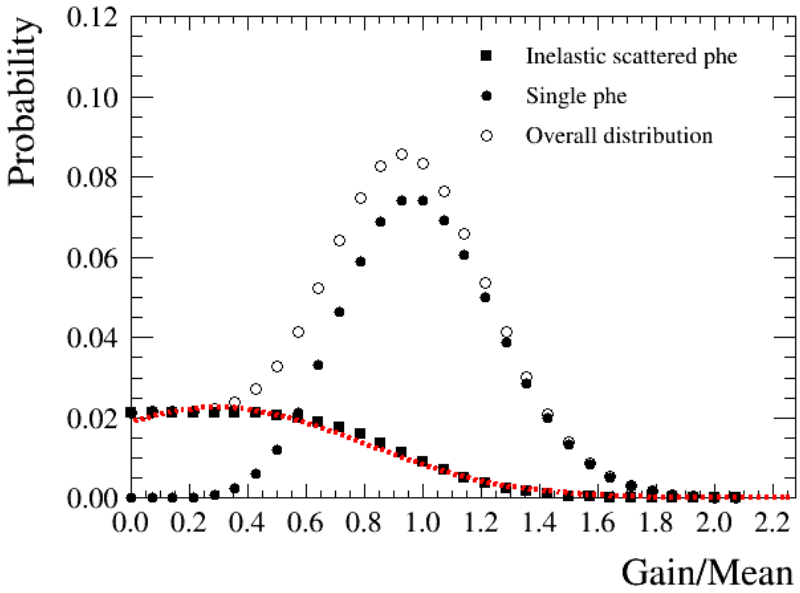

Figure 3.4: Simulated multiplication gain at the first dynode ($\mu = 14$) for single photoelectrons, distinguishing between contributions which suffered from inelastic scattering (30%) and contributions which have not. A Gaussian with mean 0.3μ and spread 0.5μ is overlaid in red, describing the general shape of the inelastic scatter distribution.

celerate in the electric field and stop just before the cathode, before returning to the first dynode after $\Delta t = 2 \times t_{c-d1}$. The multiplication process then starts as usual. An inelastically backscattered photoelectron only retains a fraction of its initial energy. It, thus, leads to an undersized pulse with a time delay $0 < \Delta t < 2 \times t_{c-d1}$ depending on how far the photoelectron backscattered. Following the discussion in [120, 119] the resulting multiplication gain distribution for inelastically scattered photoelectrons is derived in the following. The multiplication gain for pulses with inelastic scattering at the first dynode follows a Poisson distribution with mean $\mu(1-f)$, where μ is the mean of the SPE distribution unaffected from scattering, and f is the fraction of energy lost in the scattering:

$$P(m, \mu(1-f)) = e^{(-\mu(1-f))} \frac{(\mu(1-f))^m}{m!}. \tag{3.13}$$

The fraction of energy lost can range from 0 to 1. The probability distribution is integrated over all possible values for f:

$$\int_0^1 P(m, \mu(1-f))df = \int_0^1 e^{(-\mu(1-f))} \frac{(\mu(1-f))^m}{m!} df. \tag{3.14}$$

The resulting distribution is displayed in Fig. 3.4 together with the distribution for single photoelectrons not affected by scattering. It can be seen that modelling the contributions from inelastic scatters is not only important for a more accurate peak-to-valley estimate, the SPE peak is also shifted. The overlaid graph in red shows that a truncated Gaussian can approximate the elastic scatter distribution shape.

3.2.6 Ionic afterpulsing

Most PMTs do not have a perfect vacuum but contain trace amounts of gaseous elements. When a photoelectron hits such a gas atom on its way from the photocathode to the first dynode, it can create a positively charged ion. The ion travels to the cathode, as shown in Fig. 3.5f. When it hits the cathode, photoelectrons are emitted. These photoelectrons travel to the first dynode and enter the multiplication chain as usual. Afterpulses appear as large spiked signals with a time delay of tens of nanoseconds to several microseconds. The size and timing of the afterpulses depend on the ion type.

The time delay is given by τ, the time the ion takes to travel to the photocathode. The calculation of this transit time, starts from the same assumptions as the calculation of the photoelectron time of flight, again following [119]. This time the ion starts at position s_0 somewhere in the space between the cathode and first dynode. The time it takes to reach position s is given by

$$\tau = \int_{s_0}^{s} \frac{ds}{v}. \tag{3.15}$$

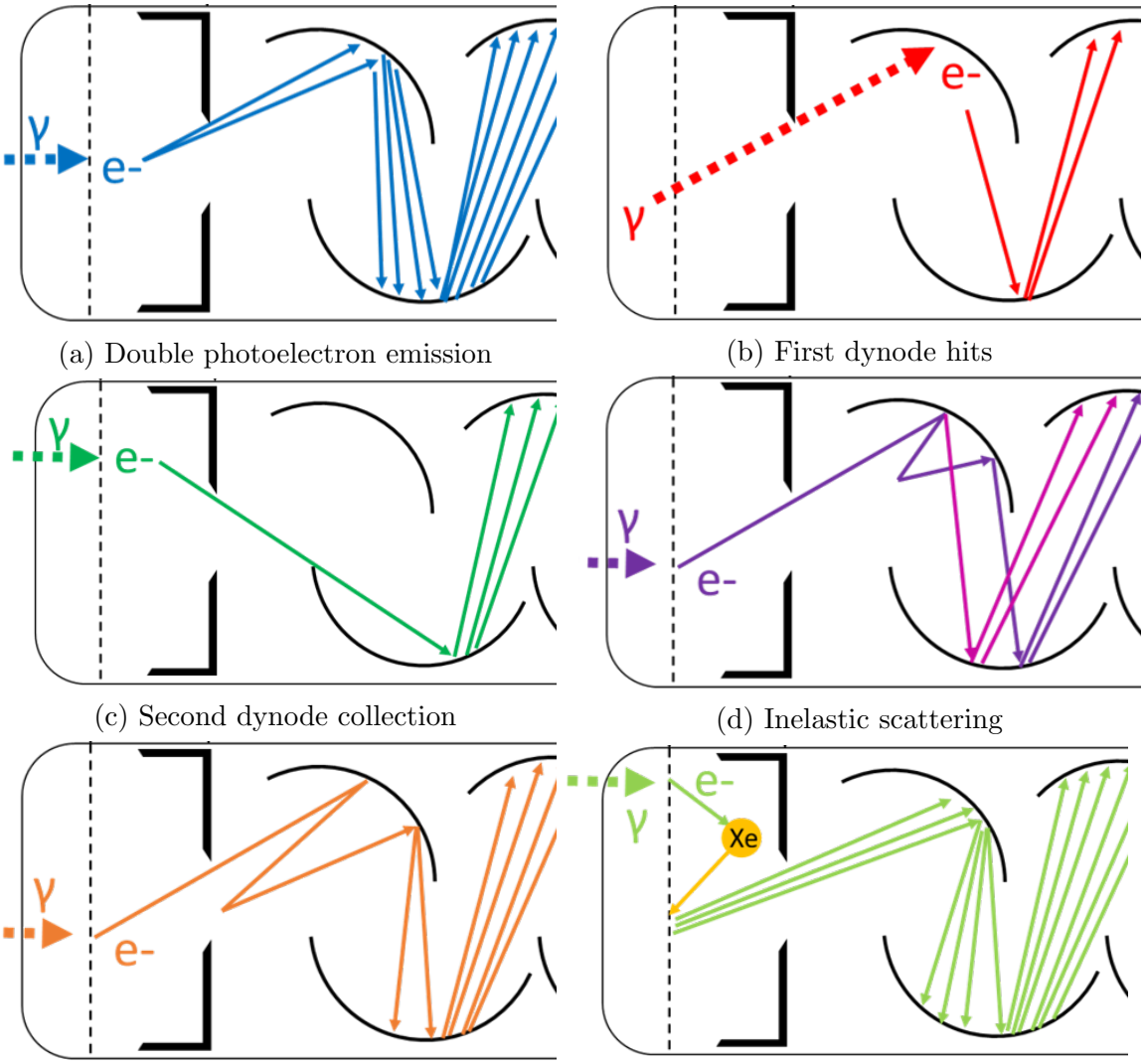

(a) Double photoelectron emission

(b) First dynode hits

(c) Second dynode collection

(d) Inelastic scattering

(e) Elastic scattering

(f) Afterpulsing

Figure 3.5: Schematic of single photons PMT response types and afterpulsing.

Using the equation of motion (Equ. 3.6),

$$\tau(s, s_0) = -\Big(\frac{m}{2q}\Big)^{0.5} \int_{s_0}^{s} [V(s_0) - V(s)]^{-0.5} ds. \tag{3.16}$$

Approximating the potential to follow Equ. 3.4, the relationship becomes:

$$\tau(s, s_0) = \frac{md^2}{2qV_d} sin^{-1}[V(s)/V(s_0)]^{0.5}|_{s_0}^{s}, \tag{3.17}$$

where d is the cathode-dynode distance. The time it takes to get to the cathode at $s = 0$, is given by

$$\tau(0, s_0) = \frac{\pi}{2}\sqrt{\frac{md^2}{2qV_d}}. \tag{3.18}$$

It can be seen that for a potential distribution following a square law, the time delay is independent of the start position of the ion. The time delay depends on the mass to charge ratio m/q of the ion. Using this relationship, afterpulses can be attributed to the initiating ion.

3.2.7 Dark counts

Dark counts are PMT pulses which are not initiated by a photon. Such pulses are typically caused by spontaneous thermionic emission of single electrons from the photocathode or early dynode stages [118]. A dark count from the photocathode has the same pulse response as a photoelectron. The rate of dark counts is dependent on temperature and typically decreases with decreasing temperature. The LZ TPC PMTs have a typical dark count rate of 40 Hz at liquid xenon temperature. Even though this is a very low dark count rate, accidental coincidences with S2-only events is a dangerous background.

3.3 Study of undersized PMT signals

3.3.1 Overview

6 spare LZ PMTs were tested at the Xenon Laboratory at Imperial College, London. The PMTs were biased to higher voltages than used for LZ to separate the SPE peak further from the noise and get a better understanding of the contribution of undersized pulses to the single photon spectrum. Data was taken with both blue LED and xenon scintillation light. An extended PMT response model is developed on the basis of the data to describe undersized signals, as well as SPE and DPE contributions.

3.3.2 Setup

The PMTs were tested in a vacuum cryostat consisting of an inner (IV), and an outer vessel (OV) displayed in Fig. 3.6 and described in [112]. A gaseous xenon scintillation cell is mounted onto the OV lid. The cell contains a 30 kBq ^{241}Am radioactive source emitting alphas during the decay. MgF_2 viewports in the scintillation cell and the IV lid allow the propagation of scintillation light into the inner vessel. The IV contains a PEEK frame which can hold seven upwards facing PMTs. The reference PMT is located in the middle, directly underneath the viewport. The 6 PMTs under test are arranged in a circular configuration around it. Both OV and IV are pumped down to a high vacuum during operation, as water vapour can absorb VUV radiation. If data is taken at cold temperature, the IV is filled with 1.5 bar(a) N_2 gas before cool-down. A pressurized LN_2 dewar is connected to the cryostat via a solenoid valve. A PID algorithm operates the valve to let LN_2 vapour into the vessel for cooling. Pt100 thermometers inside the vessel are used to monitor the temperature. A typical event from the scintillation cell is shown in Fig. 3.7.

The majority of light is seen in the first few hundreds of nanoseconds after the trigger. This is scintillation light from the decay of excited xenon atoms. As there is no electric field applied to extract the electrons, electron-ion recombination continues up to tens of microseconds, emitting luminescence light. For the scintillation cell used in these experiments, the decay time constant was measured to be 28 μs with the flux from recombination photons constituting 26% of the total flux [112]. After about 10 μs the flux becomes low enough to be a source of single VUV photons, as needed for the measurements. The scintillation light spectrum of gaseous xenon at room temperature has a mean of 171 nm with a FWHM of 10 nm [121].

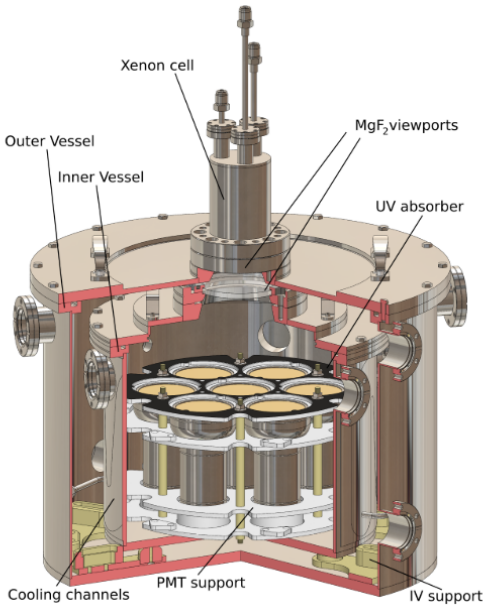

Figure 3.6: Overview of Imperial College PMT test setup [112].

3.3.3 Data acquisition and data reduction

The data was recorded using the ZEPLIN-III data acquisition system [71]. The DC265 Acquiris digitizers have 2 ns sampling and an 8-bit resolution with a dynamic range of 100 mV. All PMTs have a high and low gain channel. For the measurements presented here, the high gain channel was used, which has a ten times amplification. The DAQ is triggered on the pulse-shape sum of all high-gain channels. For each trigger, a fixed-length waveform of all HG and LG channels is recorded. The data is reduced using ZE3RA, the ZEPLIN-III analysis framework [122]. It finds pulses and calculates reduced quantities, such as time since trigger, baseline subtracted area and pulse height.

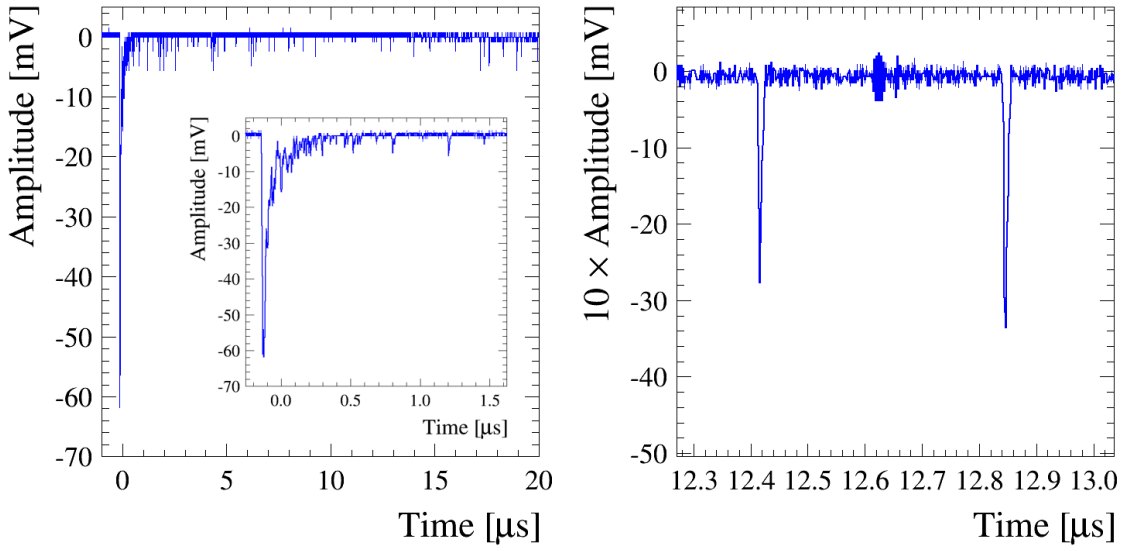

(a) (b)

Figure 3.7: Typical event from the scintillation cell following an α-particle interaction. (a) The majority of light is seen in the first few hundred nanoseconds. (b) Example of single photons in the time window 10 to 20 μs.

3.3.4 Testing procedure and data sets

The data sets presented here are from two separate runs. An overview of the data is given data in Table 3.2. The first run was dedicated to measuring the single photon distribution for VUV, and blue light (470 nm) from a fibre coupled LED pulser. The light from the LED is led into the inner cryostat using an optical fibre. For the second run, the VUV viewport was blinded with vacuum rated aluminium foil to take dark count, and blue LED data. As the viewport cannot be shut and opened without opening the OV, the data had to be taken in two separate runs. A diffuser in the form of a piece of PTFE was added to the optical fibre in Run 2 to randomize the angle at which blue LED photons reach the PMTs. As the LZ PMTs have a low dark count rate (average 4 kHz at room temperature) and the rate reduces further with lower temperatures, it was not possible to reach adequate statistics for dark count data in this setup.

Vacuum was pumped for several days previous to taking warm data. Reaching a

Run	T [°C]	Light	Gain	Threshold [mV]	SPE eff. [%]	Stats
1	RT	VUV	5×10^6	0.22 ± 0.06	99.5	30-40k
2	RT	Blue	5×10^6	0.26 ± 0.05	99.7	10-20k
1	-93 ± 1	VUV	1.4×10^7	0.25 ± 0.01	99.9	40-50k
1	-93 ± 1	Blue	1.4×10^7	0.26 ± 0.09	99.9	12-13k
2	-97.6 ± 0.3	Blue	1.8×10^7	0.25 ± 0.05	99.9	30-40k

Table 3.2: Data sets overview. The determination of noise and trigger efficiency (here presented for PMT 3) are discussed in Section 3.3.5.

good vacuum is important for being able to reach high voltages and not absorbing VUV light on water vapour. In both runs a pressure of 6×10^{-6} mbar was reached. The cool-down for Run 1 took seven hours, and cold data was taken at a temperature of -93 ± 1°C. For Run 2 the vessel was cooled for 24 hours, and the data was taken at a stable temperature of -97.6 ± 0.3°C. The longer cool-down period was chosen to allow the internal PMT structures to reach thermal equilibrium. The PMTs were powered up and left to stabilize for several hours previous to data taking for all measurements.

During Run 1, a set of blue LED and VUV data at voltages specified by the manufacturer to reach the nominal gain of 5×10^6 were taken at room temperature and liquid xenon temperature. Subsequently, the voltage on the PMTs was increased while monitoring SPE pulses on an oscilloscope until roughly three times the original gain was reached.

In Run 2, blue LED data was recorded with the PMTs biased to reach a gain of 5×10^6 at room temperature and liquid xenon temperature. The measurements were repeated at higher voltages.

For better gain alignment, the voltage gain relationship was determined using Run 1 data. The total applied voltage is related to the total multiplier gain, approximating that all dynodes have equal gain $\frac{V_{total}}{n+1}$. Equ. 3.3 becomes,

$$g = A \times V_{total}^{\kappa n}, \tag{3.19}$$

PMT	V_1 [V]	$Gain_1$	V_2 [V]	$Gain_2$	κ	A
1	1410	5.4×10^6	1570	1.5×10^7	0.81	9.03×10^{-25}
2	1431	6.3×10^6	1550	1.3×10^7	0.80	2.33×10^{-24}
3	1384	6.1×10^6	1520	1.5×10^7	0.78	2.34×10^{-23}
4	1434	5.3×10^6	1610	1.6×10^7	0.84	6.8×10^{-26}
5	1381	6.6×10^6	1550	2.1×10^7	0.84	6.8×10^{-26}
6	1393	5.1×10^6	1550	1.4×10^7	0.76	8.35×10^{-23}

Table 3.3: Gain-Voltage relationship for all 6 PMTs under test.

where $A = \frac{a^n}{(n+1)^{kn}}$. Having two gain-voltage pairs for every PMT, simultaneous equations can be solved for A and κ. The gain is estimated from the two sets of LED data at LXe temperatures. The single photon data selection is explained in the next section. The SPE area distribution is fitted using a Gaussian. The gain is the SPE area divided by the expected SPE area for $g = 1$. The voltage gain relationship for the different PMTs is shown in Table 3.3. It can be seen that κ varies between 0.76 and 0.84, which lies within what is expected from the literature. PMT 5 requires lower voltages than the other PMTs to reach the same gains. It was decided to power all PMTs to a gain of 1.8×10^7. PMT 5 was powered 2.1×10^7 gain. It was found that PMT 5 has a worse resolution than the other PMTs and was therefore excluded from the analysis presented here.

3.3.5 Noise and efficiency characterization

Baseline, noise level and threshold are determined using ZE3RA. A more detailed discussion of the software package can be found in [122]. The baseline mean $\mu_{baseline}$ and variation $\sigma_{baseline}$ are determined from the pre-trigger region. To avoid bias due to dark counts, other light or spurious signals, ZE3RA includes a consistency check across different parts of the pretrigger region. The threshold is determined as

$$threshold = \mu_{baseline} + 3\sigma_{baseline}. \tag{3.20}$$

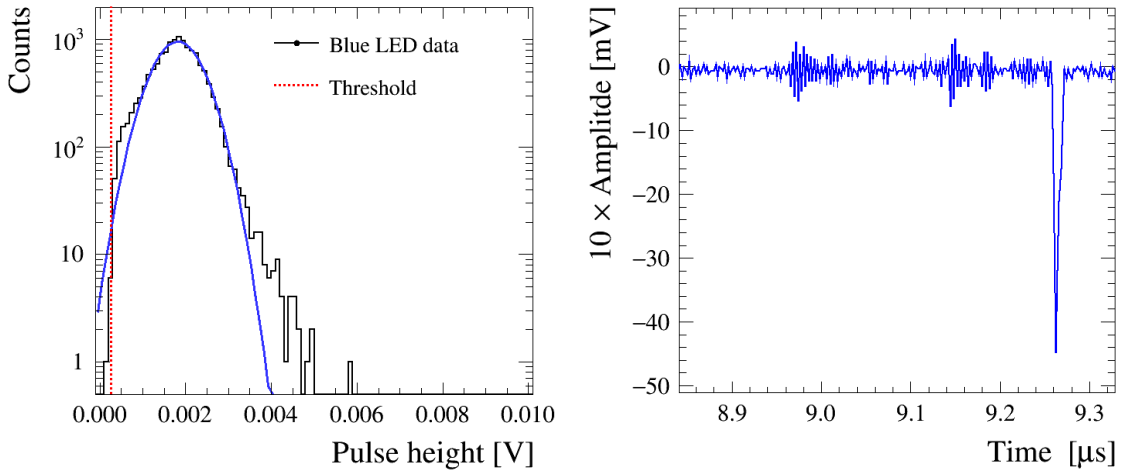

(a) (b)

Figure 3.8: (a) Single photon height distribution for blue LED data for $g = 5 \times 10^6$. The pulse finding threshold is shown in red. A Gaussian is fitted to the height distribution and the fraction of SPE pulses falling below the threshold is calculated. (b) Example of electronic pick-up noise followed by a single photon pulse.

The trigger levels for the different data sets are given in Table 3.2 together with an estimation of the SPE trigger efficiency for PMT 3. This efficiency is calculated by fitting a Gaussian to the SPE height distribution. An example is shown in Fig. 3.8a. The fraction of pulses with a height lower than the threshold is estimated. It was found that the SPE efficiency at a gain of 5×10^6 for all channels lies between 97.0% and 99.7%. At a higher gain of 1.8×10^7 the SPE efficiency for all channels is better than 99.8%. The more problematic noise is electronic pick-up noise as seen in Fig. 3.8b, which often fluctuates above the threshold. Data analysis cuts, as described in the next section, were able to reduce this noise considerably (especially for the blue LED data). However, it limits the access to low area pulses in the VUV as discussed further later.

3.3.6 Analysis

3.3.6.1 Single photon selection

The first step in data analysis is to select pulses corresponding to single photons. Similar cuts as in [112] are used. When taking data with the blue LED, the DAQ is triggered by the pulser. The pulse width and amplitude is chosen to minimize photon coincidences. The light pulse occurs in a narrow time window after the trigger, which can be determined from a time delay histogram. A 50 ns wide time window is defined in which to look for pulses. To avoid coincidence with an event from the scintillation cell (for the unblinded data), it is required that the total event area has less than 20 photons. Additionally, it is enforced that there is no coincident pulse on any other PMT, and it is checked for possible afterpulsing. There is still a remaining probability of random coincidences between blue photons and VUV photons (for Run 1 data with the open viewport) or dark counts. Additionally, there is a chance of two blue photons being detected simultaneously on the same PMT. While Run 1 data is used for comparisons between higher gain VUV and blue LED data, all fits to blue LED data presented here are from Run 2 data with the viewport blinded. The typical dark count rate for the PMTs under test is 40 Hz (4 kHz) at LXe temperatures (room temperature). For a 50 ns time window and 40,000 events, 0.08 (8) dark counts at LXe temperatures (room temperature) are expected. The dominant source of coincidence is two blue photons being detected by the same PMT. The coincidence probability for each set of data is estimated using Poisson statistics and considering the number of events seeing zero and one photon.

As discussed earlier, scintillation events from the cell are a good source for single VUV photons after about 10 μs. Therefore, a time window from 10 to 20 μs after the trigger is selected. To avoid overlapping photons from recombination scintillation, a pulse-level coincidence cut is applied to every pulse. Dark counts are expected

to contribute 0.0004 (0.04) pulses per PMT in each time window at LXe temperature (room temperature). As the time window selected in the VUV is much longer, electronic-pick up (see Fig. 3.8b) impacts this data more than the blue LED data. Pulse width and positive area fraction enable some noise reduction.

3.3.6.2 Qualitative comparison of data sets

A comparison of the single photon area spectra for blue and VUV light is shown in Fig. 3.9a (warm, $g = 5 \times 10^6$) and Fig. 3.9b (cold, $g = 1.4 \times 10^7$). Fig. 3.10a and Fig. 3.10b show an overlay of the blue LED and VUV data distributions at both gains. Here the higher gain Run 2 blue data (1.8×10^7) is shown, as it offers higher statistics and gain, while in Fig. 3.9b the Run 1 high gain blue LED data is shown to allow a direct comparison to the VUV spectrum. All distributions are from PMT 3.

Going to higher gains moves the SPE peak further away from the threshold. The distribution widens, while the resolution improves. The higher gain data allows a much more detailed view of the individual contributions to the spectra. The individual contributions are discussed in detail in the following. To quantify the observations, the data is fitted using the same model previously used for this PMT type in [112]:

$$\begin{aligned} P(q) =& (1 - f^{DPE} - f^{TPE}) P(q; \mu, \sigma) \\ &+ f^{DPE} P(q; 2\mu, \sqrt{2}\sigma) \\ &+ f^{TPE} P(q; 3\mu, \sqrt{3}\sigma). \end{aligned} \tag{3.21}$$

Additionally to SPE and DPE pulses, a small fraction of triple photoelectron (TPE) pulses is allowed. $P(q; \mu, \sigma)$ follows a Gaussian distribution. An example of the resulting fits to both nominal and high gain data is shown in Fig. 3.11.

Single photoelectron The single photoelectron area of the VUV data is centred around $14.26 \pm 0.79\,\mathrm{pVs}$ for all PMTs at nominal gain, with a SPE resolution of

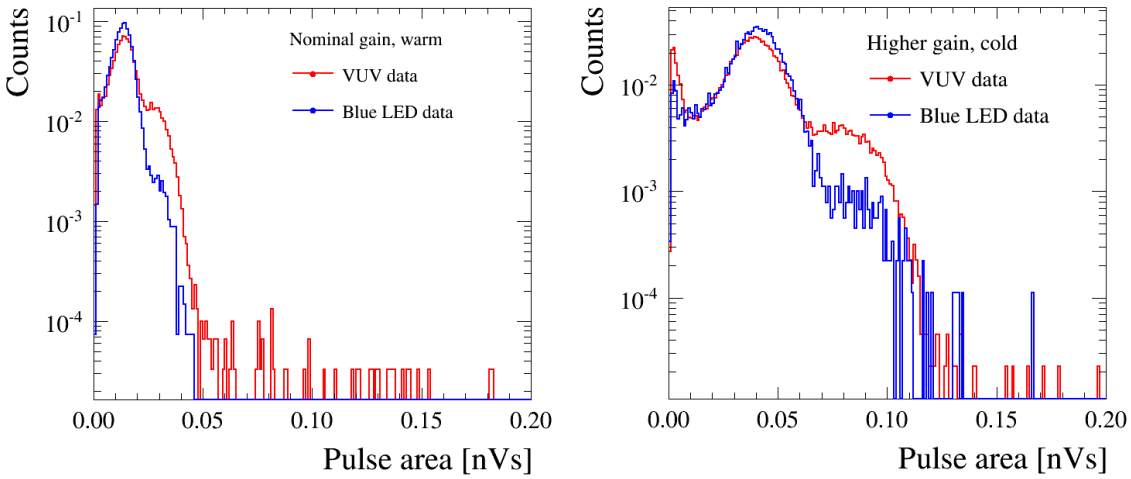

(a) (b)

Figure 3.9: Normalized single photon distributions from PMT 3 comparing blue LED and VUV data (a) at nominal gain warm (Run 1 and 2) and (b) high gain cold (both Run 1).

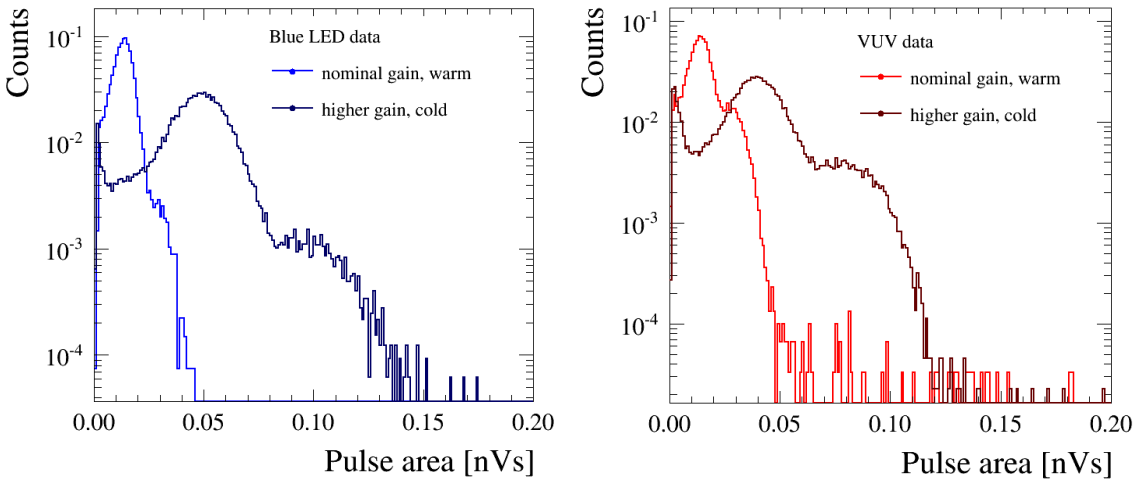

(a) (b)

Figure 3.10: Normalized single photon distributions from PMT 3 comparing nominal gain and higher gain data for (a) blue LED (Run 2) and (b) VUV light (Run 1).

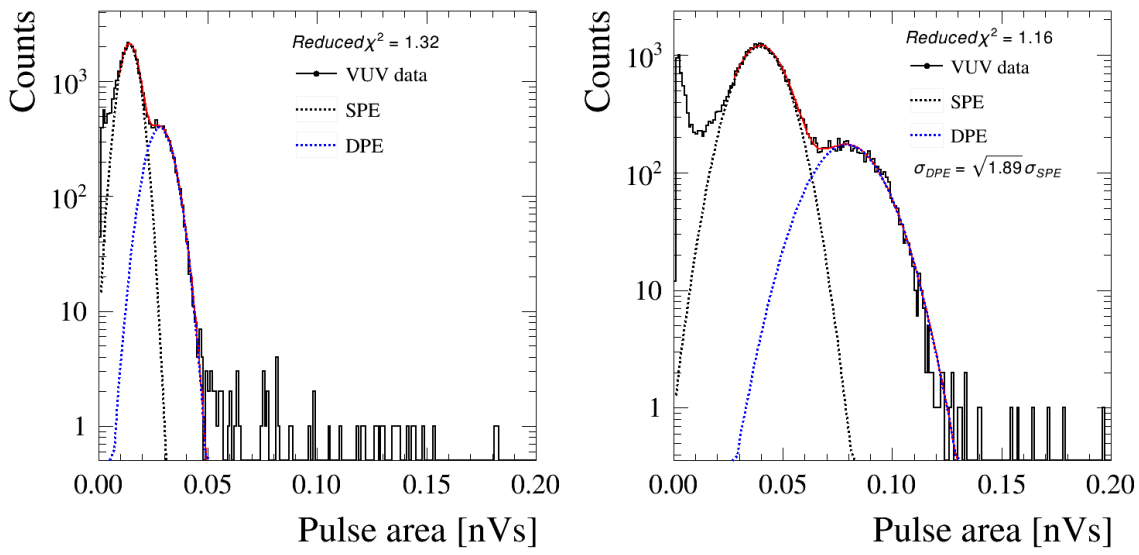

(a) (b)

Figure 3.11: Single photon distributions for VUV data at (a) nominal and (b) high gain from PMT 3 fitted with the two gaussian model.

0.29 ± 0.01. At 1.4×10^7 gain the mean moves to 40.07 ± 3.07 pVs with a resolution of 0.266 ± 0.01. Now the pedestal peak and the valley in between the pedestal and the SPE peak become visible. For the warm nominal gain data, the blue LED SPE peak coincides with the VUV peak (Fig. 3.9a). At 1.4×10^7 gain the VUV SPE peak is shifted down by 1 to 3 % compared to the blue LED data for all PMTs under test (Fig. 3.9b). It is important to note that both data sets were recorded straight after one another, and the data taking was completed within an hour. It was seen in the discussion of undersized PMT signals (see Fig. 3.4) that contributions from undersized PMT signals can shift the observed SPE mean. For this to have a different effect on blue LED and VUV data, it would need to be a wavelength-dependent effect. Another explanation could be that the dynodes inside the PMT were not fully thermalized at the time of data taking. Gain drifts due to cooling are a possibility. Future measurements should be taken in which longer thermalization is allowed before taking data, or another VUV data set is taken after the blue LED

data.

Double photoelectron It can be seen that in the VUV, a significant fraction (18-22%) of photons induce the emission of two photoelectrons (DPE effect). Blue LED photons, which are significantly less energetic than VUV photons, have a negligible probability for double photoelectron emission [113]. It can be seen that there is a small fraction of "fake" DPE pulses in the blue LED data due to overlaps. The fraction of "fake DPE" pulses from fitting (2-8% depending on PMT location) is consistent with the coincidence rate calculated from Poisson statistics (5-10% depending on PMT location). The assumption that the double photoelectron peak consists of two independent SPEs, resulting in a distribution with $\sigma_{dpe} = \sqrt{2}\sigma$, works reasonably well at nominal voltages. However, at higher gains, the double peak's width is better described by $\sqrt{1.9}\sigma$, as shown in Fig. 3.11. This is likely due to the SPE width being overestimated in the fit, due to undersized signals. Additionally, DPE pulses could contain undersized contributions too, as discussed in more detail later on.

First dynode hits The first dynode gain at nominal voltage has been provided by the manufacturer and is approximately 14. For an average SPE pulse size of 14.26 pVs, the first dynode hit pulses are expected to be centred around 1 pVs, lying just below the detection threshold. Going to 1.4×10^7 gain, the first dynode gain increases too. Using the voltage gain relationship and the κ estimated in the previous section, the first dynode gain is estimated to lie between 15 and 16. For an average SPE pulse size of 40 pVs, the average first dynode hit pulse size is expected to be at least 2.5 pVs. For the high gain data, the first dynode hits are above threshold. A peak to the left of the SPE peak appears at higher gain around the location where first dynode hits are expected. Additionally, it seems to be more significant for VUV than for the blue LED data, as would be expected from first dynode hits.

To investigate the pedestal peak and the left-hand slope of the SPE peak further,

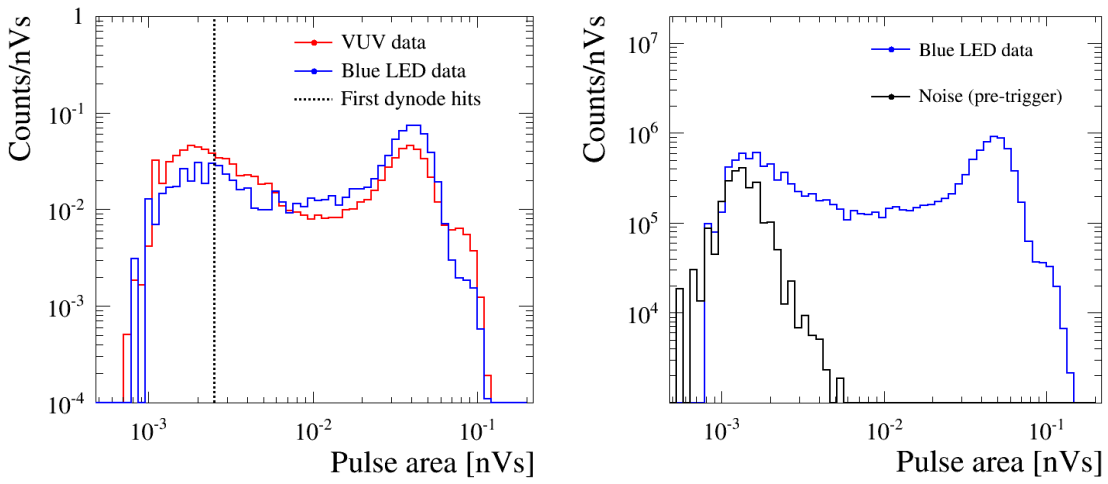

(a) (b)

Figure 3.12: (a) Comparison of blue LED and VUV data in log-log scale to look at undersized signals in more detail. The expected location of the first dynode hits is indicated. (b) Blue LED data with timing cut and overlaid noise from the same size-window in the pre-trigger region.

the area distribution is plotted as a log-log graph in Fig. 3.12a. A limiting factor is electronic-pickup noise. To investigate the contribution of noise to the pedestal peak, a window of the same size as the data acceptance window is defined in the pretrigger region of the blue LED data. No light is expected in this region, and as the dark count rate is very low, most pulses are noise. Overlaying the expected noise on Fig. 3.12b, it can be seen that for the blue LED data noise pulses make up about 50% of pulses with areas below 0.006 nVs. The remaining 50% is likely a contribution from first dynode hits. The blue LED data distributions used for fits in the next section have the noise from the off-time window subtracted. However, the statistics and resolution are too low to allow a determination of the width and exact location of the peak.

As the VUV data acceptance window is much larger, it is not possible to define a similar off-window, and the entire pedestal with noise contributions is fitted. The ratio of noise to first dynode hits is likely different than for the blue LED data. It has been seen in [113] that first dynode hits are wavelength dependent and they are expected to be much more significant for VUV light.

Other undersized signals The region in between the pedestal and SPE peak contains contributions from undersized signals. Here it is expected that inelastic scatters are dominant. These contributions have a crucial impact on the peak-to-valley ratio and the left-hand slope of the SPE peak. To be able to fit this region, the model needs to be extended to allow for undersized signals additional to first dynode hits.

3.3.6.3 Extended model

The observations discussed in the previous section motivate the extension of Equ. 3.21 to include contributions from undersized signals. The underlying Gaussian model is still assumed to be valid. It is not sufficient to add a pedestal distribution as it overestimates the peak-to-valley ratio. It is, therefore, important to consider other effects which lead to undersized pulses. As discussed in Section 3.2.5, second dynode collection and inelastically scattered photoelectrons can contribute here. From literature, it is expected that the fraction of scattered photoelectrons is as high as 20-30%. It is, therefore, assumed to be more dominant than the second dynode collection. The model for inelastic scattering described in Section 3.2.5 is used, approximating the inelastic scatter distribution as Gaussian with μ_{IES} and σ_{IES}. The extended model can be written as,

$$\begin{aligned} P(q) =& (1 - f^{DPE} - f^{TPE} - f^{pedestal} - f^{IES}) P(q; \mu, \sigma) \\ &+ f^{DPE} P(q; 2\mu, \sqrt{2}\sigma) \\ &+ f^{TPE} P(q; 3\mu, \sqrt{3}\sigma) \\ &+ f^{pedestal} P(q; \mu_{pedestal}, \sigma_{pedestal}) \\ &+ f^{IES} P(q; \mu_{IES}, \sigma_{IES}). \end{aligned} \tag{3.22}$$

Typical fits for VUV ($g = 1.4 \times 10^7$) and blue LED data ($g = 1.8 \times 10^7$) at high gain are shown in Fig. 3.13 and fit parameters for the different PMTs are summarized in Table 3.4. For blue LED data, it was decided to exclude the pedestal peak from the fit as it has not enough statistics or resolution.

The fits describe the data well with χ^2 between 0.82 and 1.45. From Fig. 3.4 is is expected that $\mu_{IES} = 0.3\mu$ and $\sigma_{IES} = 0.5\mu$. While for most data sets μ_{IES} agrees with the expectation within errors, the width of the inelastic scatter distribution is wider than expected. This is due to double photoelectrons and accidental coincidences. The impact is larger for the VUV data, as the fraction of double photoelectrons is larger than the number of accidental coincidences. Similarly to the width of the inelastic scatter distribution, the fraction of inelastic scatters is overestimated too. The fit of the pedestal peak suffers from low resolution and loss of efficiency close to the threshold. The corresponding fit parameters, thus, cannot provide much information about first dynode hits.

Allowing for a distribution of undersized signals means that DPE peak and width are now well described by $\mu_{DPE} = 2\mu$ and $\sigma_{DPE} = \sqrt{2}\sigma$. SPE mean increases by 1 -3% and the SPE resolution decreases by 2-3% compared to the fit without undersized signals, as a fraction of events at the left-hand tail of the SPE peak is now described by inelastic scatters. The peak-to-valley ratio ranges between 5.6 and 6.8.

3.3.7 Discussion

The high gain area spectra show that undersized PMTs signals have to be accounted for to model the single photon distribution accurately. Two contributions have been considered: first dynode hits and inelastic scattering. Due to the electronic pick-up noise, it is only possible to confirm the approximate location of the first dynode hit peak. Its exact location and resolution would require further improvements in noise.

It has been shown that inelastic scatter contributions are needed to account for

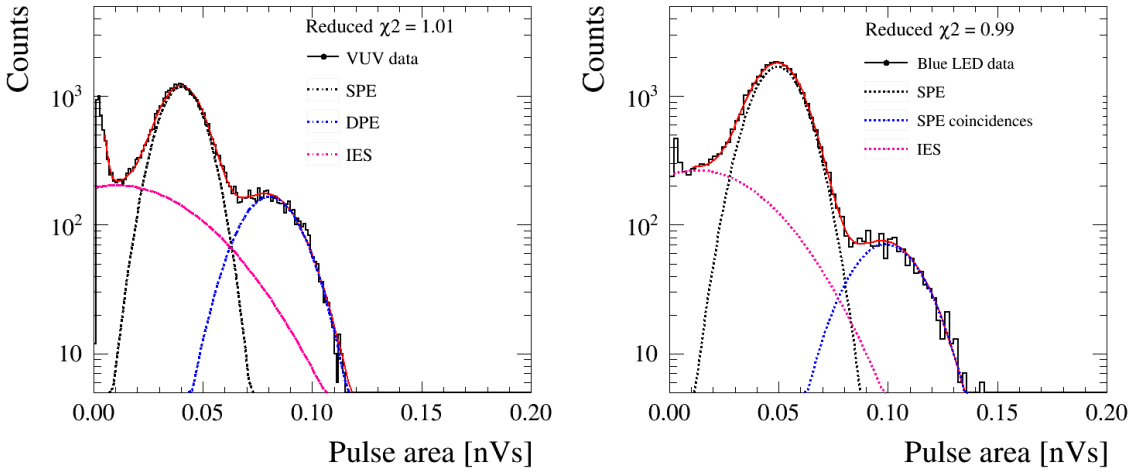

(a) (b)

Figure 3.13: Single photon distributions from PMT 3 for (a) VUV (Run 1, cold, high gain) and (b) blue LED light (Run 2, cold, high gain). The fit is shown in red and the individual contributions are indicated by dotted lines.

PMT	χ^2/ndf	μ[pVs]	σ/μ	μ_{IES}/μ	σ_{IES}/μ	f_{IES}[%]
VUV (cold, Run 1)						
1	1.24	43.1 ± 0.7	0.232 ± 0.061	0.25 ± 0.06	0.51 ± 0.89	23 ± 4
2	1.15	37.5 ± 0.1	0.252 ± 0.003	0.28 ± 0.03	0.85 ± 0.02	37 ± 1
3	1.01	40.2 ± 0.1	0.236 ± 0.002	0.25 ± 0.05	0.87 ± 0.02	34 ± 2
4	1.20	45.5 ± 0.1	0.229 ± 0.002	0.33 ± 0.08	0.84 ± 0.04	34 ± 1
6	1.45	38.4 ± 0.1	0.230 ± 0.003	0.33 ± 0.07	0.89 ± 0.38	39 ± 5
BLUE LED (cold, Run 2)						
1	0.82	48.1 ± 0.1	0.229 ± 0.002	0.26 ± 0.01	0.674 ± 0.007	31 ± 2
2	0.92	50.2 ± 0.1	0.239 ± 0.002	0.33 ± 0.08	0.530 ± 0.004	26 ± 2
3	0.99	49.5 ± 0.1	0.222 ± 0.002	0.25 ± 0.06	0.612 ± 0.001	30 ± 1
4	1.25	50.4 ± 0.1	0.238 ± 0.002	0.31 ± 0.02	0.653 ± 0.002	30 ± 1
6	1.32	53.3 ± 0.1	0.225 ± 0.002	0.25 ± 0.01	0.854 ± 0.003	43 ± 1

Table 3.4: Parameters of fit of VUV and blue LED data taken with PMT biased to high gain.

the left-hand slope of the SPE peak and the peak-to-valley ratio. The fraction of inelastic scatters in these fits is impacted by the double photoelectron (or accidental coincidence) contribution. To disentangle the different contributions, a stand-alone simulation is used, treating DPEs as two coincident single photoelectrons and setting the triple photoelectron probability to zero. All other populations are simulated using Equ. 3.22 with $\mu = 40.2\,\mathrm{pVs}$, $\sigma/\mu = 0.236$, $\mu_{IES} = 0.3\mu$ and $\sigma_{IES} = 0.5\mu$. The pedestal peak was assumed to be solely made of first dynode hits. Assuming the first dynode gain to be 15, $\mu_{pedestal} = \mu/15$ and $\sigma_{pedestal} = \sigma/\sqrt{15}$. Fig. 3.14 shows the simulated VUV response spectrum for 50,000 events overlaying the VUV data from PMT 3. It can be seen that the developed model describes the data very well with a fraction of 0.25 inelastic scatters and 0.18 double photoelectrons. 8% of pulses are first dynode hits. The first dynode model describes the pedestal peak well. However, from studying the impact of noise on the pedestal of the blue LED data (Fig. 3.12b), it can be expected that a significant fraction of the pulses contributing to this peak are noise pulses. As the peak is close to the threshold, it is also clear that not all first dynode hit pulses are detected.

By switching the different contributions on and off, it can be seen that the peak-to-valley ratio is impacted by both the fraction of inelastic scatters and the width and location of the pedestal peak. The fraction of inelastic scatters also impacts the width of the SPE peak. Setting the inelastic scatter fraction to 0.25, an SPE resolution of 0.23 leads to an observed resolution of 0.25, as expected for the LZ PMTs at high gain.

Comparing the blue LED and SPE data, it was previously seen that the SPE peak in the high gain data was shifted. Increasing the number of first dynode hits cannot account for such a shift. A higher fraction of inelastic scatters does lead to a small shift. However, a shift of 1% would require a difference in inelastic scatter fraction of 10%. In Fig. 3.9b the peak-to-valley is similar for blue LED data and VUV data. It

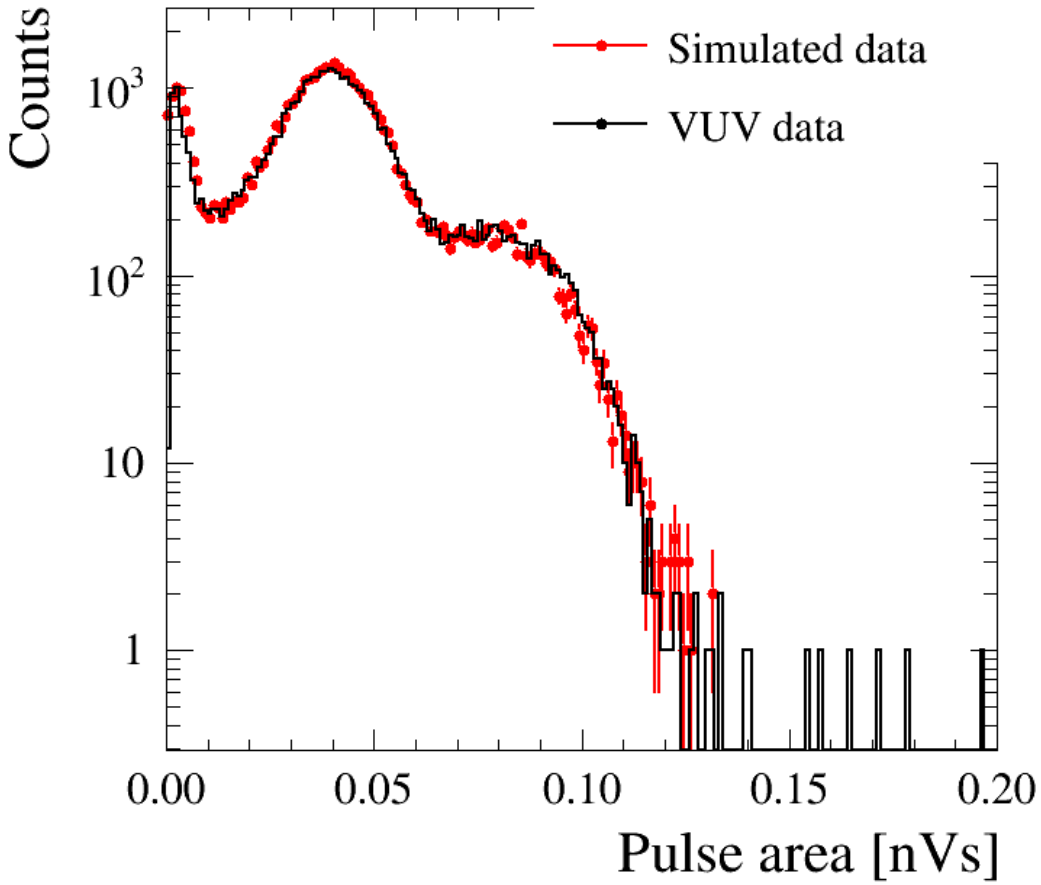

Figure 3.14: Comparison of simulation to VUV data from PMT 3.

is, therefore, unlikely that a different fraction of inelastic scatters would be the reason for the shift. More data is needed to investigate the observed shift.

While there are still some areas requiring further investigation, this study has shown the importance of modelling undersized signals and developed a model which can be used as a basis of the PMT module in the LZ simulation framework discussed in the next section.

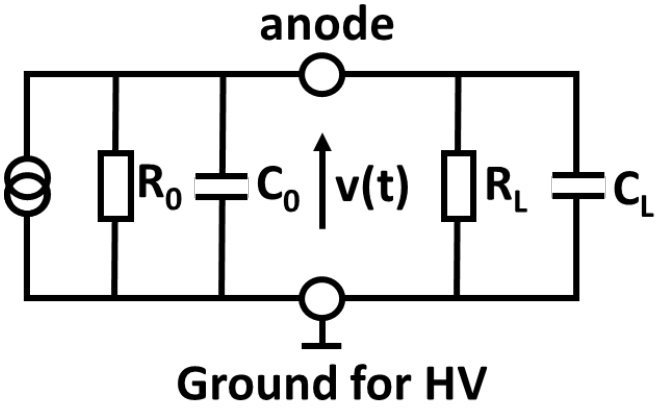

Figure 3.15: PMT equivalent circuit [124].

3.4 PMT simulation

3.4.1 DER

The model developed from the measurements discussed in the previous section is implemented in the LZ simulation. To train data analysis tools, it is important to simulate realistic PMT waveforms in the time domain, including secondary PMT effects. The PMT simulation discussed in this section is part of the Detector Electronics Response Simulation (DER). The PMT module produces analogue PMT output waveforms. Subsequently, the cable attenuation, amplification, digitization and triggering are simulated as described in [91, 123].

3.4.2 PMT pulse

The PMT response readout via a load resistance R_L and load capacitance C_L in the time domain can be modelled using the equivalent circuit displayed in Fig 3.15 [124]. The PMT is an ideal current generator with resistance R_0 and self-capacitance C_0 ($< 10\,\mathrm{pF}$). The current at the PMT anode has a quick, but finite signal rise time due to the different trajectories of electrons through the multiplier [125]. For the LZ TPC PMTs, the anode rise time is specified as 5.5 ns. As in LZ, the signal is sampled

at 10 ns, it is sufficient to model it as a decaying exponential with a time constant τ_i. The current at the anode is therefore assumed to be

$$i_a(t) = -\frac{Q_a}{\tau_i} \exp\left(-t/\tau_i\right), \tag{3.23}$$

where Q_a is the total charge collected at the anode. The total charge collected depends on the number of photons incident on the PMT N, the electron charge e and multiplication gain G. Analysing the equivalent circuit the measured output voltage at the anode generated by the input excitation $i_a(t)$ can be written as

$$v(t) = \frac{NeGR}{\tau - \tau_i}\left[exp\left(\frac{-t}{\tau_i}\right) - exp\left(\frac{-t}{\tau}\right)\right], \tag{3.24}$$

where

$$R = \frac{R_0 R_L}{R_0 + R_L}. \tag{3.25}$$

The time constant of the readout circuit is:

$$\tau = RC = R(C_0 + C_L). \tag{3.26}$$

For the LZ PMTs the time constants were estimated from data. The best approximation found is $\tau = 3.2$ ns and $\tau_i = 3.4$ ns. The combined resistance is $R = 25$. Fig. 3.16 shows a comparison of the PMT signal to the amplified and digitized signal after the entire electronics chain (both from simulation). The PMT pulse gets amplified and shaped by the front-end electronics. The shaping (30 ns for low gain and 60 ns for high gain) has been chosen in order to provide sufficient samples at 10 ns sampling [75]. That also means that the time structure inherent to the PMT pulse becomes less visible and the decaying exponential approximation of charge arriving at the anode is sufficient.

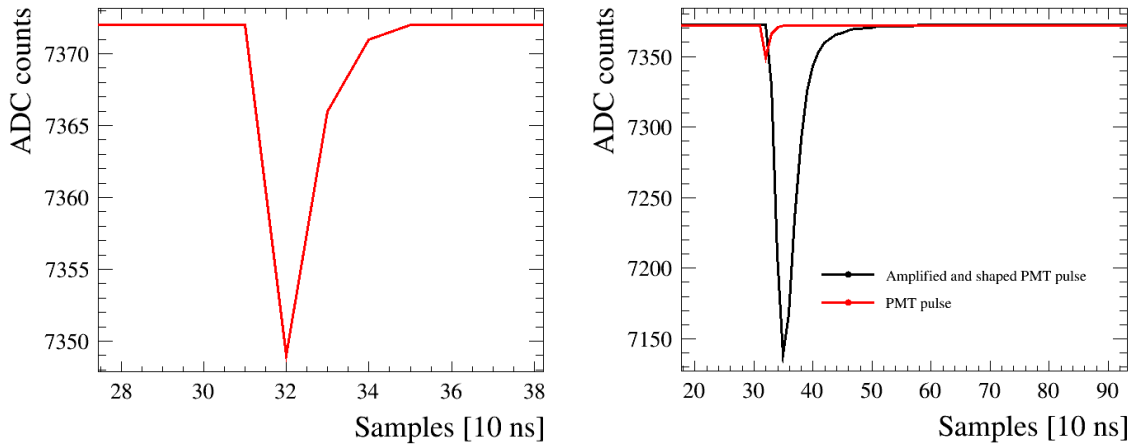

(a) (b)

Figure 3.16: (a) PMT pulse after simulation (digitized for comparison). In (b) it is shown, the effect of shaping and amplification is highlighted as both the PMT pulse (red) and the high gain amplified and shaped pulse (black) are displayed.

3.4.3 Quantum efficiency

The quantum efficiency has been implemented as a biased die random number process in the simulation. An important improvement to the simulation was to account for PMT to PMT variations in quantum efficiency. The QEs measured for each PMT are used in the simulation to make the light collection efficiency in the detector as realistic as possible.

The scintillation wavelength of liquid xenon is 174.8 ± 10.2 nm [126]. Gaseous xenon emits electroluminescence light at 171 ± 12 nm [121]. The QE for LZ PMTs at VUV wavelengths has been measured to be between 0.25 and 0.35 [112]. For the VUV response, the measured average QE for each PMT across the VUV spectrum is used. Compared to the variation of QEs between different PMTs, accounting for wavelength-dependence within the VUV is negligible. A cutoff at 160 nm is applied. At this wavelength, no light is transmitted through the PMT window anymore. Blue LEDs (470 nm) are installed in the detector for in-situ gain calibration and afterpulsing checks. At 470 nm the QE is expected to be around 0.23 [107].

The quantum efficiency of Skin PMTs is treated the same way as for the TPC PMTs. The wavelength dependence of the QE is also considered for the Outer Detector PMTs using a fit to the data provided by Hamamatsu.

3.4.4 Single photon response

Different PMT response types are simulated using Equ. 3.24. For each response type, the gain and transit time distributions need to be estimated using the relationships discussed in Section 3.2.5 and the measurement results presented in Section 3.3. The probability for first dynode hits and double photoelectron emission is wavelength-dependent. For VUV light, the fraction of double photoelectrons is set to 25%, and 10% of photons induce a response at the first dynode. For blue LED light, the probability for double photoelectrons is negligible, and only 2% of photons are assumed to cause first dynode hits. The wavelength dependent probability for these two effects is estimated from [113].

Multiplication Gain All LZ TPC PMTs are operated at a gain 3.5×10^6. The required voltages to reach this gain were determined during calibration. Blue LEDs in the TPC are used to re-calibrate the PMTs regularly. From the multiplication gain, the PMT pulse area can be calculated. The total charge collected at the anode is

$$Q_a = NGe = (3.5 \times 10^6) \times (1.602 \times 10^{-19}\text{As}) = 0.56\,\text{pAs}. \tag{3.27}$$

The load resistance on base and cable leads to a single photoelectron (SPE) area of 14 pVs. Fig. 3.2 has shown that the variation in gain, while physically better described by a Poisson process, can be well approximated as a Gaussian. It has been confirmed using the data from LZ PMTs discussed in Sec. 3.3, that as long as undersized signals are taken into account, the Gaussian approximation is valid. As a negative gain is unphysical, the Gaussians are truncated at zero. The width of the

distribution, described by the SPE resolution, has been measured for all LZ PMTs by collaborators, fitting a Gaussian distribution to the data. These measurements are used as input to the simulation to reflect the actual performance of the PMTs in the detector. The resolution is scaled as inelastic scatters contribute to the measured SPE resolution. The two types of undersized signals simulated are first dynode hits, and inelastic scatters. For the first dynode hits the multiplication gain is reduced by a factor 14 (first dynode gain), and the width reduces by a factor $\sqrt{14}$. Inelastic scatters are modelled with $\mu_{IES} = 0.3\mu$ and $\sigma_{IES} = 0.5\mu$. While second dynode collection might contribute to the single photon area spectrum, it is difficult to estimate its contribution, and it is assumed to be subdominant.

Transit time Hamamatsu specifies the transit time of the R11410 PMTs to be 46 ns with a FWHM of 9 ns [88]. It is common practice to approximate the transit time variation with a normal distribution [119]. To estimate the timing response of first dynode hits and scatters, the time of flight of the photoelectron between the cathode and the first dynode has to be calculated. The distance between the two is assumed to be 4.1 cm [111] and the voltage distribution in Table 3.1 is used. It is approximated that the photoelectron is emitted with a potential energy close to zero ($V_0 = 0.01$ eV). Using Equ. 3.9, the time of flight of the electron between the cathode and the first dynode is approximately 45.2 ns. The time of flight of a photon across the same distance is negligible. The first dynode hit pulses are therefore expected around 45 ns earlier than regular pulses. This corresponds to what has been observed in tests of the closely related R11410-10 PMT type [111]. Elastic scatters, while having the same area response as normal SPEs, can be distinguished in the timing spectrum as pulses with a time delay of twice the time of flight between dynode and photocathode compared to regular pulses. Inelastic scatters have a time delay of up to twice the time of flight between dynode and photocathode. All gain and timing

	Multiplication Gain		Transit time [ns]	
Type	**Mean**	**Standard dev.**	**Mean**	**FWHM**
SPE	3.50×10^6	0.88×10^6	46	9.00
FDH	2.50×10^5	2.80×10^5	0.93	1.28
IES	1.05×10^6	1.75×10^6	91	29.7
ES	3.50×10^6	0.88×10^6	136	36.6

Table 3.5: Gain and timing parameters for the different PMT effects for the R11410 PMTs.

parameters used as input to the simulation are summarised in Table 3.5.

Double photoelectron In the previous section, it has been shown that it is important to account for the probability that one or both of the photoelectrons emitted in the DPE scatter off the first dynode. In the simulation, both photoelectrons are treated independently in terms of transit time and scattering. Each photoelectron has a 20% chance of being inelastically scattered and a 10% chance of being elastically scattered. The fraction of inelastic scatters is chosen to match the peak-to-valley ratio at nominal gain. The fraction of elastic scatters is set at a value typical for linearly focused PMTs, as this fraction has not been measured for R11410 PMTs [119].

Simulated spectra - PMT stage The pulse area and timing spectrum from the simulation after the PMT stage is shown in Fig. 3.17a and Fig. 3.17b. The dotted lines indicate the contributions from the different response types. There are three distinct peaks in the area spectrum, corresponding to the first dynode hits, single photoelectrons (including ones which were elastically backscattered) and double photoelectrons. Inelastic backscatters contribute to the valley between the first dynode hits and SPEs. The timing histogram shows the time of the response maximum relative to the average response of 46 ns. SPEs and DPEs are normally distributed around zero. Early pulses appear 40 to 50 ns earlier and are first dynode hits. Delayed pulses up to 150 ns later come from elastic and inelastic scatters.

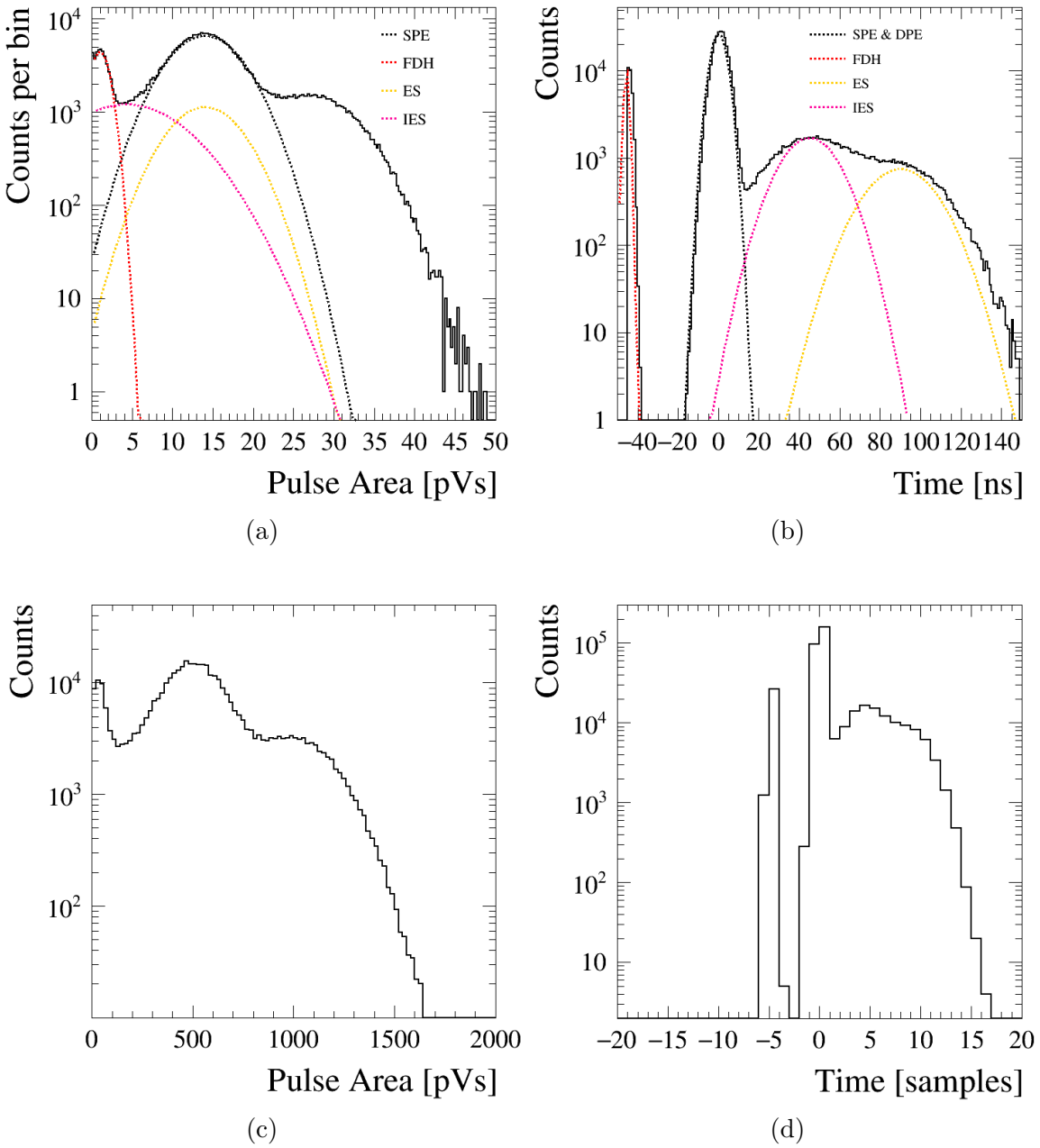

Figure 3.17: Pulse area (a) and response time (b) spectrum for single photon response after PMT stage. The dotted lines indicate the distributions simulated. The double photoelectron is simulated as two independent photoelectrons emitted simultaneously from the photocathode. The time is given relative to the transit time of an ideal SPE. Pulse area (c) and response time (d) after the entire simulation chain.

Simulated spectra - entire electronics chain Fig. 3.17c shows the single photon area distribution after the entire electronics chain. The area distribution closely resembles the shape of the spectrum after the PMT. The double photoelectrons make up about 22% compared to the SPE peak. The SPE resolution, when fitted with a Gaussian is 30%, and the peak-to-valley is 7. The simulated single VUV photon spectrum is in excellent agreement with nominal gain measurements for LZ PMTs presented in this chapter and in [112].

Fig 3.17d shows the transit time effects in samples after the entire electronics chain simulation. As the signal is sampled at 10 ns, it is expected that transit time variations only have a minor effect on the signal timing. The variation in SPE transit time is only 1-2 samples. First dynode hits happen up to 6 samples earlier. The time delay of elastic scatters of up to 18 samples is the most significant effect here. Overall, it can be seen that the different secondary effects impact the variation in the PMT area response to a single photon. Allowing for variation in transit time is vital to define the time window of coincident events between PMTs. The smaller the time window, the smaller the probability of random coincidences.

For the response of Skin and OD PMTs, the same model is assumed to be valid. The gains, SPE resolutions, transit times and transit time spread are used as specified for those PMT types, allowing for PMT-by-PMT variation. For Skin PMTs which see LXe scintillation light, the DPE effect is included, while it plays no role for the OD PMTs.

3.4.5 Ionic afterpulsing

Afterpulsing is simulated for all four LZ PMT types. Every photon inducing a response in the PMT can potentially induce an afterpulse. A random number process similar to the QE is used to decide whether a photon has an afterpulse. If an afterpulse occurs, the ion type is determined in a second random number process. For

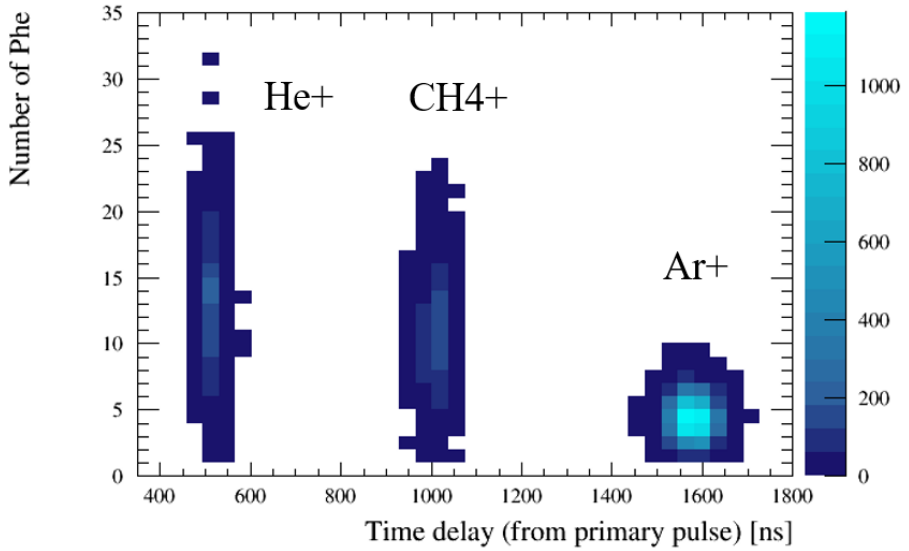

Figure 3.18: Afterpulse timing and number of photoelectrons for several ion types typically present in R11410 PMTs.

each PMT type, a range of ion types is provided with their rate, timing distribution and the average number of photoelectrons emitted. For each of these parameters, a mean and standard deviation are given. A Gaussian distribution is assumed when sampling for time delay and the number of photoelectrons.

The afterpulse time delay for each ion and PMT type is calculated using Equ. 3.18. It is assumed that all afterpulses are from ions in the region between the cathode and first dynode. The voltage distribution is known for all PMTs. The exact distance between the first dynode and cathode is only known for R11410. For all other PMTs, it is estimated using afterpulsing measurements of one or several ions. Compared to merely using measured values, this has the advantage that a wide range of possible afterpulsing can be predicted and used in the simulation. A variety of ions and their afterpulsing timings are summarized in Table 3.6. The number of photoelectrons induced for each ion varies widely. In general, the lighter the atom, the more photoelectrons are emitted. Mean, and standard deviation for the pulse sizes are estimated from published measurements [111] and measurements from collaborators.

PMT	H+	H2+	He+	CH4+	Ne+	N2+	Ar+	Xe++	Xe+
R11410	0.26	0.37	0.52	1.03	1.15	1.37	1.63	2.08	2.96
R8778	0.26	0.36	0.52	1.03	1.15	1.37	1.63	2.08	2.95
R8520	0.82	1.16	1.65	3.29	3.68	4.36	5.21	6.64	9.42
R5912	0.87	1.23	1.73	3.47	3.88	4.59	5.49	6.99	9.93

Table 3.6: Afterpulse time delay in μs for different ions and PMTs

3.4.6 Dark counts

To allow for realistic dark counts, it is necessary to add them randomly to all PMTs. In the simulation, the number of dark counts for each PMT is determined at the input stage using a Poisson probability distribution. The time is then selected at random from within the event window. The dark count can occur in a user-defined time window before the first photon in the event and also after the last photon of the event. This implementation allows for false coincidences of dark counts with one or two-photon S1 or S2-only events. Each PMT is supplied with a measured dark rate. On average the rate for TPC PMTs is around 40 Hz [88] and 1 kHz for OD PMTs [127]. Fig. 3.19 shows the SPE rate estimated from one month of WIMP search simulation data for TPC and OD PMTs. The average daily rates are similar to the dark count rates, as most SPE pulses are due to dark counts. It can be seen that the average dark count rate is different for each PMT.

3.5 Impact of PMT effects on LZ data analysis

3.5.1 Overview

The different PMT effects implemented in the simulation impact the detector performance in terms of detection efficiency and energy resolution. The PMT quantum efficiency, as well as pulse size, impact the experiment's detection efficiencies of low energy recoils. First-dynode hits are not included in quantum efficiency measurements.

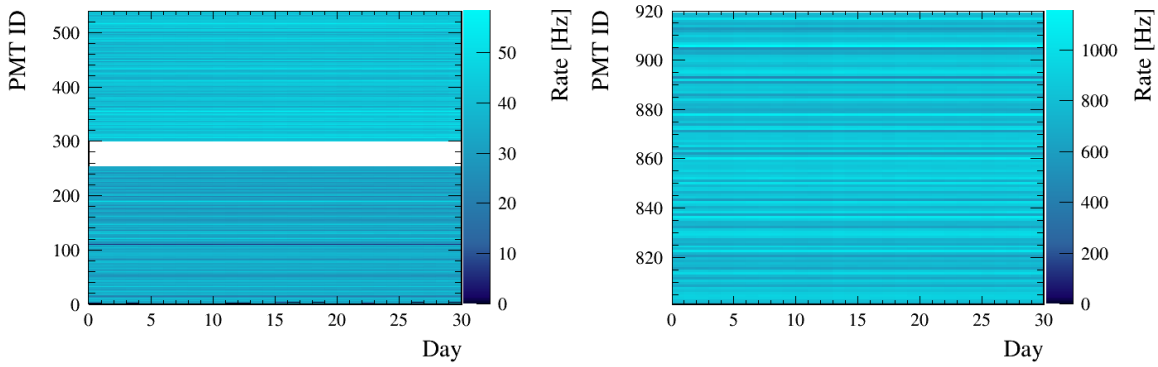

(a) (b)

Figure 3.19: Average SPE rate [Hz] for each individual PMT (y-axis) and day (x-axis) estimated from one month of MDC-2 data for (a) TPC PMTs and (b) OD PMTs. This rate is dominated by the dark count rate

Using the simulation, it can be assessed how the detection of these pulses could lead to an improvement in detection efficiency for low energy recoils. While the gains and timing of the 494 PMTs in the LZ TPC can be aligned using calibrations, the variation introduced by the probabilistic processes and non-standard responses impact the detector resolution in terms of energy and timing. The realist to understanding the detector response in detail, simulating the different PMT effects is important for the training of data analysis tools. The example of position reconstruction shows, how afterpulsing, dark counts and variation of PMT signals play a role in the performance of data analysis methods.

3.5.2 Detection efficiency

3.5.2.1 Quantum efficiency

PMT characteristics and efficiencies have a major impact on the experiments low energy threshold. Fig. 3.20 shows the number of S1 and S2 photons hitting PMTs and producing a response in the PMTs for nuclear recoils of different energies. For nuclear recoils below 20 keV less than 100 S1 photons are collected on the PMTs. Assuming the projected average QE of 26.9% [86], the collection efficiency of S1 light g_1 is

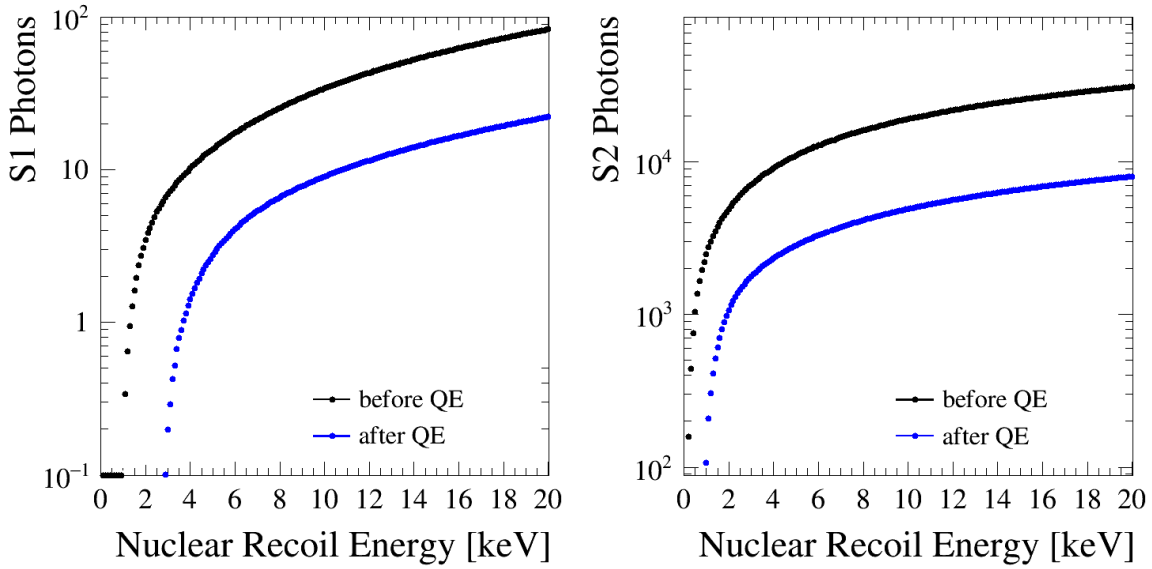

(a) (b)

Figure 3.20: NR yields for S1 and S2 signals before and after QE.

0.119 and the projected collection efficiency of S2 light $g_{1,gas}$ is 0.102 (see Section 4.3 for more detail). For nuclear recoils of less than 10 GeV, the average number of S1 photons inducing a response in the PMTs falls below 10. It can be seen that in the low energy regime, the quantum efficiency is one of the limiting factors. To get a better estimate of light collection efficiency, it was evaluated by simulating 4×10^7 nuclear recoils in the energy range 0 to 60 keV uniformly distributed in the detector volume. The full simulation chain (see Fig. 2.7) was used, including the PMT module presented in this chapter with PMT-by-PMT varying QEs informed by measurement. Taking the ratio of detected photons to photons produced in the interactions, the light collection efficiencies are $g_1 = 0.149$ and $g_{1,gas} = 0.1223$. The actual measured quantum efficiencies lead to a significant improvement in light collection efficiency.

3.5.2.2 Dark counts

The three-fold coincidence requirement between PMTs is applied in data analysis to reduce the probability of dark counts mimicking S1 pulses. If they coincide with S2-

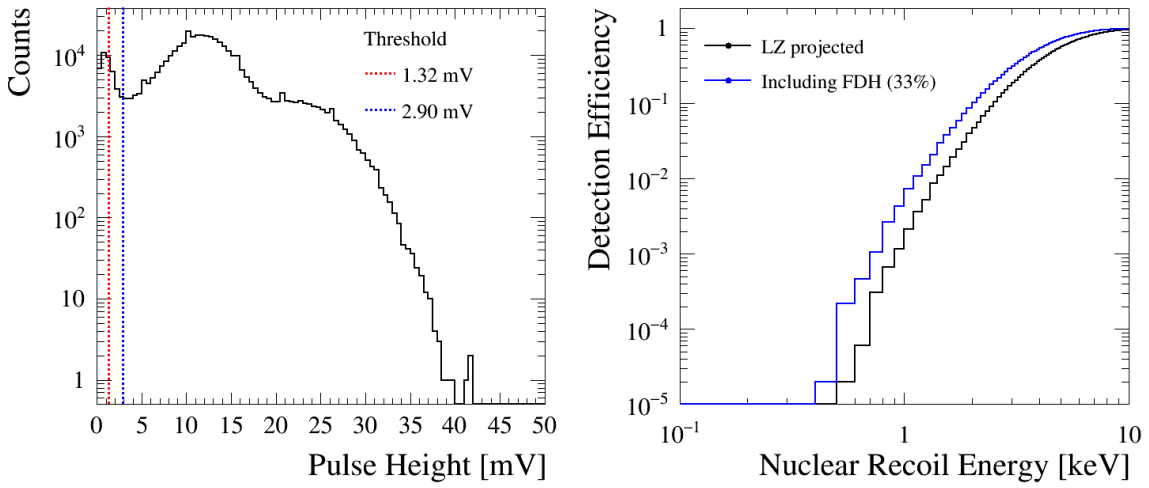

(a) (b)

Figure 3.21: (a) Pulse height of simulated PMT pulses for the entire single photon response spectrum. (b) Improvement in low energy NR detection efficiency by including first dynode hits (FDH), assuming the more optimistic threshold of 1.32 mV.

only events, these two signals can be combined to create fake S1-S2 pairs. Such events can land within the NR region and be a dangerous background. For an average dark count rate of 20 Hz and an S2-only estimate of 1 mHz (estimated from LUX) 0.16 fake events are expected in 1000 days of data taking [86]. This three-fold coincidence requirement lowers the efficiency of detecting low energy events further. The 50% nuclear recoil detection efficiency threshold goes from 3 to 5 keV as seen in Fig. 3.20a.

Any differences in response spectra between single photons and dark counts could potential allow distinguishing between the two. A recent analysis of the LUX collaboration has shown how low energy sensitivity can be improved by using the DPE effect to lower the coincidence requirements [128]. The realistic simulation of dark counts and double photoelectrons allows the study of similar possibilities for LZ.

3.5.2.3 Trigger efficiency

In the low energy recoil regime, it is also important to account for the efficiency of triggering on the single photon response. In LZ, the baseline requirement is 95%

Response type	**Detection Efficiency** [%]	
	th = 1.32 mV	th = 2.90 mV
SPE	99.98	99.86
FDH	33.21	3.53
SPE + IES	98.09	95.07
SPE + IES + FDH	93.74	88.71
SPE + IES + FDH + DPE	94.20	89.91

Table 3.7: Detection efficiencies for different response types and thresholds.

trigger efficiency on single photoelectrons. However, it is expected that noise performance in LZ is considerably better. To assess the detection efficiency not only for SPEs but also undersized PMT pulses, 100,000 photons hitting PMTs are simulated with different PMT effects switched on and off. Two noise scenarios are considered. The conservative scenario assumes that the trigger threshold can be set at 25% of the SPE size. This is informed by LUX, and it is expected that LZ will be able to do better than that [75]. The more optimistic scenario assumes that the dominant noise is the RMS ADC noise. For LZ prototype boards this was measured to be $\sigma = 1.19\,\mathrm{ADCC} = 0.44\,\mathrm{mV}$ [75]. A constant trigger threshold is set at 3σ. Fig. 3.21a shows the pulse height spectra for the entire single photon spectrum with the two trigger thresholds. The detection efficiencies are summarized in Table 3.7. The detection efficiency for pure SPE pulses is 99.98% in the optimistic scenario. Allowing for elastics scattering and therefore introducing a population of undersized signals reduces the efficiency to 98.09%.

3.5.2.4 First dynode hits

Only 33% of the first dynode hits have a pulse height above the optimistic trigger threshold. For the pessimistic scenario, only 3.53% are detected. PMT quantum efficiencies are determined by measuring the PMT response to a light source of known intensity. Small pulses as these first dynode hits, thus, do not contribute significantly to the measured QE. It is estimated from spectra presented in [113], that about

10% of incident photons cause first dynode hits. In the low energy regime in which individual photons can be detected using digital photon counting (further explained in the next section), first dynode hits could lead to a significant improvement in detection efficiency for low energy recoils. If 33% of first dynode hits are triggered on, the light collection efficiency increases by 3.5%. The corresponding improvement in NR detection efficiency is illustrated in Fig. 3.21b. For a 6 GeV WIMP, this would correspond to an improvement in the projected sensitivity limit from $1.09 \times 10^{-45}\,\mathrm{cm}^2$ to $8.06 \times 10^{-46}\,\mathrm{cm}^2$ at 90% confidence. While the fraction of first dynode hits needs to be further quantified by measurement, including this effect in the simulation is essential to start developing data analysis methods to take advantage of it.

3.5.3 PMT calibrations

3.5.3.1 Gain

Traditionally, the pulse area induced by one photoelectron (phe) is the standard unit. In LZ, due to the double photoelectron effect, the area is calibrated to photons detected. For the outer detector, no DPE emission is expected, as the scintillation light has much longer wavelengths than VUV light. Therefore, phe and phd are the same for OD PMTs, while there is a difference for all PMTs detecting VUV light. Blue LEDs are installed in the detector to calibrate the SPE size per channel. Additionally, a population of single photoelectrons in the VUV has to be selected to calibrate the fraction of double photoelectrons per channel. While the mean of the area can be aligned very well by adjusting voltages, the spread due to probabilistic processed in the PMTs remains. From the simulation the fitted SPE peak resolution is $\sigma_{phe} = 0.30$. Including both DPEs and inelastic scatters, the resolution becomes $\sigma_{phd} = 0.48$. A way to improve the variation is to use photon counting to estimate pulse areas. Photon counting looks for peaks in the signal trace, which correspond to individual photons. It, thus, reduces the impact on secondary emission statistics on

data analysis. However, this method can only be employed when little photon pileup is expected.

3.5.3.2 Timing

The contributions to channel-by-channel timing differences in PMT signals are the photoelectron transit time in the PMT, the difference in cable lengths and timing differences in digitizer clock cycles. As each PMT voltage is adjusted to align the gain, the voltage-dependent transit time varies PMT by PMT. This timing is corrected using pulsed LEDs and accounting for the path difference between LED and different PMTs. The transit time FWHM spread for the LZ TPC PMTs is 9 ns. After digitization, this results in a standard deviation of 0.5 samples. However, early and late pulses due to the different PMT effects discussed previously lead to a standard deviation of 3.5 samples. Spread in timing is important for the estimation of photon arrival times, which in turn are used for pulse shape discrimination. It has been shown on LUX that pulse shape discrimination could improve background discrimination, especially at higher energies [129]. Photon arrival times are also of interest for vetoing of Cerenkov light emitted from PMT windows as discussed in Section 4.6. Additionally, the variation in response time impacts whether two photons are resolved as two peaks, as shown in Fig. 3.22. This impacts the performance of photon counting, which looks for individual peaks in the signal trace.

3.5.4 Energy resolution

The variation in PMT response contributes to the energy resolution in the detector. A better energy resolution leads to narrower ER and NR bands and allows for better background discrimination. The following discussion focuses only on the detector resolution and the impact of PMT response variations on it based on [95]. Variations in recombination impact the resolution but are not considered here. The formal-

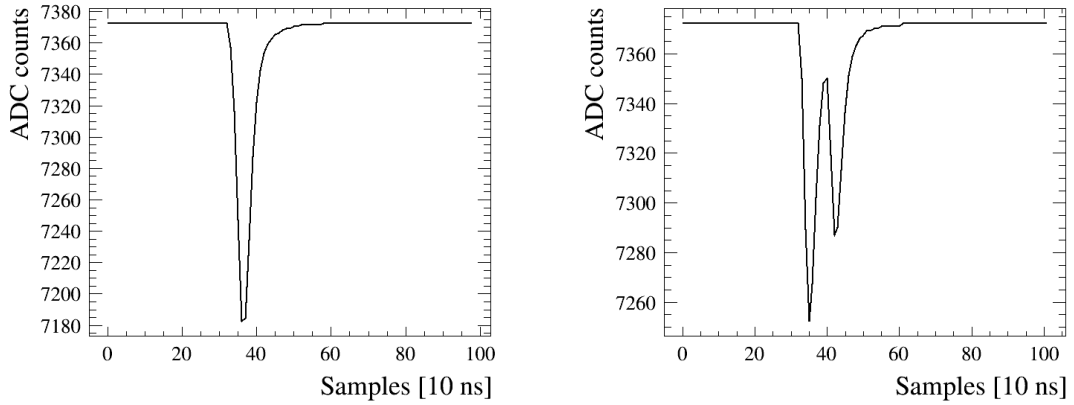

(a) (b)

Figure 3.22: Example of waveforms (processed through the entire electronics chain simulation) corresponding to two photons arriving at the same PMT with 40 ns time difference. Transit time variation impact whether the photons are resolved as individual peaks.

ism introduced in Section 2.2.4 is used. The detector resolution is described by the variation in photon detection $\sigma(n_\gamma)$ and the variation in electron detection $\sigma(n_e)$.

Photon detection depends on the optical properties of the detector. The average light collection efficiency across the detector is g_1. As the detection of S1 photons follows a binomial process, the variance is given by:

$$\sigma^2_{S1,bino} = (1 - g_1)g_1 n_\gamma = (1 - g_1)S1. \tag{3.28}$$

Using $g_1 = 0.149$ leads to $\sigma^2_{S1,bino} = 0.851 \times S1$. The variation introduced due to the PMT resolution is described by:

$$\sigma^2_{S1PMT} = g_1 n_\gamma \sigma^2_{phd} = \sigma^2_{phd} \times S1. \tag{3.29}$$

With $\sigma_{phd} = 0.48$, this becomes $\sigma^2_{S1PMT} = 0.2304 \times S1$. Combining the two and using $n_\gamma = \frac{S1}{g_1}$ the variance in average number of measured photons is given by:

$$\sigma^2_{n_\gamma} = \frac{(1 - g_1 + \sigma^2_{phd})}{g1} n_\gamma = 7.26\,\mathrm{phd}/n_\gamma. \tag{3.30}$$

It can be seen that while the variation in light collection efficiency is the larger contribution, the PMT resolution has a substantial impact on the spread in measured photons.

The variance in S2 signal can also be described assuming an underlying binomial process:

$$\sigma^2_{S2,bino} = (1-\epsilon)\epsilon(\kappa n_e)N^2_{ph}. \tag{3.31}$$

The electron extraction efficiency from liquid to gas phase ϵ is expected to be 0.95 in LZ. κ describes the probability of the electron to survive, which again is projected to be 0.95. N_{ph} is the average number of photons detected per electron. In LZ this is estimated to be 83 phd [86]. $\sigma^2_{S2,bino}$, thus becomes $310.9 \times n_e$. The variation in S2 signal due to the PMT resolution is:

$$\sigma^2_{S2PMT} = \epsilon(\kappa n_e)\sigma^2_{phd} = 0.21 \times n_e. \tag{3.32}$$

It is assumed, based on LUX, that the variation in electron attenuation $\sigma_{n_{e,att}}$ due to the finite electron lifetime is subdominant [95]. Remembering that $n_e = \frac{S2}{g_2}$, the variance in average number of measured electrons becomes:

$$\sigma^2_{n_e} = \frac{(1-\epsilon)\epsilon N^2_{ph} + \epsilon\sigma^2_{SE}}{g_2}\kappa n_e = 3.93\,\mathrm{phd}/n_e. \tag{3.33}$$

From this discussion, it can be seen that the PMT resolution impacts the detector resolution by introducing variance in the S1 signal. Its contribution to the spread in the number of detected electrons is subdominant as each electron on average leads to the detection of 83 electroluminescence photons.

3.5.5 Position reconstruction

So far, it has been discussed how the different properties of the PMTs impact overall detector performance like detection efficiency and energy resolution. It is also im-

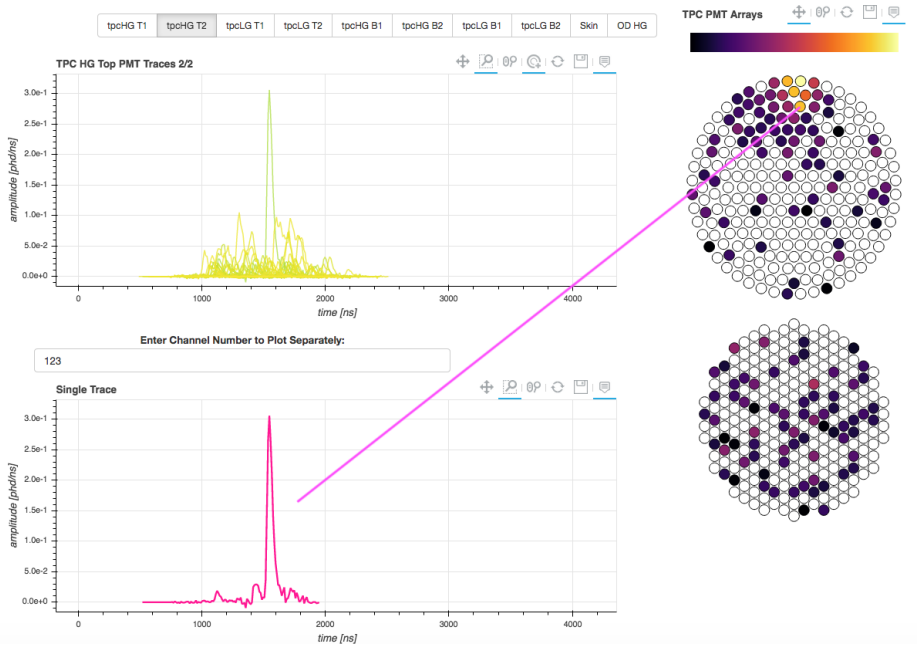

Figure 3.23: Event display for simulated wall event with afterpulse on PMT 123. The large area on this PMT leads to a reconstruction of the event further inside the fiducial volume.

portant to consider the impact on the performance of crucial data analysis tools like position reconstruction. Reliable position reconstruction is needed for efficient fiducialization, which in turn is essential for background reduction. It is only possible, if position reconstruction works reliably, even for low energy signals. For LZ, position reconstruction will be done using Mercury (see Section 2.6.3). The analysis threshold for S2s is 5 electrons. 5 electrons near the wall lead to pulses of 200-300 phd, with an average of 32 photons on the two PMTs closest to the location of emission. In this regime of very small areas on the different PMTs, statistical fluctuations, dark counts and afterpulsing can have a devastating impact. To assess this, 1×10^6 events with 5 electrons each are simulated using BACCARAT and the DER. The electrons are placed just below the liquid surface and 1 mm away from the detector wall. Fig. 3.23 shows such an event where an afterpulse occurs in one of the PMTs further away from the wall. The resulting pulse area distribution across the PMTs makes it more likely for the position of the event to be 50 to 60 mm inside the wall. Such events will be

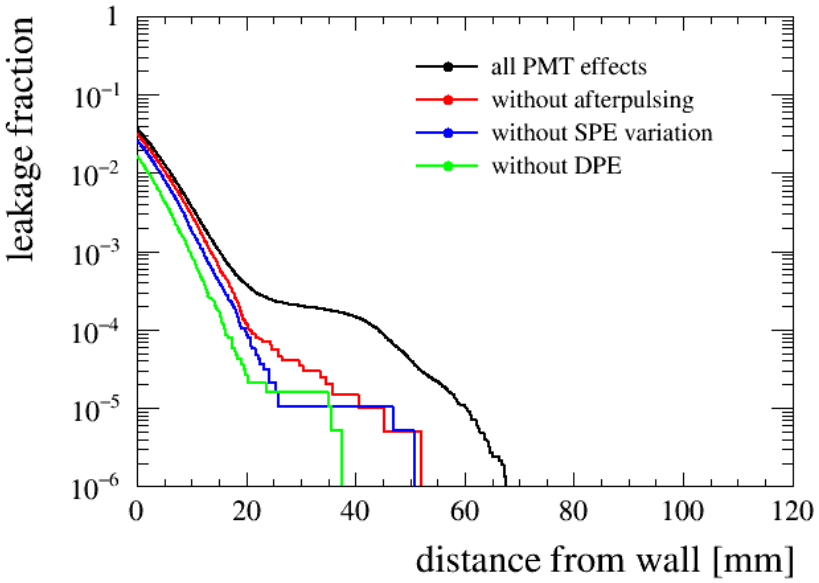

Figure 3.24: Wall leakage for 5 electron signal with and without different PMT effects.

reconstructed inside the 40 mm fiducial radius. It is important to include afterpulsing cuts in pulse finding and classification. They appear as large SPE like pulses and can be cut effectively.

Fig. 3.24 quantifies the improvement in leakage if afterpulses are removed. Even without afterpulsing, there are events which still leak into the fiducial volume. This is mostly due to statistical fluctuations in gain and the double photoelectron effect. Fig. 3.17c shows that a single photon can initiate pulse responses varying by up to a factor 100 in the area due to dynode and the DPE effects. Up until now, Mercury has not taken these effects into account. Fig. 3.24 shows that it performs well if all variations and DPE effects are switched off in the simulation. The position reconstruction for LZ needs to use a statistical model accounting for these variations.

3.6 Conclusion

This chapter has presented the development of a new extended model of the single photon response of LZ TPC PMTs to VUV light and shown the impact of PMT

properties on LZ detector performance and data analysis.

A first dedicated study of undersized PMT signals has been conducted for the R11410 PMT type. Going to higher gains allows a better characterization of the single photon area spectrum. The first dynode hits contribute to the distribution, but electronic pick-up noise limits the ability to extract more information about these pulses from the data. Inelastic scatters have to be included to account for the observed peak-to-valley ratio. Undersized signals also play an important role when looking at double photoelectrons. It had previously been observed that the double photoelectron distribution does not precisely correspond to a distribution of two photoelectrons following a Gaussian SPE distribution [112]. This discrepancy becomes more apparent at higher gains than at nominal. It was shown that allowing for undersized signals and treating both photoelectrons in the double photoelectron emission independently, allowing for them to scatter, accounts for this discrepancy. An extended model taking all these observations into account has been developed, and it has been shown to describe the data very well.

The extended model has been implemented in the PMT simulation accounting for variation in both gain and timing. Additionally, PMT noise in the form of dark counts and afterpulses has been modelled using published data and measurements from collaborators. The simulation takes measured parameters for each PMT as input to allow for PMT-to-PMT variations.

Including these effects in the simulation is essential for understanding the LZ detector performance in terms of detection efficiencies and resolutions. It has been shown that PMT properties such as QE and dark rates impact the low energy detection efficiency and threshold. Considering the response induced by first dynode hits could lead to a substantial improvement in detection efficiency of low energy events if sufficiently good noise levels are achieved. The PMT resolution impacts the variation in detected S1 photons and thus the detector resolution. The example of position

reconstruction has shown the importance of training data analysis tools with realistic simulation data, including different PMT effects. The realistic PMT simulation is also useful for studies assessing detector performance in different scenarios, as done in the following chapter for PMT failures.

Chapter 4

Impact of PMT failure on LZ sensitivity

A comprehensive simulation study is presented in this chapter, assessing the effect of inactive PMTs on LZ data analysis and sensitivity. Previous experiments have shown that there is a severe risk for PMT failure during long term operation. Firstly, it is investigated how fewer working PMTs affect the light collection and event detection efficiencies. Subsequently, the impact of different scenarios of failed PMTs on background reduction is discussed. Efficient background reduction relies on ER-NR discrimination, position reconstruction and effective cuts on background topologies. All three methods are assessed. Finally, the reduction in LZ sensitivity for different scenarios is estimated. It is shown that while backgrounds are essential to consider, the effect of inactive PMTs on low energy thresholds and fiducialization dominates. It is important to note that the locations of non-operational channels matter. PMTs on the outermost row of the top PMT array are essential for fiducialization. Bottom array PMTs are more critical for S1 light collection and therefore low mass WIMP sensitivity than top array PMTs. For 4% random initial PMT loss (LZ requirement), the impact on the sensitivity limit is 6% at 40 GeV, increasing to 11% at 6 GeV. The

decrease in sensitivity at low WIMP masses is dominated by the reduced S1 light collection efficiency. For a 40 GeV WIMP, the contributions from reduced fiducialization and light collection efficiency are approximately equal, assuming that passive PMTs are randomly distributed. A loss of 16% of PMTs leads to a reduction of sensitivity of 15% at 40 GeV and 56% at 6 GeV.

4.1 Motivation

An important parameter in the performance of the LZ detector is the efficiency of S1 and S2 light detection. Especially the scintillation light detection efficiency depends on many factors, such as VUV reflectivity of internal surfaces, the absorption length in the liquid bulk, the geometric transparency and reflectivity of all grids. It also depends critically on the PMT coverage and the performance of the PMTs. The layout of the PMT arrays was optimised to allow maximal light collection efficiency across the detector [75]. The light collection efficiency of the scintillation light g_1 and the electroluminescence light collection efficiency $g_{1,gas}$ have to be assessed individually. The S1 signal, originating in the liquid phase, is preferentially detected by the bottom array PMTs which are immersed in the liquid. The S2 signal, which is emitted in the gas phase, is mostly seen by the top array. The bottom array has a closely packed hexagonal structure. The PMT photocathodes cover 54% of the array, and highly reflective PTFE covers the remaining surfaces. For the top array, an important factor was the placement of the outer row PMTs to allow excellent position reconstruction at the outer edges of the TPC. The array has, therefore, a hexagonal pattern in the centre with two nearly circular rows on the outside. The outermost row overhangs the edge of the TPC. Both array layouts are displayed in Fig. 4.1.

All LZ PMTs have undergone thorough acceptance tests before installation. However, previous experiments have shown that PMT failures are a significant risk during

long term operation. PMTs can be inactive, i.e. not used in data analysis, for several reasons. A PMT could be broken or unresponsive, switched off to avoid noise, or masked in the analysis. The Xenon1T experiment, which has 248 PMTs of a closely related PMT type as the LZ PMTs, had 27 PMTs switched off during running and masked an additional eight during analysis [130].

A simulation study has been conducted to assess the impact of PMT failures on LZ analysis. Having fewer working PMTs impacts the light collection efficiency across the detector. A high and uniform scintillation light collection efficiency is vital for a low energy detection threshold. ER-NR discrimination relies on the ratio of detected S1 and S2 photons. With varying light collection efficiency across the detector, leakage of ER events below the NR median could increase. An excellent S2 light collection efficiency across the gas phase allows precise S2 position reconstruction and therefore, efficient fiducial cuts on wall events and multiple-scatter vertex resolution. Additionally, there are specific background topologies like gamma-X events and Cerenkov light from PMT windows which are typically identified by specific hit patterns on the bottom array. Therefore, losing even individual PMTs on the bottom array can be potentially problematic.

All these effects of PMT loss are discussed in detail, and their effects on LZ data analysis and sensitivity are assessed in the following. This study only focuses on TPC PMTs. PMT failures in the skin and outer detector would have an impact on veto efficiency. Scenarios with 10, 20, 40, 60 and 80 inactive PMTs are considered which corresponds to 2-14% of the TPC PMTs. Due to the symmetry of the PMT arrays, not every possible configuration needs to be tested separately. However, it is essential to test the impact of top and bottom array independently. For some parts of this study, the arrays are split into inner and outer arrays. Here the outermost three rows are defined as the outer part of the array, the rest as the inner part, as indicated in Fig. 4.1.

4.2 Simulation and analysis tools

The data for this study is produced using the LZ simulation framework discussed in Section 2.6.2. For the estimation of light collection efficiency, the BACCARAT output is directly analysed. For ER-NR discrimination and wall background studies, both BACCARAT and DER are used, and the events are reconstructed with LZap. As part of this study, a new feature was added to LZap to allow switching PMTs off at the LZap stage. Any data on PMTs marked as inactive is ignored, and the PMTs are marked as passive for position reconstruction. Unless specified the location of inactive PMTs was chosen randomly.

The standalone NEST package was used to assess average effects such as yields and detection efficiencies [100]. Another data set used for parts of this study is data produced for a collaboration-wide mock data challenge (MDC-2). The MDC-2 data was produced with the entire analysis chain and contains the expected backgrounds for the first six months of data taking.

The S1 is corrected for position dependent light collection efficiency. Electron lifetime corrections are applied to the S2 signal. The standard analysis cuts applied for event selection are a 3-fold coincident requirement for S1s and a maximum S1 signal of 80 phd. The S2 needs to be larger than 400 phd to allow good position reconstruction. The fiducial volume is defined as $r_{max} = 68.8\,\text{mm}$, $z_{min} = 2.0\,\text{mm}$ and $z_{max} = 132.6\,\text{mm}$. Any additional assumptions and specific cuts are described in the individual sections.

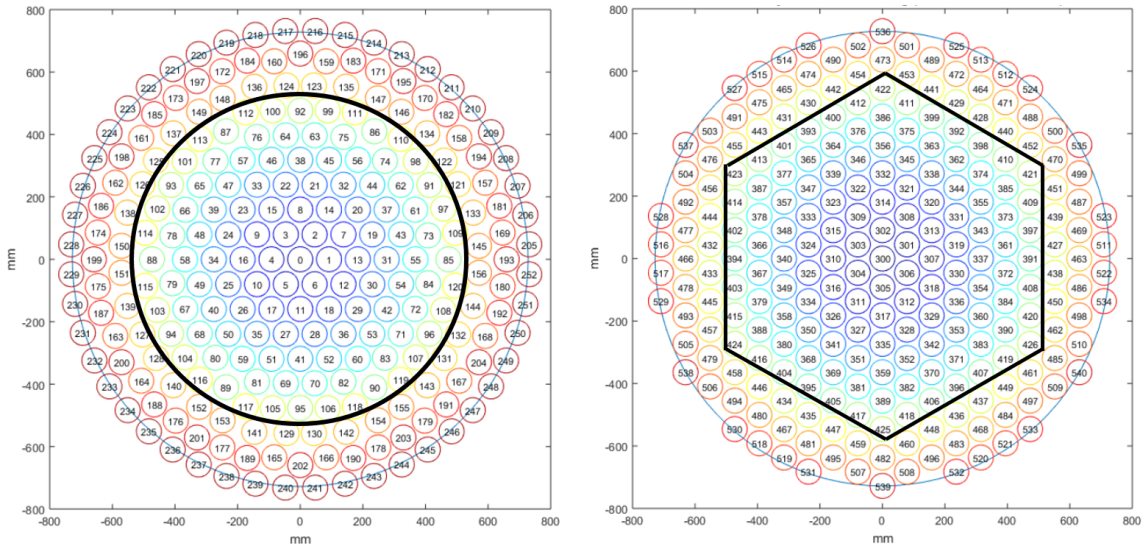

Figure 4.1: PMT array layout for top (left) and bottom (right) arrays. The colours indicate a similar distance from the centre. The thick black line indicates inner and outer parts of the arrays for the purpose of this study [75].

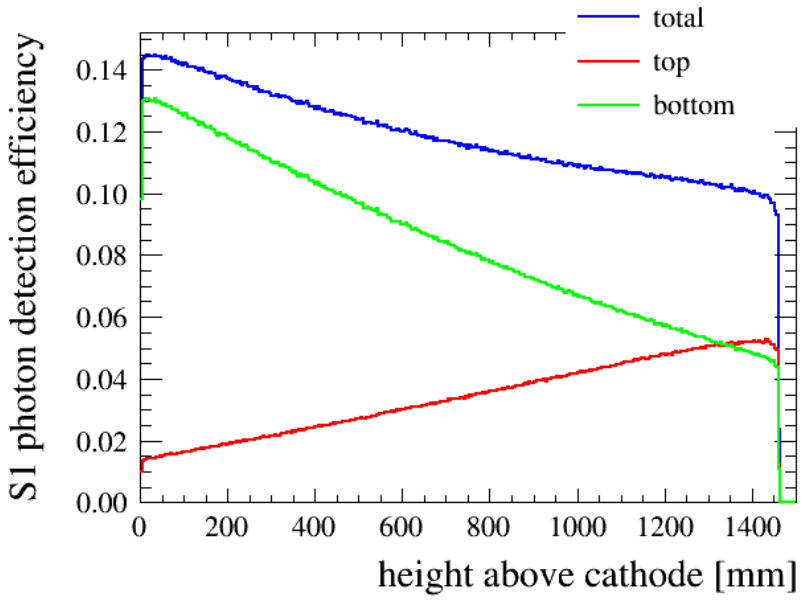

Figure 4.2: S1 light collection efficiency for the LZ projected scenario with all PMTs working.

4.3 Light collection and detection efficiency

4.3.1 S1 light collection efficiency

The S1 light collection efficiency describes the efficiency with which scintillation photons from the liquid xenon active detector volume are detected. One hundred million photons distributed uniformly in the liquid phase are simulated. If a photon hits a PMT photocathode, the PMT number is recorded in the simulation output file. Additionally, the initial xyz-position of the photon is recorded. The position-dependent light collection efficiency is estimated using an average PMT QE of 26.9%. As discussed in the previous chapter, this is a very conservative estimate for the LZ TPC PMTs at LXe temperatures. It was chosen to match the assumptions made for the projected LZ scenario [86]. Randomly chosen PMTs are marked as passive in the analysis and the light recorded on them is ignored. Various scenarios with different ratios of inactive PMTs on the top and bottom array and inner-outer array location are considered. Each scenario is repeated ten times with randomly chosen PMTs, to get an estimate of the position dependence of PMTs.

The projected LZ S1 light collection efficiency (LCE) as a function of z is shown in Figure 4.2. It shows the total efficiency as well as the separate top and bottom array efficiencies. The top array sees a significant fraction of light for events occurring near the top of the detector. The bottom array sees much more S1 light for the majority of the events due to the strong internal reflection of VUV light at the liquid surface and the fact that the PMT windows and liquid xenon have an excellent match in VUV refractive index. Additionally, the PTFE walls in the liquid have high reflectivity. The projected average g_1 across the detector is 0.119.

Figure 4.3a shows the reduction of S1 LCE for an increasing number of passive PMTs. As to be expected, the S1 LCE suffers more from losing PMTs on the bottom array than from losing PMTs on the top array. Fitting the curves one gets a linear

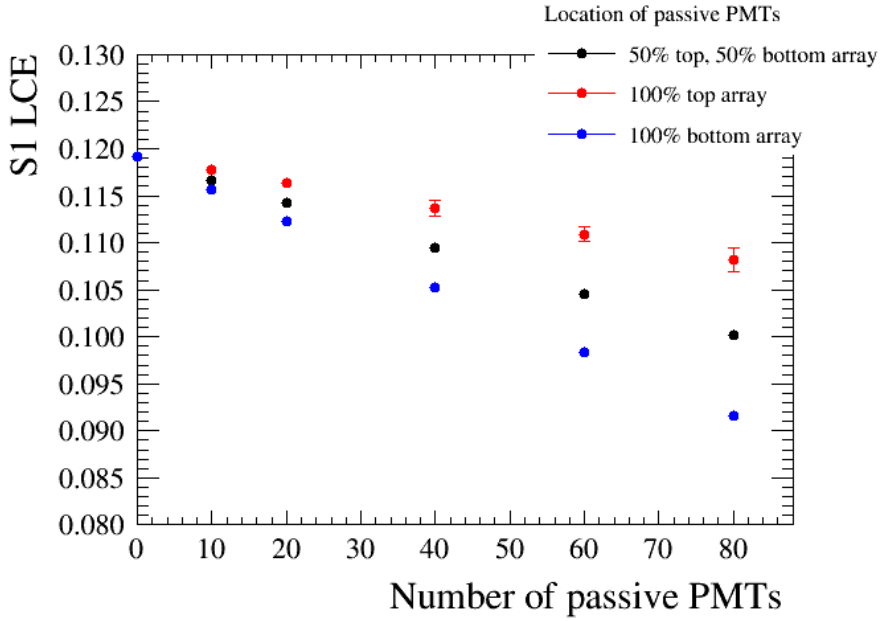

(a)

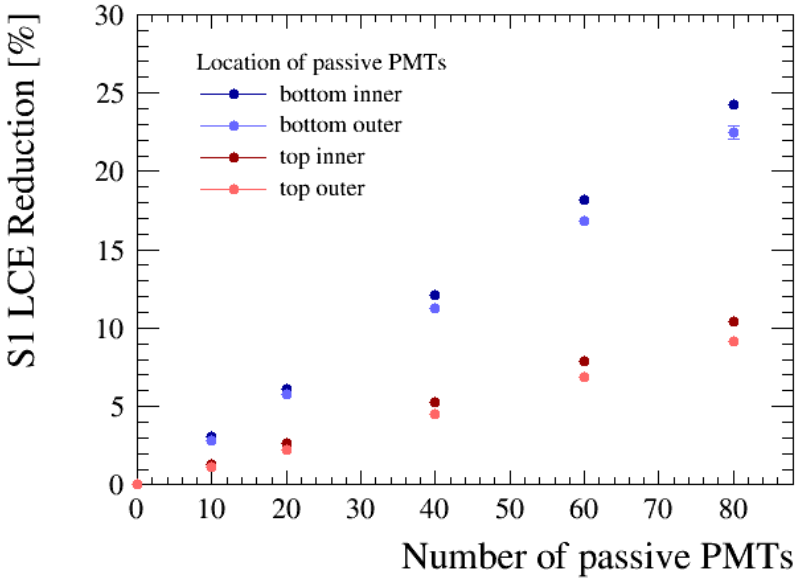

(b)

Figure 4.3: Average S1 light collection efficiency in the fiducial volume for different scenarios of inactive PMTs.

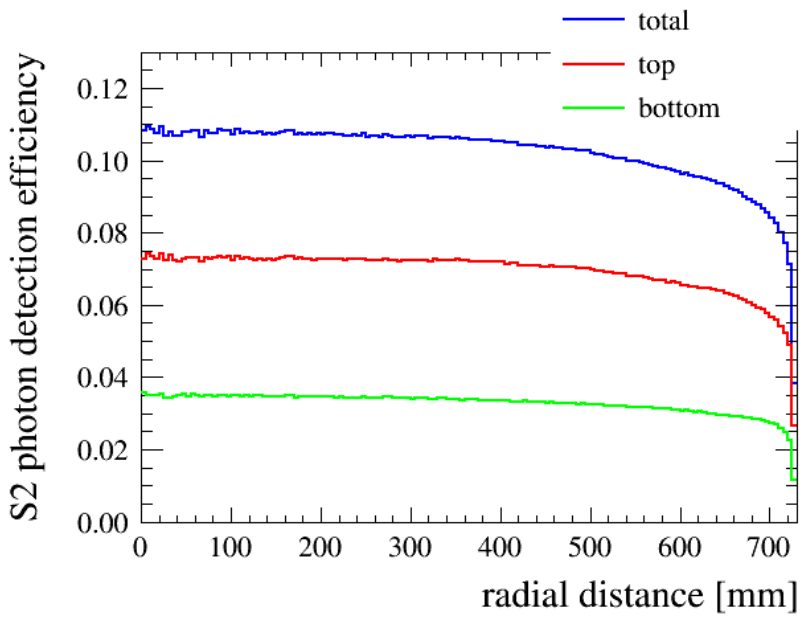

Figure 4.4: S2 light collection efficiency for the LZ projected scenario with all PMTs working. The efficiencies for top and bottom arrays are shown separately.

relationship which can be used to estimate the S1 LCE for any number of inactive PMTs. The average loss in LCE per passive PMT is summarised in Table 4.1. The linear relationship of approximately 0.2% efficiency loss per inactive PMT still holds even if 250 PMTs fail. If 250 out of 494 PMTs are not working, the LCE is reduced by approximately 50% as to be expected from reducing the area covered by active photocathodes by about half. Additionally, the effect of the radial location on the PMT arrays was assessed. PMTs located in the inner region of the arrays lead to 0.01-0.02% higher losses per PMT than PMTs on the outer part of the array, as shown in Fig. 4.3b. The small difference is expected as S1 light disperses widely in the TPC and is detected by many different PMTs.

4.3.2 S2 light collection efficiency

The S2 light collection efficiency describes the efficiency with which electroluminescence photons from the gas region are detected by the PMTs. Again one hundred

million photons are simulated. To assess the S2 light collection efficiency, they are distributed uniformly in the gas phase. The same analysis, as described in the previous section, is used. Figure 4.4 shows the S2 light collection efficiency as a function of radius in the projected LZ scenario. The efficiency is uniform in radius with a drop off at large distances from the centre. The top array sees most electroluminescence light. Again this is due to the optical mismatch at the boundary between liquid and gas phase, the anode transparency and the reflectivity of PTFE in the gas phase [75]. The average $g_{1,gas}$ across the detector is 0.102. The reduction of $g_{1,gas}$ with inactive PMTs is summarized in Figure 4.5a.

As for S1 LCE, the reduction can be approximated to be linear. For S2 signals failure of top-array PMTs has a more significant impact. The parameters for fitting the linear relationships are given in Table 4.1. It was confirmed that this linear relationship is still valid at 250 inactive PMTs. Fig. 4.5b shows how $g_{1,gas}$ varies depending on whether the passive PMTs are located in the inner or the outer part of the array. It can be seen that the location has a substantial effect on the top array. The location does not only affect the average $g_{1,gas}$ but has a substantial effect on the local S2 light collection efficiency. The light collection efficiency in areas close to the inactive PMTs is reduced by up to 40% of its original value. Whether an inactive bottom PMT is located on the inside or outside of the bottom array is a small effect of up to 1% with the PMTs located in the inner array leading to slightly higher losses.

Overall, it can be seen that inactive PMTs affect the LCE of S1 and S2 light similarly. The loss in both g_1 and $g_{1,gas}$ is approximately 0.2% of their original values per lost PMT. Passive PMTs in the bottom array mostly affect the S1 light collection efficiency, whereas they have less effect of the S2 light collection efficiency.

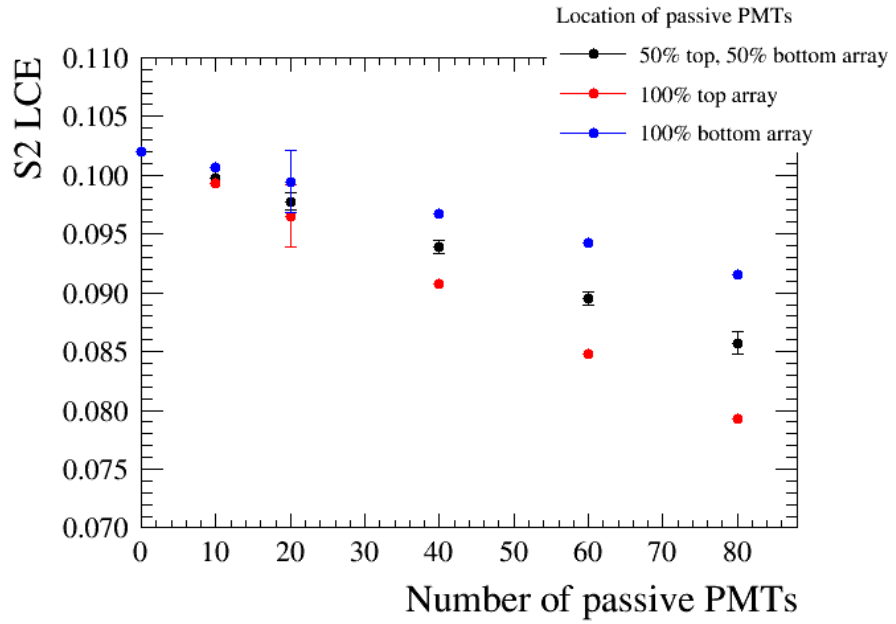

(a)

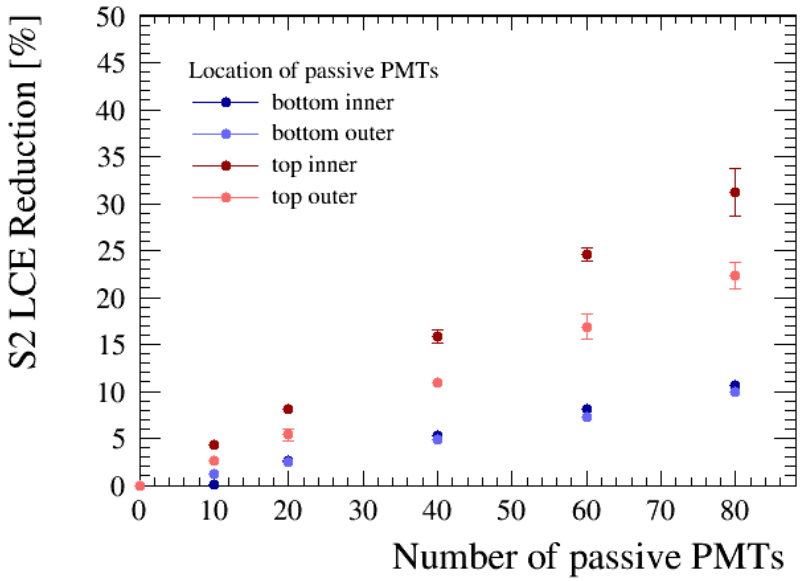

(b)

Figure 4.5: Average S2 light collection efficiency in the fiducial volume for different scenarios of inactive PMTs.

	Reduction in LCE per PMT [%]	
PMT location	**S1**	**S2**
top array	0.113 ± 0.005	0.279 ± 0.001
bottom array	0.290 ± 0.003	0.128 ± 0.001
average	0.203 ± 0.002	0.202 ± 0.006

Table 4.1: Average reduction of S1 and S2 LCE from fit as percentage of original LCE.

4.3.3 Signal yields and detection efficiencies

A reduction of light collection efficiency leads to fewer detected photons per event, as characterised by the signal yield. The signal yield is defined as the number of detected S1 or S2 photons per keV energy deposition. 10,000 ERs and NRs are simulated for each of the energies in the range 0 to 100 keV using NEST. The light collection efficiency results from Section 4.3, parameterized as g_1 and $g_{1,gas}$, are used to simulate the different PMT loss scenarios. The resulting yields are displayed in Fig. 4.6. As expected, the S1 and S2 yields reduce with an increasing number of inactive PMTs. The reduction for both ER and NR signals is proportional to the reduction in light collection efficiency, which is approximately 2% per 10 inactive PMTs.

PMT failures affect the detection of ERs below 3 keV, and NRs below 10 keV deposited energy. Above these energies, the detection efficiency is unchanged. The S1 and S2 detection efficiency for nuclear recoils are plotted in Figure 4.7 for all PMTs working and 40 PMTs lost on the bottom (left) or top (right) array. The efficiency curves illustrate again that the bottom array mostly impacts the S1 detection efficiency, while the top array mostly affects the S2 detection efficiency. It can also be seen that the S1 signal, as the smaller signal, dominates the NR detection efficiency for low energy deposits. A reduced light and charge yield will, therefore, lead to a lower nuclear recoil detection threshold. The detection efficiency of 1, 5 and 10 keV

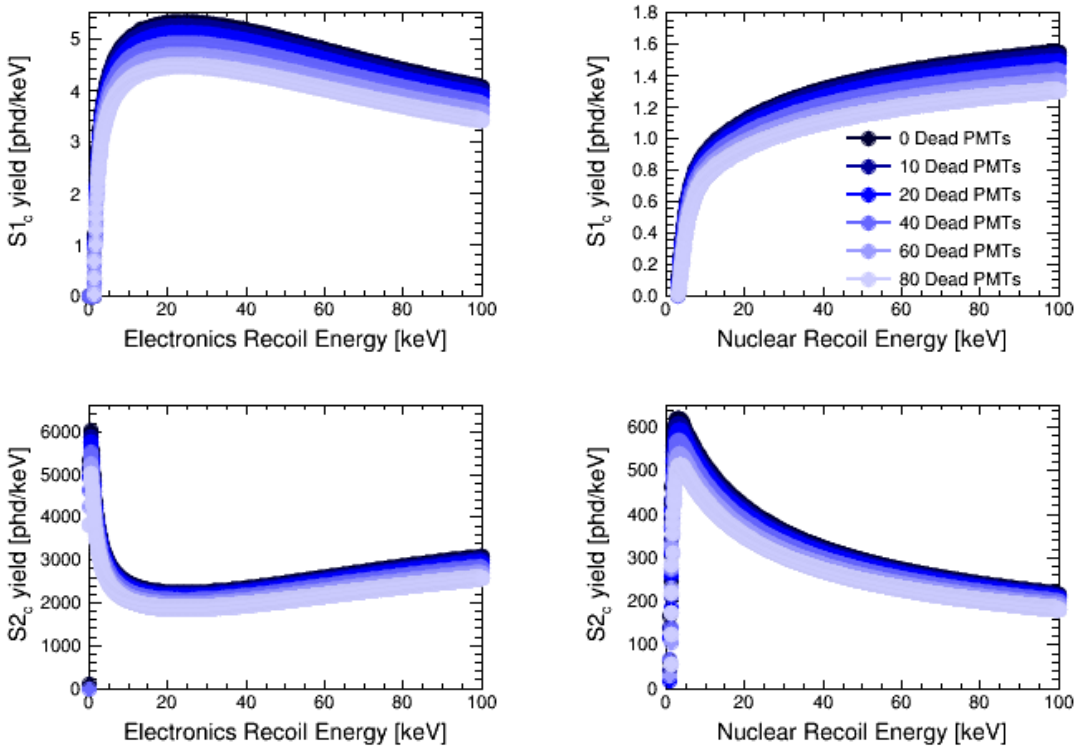

Figure 4.6: Effect of lost PMTs on S1 and S2 yields for both NRs and ERs.

nuclear recoils for different scenarios is summarized in Table 4.2. In the LZ projected scenario, 50% NR detection efficiency is reached at 4.75 keV deposited energy. Losing top PMTs does not have a significant impact on this threshold. The threshold only starts shifting to higher energies when there are also bottom array PMTs failing. For 80 inactive PMTs (40 top and 40 bottom) the threshold would increase to 5.35 keV. It can be seen that especially the bottom PMTs are essential for high detection efficiency at low recoil energies.

4.4 ER-NR discrimination

4.4.1 ER and NR bands

As discussed in more detail in section 2.2.5, ERs and NRs form two distinct bands in the $\log_{10}$(S2/S1) vs S1 parameter space, allowing ER-NR discrimination by only

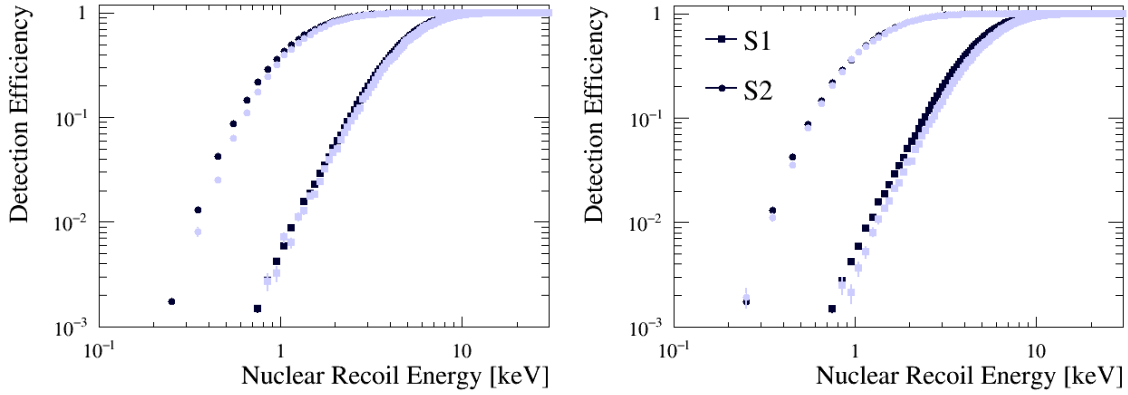

(a) (b)

Figure 4.7: Effect of inactive PMTs on NR detection efficiencies for S1 and S2 signals. Events are required to have at least 3 detected S1 photons, $S1_c < 80$ and $S2_c > 420$. Black shows all PMTs working, light blue show the recoil detection efficiencies for 40 inactive PMTs on (a) top and (b) bottom.

Passive PMTs		**NR Detection Efficiency [%]**		
top	**bottom**	**1 keV**	**5 keV**	**10 keV**
0	0	0.12 ± 0.01	55.05 ± 0.29	96.612 ± 0.44
5	0	0.11 ± 0.03	55.01 ± 0.92	96.68 ± 1.38
10	0	0.11 ± 0.03	54.08 ± 0.91	96.56 ± 1.38
20	0	0.08 ± 0.03	54.44 ± 0.92	95.92 ± 1.37
40	0	0.09 ± 0.03	53.44 ± 0.91	95.46 ± 1.37
0	5	0.1 ± 0.03	54.1 ± 0.91	96.34 ± 1.38
0	10	0.12 ± 0.03	54.18 ± 0.91	96.12 ± 1.38
0	20	0.1 ± 0.03	50.67 ± 0.87	95.31 ± 1.36
0	40	0.03 ± 0.02	47.72 ± 0.84	93.75 ± 1.35
5	5	0.09 ± 0.03	54.53 ± 0.92	95.98 ± 1.37
10	10	0.11 ± 0.03	53.73 ± 0.91	95.64 ± 1.37
20	20	0.05 ± 0.02	49.70 ± 0.86	94.64 ± 1.36
40	40	0.04 ± 0.02	43.87 ± 0.79	93.28 ± 1.34

Table 4.2: Reduction in NR detection efficiency showing the mean and standard deviation over 10,000 data points.

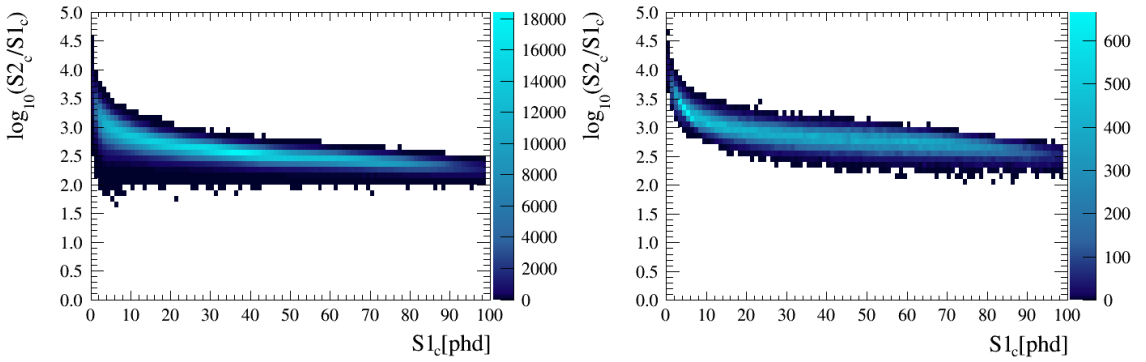

(a) (b)

Figure 4.8: (a) NR and (b) ER band from simulation.

accepting events below the NR median line. The LZ sensitivity projections assume a 99.5% ER-NR discrimination at 50% NR acceptance. To assess how PMT loss affects the discrimination and leakage, flat spectra of ER and NR events distributed evenly in the detector volume were simulated. 4×10^7 single scatter NR events were simulated in the fiducial volume to calculate the NR band. In the first 1000 days of data taking about 1195 ER events are expected in the 5.6 t fiducial volume. For this study, 8×10^4 single scatter ER events were simulated in the fiducial volume of which 6×10^4 fall in the region of interest for a 40 GeV WIMP. Both distributions are displayed in Fig.4.8. The bands are determined by fitting a Gaussian to the $\log_{10}$(S2/S1) distribution in each $S1_c$ bin. The assumption of the bands being Gaussian is valid for the NR band and a good approximation for the ER band. As the ER band is only used to quantify any changes in the location and spread of the bands, but not used to evaluate the leakage, the Gaussian approximation was found to be sufficient. The study was repeated for two different electric field scenarios. The results presented here are for a projected drift field of 310 V/cm. The study was repeated with a more optimistic scenario with 640 V/cm. While absolute leakage values vary, the relative impact of PMT loss on leakage is the same for both scenarios.

The leakage fraction is defined as the number of ER events below the NR mean

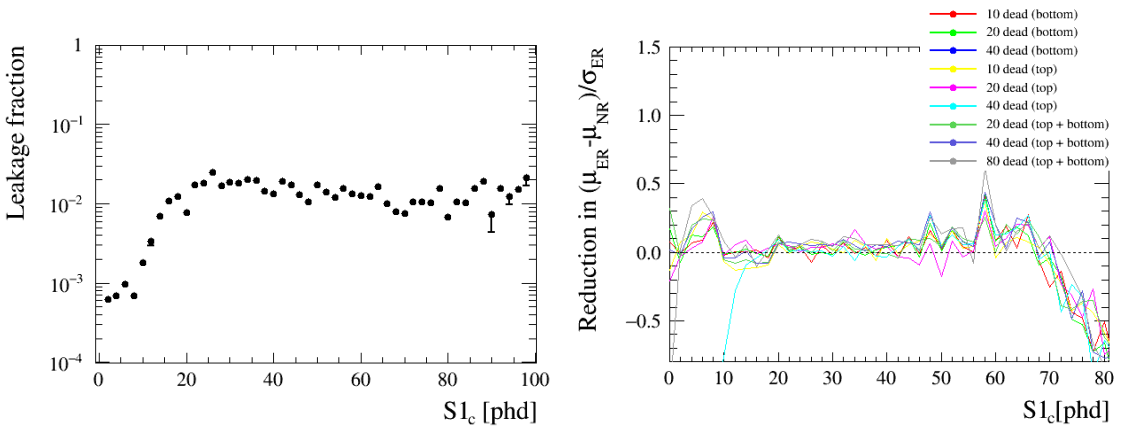

(a) (b)

Figure 4.9: (a) ER leakage original without any PMT loss. (b) Reduction in ER and NR band separation for different scenarios of inactive PMTs.

n_{ER}^{leaked} divided by the total number of ER events n_{ER}^{total}. The error on the leakage is twofold, the uncertainty of the mean and counting errors. The error in leakage due to uncertainty in the mean is estimated by finding how many more or fewer events would have leaked if the NR mean shifted by its standard deviation. The counting error is defined as

$$\frac{n_{ER}^{leaked} + \sqrt{n_{ER}^{leaked}}}{n_{ER}^{total} + \sqrt{n_{ER}^{total}}}. \tag{4.1}$$

The ER leakage for the scenario with all PMTs working is shown in Fig. 4.9. The overall discrimination within the region of interest for a 40 GeV WIMP (S1 $<$ 50 phd) for this simulation data is 98.8% (99.3% for the more optimistic electric field scenario) which is lower than the LZ target discrimination. Improvements in event reconstruction algorithms are needed to achieve the target discrimination. This study focuses on the relative change between the different scenarios to see which PMTs have the biggest impact on the leakage. As seen in section 4.3, the higher the number of lost PMTs, the smaller the light collection efficiency. To compare the same events to each other, the S1 and S2 areas are corrected for the average change in g_1 and $g_{1,gas}$.

4.4.2 Change in ER and NR band

With fewer PMTs working, both ER and NR means shift upwards. The shift is most pronounced for events with S1s smaller than 10 phd. A change in S1 light collection efficiency has the most significant impact on low energy events. Both ER and NR bands widen with PMT loss. The reason for this is two-fold. The variance in the average number of detected photons and electrons as described by Equ. 3.30 and Equ. 3.33 increases with decreasing light collection efficiency. Additionally, the light collection efficiency becomes less uniform and more position-dependent.

Fig. 4.9b shows the reduction in band separation of the ER and NR bands for different scenarios. It can be seen that the band separation reduces overall. The reduction is most significant for events with S1s smaller than 10 phd and larger than 40 phd. For S1s larger than 70 phd the bands move further apart again. It can, therefore, be concluded that with a loss in light collection efficiency, the bands are less well separated and become wider, i.e. less well defined.

4.4.3 Change in leakage

From the change in the band separation and width, it can be expected that the leakage increases with increasing PMT failure. The leakage for different scenarios is shown in Fig. 4.10 and Fig. 4.11. The overall leakage for the different scenarios is summarised in Table 4.3.

Comparing the different curves, it can be seen that there is an increase in leakage with PMT loss. However, this increase depends on the size of the event. For events with very small S1 pulses ($<$ 10 phd), the leakage first increases significantly with passive PMTs, but simultaneously the efficiency of detecting such events drops. The leakage in this region is especially affected if many PMTs in the bottom array are passive. Losing bottom array PMTs, reduces g_1 and thus increases the variance in the number of detected photons. Such an increase in variance is most significant for

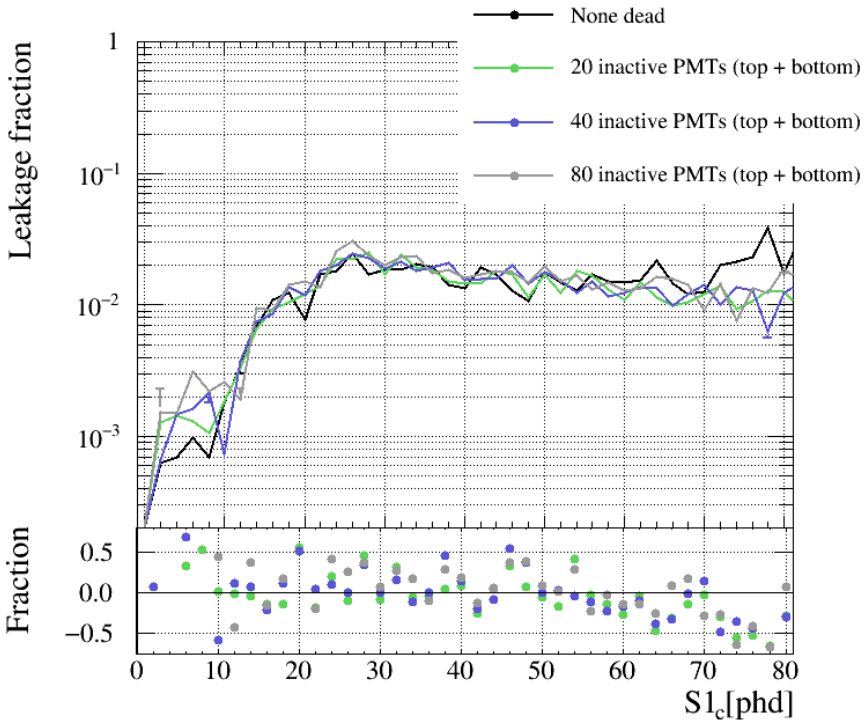

Figure 4.10: ER leakage for scenarios with equal amounts of inactive PMTs on top and bottom arrays.

small S1s. For S1 values between 10 and 70 phd the leakage fraction fluctuates but increases overall. From Table 4.3 it can be seen, that losing top array PMTs leads to a more significant increase in overall leakage than losing bottom array PMTs.

To investigate this further, four additional scenarios were considered with 40 PMTs inactive on top (bottom). In one scenario, all passive PMTs are located on the three outermost PMT rows. In the second scenario, they are all located in the middle of the array. In Section 4.3 it is shown that the location of inactive top PMTs has a more significant impact on light collection efficiency than the location of inactive bottom PMTs. A similar result is seen here. For the bottom array, it makes very little difference, which exact PMT is inactive. The leakage fraction for 40 passive bottom outer and 40 passive top inner PMTs are almost identical, and when comparing the r-z location of the leaked events in both scenarios, these coincide. The location of passive PMTs on the top array does matter. Losing PMTs on the top array can increase the variation of S2 light collection efficiency with position considerably. S2s from interactions at larger radii in the detector are typically seen by a smaller number of PMTs than interactions in the centre of the detector. Losing several PMTs in the outer rows of the top array can lead to a considerable reduction in S2 size for such events, while the more dispersed S1 signal stays almost unchanged. Therefore, the S2/S1 ratio reduces and ER events at larger radii are more likely to leak into the NR region.

Overall, it can be seen that losing a significant number of PMTs increases the probability for an ER event to leak below the NR mean. The increase in leakage depends on the location of the PMTs. In general, it can be approximated that 20 (40) passive PMTs roughly lead to a 5% (10%) increase in leakage. This increase in leakage is mostly due to a less uniform light collection efficiency. Notably, losing top outer row PMTs has the biggest impact on the ER leakage.

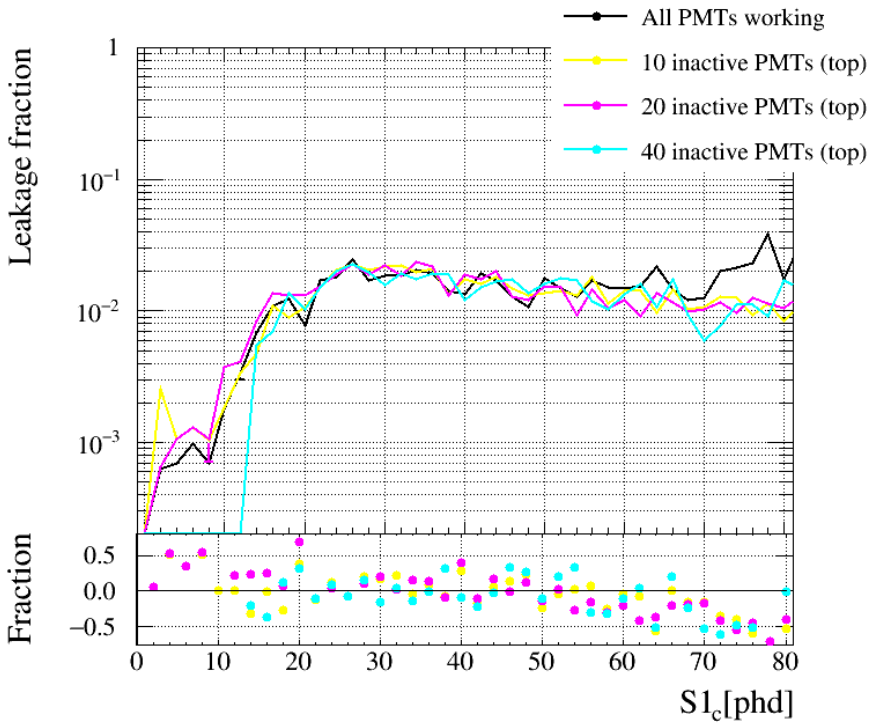

(a)

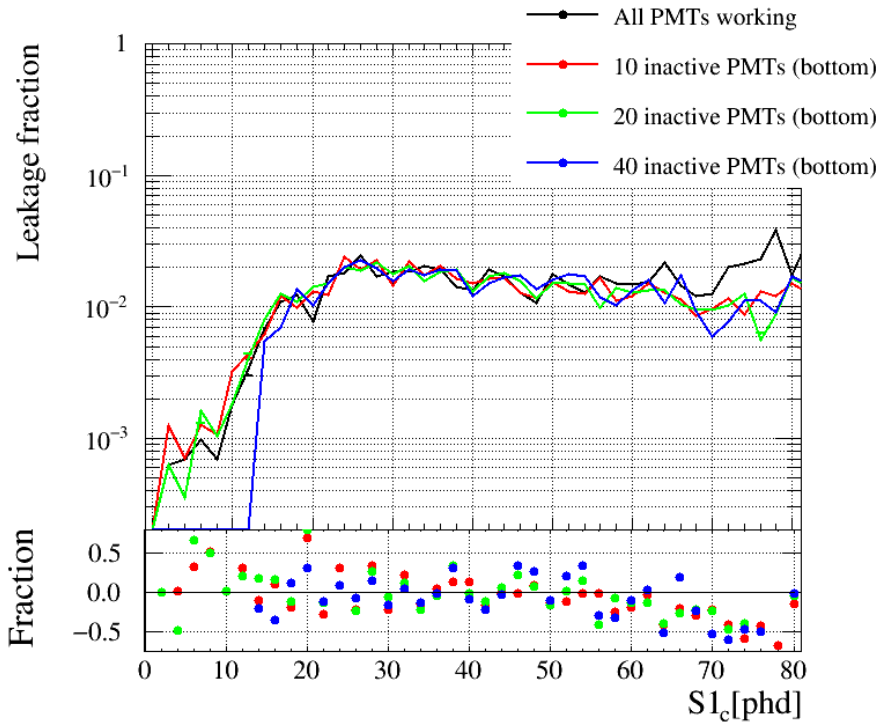

(b)

Figure 4.11: ER leakage fraction vs $S1_c$ for scenarios where all inactive PMTs are located on the (a) top or (b) bottom array.

Passive PMTs		ER Single Scatters	Leaked Events	Leakage Fraction
Top	Bottom	[counts]	[counts]	[%]
0	0	62825	747	1.19
0	10	62920	766	1.22
0	20	62945	778	1.24
0	40	55488	725	1.31
10	0	62604	773	1.23
20	0	61619	802	1.30
40	0	55955	821	1.47
10	10	62676	783	1.25
20	20	61920	822	1.33
40	40	60946	874	1.43

Table 4.3: ER leakage in the region of interest for a 40 GeV WIMP ($S1 < 50$phd) for different PMT loss scenarios.

4.5 Position reconstruction

4.5.1 Wall events

As discussed in Section 2.5.2 charged radon-progeny which has plated out onto detector surfaces during construction are a potentially dangerous background in LZ. The PTFE walls of the TPC are especially problematic, as α decays from ^{210}Po can produce neutrons via (α, n) reactions. Position reconstruction of events close to the TPC inner walls is challenging, and therefore, it is expected that some of the events leak radially towards the fiducial volume of the detector. To reach LZ background requirements, it is necessary to even reduce the faintest events from these backgrounds by a factor 1×10^{-6} at 40 mm distance from the wall. The top PMT array layout was optimised to allow excellent position reconstruction for events at the edges of the TPC [75].

For this study, S2 light just above the LZ acceptance threshold is simulated. Five electrons were placed just below the liquid surface 1 mm from the wall of the detector. Fig. 4.13 illustrates the position of the electrons relative to the top array PMTs. For the expected fields in LZ, these 5 electrons produce around 4000 electroluminescence

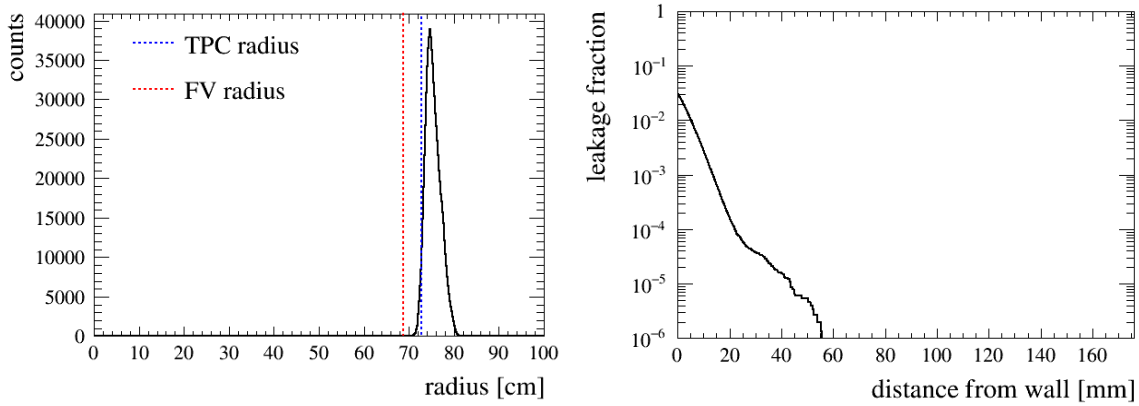

(a) (b)

Figure 4.12: Wall event reconstruction for all PMTs working showing (a) the reconstructed radius, where the blue line indicates the location of the TPC wall, and (b) the leakage fraction as a a function of distance from the TPC wall.

photons, resulting in S2 pulses of the order 200 - 300 photons detected (phd). In total, 10^7 events were simulated. Fig. 4.12 shows the reconstructed radius and leakage fraction as a function of radius for all PMTs working. A reduction of 1×10^{-6} is only achieved at 60 mm from the wall. As discussed in the previous chapter, variations in the PMT signal are significant enough for low energy signals to lead to reconstruction further away from the wall. Better analysis techniques are being developed to account for these statistical fluctuations. From Fig. 4.12a, it can be seen that more than 50% of events are reconstructed outside the fiducial volume. The LRFs used by Mercury were constructed using events further inside the fiducial volume. There is, therefore, a bias for events seen by only the outermost PMTs to be reconstructed outside, while this bias disappears when looking at events inside the fiducial volume. This bias is not problematic for this study. A second scenario of 10 electrons was simulated. These S2 pulses have an area of $500 - 600$ phd, and PMT variation statistics have less impact than for the smaller 5 electron pulses. For this scenario, no events leak further than 20 mm from the wall.

As the PMT array is symmetric, the leakage can be assessed for just one point

at the wall. Different configurations of the top array PMTs marked with black in Fig. 4.13 were tested. The bottom array plays no role in x-y-position reconstruction and is therefore not considered here.

The leakage fraction for the different scenarios for the 5 electron case is summarised in Table 4.4. Fig. 4.14 shows the leakage fraction as a function of distance from the wall for both 5 and 10 electron cases and all different scenarios. A subset of the 5 electron scenarios are also shown as x-y displays in Fig. 4.15. For the 5 electron case, the wall leakage fraction increases in all scenarios apart from (ii). Here one of the second row PMTs is inactive, which pushes the reconstructed radius further outside the fiducial volume and reduces the leakage slightly (see Fig. 4.15b). For the larger, 10 electron signal, this scenario has an increase in leakage but shows a small decrease in leakage for 2 second-row PMTs (iv). The effect of PMT loss does vary with signal size. Comparing Fig. 4.14a and Fig. 4.14b, it can be seen that the overall trends are consistent for both signal sizes.

Figure 4.13: Zoom of one area on the top PMT array. The PMTs marked in black are the ones switched off for this study.

The different scenarios can roughly be split into three categories of varying problematic. One or several inactive PMTs in the second row (scenarios ii-vi), even when combined with a third row PMT are least problematic, including the scenario where three adjacent PMTs in one row are inactive (scenario v). Having one passive PMT in the outermost row, but not directly next to the event also falls into this category (scenario ix). For these scenarios, the fiducial volume would need to move 5 mm further inside for the 5 electron case. For the 10 electron case, these scenarios still fulfil the 1×10^{-6} reduction at 40 mm from the wall.

One inactive first-row PMT in the immediate surrounding area of the event is always problematic (scenarios vii-xii, excluding ix). The closer the PMT is located

Passive PMTs (rows)			Leakage fraction		
first	**second**	**third**	**40 mm**	**80 mm**	
-	-	-	1.94×10^{-5}	0	i/a
-	196	-	1.38×10^{-5}	0	ii/b
-	196, 159	-	5.86×10^{-5}	0	iii/c
215	-	-	1.16×10^{-5}	0	ix/e
-	160, 159	-	1.05×10^{-4}	0	iv
216	196	-	1.09×10^{-4}	3.49×10^{-7}	x/h
-	159, 160, 196	-	1.46×10^{-4}	0	v/d
217	160, 196	-	7.75×10^{-4}	1.75×10^{-7}	xi
-	196, 159	123	1.10×10^{-4}	0	vi
217	-	-	1.97×10^{-3}	1.57×10^{-5}	vii/f
216	-	-	1.94×10^{-3}	6.98×10^{-7}	viii
217	-	124	2.1×10^{-3}	2.79×10^{-6}	xii/g
216, 217	196	-	7.26×10^{-2}	3.27×10^{-3}	xv, k
216, 217	196, 159	-	6.2×10^{-2}	4.08×10^{-3}	xvi/l
216, 217	-	-	0.23	8.06×10^{-3}	xiii/i
215, 216, 217	-	-	0.27	0.015	xiv/j

Table 4.4: Leakage fraction and number of events leaked inside the fiducial volume for the different scenarios using the 5 electron signal. The scenarios are sorted from least to most problematic. Roman numerals are used as reference to Fig. 4.14 and the letters refer to xy-plots displayed in Fig. 4.15.

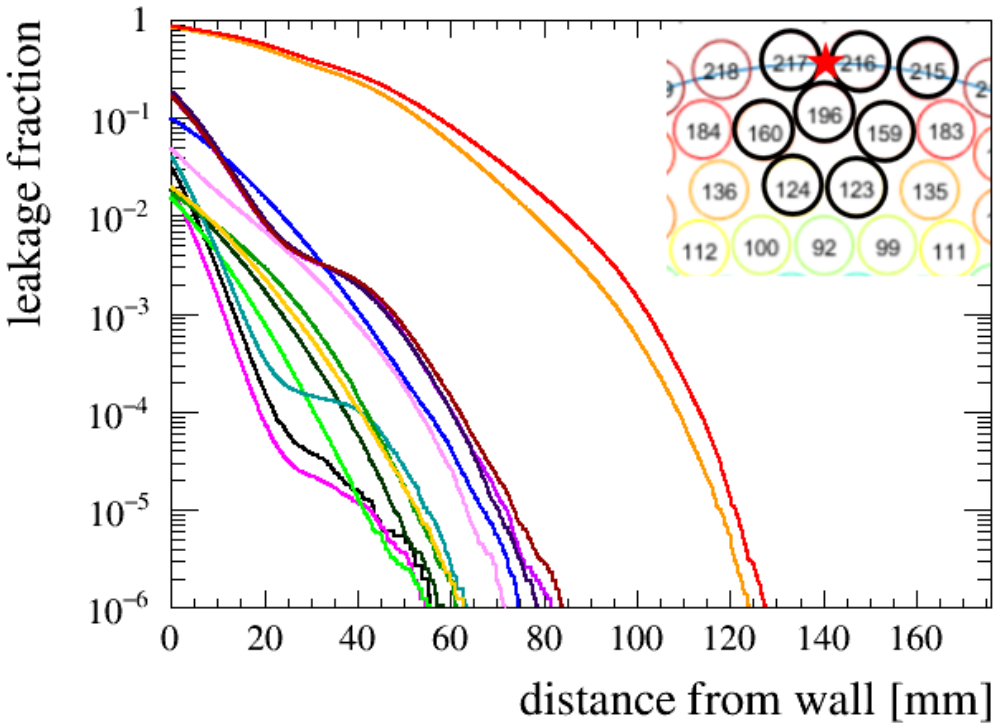

(a) S2 size of 5 electrons

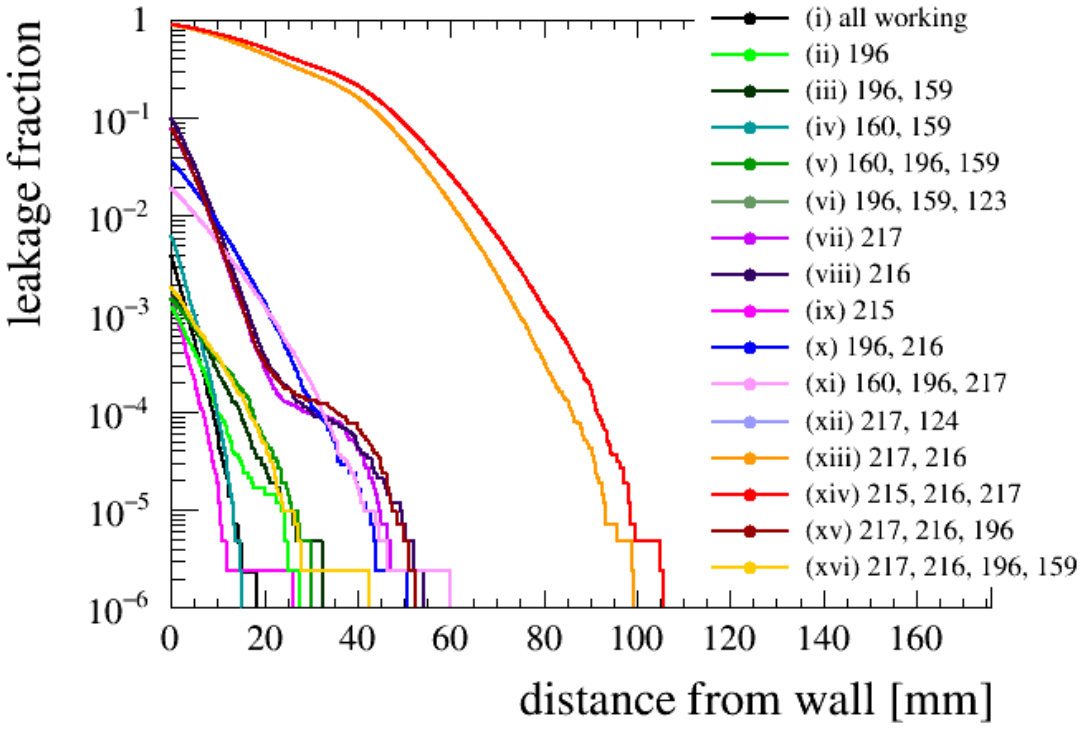

(b) S2 size of 10 electrons

Figure 4.14: Leakage fraction as function of distance to the wall for different scenarios.

to the event, the more significant the impact. If an adjacent second row PMT is also not working, it gets more problematic. For these scenarios, both signal sizes would require a decrease in fiducial volume by 15-25 mm ($20 - 25\,\text{mm}$) radius for 5 (10) electrons signal sizes.

In cases where there is more than one adjacent inactive PMT in the outer row, the leakage increases drastically, with more than 10% of the events leaking beyond 40 mm from the wall. The radial fiducial cut would need to be increased to $100 - 110$ mm distance from the wall to reach a reduction of 1×10^{-6}. If instead whole patches of PMTs surrounding the truth position are inactive (scenarios xv and xvi), the position reconstruction fails for many events. The leakage is less than in scenarios where only the outer most row is affected, as there are fewer events reconstructed than without PMT loss.

Overall, these results show that the loss of PMTs in the first-row has the most impact on wall event position reconstruction. Any failure of such PMTs makes a redefinition of the fiducial radial cut necessary. If two or more adjacent first-row PMT fail, increase of the radial cut up to 110 mm from the wall might be necessary. Inactive second-row PMTs only lead to a substantial increase in leakage if combined with a passive first-row PMT. It is crucial to keep in mind that the leakage increase due to passive PMTs would be localised to the immediate surrounding area of the inactive PMTs. A more complicated fiducial volume could be defined, increasing the radial cut only in those areas to keep the fiducial volume as large as possible.

4.5.2 Multiple scatters

Position reconstruction is an essential tool for the identification of multiple scattering. A WIMP is expected to only scatter once in the detector. All multiple scatters are, therefore, background events. A large fraction of multiple scattering can be identified by the fact that they have distinct S2 pulses. However, if the scatters happen at the

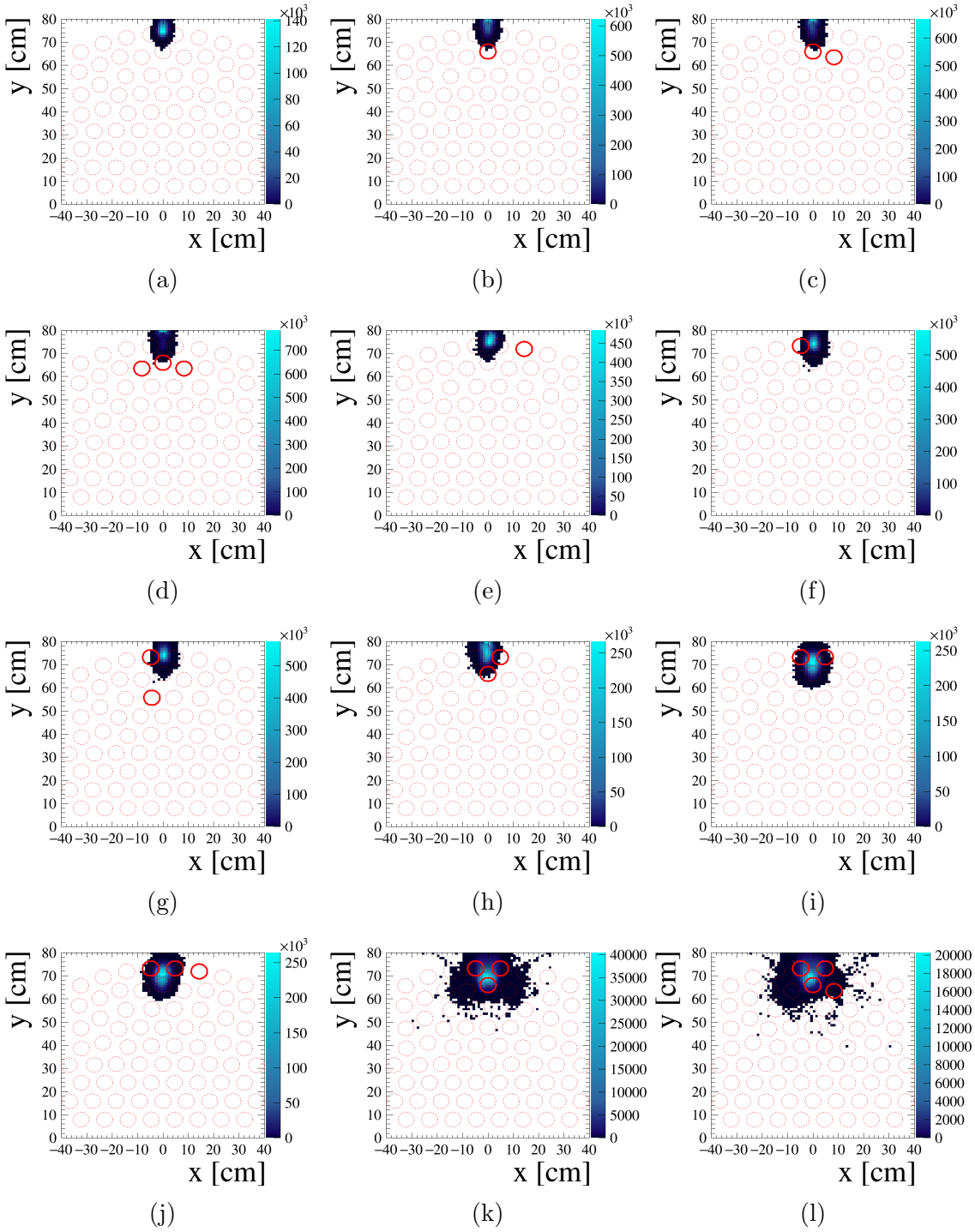

Figure 4.15: Reconstructed position in x-y plane for different PMT loss scenarios for the 5 electron signals. The passive PMTs are indicated by the thick solid red lines.

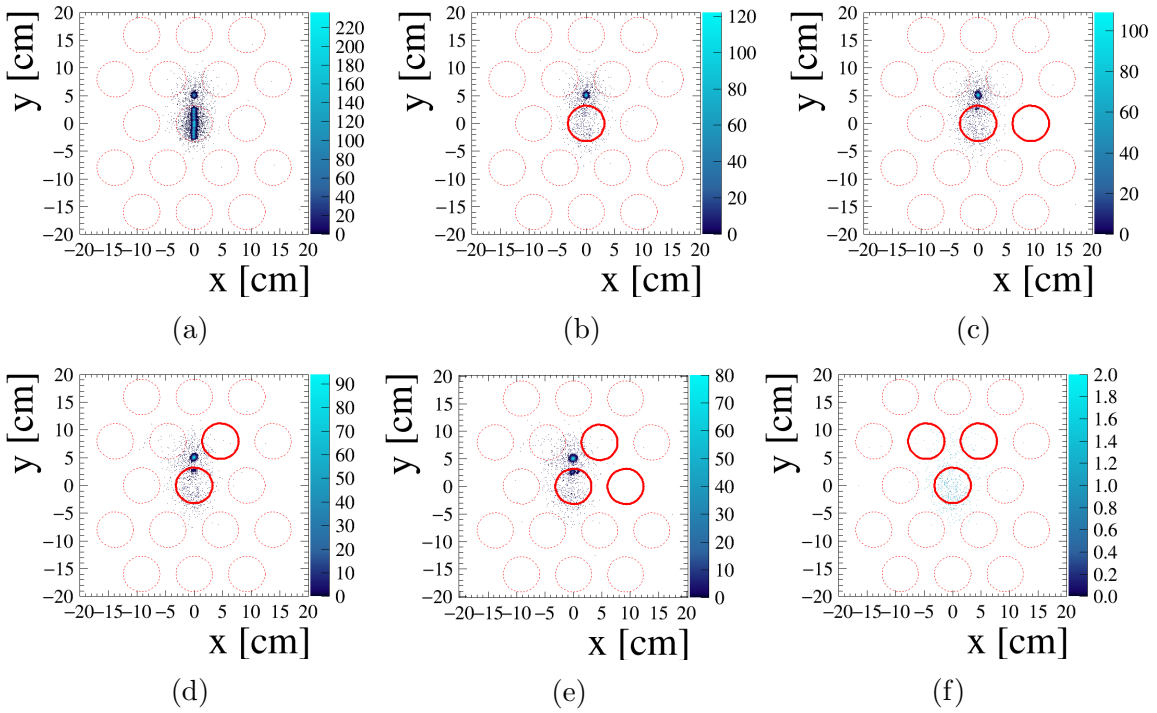

Figure 4.16: Reconstructed position for 5 keV electron recoils for different scenarios of inactive PMTs. The passive PMTs are indicated by the thick solid red lines.

same height in the detector, the two S2 pulses overlap and cannot be distinguished anymore. To veto such events, excellent spatial resolution in the entire detector volume is essential. In LUX the spatial resolution for small S2s in the radial direction was 3 cm and in the z-direction was 0.2 cm [86]. For large S2s, the minimum vertex separation needed to identify multiple scattering is 3 mm.

A qualitative assessment of how PMT failure impacts position reconstruction inside the fiducial volume has been conducted using 5 keV electron recoils, simulated at ten distinct points in the detector. Nine points are directly located under the central PMT (PMT 0). Those events are separated by 2.5 to 5 mm. All other events are 5 cm from the centre. As for the previous study, different scenarios of inactive PMTs were considered. Fig. 4.16 shows the reconstructed positions in x-y for the different scenarios, indicating the passive PMTs.

In scenario (a) all PMTs are working. All different event positions can be seen as

distinct hot-spots on the 2D-histogram, but the variation in position reconstruction means that they blend into each other. The only vertex distinct is the one 5 cm from the centre. The mean reconstructed position for these events is within 0.4 mm of the truth radial position, and the RMS is 4 mm in x and 4.5 mm in the y-direction.

In scenario (b) PMT 0 is passive. For scenarios (c) to (e), PMT 0 plus an additional one or two adjacent PMTs are passive. When PMT 0 is passive, the position reconstruction fails for most of the events taking place directly underneath that PMT. For events directly below a PMT, it is expected that most light is concentrated in that PMT and equal amounts of light are distributed in the surrounding PMTs. So if the central PMT fails, there is no significant hit pattern allowing position reconstruction. Some of them can again be reconstructed once more PMTs on the other side are failing too, which is due to the relative number of PMT hits. Looking at the events 5 cm from the centre of PMT 0, it can be seen that the position can still be well reconstructed. Depending on which specific PMTs are switched off and their location relative to the events, the mean of the reconstructed position shifts by ± 0.5 mm. The distribution of reconstructed position gets only slightly wider with an RMS of 6 mm in x and 5.1 mm in the y-direction.

Scenario (f) has all three PMTs surrounding the position of the event 5 cm from the centre switched off. All PMTs which are expected to see a significant fraction of light are now inactive. Therefore, the position reconstruction for the majority of events starts to fail.

The above indicates that the effect of PMT loss on position reconstruction in the centre of the fiducial volume depends on the position of the vertex relative to the PMTs. For events taking place directly underneath a PMT, this PMT is essential for position reconstruction. For events where the majority of the light is concentrated in more than one PMT switching off one or two, does not affect the reconstruction much. Only if all of them fail, position reconstruction does not work anymore.

4.6 Background topologies

4.6.1 Overview

There are certain background topologies which are identified by specific hit patterns. Losing PMTs can reduce the efficiency of analysis cuts identifying such events. For both gamma-X and Cerenkov events, it is the concentration of light in one PMT or a small cluster of PMTs which allows them to be identified. Should exactly this be one of the PMTs not used in the analysis, there is a danger that the event might wrongly be identified as a normal single scattering event.

4.6.2 Gamma-X events

Gamma-X events are double scatters, where one scatter happens in the main xenon target, and another scatter happens in the reverse field region (RFR) as illustrated in Fig. 4.18. A recoil event in the RFR causes scintillation light and ionisation; however, the ionisation electrons are not extracted. The detected signal has a large combined S1 from both scatters and a single S2 from the first scatter. As not much time delay is expected between the two S1s, the interaction is not identified as multiple scattering. The additional S1 light leads to a reduction in S2/S1 ratio. Gamma-X events are therefore more likely to leak into the NR signal region than single scatter electron recoils. If not identified and vetoed, gamma-X events can lead to problematic events in the WIMP signal region. They can typically be identified by looking at

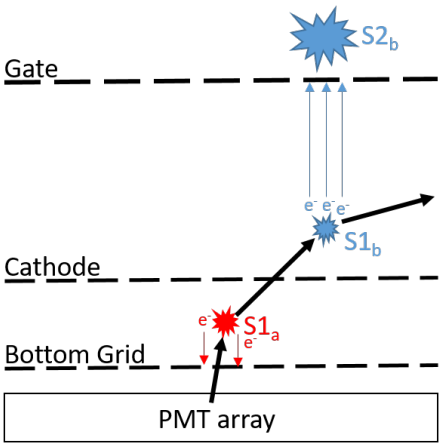

Figure 4.18: Schematic of a gamma-X event (not to scale). One of the vertices of the multiple scatter lies in the reverse field region. This vertex only produces scintillation light as the electrons are extracted towards the bottom grid.

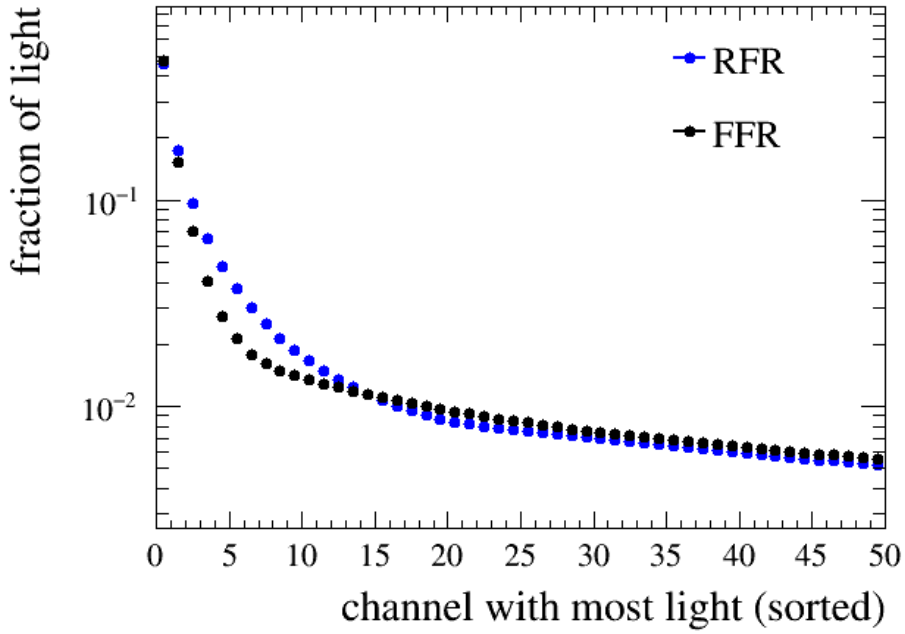

(a)

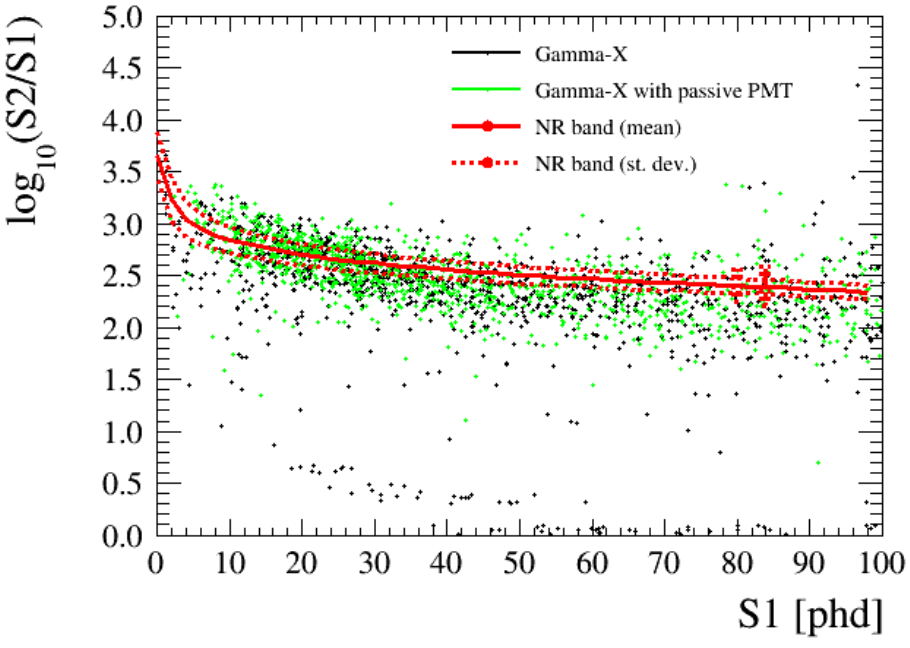

(b)

Figure 4.17: MDC-2 gamma-X events (a) Looking at the fraction of light seen by the channel with most light for the S1 in the reverse field region (RFR) and the forward field region (FFR). (b) Gamma-X events in log(S2/S1) space with and without inactive PMT.

the hit pattern in the bottom PMT array. Compared to S1s from the forward field region, the S1 light is more clustered in a few PMTs, as the light emission happens much closer to the PMT array.

Looking at one month of MDC-2 data, 70,000 gamma-X events are identified using Monte Carlo Truth information. These events are displayed in black in Fig. 4.17b. The channel light fraction sorted by the amount of light seen per channel for both the reverse field region and forward field region S1 is shown in Fig. 4.17a. It can be seen that the light from the reverse field region is more clustered in a few PMTs. This clustering distinguishes gamma-X events from regular scatters in the detector. As it is a whole cluster of PMTs, one of the PMTs failing still allows the identification of the gamma-X event, as long as the location of the passive PMT is taken into account. Losing one of the PMTs seeing a larger fraction of light, changes the S2/S1 ratio. Some gamma-X events become less problematic as they move above the NR band. Others which had very low S2/S1 ratios previously, now look more likely to be NR events. This is illustrated in Fig. 4.17b, where the green interactions have the PMT with the largest S1 channel pulse area switched off. Overall, it is to be expected that PMT loss might make the identification of gamma-X events more challenging, but - unless whole clusters of PMTs die - not impossible. Any gamma-X veto cut should be tested on how it handles passive PMTs in detail, to avoid any potential problems.

4.6.3 Cerenkov from PMT windows

Cerenkov light is emitted, if a charged particle passes through a dielectric medium at a speed greater than the phase velocity of light in that medium [131]. In LZ, it is expected that Cerenkov light can be caused by relativistic beta particles in the PMT window glass or the PTFE of the field cage. It has been shown that ^{60}Co and ^{40}K contaminants in PMT windows are the dominant source of detected Cerenkov light in the detector. Some of these events have a similar topology to S1 signals [132]. From

radioassay measurements the average activity in the PMTs are 15.41 mBq/kg for ^{40}K and 2.91 mBq/kg for ^{60}Co [86]. Each PMT weighs about 0.19 kg, which leads to an expected Cerenkov rate of 1.7 Hz from all PMTs in the TPC region.

For low-energy electron recoil background events, it is often only the S2-pulse which is detected. If a Cerenkov event happens just before such an S2-only event, the two pulses can mistakenly be paired together. The S1-S2 ratio for such events is larger than that for a typical electron recoil, and the Cerenkov-S2-only coincident event is likely to leak into the NR region. The conservative expectation for S2-only events in LZ is 1 mBq based on rates observed in LUX [86]. It can, therefore, be seen that Cerenkov coincidence with S2-only is a potentially dangerous background. Previous studies [132, 133] have developed cuts to reduce the number of such events. 150, 750 ^{40}K and 150, 750 ^{60}Co events are simulated in the PMT windows. For comparison of pulse parameters, 150,750 ER and NR events in the WIMP region of interest are simulated additionally. This is the same set of data as used in [133].

79% of simulated ^{40}K and 30% of simulated ^{60}Co events induce a signal in the detector. Cerenkov light from PMT windows has a distinctive hit and arrival time pattern distribution which can be used to identify and cut these events. Averaging over all events, almost 60% of the light is concentrated in the PMT seeing most light, i.e. the PMT, from whose window the radiation originated. Many Cerenkov events, therefore, do not pass the 3-fold coincidence requirement for S1 pulses. For the remaining events, a fraction of light escapes and is detected by other PMTs following some reflections. The reflections are also responsible for the S1-like pulse width. Taking these percentages and applying them to the expected activity from contaminants in the PMTs, the expected rate of S1-like Cerenkov pulses is 1.21 Hz. Fig.4.19a shows Cerenkov events classified as S1 pulses compared to S1s from nuclear recoils. It can be seen that some Cerenkov pulses are shorter than normal S1s, but the best way of distinguishing the pulses is the maximum fraction of light detected

by a single PMT. A graphical cut was developed in [133] with 96% efficiency for ^{40}K events. For the work presented here, the cut was improved to 98% efficiency for ^{40}K and 90% efficiency for ^{60}Co, while keeping the signal acceptance at 98%. The cut is displayed in Fig.4.19a. The rate of remaining Cerenkov events per PMT is 23 µHz. If such a pulse coincides with an S2-only event, the fake S1-S2 pair falls within the signal-acceptance region, as shown in Fig.4.19b. The S2-only rate is predicted to be 1 mBq based on the experience with LUX [86]. The coincidence rate of Cerenkov events within a maximum drift time of 1000 µs is 11.4 nHz.

To assess the effect of inactive PMTs on the rate of Cerenkov events, the data was reanalysed ignoring the pulse recorded on the PMT in which the Cerenkov event originates, i.e. the PMT seeing the largest pulse fraction. Losing this PMT affects the maximum fraction of light parameter heavily, while it can be assumed that the pulse width is unchanged. The photons detected in other PMTs dominate the pulse width. The resulting distribution in the cut-parameter space can be seen in Fig. 4.20a. With PMT loss, 6.3% ^{40}K and 1% of ^{60}Co initiated Cerenkov events survive the cut. Fig. 4.20b shows the surviving Cerenkov pulses randomly paired with S2-only events. Compared to Fig. 4.19b now also larger area Cerenkov pulses survive. The rate of Cerenkov events per inactive PMT surviving all S1 and Cerenkov cuts is now 0.18 mHz, which is a factor of 7.8 times larger than the Cerenkov rate for a working PMT.

It can be seen that the passive PMTs reduce the efficiency of identifying Cerenkov events in the data drastically. For an S2-only rate of 1 mHz and 20 dead PMTs, the accidental coincidence rate is 14.5 nHz, corresponding to 0.12 events in 1000 days of data taking. Table 4.5 summarises the increase in the rate of accidental coincidence of Cerenkov and S2-only events and the number of counts in 1000 days of data taking. Compared to the expected 6.49 background events in the signal acceptance region for a 40 GeV WIMP, this is a subdominant background. However, it can potentially

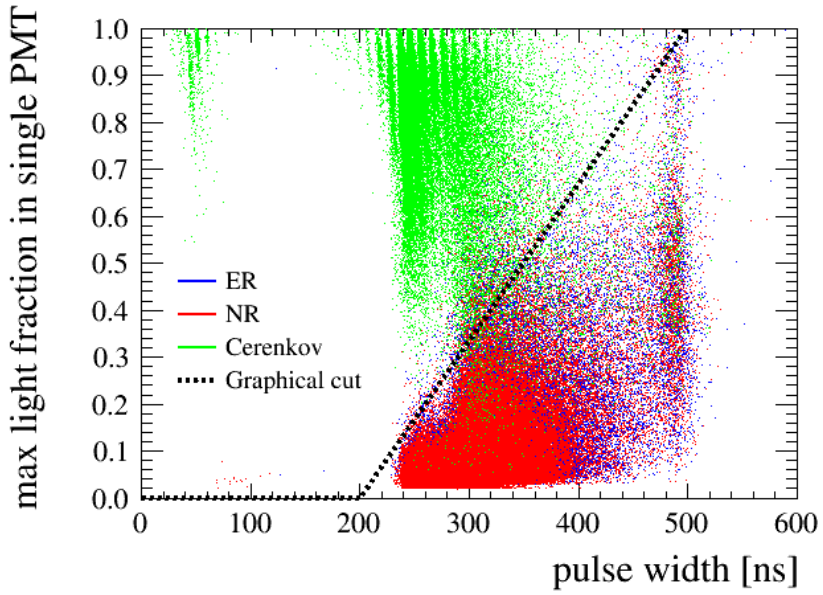

(a)

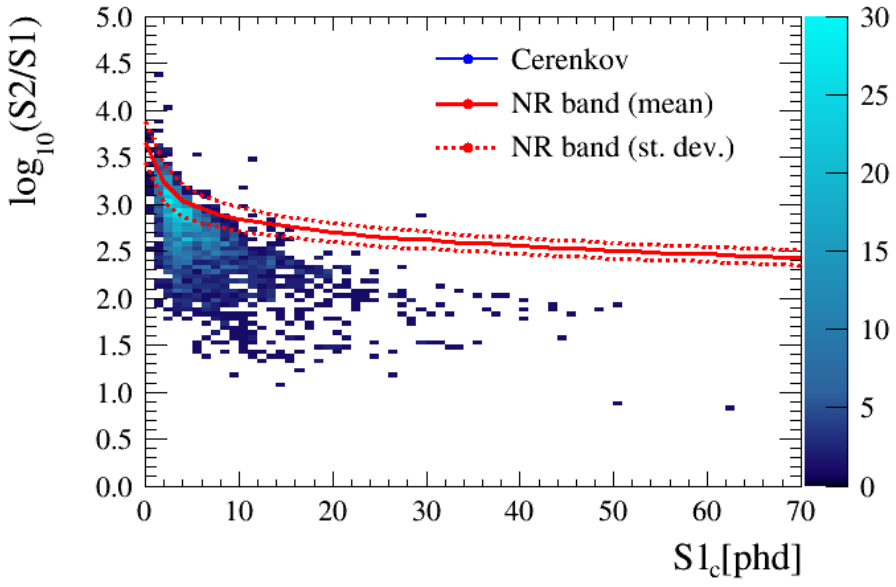

(b)

Figure 4.19: Pulse width and maximum fraction of light in single PMT for Cerenkov, ER and NR events from simulation data. (b) The Cerenkov pulses surviving the cut are randomly matched with S2 pulses and displayed in the $log_{10}(S2/S1)$ parameter space.

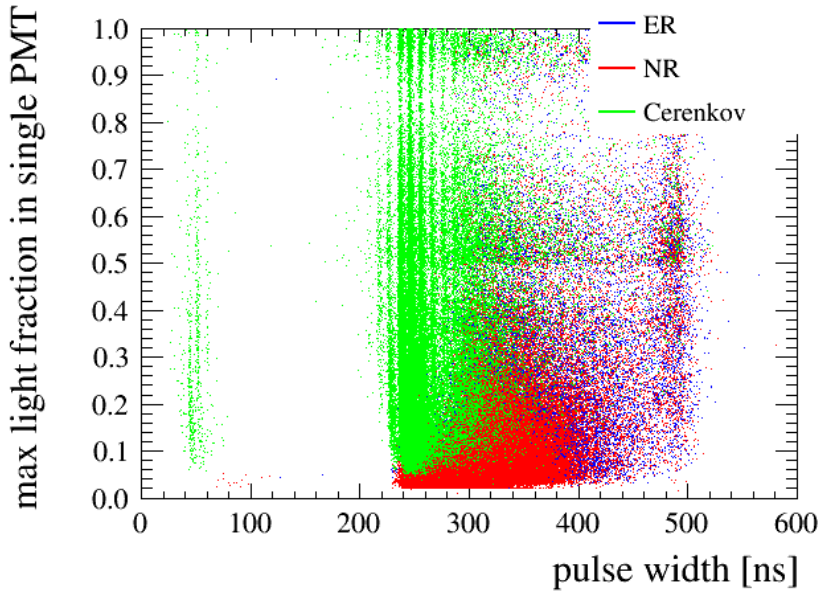

(a)

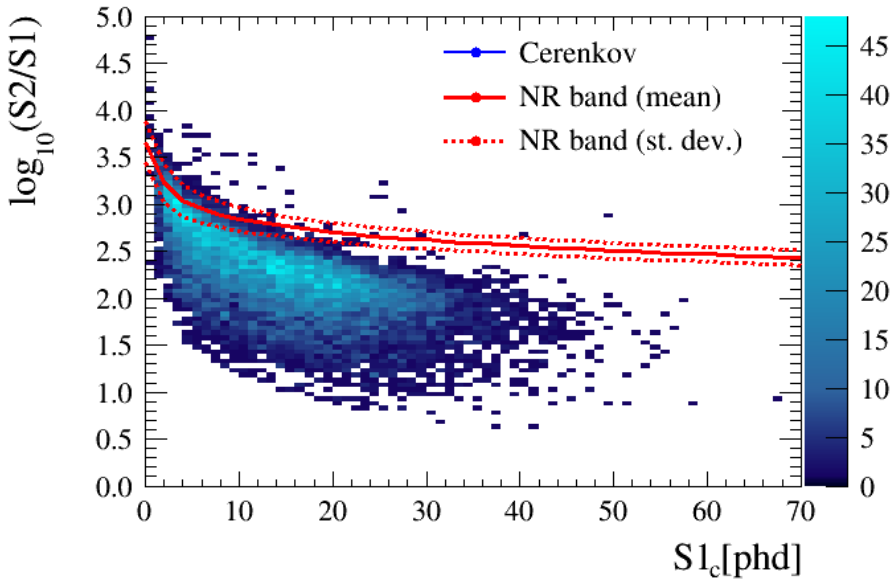

(b)

Figure 4.20: Pulse width and maximum fraction of light in single PMT for Cerenkov, ER and NR events from simulation data with inactive PMT. (b) The Cerenkov pulses surviving the cut are randomly matched with S2 pulses and displayed in the $log_{10}(S2/S1)$ parameter space.

passive PMTs	Cerenkov coincidence rate [nHz]	events in 1000 days [cnts]
0	11.4	0.10
10	12.9	0.11
20	14.5	0.12
40	17.6	0.15
80	13.9	0.21

Table 4.5: Rate of accidental coincidences of Cerenkov and S2-only events.

become dangerous if the S2-only rate is higher than expected, for example, due to possible electron emissions from the grids. From this study, it can be concluded that it would be advantageous to collect data with PMTs having low gain, high afterpulsing rates or noisy baselines and only exclude them during data analysis. That way, they could still be used as a potential veto for Cerenkov events.

4.7 Impact on LZ sensitivity

4.7.1 Overview

The effects of PMT loss on LZ performance can be split into three categories: light collection efficiency, fiducial volume, background discrimination. In this section, the sensitivity impact of such changes is discussed. The change in sensitivity due to changes in light collection efficiency and fiducial volume are assessed using the LZ PLR framework discussed in Section 2.6.4. Regarding the change in backgrounds, only the change in ER-NR leakage is considered as it has a more severe impact than the background topologies discussed in Section 4.6. The PLR framework uses NEST to model signal and background distributions. NEST cannot account for localised changes in light collection efficiency due to passive PMTs. Therefore, a cut-and-count method is used to assess the impact of a change in the ER-NR leakage.

PMTs	Signal acceptance			Limit 90% CL [cm^2]		
passive	6 GeV	9 GeV	40 GeV	6 GeV	9 GeV	40 GeV
0	0.25%	3.30%	61%	1.09×10^{-45}	4.43×10^{-47}	1.28×10^{-48}
20	0.21%	2.90%	60%	1.19×10^{-45}	4.59×10^{-47}	1.33×10^{-48}
40	0.16%	2.70%	59%	1.34×10^{-45}	4.95×10^{-47}	1.36×10^{-48}
80	0.12%	2.10%	57%	1.62×10^{-45}	5.36×10^{-47}	1.37×10^{-48}

Table 4.6: Change in signal acceptance and projected limit for varying light collection efficiency.

4.7.2 Light collection efficiency

It was shown in Section 4.3.3, that PMT loss and the subsequent reduction in light collection efficiency leads to a reduced detection efficiency for low energy deposits. It is, therefore, to be expected that the sensitivity for low-WIMP masses suffers. To assess how the impact of LCE on the LZ signal acceptance and sensitivity estimate, the different detector performance scenarios were implemented into the LZ PLR framework while using the probability density functions for background and signal models as for the projected LZ scenario. The signal acceptance and 90% confidence limit was estimated for 6, 9, and 40 GeV WIMPs. The scenarios considered here are 20, 40 and 80 passive PMTs randomly distributed across the top and bottom arrays.

The results are summarized in Table 4.6. The signal acceptance for a 6 GeV WIMP is reduced by a third for 40 inactive PMTs and by more than half for 80 inactive PMTs. For a 9 GeV WIMP, 80 passive PMTs constitute a reduction in signal acceptance of about a third. It is the low mass WIMPs which are impacted in these scenarios as the reduction in signal acceptance for a 40 GeV WIMP would be less than 10% for 80 passive PMTs. Looking at sensitivity, 40 inactive PMTs lead to a reduction by 20% for 6 GeV WIMPs, while it is only a reduction of 6% for 40 GeV WIMPs.

Losing PMTs also impacts the signal acceptance of secondary science goals physics events, such as Boron-8, hep solar neutrinos and coherent neutrino-nucleus scattering

Scenario	Signal Acceptance			
	8B solar ν	**hep solar ν**	**atm ν-A**	**dsn ν-A**
LZ Projected	0.22%	2.1%	73%	21%
20 PMTs passive	0.18%	1.9%	73%	20%
40 PMTs passive	0.15%	1.6%	73%	19%
80 PMTs passive	0.11%	1.3%	71%	18%

Table 4.7: Signal acceptance for secondary science goal physics events in region of interest.

of atmospheric or supernovae neutrinos. The results are summarized in Table 4.7. Passive PMTs reduce the chance to detect Boron-8 and hep solar neutrinos considerably. The signal acceptance of hep solar neutrinos and coherent neutrino-nucleus scattering is not affected significantly.

4.7.3 Fiducial volume

It was shown in Section 4.5.1 that outer row PMT failure makes a reduction in the fiducial volume necessary. Assuming that the run time stays constant (1000 days), the exposure and therefore also the sensitivity is reduced. Assuming a symmetric cut, the radial cut from the wall would need to be increased to up to 130 mm from the wall. The different scenarios in Section 4.5.1 can roughly be split into three groups, leading to a worst-case radial cut of 70, 90 and 130 mm from the wall. Table 4.8 shows the reduced fiducial volume and sensitivity for a 40 GeV WIMP in the different scenarios. A radial cut of 70 mm from the wall leads to a reduction of 9%. If a cut of 130 mm from the wall would be necessary, almost 26% reduction in sensitivity is expected. By running longer, the target exposure of 5600 t-days could be reached again. However, this would require 98 (333) days more physics search data for the 70 (130) mm cut. If only a few isolated PMTs on the outer array fail, it is worth defining a non-symmetric fiducial volume cutting further into the detector only in the areas around the passive PMTs. The results in Section 4.5.1 have shown that for

Radial Cut from wall [mm]	**FV mass[t]**	**40 GeV sensitivity (90% CLU)**
40 mm	5.6	$1.28 \times 10^{-48}\,\mathrm{cm}^2$
70 mm	5.1	$1.39 \times 10^{-48}\,\mathrm{cm}^2$
90 mm	4.8	$1.47 \times 10^{-48}\,\mathrm{cm}^2$
130 mm	4.2	$1.61 \times 10^{-48}\,\mathrm{cm}^2$

Table 4.8: Impact of reduced fiducial volume on 40 GeV WIMP sensitivity.

two inactive PMTs it would be sufficient to define an approximately rectangular area with one side length being the required radial cut and the other being the equivalent width of 4 PMTs. Such a cut would reduce the fiducial volume by approximately 2% (20 days more physics data) instead of the 25% (333 days more physics data) a symmetric radial cut of 130 mm from the wall would constitute.

4.7.4 Background discrimination

As discussed in Section 2.5, LZ expects 1195 ER and 1.03 NR events in 1000 days lifetime and 5.6 t fiducial volume. With the nominal 99.5% ER discrimination and 50% NR efficiency, this leads to an expected 5.97 ER and 0.52 NR background counts in the region of interest for a 40 GeV WIMP. While the intrinsic radioactivity and expected background sources are unchanged, a change in ER-NR discrimination in the detector due to PMT loss changes the number of background events expected to leak into the region of interest. At 20 inactive PMTs, the ER leakage increases by 0.02-0.03%.

The impact of increased ER Leakage on sensitivity is assessed using a cut-and-count Feldman-Cousins method. In the cut-and-count approach, the number of candidate events in the signal region is compared to the expected rate of background events. It should be noted that a PLR compares the data with signal and background models on an event-by-event basis, which allows better discrimination. Therefore, the results obtained with the cut-and-count approach are worse than what can be expected from

the PLR.

The probability of measuring N signal and background events are Poisson distributed with means μ and b.

$$P(N) = \Sigma_{i=0}^{N} P_{signal}(i;\mu) P_{background}(N-i;b) \tag{4.2}$$

The Feldman-Cousins method employs a likelihood ratio ordering,

$$R(n,\mu) = \frac{L(n|b+\mu)}{L(n|b+\mu_{best})}. \tag{4.3}$$

For every possible value of μ, a horizontal acceptance region is defined. For each μ, $P(N|\mu)$ is calculated and divided by $P(N|\mu_{best})$, where μ_{best} is the value maximizing $P(N|\mu)$. For a fixed μ, values of N are added to the acceptance interval from high to low likelihood ratio until the desired probability content is reached. Once all acceptance regions are defined, the confidence interval can be determined by drawing a vertical line at the observed N. Given a number of observed events, N, a 90% confidence upper limit number of signal events N_{CL} is calculated.

Having estimated an upper limit on the number of events and comparing this to the expected number of events from the WIMP signal model, an upper limit on the cross-section for the specific mass can be extracted. The differential rate for a chosen mass is calculated using the functional form given in Section 1.3.2. To get the number of events, the differential rate is integrated over the energy range of the signal region and multiplied by the exposure (3,500 t-days).

$$N_{evt} = \int_{E_{min}}^{E_{max}} \frac{dR}{dE} dE \times \text{mass} \times \text{time} \tag{4.4}$$

The ratio of expected events is directly proportional the WIMP-nucleus spin-independent cross-section. Therefore, the 90% confidence upper limit on the cross-section for a

ER-NR discrimination	**40 GeV WIMP (90% CLU)**
99.9%	$1.46 \times 10^{-48}\,\mathrm{cm}^2$
99.5%	$2.38 \times 10^{-48}\,\mathrm{cm}^2$
99.3%	$2.61 \times 10^{-48}\,\mathrm{cm}^2$
99.0%	$3.05 \times 10^{-48}\,\mathrm{cm}^2$

Table 4.9: Impact of reduced ER-NR discrimination on 40 GeV WIMP sensitivity.

specific WIMP mass can be calculated.

$$\sigma_{CL} = \frac{N_{CL}\sigma_n}{N_{evt}} \tag{4.5}$$

To get an estimate of the impact of increased leakage, it is assumed that on average the expected background will be the observed background. Different leakage scenarios from 99.9% to 99.0% are considered. For each scenario, the number of background events is estimated applying the ER-NR discrimination and a 50% NR acceptance to the number of ERs and NRs from the backgrounds table. The 90% upper confidence limits on the cross-section for a 40 GeV WIMP are shown in Table 4.9. At 40 GeV and for 99.5% discrimination, the sensitivity projection of the Feldman-Cousins method is a factor of 1.8 worse than the projected scenario using the PLR. This study can therefore only give an indication on how the increase in leakage would impact LZ in a cut-and-count regime. Reducing the discrimination efficiency from 99.5% by 0.3% (0.5%) decreases the sensitivity for a 40 GeV WIMP by 11% (28%).

4.8 Discussion

The different components of this study show how the failure of PMTs can impact LZ sensitivity. The reliable performance of bottom array PMTs is essential for reaching low energy thresholds with LZ. Losing bottom array (and to some extent top array) PMTs means that a fraction of S1 light is not detected anymore. For events of

very low energies, the S1 is lost completely. It can be seen that with 20 or more passive bottom PMTs, there is a considerable effect on the detection efficiencies for low energy events and therefore an impact on the sensitivity to low mass WIMPs, Boron-8 neutrinos and hep solar neutrinos. Some sensitivity to these low energy events might be recovered using S2-only searches. However, without S1, there is no more background discrimination power.

It is also clear that each inactive bottom array PMT impacts LZ when looking at gamma-X events. Any algorithm developed to veto such events should always be stress tested for performance with inactive PMTs. Every PMT failure increases the rate of Cerenkov events surviving cuts and therefore, the chance for Cerenkov S2-only coincidences. Depending on the S2-only rate in the experiment, Cerenkov events could be a problematic background. It is worth considering collecting data with under-performing or noisy PMTs. The large amount of light seen in the PMT, which is the origin of Cerenkov light should still be identifiable in such a PMT.

Failures of the outer-row top array PMTs lead to a leakage of wall events. Even a few failed PMTs on the outermost row of the array can have a serious impact on LZ performance. A smaller fiducial volume needs to be defined, impacting the experiments exposure and therefore, the sensitivity to all WIMP masses equally. The target exposure could still be reached by collecting data for longer. Assuming that localised cuts are possible, five positions with two adjacent PMTs failing would necessitate the extension of the physics run by three months.

Losing the outermost top array PMTs also has the most substantial impact on ER leakage due to local reductions in light collection efficiency. ER leakage due to PMT loss might be mitigated by having 3D position-dependent area corrections for both S1 and S2 pulses, taking PMT loss into account. An increase in ER leakage has a significant impact on sensitivity using a cut-and-count analysis. The PLR evaluates the probability of each event to be signal or background by comparing them to signal

and background probability density functions. The impact of leaked events will, therefore, be less than for the cut-and-count method.

Central top array PMTs are essential for Cerenkov events, S2 light collection efficiency and position reconstruction. It was shown in Section 4.5.2, that as long as there is some information in terms of hit pattern left, Mercury can reconstruct the position of these events very well.

4.9 Conclusion

The simulation study conducted has shown the impact of inactive PMT channels on LZ performance. It has shown that while backgrounds are important to consider, the effect of inactive PMTs on low energy thresholds and fiducialization dominates. It is important to note that the locations of non-operational channels matter. PMTs on the outermost row of the top PMT array are essential for fiducialization. Bottom array PMTs are more important for S1 light collection and therefore low mass WIMP sensitivity than top array PMTs.

The initial failure fraction required for detector acceptance should be kept at 4% random loss. At this requirement the impact on the sensitivity limit is 6% at 40 GeV, increasing to 11% at 6 GeV. The decrease in sensitivity at low WIMP masses is dominated by the reduced S1 light collection efficiency. For a 40 GeV WIMP, the contributions from reduced fiducialization and light collection efficiency are approximately equal, assuming that passive PMTs are randomly distributed. A loss of 16% of PMTs leads to a reduction of sensitivity of 15% at 40 GeV and 56% at 6 GeV.

Additional to keeping the overall fraction of non-working PMTs low, it is important to avoid outermost PMTs failing. Even a small number of outermost PMTs will lead to a reduction of fiducial volume. In case of failure of top outer array PMTs, local fiducial cuts should be considered to minimise the fiducial volume reduction.

If a PMT has a low gain or high afterpulsing levels, it is recommended to still record data on it. Under-performing PMTs can still be used for vetoing Cerenkov events and can provide some information for position reconstruction.

Chapter 5

Loop Antenna Development

A potential danger to PMTs and cause of PMT damage are high voltage discharges in the detector. A loop antenna system has been developed as the first dedicated EM environment monitoring system in an LXe TPC. Two arrays of four loop antennae monitor the LZ detector for HV breakdowns, discharges and phases of electric instability. The sensor development is discussed with a focus on performance characterisation and optimisation. Prototype sensors were tested in controlled laboratory environments, as well as, in realistic detector conditions at the LZ system test at SLAC. These test results and numerical simulations of the antenna and the array system have informed the final antenna design and triggering algorithm. The installation and first data taking during LZ assembly are discussed.

5.1 Motivation

5.1.1 HV in LXe TPCs

High voltages are applied to cathode, anode and grids to establish a vertical electric field. As discussed in Chapter 2, this field is needed to drift ionisation electrons up towards the liquid surface and extract them to the gas phase, where they produce

secondary scintillation in the gas phase. Past Liquid Noble Gas experiments in Dark Matter and Neutrino Physics have shown that reaching high voltages and maintaining a stable electric field is difficult [134]. High voltage breakdowns or partial discharges are often accompanied by light emission such as glowing and sparking. Sparking can cause severe damage in the detector, for example, to the PMTs. Additionally, it can produce false light signals which need to be vetoed in data analysis.

LZ uses voltages up to 50 kV. The LZ collaboration has conducted extensive testing to ensure minimal risk of breakdown. However, if an HV breakdown occurs, it is crucial to be able to immediately lower the cathode voltage to prevent damage to components like the PMTs. Additionally, monitoring the EM environment of the detector allows the identification of phases of electric field instability. Events during such periods should be vetoed in the analysis.

5.1.2 EM discharge theory

To design a sensor monitoring the detector for high voltage discharges, it is important to understand the physics behind discharges and the signatures which can be detected. A discharge occurs when the electric field across an insulation gap is higher than the breakdown field of the insulating medium. The insulating medium is ionised, and current can flow. If the current is high enough, the ionised plasma emits a visible glow. At even higher currents a visible arc forms. The fast increase in pressure and temperature can also lead to an audible sound. The current flowing over a spark gap of length δ is always accompanied by electromagnetic radiation,

$$E_{rad}(R,t) = \frac{\sin\theta}{4\pi\epsilon_0 R c^2} \int_0^{\delta} \frac{di}{dt} dx. \tag{5.1}$$

R is the distance from the spark, and θ is the angle between the current and R [135]. The radiation emitted is proportional to the temporal and spatial evolution of the

current. For a point discharge this can be approximated as $E_{rad} \propto \frac{di}{dt}$. The discharge arc develops a self-inductance, L_α and resistance R_α. $I(t)$ can be found by considering the discharge of capacitance C_s through an inductor and resistor connected in series. The RLC differential equation gives:

$$\frac{dI_{arc}^2}{dt} + 2\alpha\frac{dI_{arc}}{dt} + \omega^2 I_{arc}, \tag{5.2}$$

with an arc-inductive damping rate $\alpha = \frac{R_\alpha}{2L_\alpha}$ and the arc equivalent circuit's natural frequency $\omega = \frac{1}{\sqrt{L_\alpha C_s}}$.

From the typical arc current behaviour a steep rise and an exponential fall is expected in the arc current. An overdamping condition can be assumed. Additionally, it is imposed that the initial current is 0, $I_{arc}(0) = 0$. This leads to the solution:

$$I(t) = \frac{\dot{I}_{arc}(0)}{\beta} exp(-\alpha t) sinh\,(\beta t)) = 0, \tag{5.3}$$

where $\dot{I}_{arc}(0)$ is the initial arc current rise rate and $\beta = (\alpha^2 - \omega^2)$.

The broadcast signal therefore becomes

$$E_{arc}(t) = k\dot{I}(t) = k\dot{I}(0) exp(-\alpha t)[cosh(\beta t) - \frac{\alpha}{\beta} sinh(\beta t)], \tag{5.4}$$

where k is a constant. The corresponding power spectrum is given by:

$$P_{arc}(t) = |\int_0^\infty E_{arc}(t) e^{-j\omega t} dt|^2 = \frac{k^2 \dot{I}_{arc}(0)^2 \omega^2}{(\omega_a^2 - \omega^2) + (4\alpha^2\omega^2)}. \tag{5.5}$$

This indicates that the peak of the power spectrum occurs at the natural frequency of the LRC circuit. The natural frequency is determined by the arc inductance and resistance [136]. Previous measurements of the EM field associated with a discharge show the expected topology of a fast rise and slow decaying signal with fast oscillations in the MHz frequency range [137, 138, 139]. It can be seen that besides sound and

light emission, discharges have a well defined EM signature, which can be used for detection.

5.1.3 Sensor requirements

It is desirable to be able to monitor the detector for breakdown and discharge events. Knowledge about such events is useful auxiliary information about detector performance and helps with detector operation. A dedicated sensor could detect light, electromagnetic radiation or sound from such an event. There is no literature on dedicated in-situ HV breakdown monitoring sensors in LXe TPCs. In LUX one of the PMTs was used to look for light emission during grid conditioning [140]. CMOS cameras located at viewports have been used to monitor LAr TPCs. The DUNE experiment is developing cryogenic CMOS cameras for in-situ monitoring [141]. Discharge detection by light emission with dedicated or re-purposed light detectors is the only established discharge detection method in Liquid Noble Gas detectors.

In HV engineering a variety of methods are used for partial discharge detection, making use of all three signatures of the discharge [142]. One of the most common instruments for discharge detection is an antenna. Compared to light detectors, antennae have the advantage that they do not require an unobstructed view of the area they are monitoring and are sensitive to even small changes in the electromagnetic environment. While discharge sensors for industrial use are readily available, a sensor for LZ needs to be designed to be able to work reliably at cryogenic temperatures and comply with radio-purity requirements.

For these reasons, a custom low-background loop antenna has been developed as a dedicated HV breakdown monitoring sensor for LZ. The main design drivers were the following. Firstly, it needs to be sensitive to MHz frequencies and allow for good sensitivity coverage of the detector. Secondly, the sensor needs to have a fast time response to allow for a quick resolution of the problem. It also has to be easy to

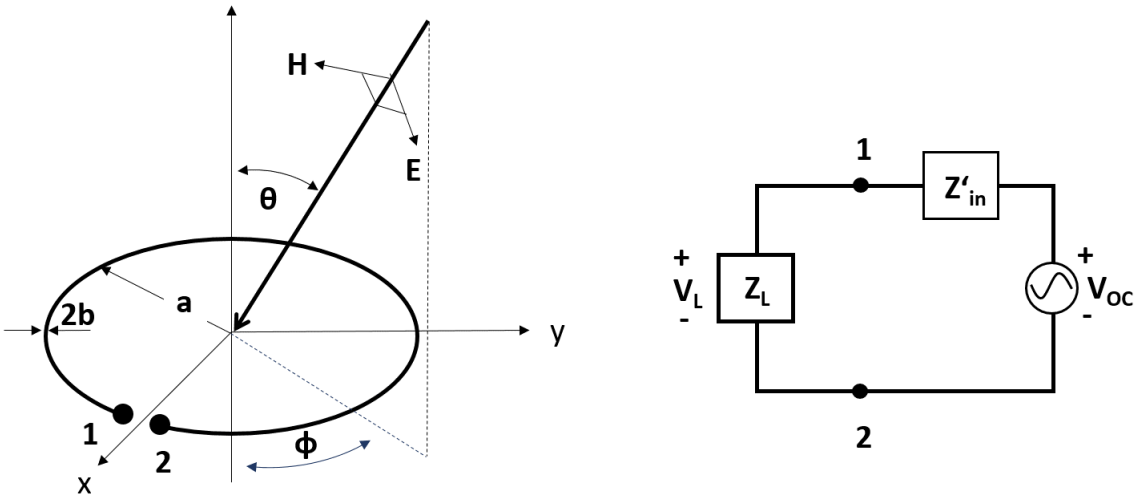

Figure 5.1: Left: Loop antenna schematic with incident plane wave. Right: Receiving mode loop antenna equivalent circuit. Both using same parameterisation as in [143].

integrate into the detector and operate reliably at cryogenic temperatures. Care has to be taken when choosing materials to minimise trace-radioactivity in the detector.

5.2 Sensor development

5.2.1 The small loop antenna

A loop antenna consists of at least one closed loop of wire, which can take different shapes, e.g. triangular, rectangular, circular. They are usually categorised into electrically large and small. A loop antenna is electrically small if its maximum dimension is less than 10% of the signal wavelength. Electrically small antennae have a small radiation resistance and are therefore usually used as receiving antennae [143]. An electrically small antenna works well for LZ as the frequency range of interest is tens of MHz, and the antenna has to be substantially smaller than the TPC diameter of 1.5 m.

When an EM wave impinges onto a loop antenna with radius a as depicted in

Fig. 5.1, a voltage develops between its two ends. This open circuit voltage is proportional to the incident magnetic flux density B_z^i, which is normal to the plane of the loop:

$$V_{OC} = j\omega\pi a^2 B_z^i. \tag{5.6}$$

When a load with impedance, Z_L is connected to the loop antenna terminals, as shown on the right of Fig. 5.1, the voltage developed across this load is given by:

$$V_L = V_{OC}\frac{Z_L}{Z_{in} + Z_L}. \tag{5.7}$$

Z_{in} is the loop antenna impedance. From Equ. 5.6, it is clear that the bigger the area enclosed by the loop, the bigger the open-circuit voltage. The ohmic loss increases with wire length. A circular loop maximises the area for a given conductor length. The radiation resistance of small loops can be improved by adding more turns. However, multiple turns make the radiation pattern more complicated due to the proximity effect. High-frequency EM waves concentrate in the surface region of the conductor. For larger wire diameters, the skin region is larger. The resistance is, therefore, smaller, and the signal becomes larger [144]. Overall, to maximise the sensitivity of the antenna, a circular loop made of thick wire is preferred.

5.2.2 Material considerations

One of the main reasons for producing a custom loop antenna is that it has to be very radio-pure. Additionally, it has to be taken into account that the sensors need to operate safely at cryogenic temperatures and while exposed to liquid and gaseous xenon.

OFHC copper and PEEK (polyether ether ketone) were chosen as primary materials as they typically have low levels of radioactivity and cannot be activated. Copper is an excellent conductor and is used as the conducting loop of the antenna. The cop-

per wire used, was ICP-MS [1] screened by collaborators at UCL. The screening showed that the copper wire is close to the blank rate and detection limit [145]. PEEK is needed to hold the wire in the circular shape. Screening in Germanium Detectors at the Boulby Underground Laboratory showed acceptable cleanliness. Lead and flux-free solder was found and approved for usage by collaborators. It was also decided to use the same connectors and receptacles as for the PMT bases. Most commercially available connectors contain beryllium copper (BeCu), which is problematic due to its high (α, n) yield. The UK-based manufacturer Harwin offers connectors which are BeCu free. Germanium screening showed that these connectors have low radioactivity. Another material which was approved for use in the PMT bases and is therefore available for sensor construction is cirlex. Cirlex is a thick polyimide which is quite radio-clean and has reasonable radon-emanation levels [146]. Stability at cryogenic temperatures was tested by thermocycling the antennae with liquid nitrogen, which is well below liquid xenon temperature.

5.2.3 Prototype design

With a radius of 25 mm, the prototype loop antenna design was optimised for easy integration into the LZ system test at SLAC. To take advantage of the skin effect, but still be able to bend the wire in shape, a wire diameter of 2 mm was chosen. The wire is bent in a single loop around a PEEK disk. A single-turn antenna was chosen to simplify the radiation pattern [147]. On one side the PEEK disk has a cutout allowing for the installation of a cirlex board with two separate copper pads. Harwin receptacles and the two ends of the copper wire are soldered to the copper pad. The antenna is grounded in-situ using a grounding wire soldered to the middle of the copper wire to allow a differential readout scheme. Such a readout scheme has the advantage of lower noise levels. As the voltage difference between the two parts

[1] Inductively coupled plasma mass spectrometry

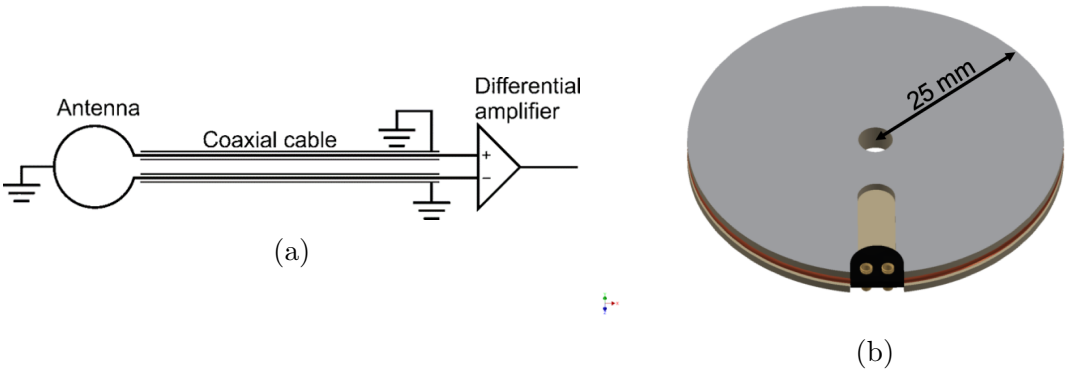

(a) (b)

Figure 5.2: Loop antenna prototype design showing (a) the electrical readout scheme and (b) the CAD drawing.

of the loop antenna is measured, it is immune to noise introduced by the change of the common electrical potential of the loop antenna. The peek disk has a hole in the middle to allow easy installation. The electrical readout scheme and the CAD drawing for the prototype are displayed in Fig. 5.2. For all tests with the prototype loop antenna discussed in the following sections, a transformer-coupled single-ended readout board was used. This DAQ system only has a single channel and is optimised for PMT readout. It samples at 200 MHz, has a 14-bit digitiser and a dynamic range from -0.75 V to $+0.75$ V. For the measurements at the system test, an add-on board was added to this board, allowing differential readout.

5.2.4 Antenna characterization

5.2.4.1 Loop antenna parameters

The prototype loop antenna has a radius, $a = 25$ mm and a wire diameter, $2b = 2$ mm. The copper wire has a conductivity, $\sigma = 5.8 \times 10^7$ S/m. Table 5.1 contains the different contributions to the loop antenna impedance,

$$Z_{in} = R_r + R_{ohmic} + j\omega L_A + j\omega L_i. \tag{5.8}$$

Parameter	**Formula**	**Resistance** [Ω]
Radiation resistance	$R_r = 20\pi^2(\frac{2\pi a}{\lambda})^4$	1.489×10^{-7}
Ohmic Resistance	$R_{ohmic} = \sqrt{\frac{2\pi f\mu}{2\sigma}}$	8.250×10^{-4}
External inductance	$L_A = \mu a[ln(\frac{8b}{a} - 2)]$	6.645×10^{-9}
Internal inductance	$L_i = \frac{a}{\omega b}\sqrt{\frac{\omega\mu}{2\sigma}}$	5.252×10^{-12}

Table 5.1: Prototype loop antennae parameters at 10 MHz in vacuum, where μ is the vacuum permeability, a is the antenna radius, b is the wire radius, σ is the conductivity of the wire. [143].

The voltage developed across a load connected to the loop antenna terminals can be calculated using Equ. 5.7.

In the following, the LZ loop antenna response is characterised further using analytical calculations, simulations and measurements. It is calibrated over the frequency range of interest, and the radiation pattern is simulated.

5.2.4.2 Antenna factor

The sensitivity of the loop antenna prototype is determined, by measuring the antenna factor A_F over a range of frequencies. The antenna factor expresses the relationship between the impinging EM field strength on the loop antenna surface and the measured loop antenna output voltage [144]. In terms of the electric field component, it is defined as

$$A_F = \frac{E_{incident}}{V_{received}}. \tag{5.9}$$

The measurement setup is shown in Fig. 5.3a. A uniform EM field is generated using a radiating antenna. A loop geometry is chosen to simplify the field calculations. As the transmitting loop antenna is electrically small, it can be assumed that the current through its conductor is uniform. This current I can be determined us-

ing Ohms law and measuring the voltage drop across a resistor. The receiving and radiating antennae are facing each other separated by a distance d. The distance was chosen to be small to minimise effects due to field reflections from the ground. The near zone field of the loop antenna is primarily magnetic, but as $E = \eta_0 H$, the equivalent free-space rms electric field strength can be used. Its magnitude in V/m is calculated, using

$$E = \frac{60AI}{R_0^3}\left[1 + \left(\frac{2\pi R_0}{\lambda^2}\right)^2\right]^{1/2}. \tag{5.10}$$

A is the area of the radiating antenna. λ is the free space wavelength. The distances and antenna radii are taken into account as $R_0 = \sqrt{d^2 + r_1^2 + r_2^2}$ [148].

The voltage across the detecting loop antenna terminals is measured, and a sine wave was fitted to the recorded data to extract the signal amplitude. Knowing the EM field strength and the voltage response of the receiving loop antenna, the loop antenna factor can be calculated using Equ. 5.9. The measurement was repeated for frequencies in the range 1 to 80 MHz in steps of 5 MHz.

A plot of the antenna factor for the prototype antenna is displayed in Fig. 5.3b. It can be seen that the antenna factor is largest at smaller frequencies and stays approximately constant between 40 and 80 MHz. The antenna factor can be interpreted as the field strength needed to induce the same voltage output in the antenna at different frequencies. The antenna is most sensitive to frequencies around 30 MHz. This is favourable for the use in discharge detection as was discussed in Section 5.3.

5.2.4.3 Radiation pattern

Another important aspect to consider is how the antenna sensitivity varies with orientation. Radiation patterns visualise the radiated EM field over a sphere centred on the antenna. Directivity is the ratio of radiated power in a particular direction to the average radiation intensity in all directions [144]. The gain of an antenna depends

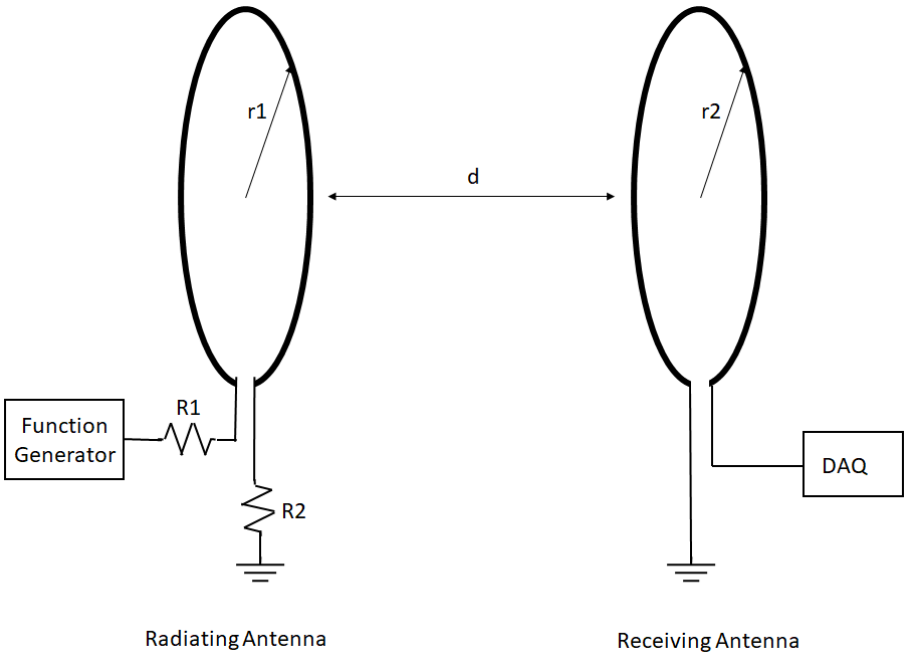

(a)

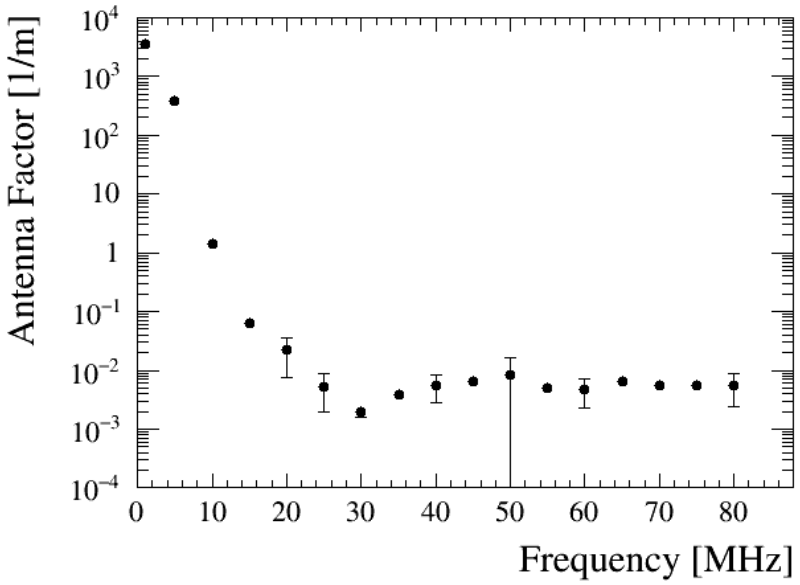

(b)

Figure 5.3: Antenna factor measurement (a) setup and (b) results for the prototype antennae over a range of frequencies.

on the directivity and efficiency of the antenna. The radiating and receiving properties of the antenna can be used interchangeably due to the principle of reciprocity. This principle states that any antenna constructed of linear materials has the same properties in receiving and radiating mode if the receiving and sending modes are polarisation-matched [149].

As mentioned in the previous section, the current along the conductor of a small loop antenna can be approximated to be uniform. From this the radiation pattern can be derived by solving the potential function. It can be shown, that the small magnetic loop can be replaced by an ideal linear magnetic dipole of constant current [143]. Using this knowledge, the resulting far-field expressions are [144]

$$E = -I^m \Delta z j\beta \frac{e^{-j\beta r}}{4\pi r} \sin\theta \hat{\phi} \tag{5.11}$$

and

$$H = I^m \Delta z j\omega\epsilon \frac{e^{-j\beta r}}{4\pi r} \sin\theta \hat{\theta}. \tag{5.12}$$

The loop antenna radiation pattern is omnidirectional and proportional to $\sin\theta$.

The directivity pattern of the prototype loop antenna was numerically simulated in MATLAB. The current along the loop is estimated using the methods of moments. A built-in MATLAB function meshes the antenna surface and uses the Rao-Wilton Glisson (RWG) basis functions to determine the current. The antenna current is divided into small elementary electric dipoles. The resulting impedance matrix describes the interaction between different elementary dipoles [150]. Once the current along the conductor is known, the directivity pattern can be calculated. The equivalence of EM properties of a circular radius and non-circular geometry with equal capacitance allows the wire to be modelled as a strip with width 4× wire-radius [143].

The 3D directivity patterns of the LZ loop antennae at 1 and 200 MHz are shown

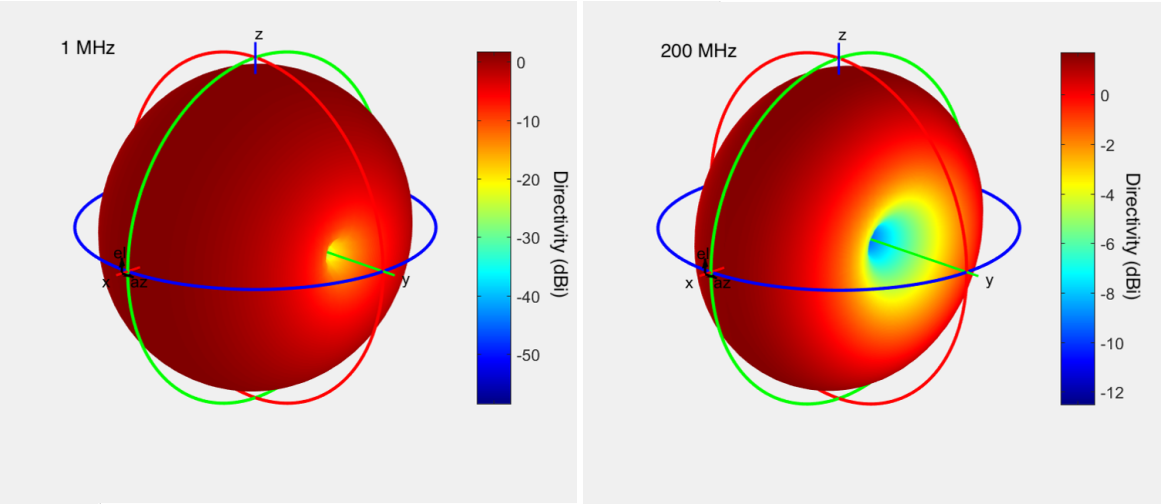

(a) (b)

Figure 5.4: Loop antenna directivity pattern simulated with MATLAB for (a) 1 MHz and (b) 200 MHz. The antenna lies within the x-z plane with the antenna axis pointing along the y-axis. Units are directivity in dBi.

in Fig. 5.4. The loop axis is oriented along y. The pattern at 1 MHz (Fig. 5.4a) agrees with the expectations of the analytical expression in Equ. 5.11 and Equ. 5.12 for a single-loop antenna. The numerical simulation confirms that the uniform current assumption is justified up to several tens of MHz. At 200 MHz (Fig. 5.4b), the current becomes less uniform, and the radiation pattern minima in the axial direction become smaller than previously. At even higher frequencies, the loop antenna can no longer be defined as small, and the directivity minima move away from the antenna axis to the radial direction. However, for the frequencies of interest for LZ, the analytical pattern calculated above is sufficient. The omnidirectional pattern is favourable for LZ, as the loop antenna is sensitive in all directions.

5.3 Discharge detection

5.3.1 Spark detection in air

It is also important to investigate the response of the antenna to radiation from a discharge. A spark in air can be generated using an ignition coil connected, as shown in Fig. 5.5. A function generator controls a relay switch by sending out a square wave. When the switch in the relay is connected, a battery powers the primary ignition coil. When the switch suddenly disconnects, the secondary ignition coil generates a voltage of the size $V_{induced} \times \frac{N_2}{N_1}$, in which N_2 and N_1 are the number of turns in the primary coil and secondary coil respectively and $V_{induced}$ is the voltage induced in the primary coil. L is the inductance of the primary coil. The voltage generated by the secondary coil is high enough to cause a breakdown in air, generating a spark. Power loss in the ignition coil is due to resistance in the windings, capacitive and re-magnetisation losses, as well as deviations from the ideal configuration for a magnetic circuit. The spark energy is, therefore, typically 50 to 60% of the stored primary energy. A loop antenna is placed several meters away from the ignition coil spark generating setup and data of the sparking event is recorded. This test allows investigating the ability of the loop antenna to detect a sparking event and get a first idea of the event topologies.

A typical sparking event is displayed in Fig. 5.6a. The pulse has a short rise time (20 - 40 ns) and a much longer fall time of several 100 ns, due to a sudden increase in voltage, which then discharges. The pulse substructure shows high-frequency oscillations. The Fast-Fourier Transform of the event is displayed in Fig. 5.6b, a maximum is observed between 20 and 30 MHz. This is not surprising as the Antenna Factor measurement (Fig. 5.3b) has shown that 30 MHz is the maximum sensitivity of the prototype antenna. Even without differential readout, small ignition coil sparks can be detected at distances larger than 3 meters. Compared to interference from surrounding electronics in the lab, the pulses from sparking are much more significant.

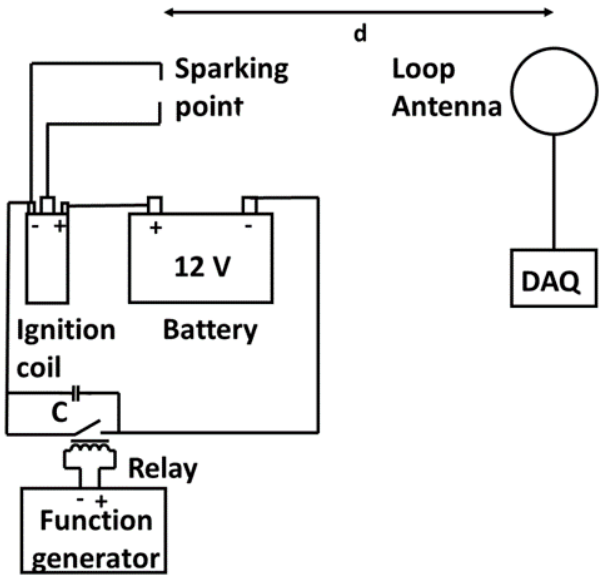

Figure 5.5: Sparking test setup with ignition coil and spark gap.

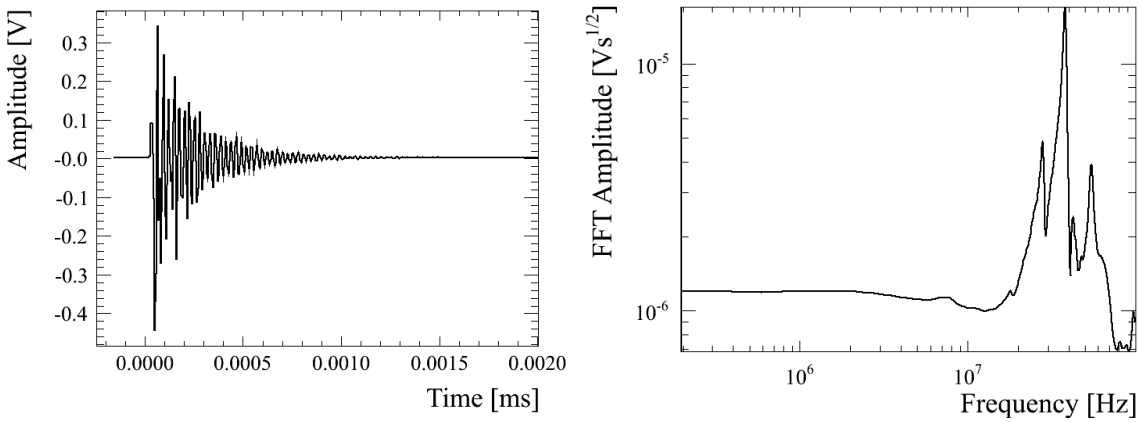

(a) (b)

Figure 5.6: (a) Typical sparking event as picked up by the prototype loop antenna. (b) Fast-Fourier-Transform of same sparking waveform.

Not every pulse records the same amplitude, which is probably due to the different sizes of sparks generated. Overall, it was found that the peak voltage is a good indicator of the relative discharge size.

The ignition coil tests show that the prototype loop antenna is sensitive to HV breakdowns in air and allow the determination of the typical sparking event topology, which agrees with expectations from theory discussed in Section 5.1.2.

5.3.2 Prototype testing at LZ system test

The loop antenna functionality of detecting discharge events in a setup similar to LZ was tested using prototype antennae at the LZ system tests at SLAC (Stanford National Accelerator Laboratory). The system test was an opportunity to test the antenna in liquid and gaseous xenon and to get feedback on the antenna design in terms of stability, installation and operation.

Figure 5.7: System Test TPC with loop antennae installed.

A large LZ system test platform containing more than 100 kg of LXe has been set up by collaborators at SLAC. This system test is testing methods of xenon handling, purification and circulation. Additionally, integrated tests of the broader HV performance are conducted. The surface and bulk fields reached in the system test TPC prototype are of the order of magnitude expected for LZ [75]. It is, therefore, an ideal test environment for the loop antenna prototype. Two loop antennae were installed above and below the TPC as indicated in Fig. 5.7, similarly to how they are installed on LZ. The loop antenna data taking was controlled remotely from Oxford. The main difficulties were a very noisy EM environment and cable cross-talk, which resulted in high trigger and data rates. Despite these difficulties, both loop antennae were shown to be sensitive to the EM environment. Both antennae recorded

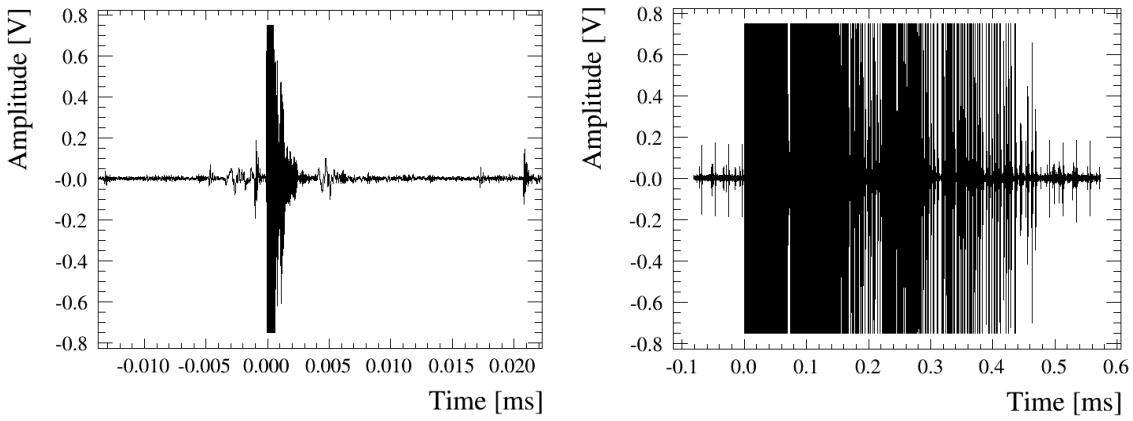

(a) (b)

Figure 5.8: (a) Typical loop antenna events recorded at SLAC System Test during HV ramp tests. (b) Large discharge events with several pulses following in quick succession with a periodic background interference.

events with the typical sparking event topology during liquid and gas operations. The event topology (Fig. 5.8a) in xenon is very similar to that in air. While the previous tests in air were isolated sparks, here discharge events are often detected as groups of pulses of the discharge topology. An example event display is shown in Fig. 5.8b. The topology is the result of a succession of several sparks, as well as reflections inside the cryostat. Depending on the location of discharges, they were seen by only the top, only the bottom or both loop antennae. Events seen by the loop antennae can be correlated to changes in the high voltage environment and phases of light emission. Fig 5.9 shows a period of high voltage ramps on the gate and anode. On top of the plot, the voltages applied to gate and anode are shown. The middle plot shows the PMT data rates and the bottom plot displays the amplitude of the loop antenna signal. It can be seen that during periods preceding anode trips, both the PMT rate and the loop antenna amplitude increase drastically. The loop antenna events during this period have the typical sparking topology and are saturated. These are periods of partial discharges in the xenon gas, which are detected by the PMTs in the form of light and the loop antennae in the form of EM radiation.

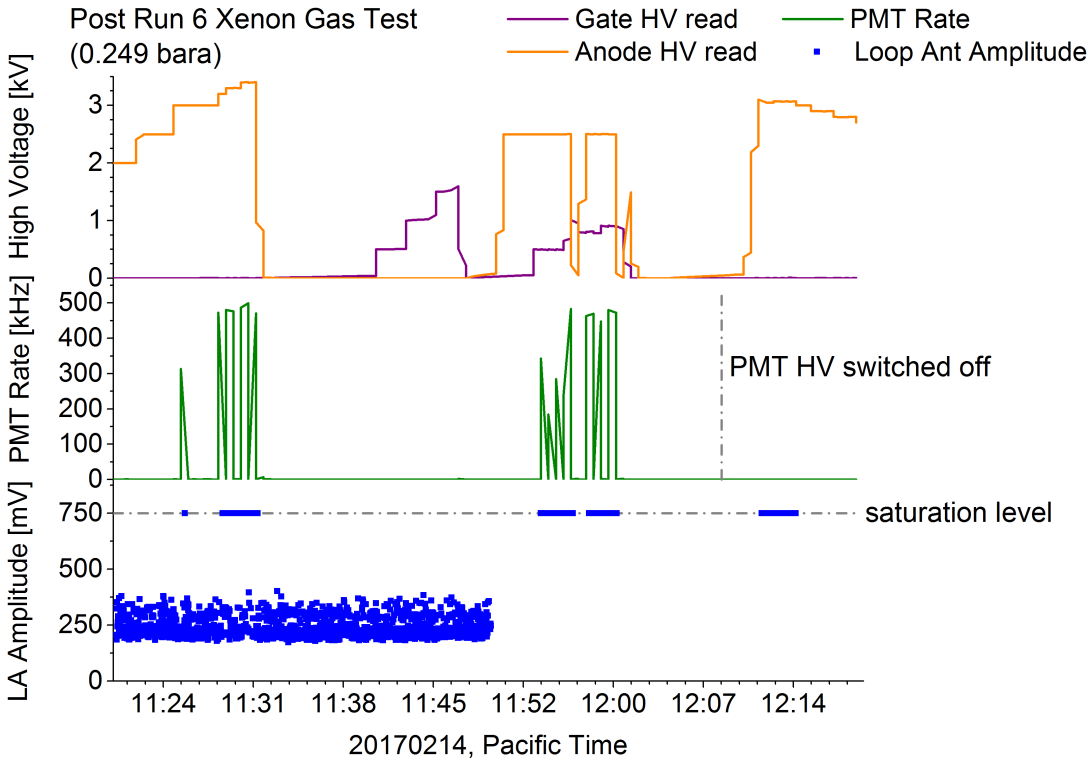

Figure 5.9: Gate and anode voltage readings, PMT rates and Loop Antenna signal amplitude during a period of ramp tests.

The operation of two loop antennae in the system test has shown that they are sensitive to the EM environment in a setup similar to LZ. Both antennae were able to detect sparking events which have a very similar topology to discharges in air. These sparking events were correlated to high voltage trips and corresponding light emission. The operation of loop antennae in these runs has also shown the need for better grounding, triggering and filtering.

5.3.3 Discharge localization

The LZ TPC has a height and width of 1.5 m. Therefore, the largest distances between potential discharge locations and loop antennae would be around 2 m. The refractive index of liquid xenon was measured to be $n = 1.69 \pm 0.02$ [151]. The speed of EM

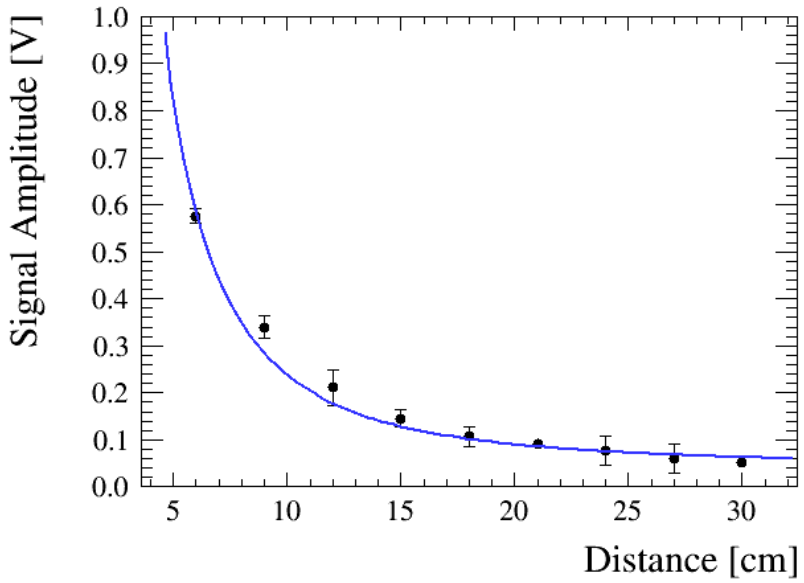

Figure 5.10: change in maximum voltage with increasing distance between radiating and measuring antenna. The blue fit line shows that this data is well described by the inverse square law.

waves inside the liquid is therefore 1.78×10^8 m/s. The time difference between the signal recorded by antennae at opposite ends of the detector would be of the order of 10 ns, which corresponds to 2 samples difference. Localisation due to time difference is therefore almost impossible.

The magnetic field associated with a discharge is expected to follow the inverse square law and fall proportional to $\frac{1}{d^2}$. This relationship is verified using the same setup as in Fig. 5.3a and varying the distance between radiating and receiving antenna at a fixed frequency. The measurement result is displayed in Fig. 5.10 and the inverse square law fit describes the data well. The orientation of the antenna relative to the discharge has only a small effect, as shown by the radiation patterns in Section 5.2.4.3. In LZ, the only information available is the positions of the loop antennae installed in the experiment and the relative signal sizes they detect. The location and installation of LZ loop antennae are further discussed in Section 5.4.4. As there are many metallic elements inside the inner cryostat, shielding and reflection play a role. It is expected

that from the information which antenna recorded a signal and the relative size of the signal, a rough indication to the location of the discharge event can be given. However, precise localisation is not possible.

5.4 Final design, sensitivity and installation

5.4.1 Final design and production

The testing of the prototype antenna, discussed in previous sections, has proven the sensitivity of the design to HV breakdown and discharges. The operation at the System Test showed the need for a better grounding scheme to improve noise performance. Additionally, it was decided to increase the loop antenna size and change the design to avoid usage of cirlex to simplify the production process. The connector was changed to use the same connectors and cabling as the PMTs in LZ.

The LZ loop antenna final design consists of two copper rings of equal length, stacked on top of each other. Each ring is connected to one coaxial cable. One terminal of the copper wire is connected to the conductor of the cable and the other to the shield of the cable. The cable conductor is connected to the differential amplifier, and the shield is connected to ground. It is vital to ensure that the opposite ends of the copper rings are connected to the differential amplifier. This design allows taking full advantage of the shielding properties of coaxial cables as now the shield can carry the same current as the conductor in the opposite direction.

A CAD model of the loop antenna is displayed in Fig. 5.11. The main loop antenna structure is a PEEK disk with a radius of 35 mm and consisting of three parts. The outer disks contain grooves on the side, through which a copper wire of 2 mm diameter is wrapped. The copper wire ends are bent inward, where they meet the Harwin pin receptacles. The receptacles are pressed through the PEEK structure with the opening looking outward. The copper wire terminals are soldered

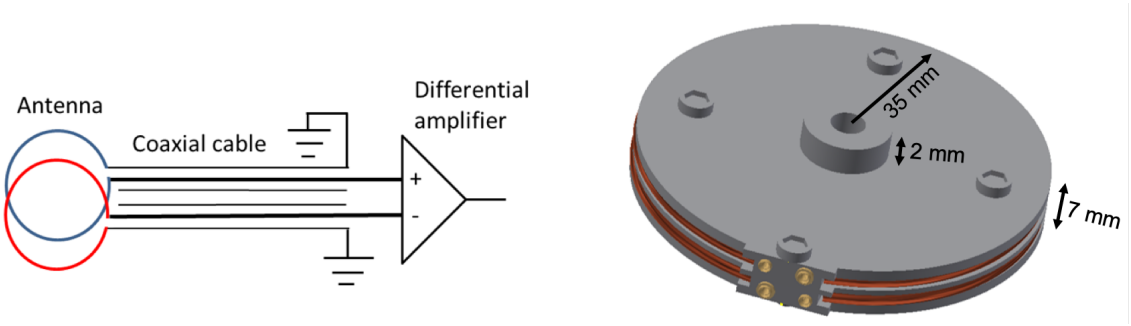

Figure 5.11: Left: Schematic of final loop antenna readout. Right: CAD model of loop antenna.

to the respective receptacles. Different size receptacles for ground and signal ensure that the wiring is connected correctly. After installation of the copper wires and receptacles, the three-disk pieces are assembled. Four M3 screws are used to hold the pieces in place. The PEEK disk also functions as a structure for mounting in the detector, through its middle M5-size hole. Stability during thermal cycling was tested down to liquid nitrogen temperatures.

The final LZ loop antennae were produced in the mechanical workshop in the Oxford Physics Department. Cleaning took place at Oxford and Imperial College, London. Radon-progeny settling onto surfaces during construction and dust containing both radon and other radioactive isotopes are problematic for low-background experiments. All components are thoroughly cleaned using ultrasonic baths and wiping with solvents like IPA and Acetone before, during and after assembly. Additionally, the loop antennae were stored in radon-barrier bags.

5.4.2 Final background estimate

After cleaning and assembly and prior to installation the loop antennae were screened by collaborators at SDSM&T and SURF. Results from Germanium screening are summarized in Table 5.2. Due to the low mass of the loop antennae it was only possible to get upper limits for ^{238}U and ^{40}K. Traces of ^{232}Th were measured .

	ppb	mBq/kg	mBq/antenna
$^{238}\mathbf{U}_e$	<9.2	<113	<6.2
$^{238}\mathbf{U}_l$	<0.4	<4.9	<0.3
$^{232}\mathbf{Th}_e$	3.8 ± 1.4	15 ± 6	0.8 ± 0.3
$^{232}\mathbf{Th}_l$	2.8 ± 1.2	11 ± 5	0.6 ± 0.3
$^{40}\mathbf{K}$	<0.7 ppm	<20	<2.3
$^{60}\mathbf{Co}$	-	-	-

Table 5.2: Final loop antenna and mounting screws bulk assay results after background subtraction per kg and per antenna. Loop antennae were screened on MORGAN (SURF) for 10 days [152].

All 8 loop antennae going into the detector add less than 1% of the expected trace radioactivity of the LZ PMT system [86]. Radon emanation of the loop antennae showed a null rate of $0^{+0.05}_{-0.00}$ mBq [153]. Additionally, the loop antennae were checked for dust and surface contamination during installation. Under UV light, no dust was observed on the loop antenna surface.

5.4.3 Sensitivity and calibrations

The sensitivity and response of the final LZ loop antennae are determined in a similar manner as for the prototype antenna using the equations in Table 5.1. The two loops of the antenna are treated as separate entities, and the response of one loop is compared to the response of the prototype antenna before differential readout. Radiation resistance, R_r and ohmic resistance, R_{ohmic} stay unchanged. Both external and internal inductance increase to $L_A = 1.599 \times 10^{-7}$ H and $L_i = 4.596 \times 10^{-10}$ H. The change in Z_{in} is negligible as the unchanged ohmic resistance is the dominant contribution. The increase in sensitivity is mostly due to the larger area of the loop. As $V_{oc} \propto a^2$ the measured voltage V_L from one loop increases by a factor of 3.8 compared to the prototype loop antenna.

The antenna factor was measured for this antenna using the same setup and method, as discussed in section 5.2.4.2. The dedicated loop antenna readout elec-

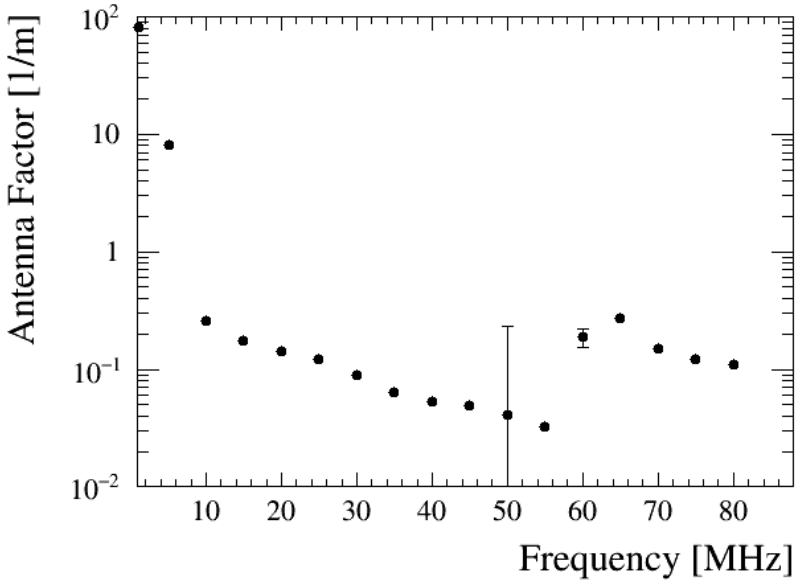

Figure 5.12: Antenna factor over a range of frequencies for LZ loop antenna.

tronics with differential readout as discussed in Section 5.5.1 are used. The resulting plot is shown in Fig. 5.12. Due to the different readout electronics, it is not possible to compare directly to the sensitivity of the prototype antenna displayed in Fig. 5.3b. However, it can be seen that the antenna factor of the final LZ design has less variation over the frequency range of interest than the prototype antenna. Its maximum sensitivity is at 55 MHz.

The radiation pattern of the final loop antenna was modelled in MATLAB using the same method as explained in section 5.2.4.3. As the LZ loop antenna consists of two separate wire loops, the antenna was modelled as an array of two loops with a distance of 2 mm. Both loop axes are oriented along the y-axis. The resulting radiation patterns are shown in Fig. 5.14. As expected, the antenna has the same omnidirectional pattern with poles along the antenna axis. The addition of a second loop means that the poles are less pronounced than for the one-loop prototype.

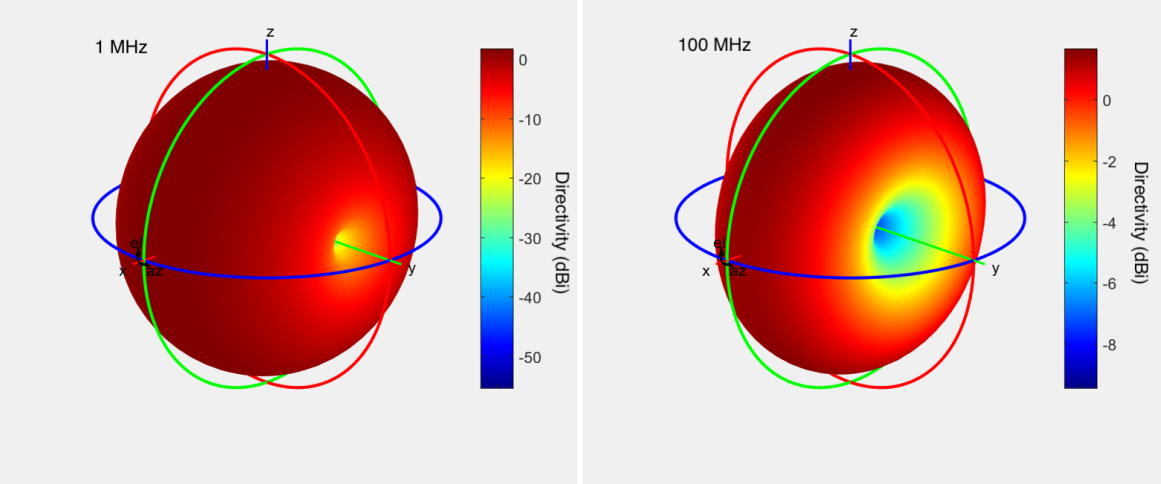

(a) (b)

Figure 5.13: Loop antenna directivity pattern simulated with MATLAB for (a) 1 MHz and (b) 200 MHz. The antenna lies within the x-z plane with the axis pointing along the y-axis. Units are directivity in dBi.

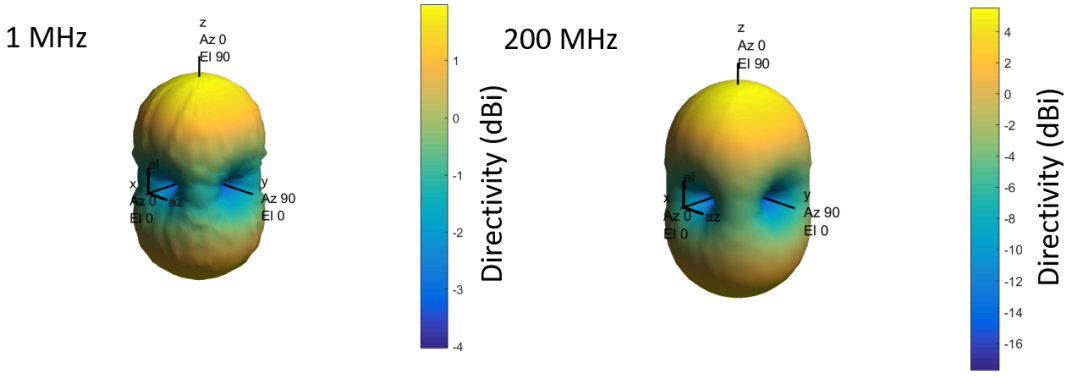

Figure 5.14: Directivity pattern for array of 4 loop antennae simulated with MATLAB.

5.4.4 Integration into the LZ detector

LZ has eight loop antennae in total. Four are located on the top PMT array, and four attach to the skin PMT truss, as shown in Fig. 5.15. The top array antennae are located close to the electroluminescence region, and the bottom antennae are located close to the cathode region. These are the two places with the highest electric fields in the detector. The antennae are in a good position to monitor discharges near the TPC cage perimeter, especially between the cage and the inner vessel wall - the skin region. A radial discharge is the most likely form of the discharge as the electric potential difference is larger in this direction [147]. To maximise the sensitivity of the antennae to sparks travelling radially between the field cage and the cryostat, the axis of the antenna needs to point radially outward of the cylindrical coordinates of the TPC. The antennae installed on the system test were located in similar locations and were able to see sparking from the grids inside the TPC.

The combined radiation pattern for four antennae installed in one plane (top or bottom array) was simulated using the methods explained in 5.2.4.3. When simulating the antenna array, the antennae axis are 90° to each other, looking outwards to model the orientation of antennae in LZ. The 3D-directivity patterns at 1 and 200 MHz are presented in Fig. 5.14. The pattern has poles along the x and y plane, as to be expected from the directivity patterns of the individual antennae. The poles are less pronounced than for the individual antennae, as the patterns are overlapping. At high frequencies, the minima get slightly larger. The simulation was also used to determine that changing the antennae orientation towards each other by a few degrees does not influence the coverage.

5.4.5 Data taking during detector assembly

The four bottom loop antennae (referred to as LA1 to LA4) were installed early on in the detector integration, together with the bottom side skin. Fig. 5.16 shows the

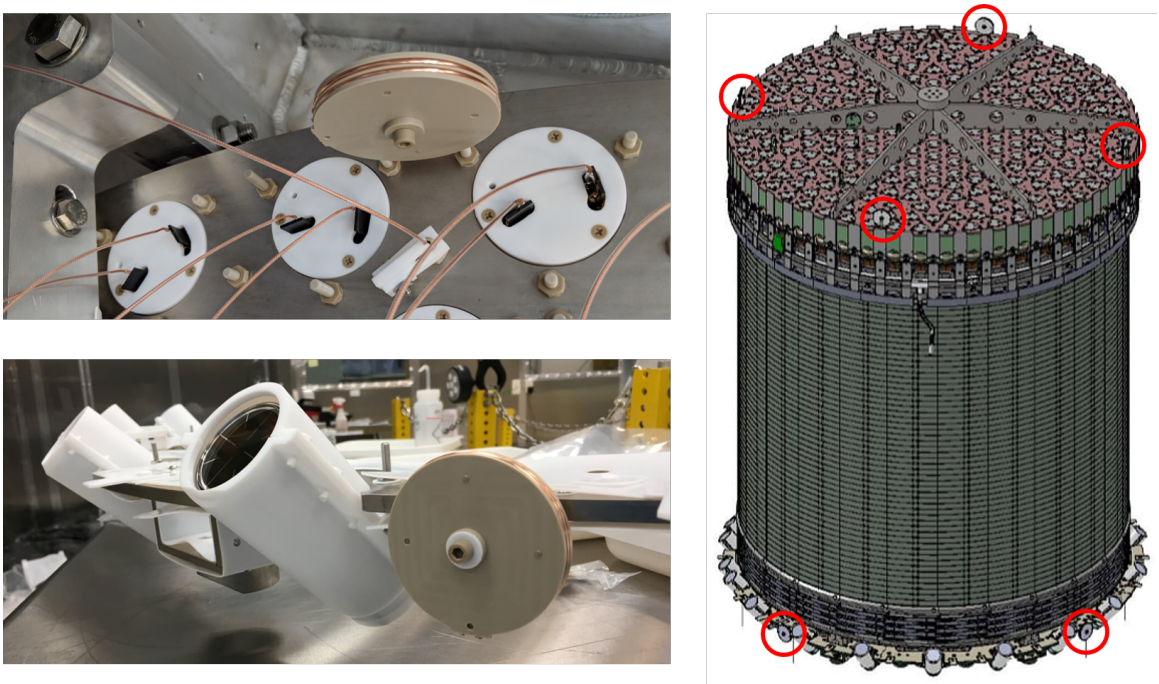

Figure 5.15: Left top: Close up of loop antenna mounting on the top array. Left bottom: Loop antenna during installation on bottom side skin structure. Right: CAD overview of TPC with top and bottom PMT arrays. Loop antenna locations on top and bottom side skin arrays are marked in red.

location of the loop antennae on the bottom side skin array. After installation, a functionality test was conducted, creating a spark using a piezo-electric crystal and recording the response of the antennae using the loop antenna readout electronics (described in Section 5.5.1). All four loop antennae passed this test. As the bottom side skin contains devices very sensitive to even small static discharges (LEDs, PMTs), additional loop antenna data was taken to monitor the EM environment inside the cleanroom. Two data sets were recorded. The first one covers about 1.5 hours during which people were working in and around the Inner Cryostat Vessel (ICV) in which the antennae were installed. The second data set is almost 12 hours long. It was taken overnight, while no one was inside the cleanroom. The trigger was set to record data if LA1 or LA2 crossed a threshold of 75 mV for the first data set and 100 mV for the second data set. During the first data taking period, more than 1000 spark-like events were recorded. Fig. 5.18c and Fig. 5.18d show the number of

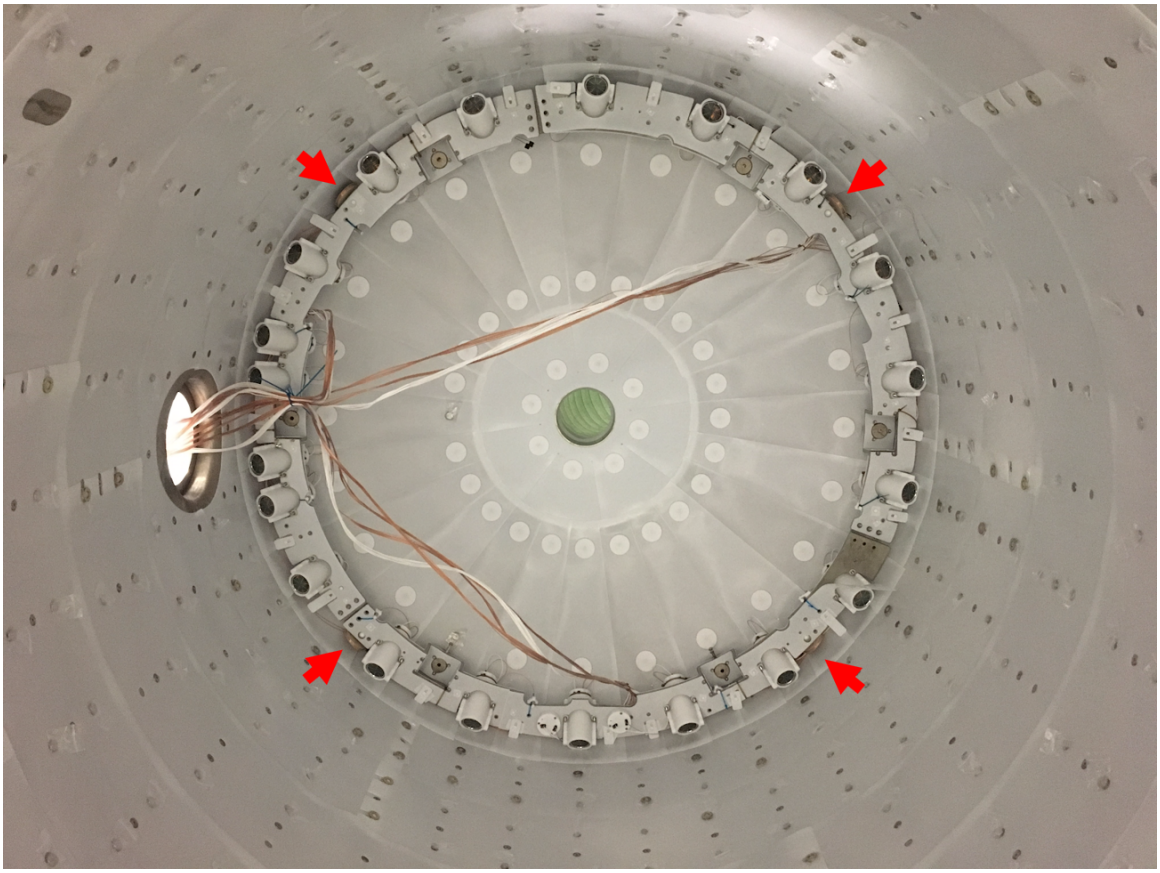

Figure 5.16: View inside the bottom of the Inner Cryostat with prototype PTFE tiling and Bottom Side Skin Array installed. The red arrows indicate the location of the loop antennae on the Bottom Side Skin Array. The cables for PMTs, LEDs and LA are fed through the HV feedthrough for QA tests.

counts per minute. Only data from LA1 and LA2 are displayed here, as these were the two loop antennae which were triggered on. Fig. 5.18a and Fig. 5.18b show the corresponding signal amplitudes. While people are working in the ICV (first data taking period), small discharges are happening almost continuously. Additionally, there are frequent larger amplitude discharges. The trigger rate during the overnight period is considerably lower. Fig. 5.17 shows a histogram comparing the signal sizes during the different data taking periods, as well as the signal size from the piezo-electric crystal. During the overnight data taking period, very few of the recorded pulses exceeded a signal amplitude of 0.3 V. It can be seen that the larger pulses recorded during working inside the ICV are comparable in size to the discharges from the piezo-electric crystal. It can, therefore, be concluded that they are sizeable and potentially dangerous to very sensitive devices such as the LEDs and the PMT bases.

Following these results, measures were taken to decrease the static charging in the cleanroom, including increasing the humidity and installation of a deioniser. Additionally, it was ensured to protect electro-sensitive devices by wearing grounding straps when working on them. To assess the effectiveness of these measures, another set of loop antenna data as taken a few weeks later. The trigger level was set to 100 mV. The data taking period was almost 12 hours, including 45 minutes during which people were working in the ICV (16:00 - 16:45) and is displayed in Fig. 5.18f and Fig. 5.18e. Again it can be seen that there is an increase in signal amplitude when people enter and work inside the ICV. There are only two clear rate spikes with many small pulses around the times when people enter and leave

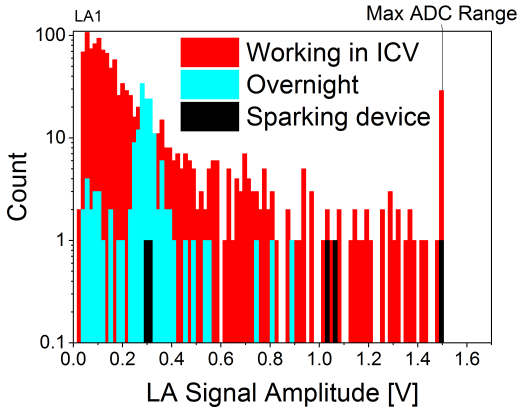

Figure 5.17: Signal amplitude for LA1 during different data-taking periods.

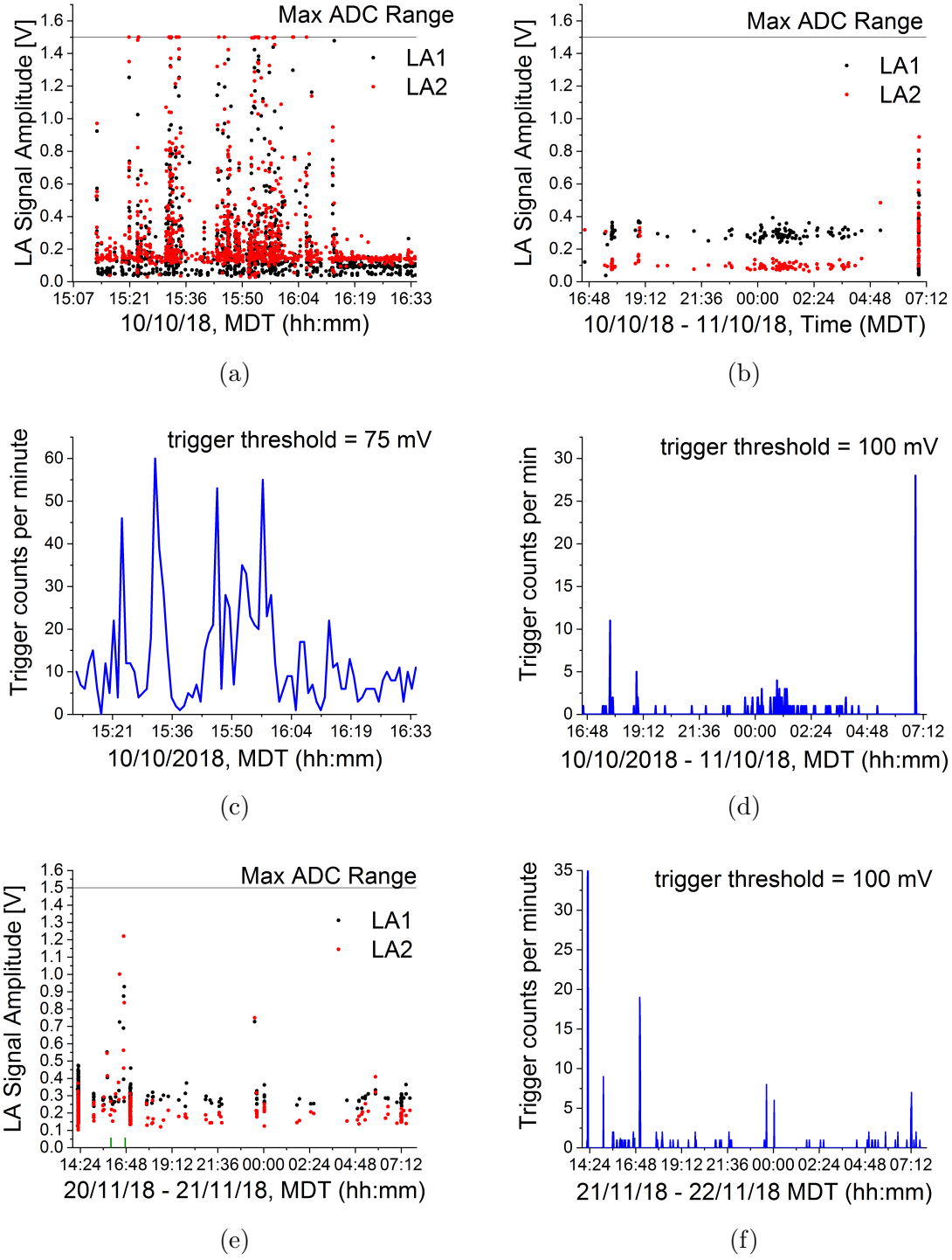

Figure 5.18: Loop antenna signal amplitude and trigger rate while shifters were working in the ICV (a,c) and overnight (b,d). Loop antenna trigger signal amplitude (f) and trigger rate (e) after implementation of mitigation methods against static charge built-up. Work was done in the clean room between 16:00 and 16:45.

the cleanroom. This is likely due to equipment being switched on and off. Most of the data consists of small sparks of comparable amplitude to the overnight data from October. However, the triggering rate has decreased, as well as the number of large pulses. Therefore, it shows that the measures taken were effective. The loop antenna was the first sensor on LZ to give useful data on the conditions of the detector during assembly. It has shown that the loop antennae work well and are a useful tool for monitoring of the EM environment of the detector.

5.5 Readout electronics and triggering

5.5.1 Readout electronics

The purpose-built loop antenna readout-board, Fig. 5.19, can read out 4 antennae simultaneously. The four loop antennae on the top and four on the bottom share a board, respectively. The loop antenna board samples at 200 MHz and has a differential readout. It has a 14-bit digitiser and a dynamic range from $-0.75\,\mathrm{V}$ to $+0.75\,\mathrm{V}$. The cards are installed directly onto the feedthrough flanges of the breakout boxes with the feedthrough flanges providing the only ground reference point. This design was chosen to protect from EMI interference and maintain the integrity of the grounding. The board communicates to slow control via an Ethernet connection.

5.5.2 Adaptive trigger

A crucial part of data taking with the LZ loop antennae is the event triggering. The loop antenna is primarily intended to detect partial discharges or HV breakdowns. It can give supplementary information about EM noise levels and interferences inside the inner cryostat vessel. These are events which should be recorded. Most of the time, it is expected that the loop antennae would not pick up anything, and therefore, only white noise would be recorded. At 200 MHz readout, a large amount of data

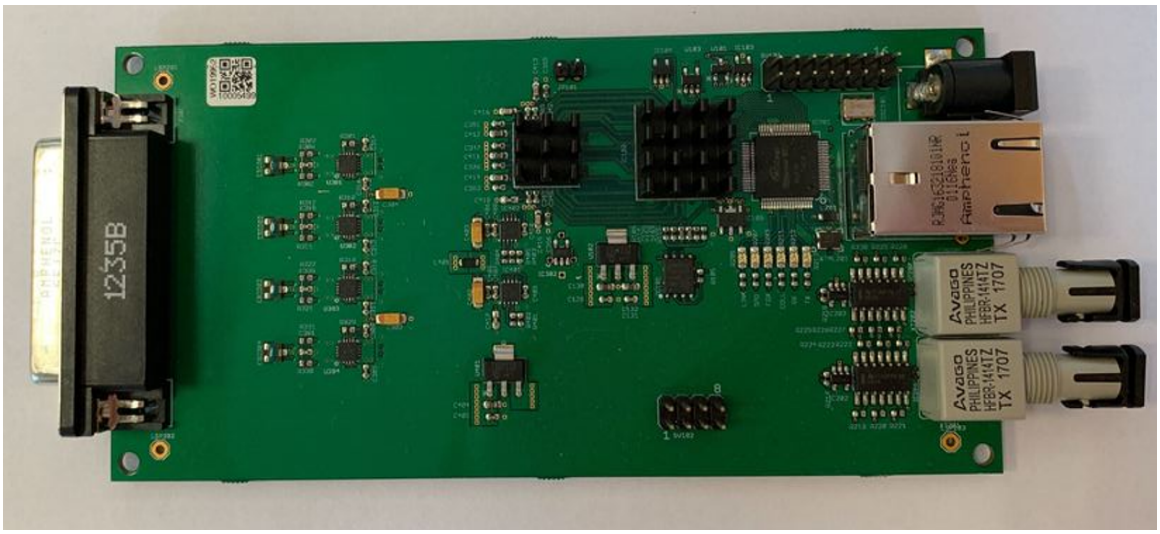

Figure 5.19: 4-channel loop antenna board.

could accumulate quickly. It can, therefore, be seen how important an efficient loop antenna trigger is.

The sparking signal is discussed in detail in section 5.3. It has a fast rise time and an exponential fall and has a substructure of fast (MHz) oscillations. The duration of a typical sparking event is less than 1 µs. However, it has to be considered that often several sparks occur shortly after another, and the entire discharge event has a duration of several microseconds as seen at the System Test.

Typical noise events are bipolar spikes of varying amplitudes. Such a noise event, for example, occurs if a power supply nearby is switched on. A more problematic type of noise event is a periodic interference, as it was seen in system test data. Such regular interference can lead to high trigger rates. While cross-talk and elevated noise levels are information of interest, a few records are entirely sufficient to inform about it. At the System Test, it was seen that such interferences often change amplitude over time. The triggering algorithm described in the following was developed to adapt to new noise levels quickly while sparking events should not affect the trigger threshold considerably. As the algorithm is to be implemented in the FPGA of the front-end electronics, it needs to be fast and straightforward to implement.

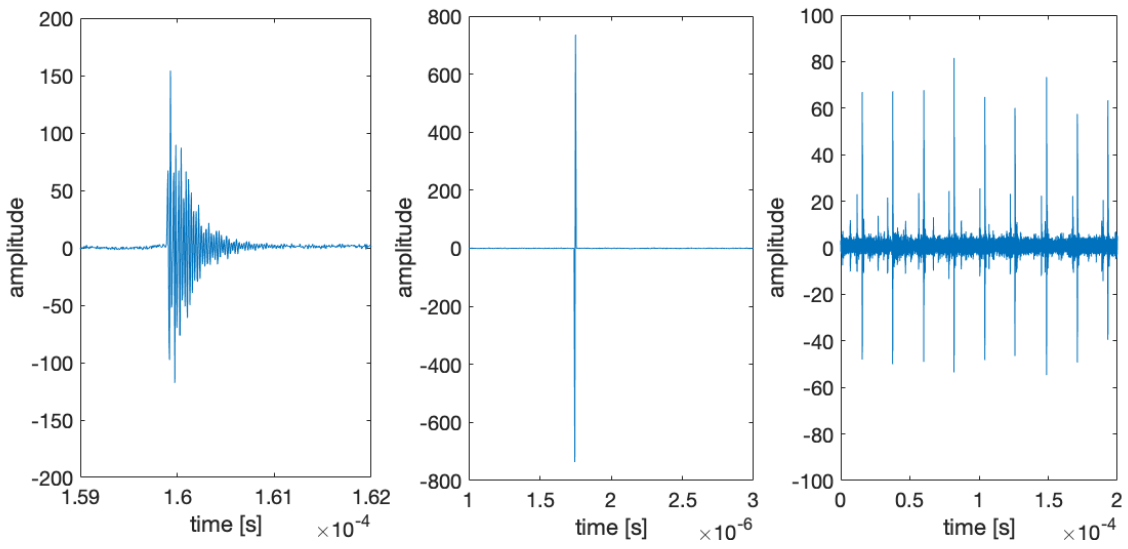

Figure 5.20: Left: Sparking signal type pulse. Middle: Bipolar spike type noise. Right: Periodic interference.

A MATLAB simulation was written to develop and test the loop antenna triggering algorithm. The triggering algorithm is applied to a several microsecond long-baseline trace with white Gaussian noise. Bipolar noise spikes, signal type pulses and periodic interference, as shown in Fig. 5.20 are added to the trace at random. The signal type pulses and periodic interference are taken from recorded loop antenna data and scaled for different signal and background sizes.

As seen previously, the loop antenna signal is bipolar. To enable a more meaningful integration, all negative signs are flipped, and the signal is made completely positive. The positive signal is then sent through a low pass filter with the time constant $\tau = 100\,\text{ns}$. If the filtered signal crosses a set threshold, it triggers data taking for a set number of samples. These steps are shown in Fig. 5.21.

The filtered signal for bipolar noise spikes is considerably smaller than for signal-type pulses. The signal pulse to noise spike discrimination therefore improves. For a constant trigger threshold of 74, no noise events are triggered on (amplitude range 0 to 750 mV), while more than 90% detection efficiency is reached for signals larger than 270 mV.

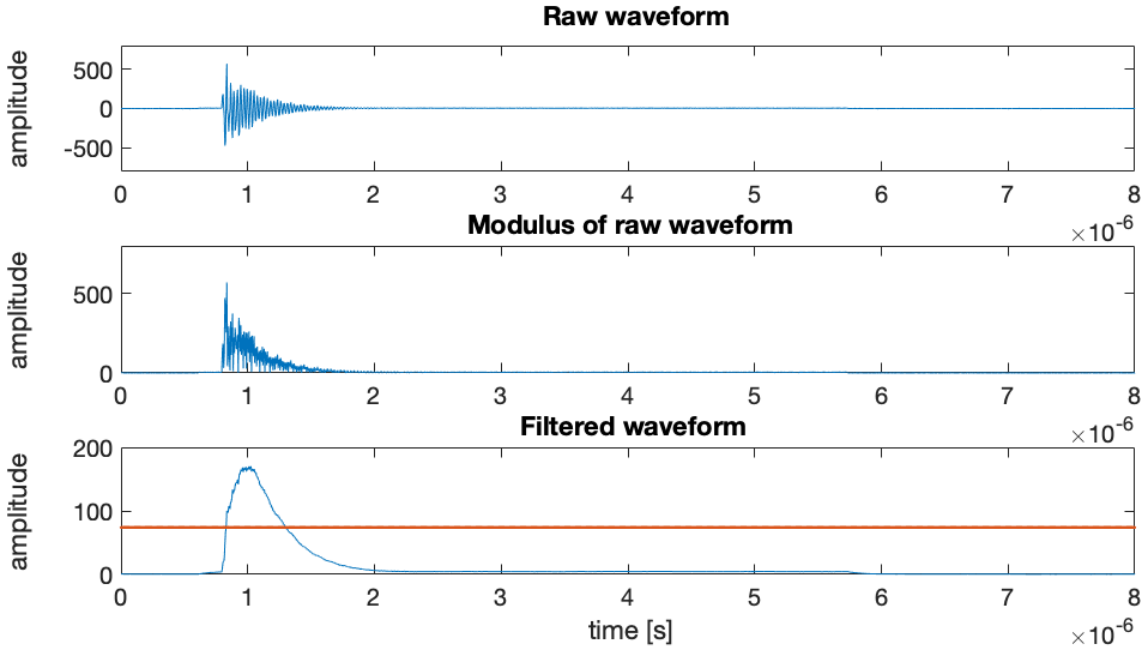

Figure 5.21: Matlab Simulation Event display. The top panel shows the raw waveform. The modulus of the waveform is displayed in the middle panel. In the bottom panel, the modulus of the waveform has been passed through a low pass filter.

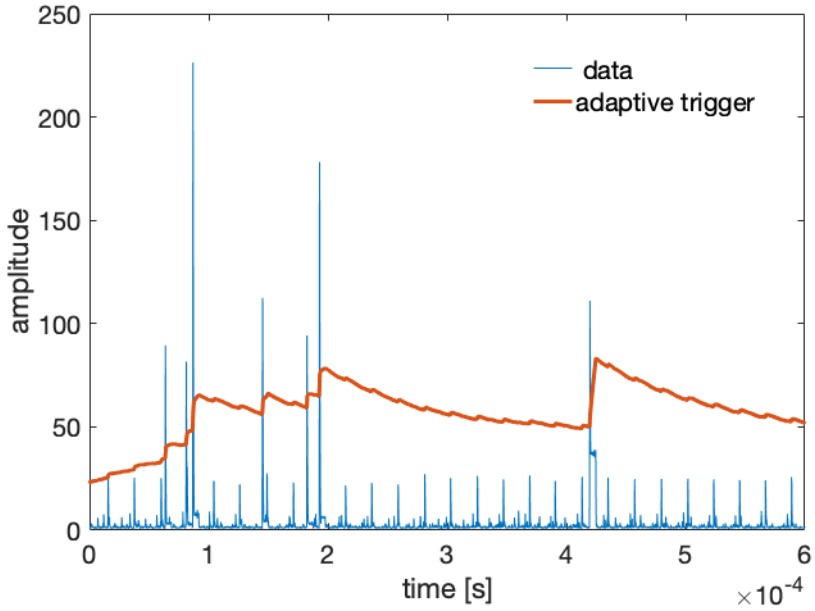

Figure 5.22: MATLAB Simulation Event Display with interference and adaptive trigger.

	Signal ampl. [mV]		
Noise ampl. [mV]	**50 % eff.**	**90% eff.**	**100% eff.**
White noise	80	100	140
10	80	110	140
40	100	130	160
80	130	180	210

Table 5.3: Trigger efficiency results from simulation.

The adaptive part of the trigger is that the threshold level is evaluated for each data point. For this purpose, a low-pass filter with a long time constant ($\tau = 100\,\mu s$) is used. The long time constant ensures that pulse features are smoothed and one-off sparking events do not increase the threshold drastically, while periodic interference pushes up the threshold. The threshold for the current data point is the result of the low-pass filter at the previous data point multiplied by a scaling factor and added to a constant minimum threshold, which ensures that the threshold never falls below a certain minimum. Fig. 5.22 shows an example of how the trigger level adapts to interference and signal pulses.

100,000 signal traces with periodic interference of fixed amplitude and randomly added sparking signals were simulated. For each event the signal amplitude and whether it was triggered on was recorded. For a periodic interference with a period of 25 µs, the trigger takes 40 µs (8000 samples) to adapt to new noise levels. After this adaption period, there are no triggers on noise. The amplitudes at which 50, 90 and 100% trigger efficiencies are reached are recorded in Table 5.3.

5.5.3 Information extraction

During LZ operations the loop antennae provide information about the current condition of the experiment via a MODBUS interface to slow control. The parameters which are supplied were chosen to indicate current noise levels, trigger rates and signal size. Additionally, the waveforms are recorded at 100 MHz sampling rate for later

Parameter	**Unit**	**Information**
trigger threshold level	mVs	current noise levels and sensitivity of triggering
trigger count	count per second	number of events of interest
filtered signal*	mV	short pulse or spark like
maximum amplitude*	mV	magnitude of the event

Table 5.4: Loop antenna parameters to be provided to slow control. Parameters with * are only provided for triggered events.

offline analysis.

From the testing of the prototype loop antenna in section 5.3 and the development of the triggering algorithm discussed in the previous section the parameters in Table 5.4 were chosen for live monitoring of detector conditions. For each period, the trigger threshold level and trigger count are provided. These two variables indicate the current noise levels and whether any potential sparks occurred. For each triggered event, the integrated signal and its maximum amplitude are provided. The integrated signal gives a good indication on whether it was a sparking event, and the maximum amplitude is a good measure of the pulse size. The amplitude can be related to the magnitude of the EM field inducing the response in the antenna using the antenna factor calibration. These parameters can be monitored in slow control. Abnormal conditions are defined as high trigger levels for several minutes accompanied by large amplitudes of the filtered event traces. This allows quick identification of critical detector conditions. The high voltage can be reduced before sensitive detector components are damaged. Additionally, the waveforms are saved for further offline analysis. In this form, they can give valuable information to veto light detected due to sparking.

5.6 Conclusion

The LZ loop antenna is the first dedicated HV-discharge sensor for an LXe TPC experiment. Such a sensor is needed in LZ to be able to react to periods of HV instability, protect sensitive detector elements such as PMTs and veto light from sparking in later analysis. The loop antenna has many properties which make its use in LZ advantageous. It has only low levels of natural radioactivity, can be operated reliably at cryogenic temperatures and provides good coverage of the detector due to its omnidirectional radiation pattern. Tests of sparking in air and operating the loop antenna at the SLAC system test have shown that it is very sensitive to EM fields from small discharges. These tests have provided knowledge about the typical event topology of a detected spark. The final design has an optimised grounding scheme allowing for reliable performance in detector environments. The antenna factor, relating the measured loop antenna response to the magnitude of the EM field inducing the response, has been measured. An adaptive trigger and signal parameterisation have been developed to provide vital information to slow control. The loop antenna has already provided useful information about the EM environment at the SLAC System Test and during the installation of the LZ Bottom Side Skin at SURF.

Chapter 6

Conclusion and Outlook

This thesis has presented the contributions of the author to hardware, software and detector modelling during the design and construction phase of the LZ experiment. The construction is now nearing its completion. Assembly of the inner detector components will be completed shortly before transporting the detector underground.

The loop antennae system presented in this thesis was one of the first subsystems to be installed on the detector. As first dedicated HV-discharge sensor in an LXe TPC experiment, it was essential to develop a radio-pure sensor which provides reliable and useful information during detector operation. The loop antenna performance has been characterized using laboratory tests, analytic calculations and simulations. The design and triggering of the loop antenna were optimised for operation in a detector environment. The four bottom loop antennae have already provided useful data, monitoring EM discharges in the cleanroom in which the detector was assembled.

The loop antenna system will be an essential source of information during the commissioning of the high voltage systems in the detector, giving a prompt indication of HV discharges. It allows quick adjustments to the high voltage settings and reduces the danger of permanent damage in the detector. During long-term operation, the reduced loop antenna data will provide useful information to veto events

during periods of HV instability and light emission due to sparking.

Looking further into the future, a possible third-generation LXe detector on the 50 to 100 t scale is being discussed at the moment. Such a detector would require even higher voltages than LZ to reach an electron drift field of the required magnitude. It will, therefore, become even more essential to monitor this detector for HV discharges. It would be interesting to see how an array of antennae could provide detailed information.

For LZ, critical next steps towards the end of construction of the detector are the final acceptance tests. The simulation study presented in Chapter 4 informs the criteria for the acceptance of the PMT arrays, providing comprehensive information on whether the number and location of non-working PMTs are sufficiently problematic to open up the detector again. The study has shown that bottom array PMTs are essential for excellent detection efficiencies of low energy recoils, while top array PMTs at large radii are essential for background reduction.

With data taking approaching rapidly, it is critical that not only the hardware is in good shape, but analysis tools need to be ready, too. The work on single photon PMT signals presented in this thesis is essential for this preparation. Improvements to the PMT response simulation were made by including noise and undersized signals. Noise in the form of dark counts and afterpulsing need to be considered when developing data analysis tools prior to data taking. A model of the single photon response including undersized PMT pulses has been developed and implemented, informed by data taken with spare LZ PMTs. It has been shown that such signals have a significant impact on energy resolution and detection efficiency. First-dynode hits are especially interesting, as they could lead to an improved detection efficiency for low energy events. The measurement of the first dynode hits in the tests presented has suffered from electronic pick-up noise. Reducing the noise by improved grounding and isolation of the HV supplies could allow a better measurement of the first dynode

hits. Such a measurement is essential to quantify the fraction of first dynode hits and get a better estimate of the improvement of detection efficiencies of low energy events.

LZ is expected to start taking data in 2020. It is in an excellent position to push down further into the dark of the WIMP parameter space than any experiment before. Maybe it will even catch a first glimpse of the elusive dark matter.

Glossary

BACCARAT	BACCARAT is the main LZ simulation using the GEANT4 and NEST packages to simulate particle interactions in the detector.
DER	Detector Electronics Response Simulation is used to convert the BACCARAT output into waveforms as recorded by the LZ DAQ. It simulated the PMTs, cables and front-end electronics.
DPE	The double photoelectron effect describes the probability of two photoelectrons being emitted from a photocathode after absorption of a single photon.
ES	Photoelectrons can backscatter elastically off the first dynode or the metal structures around the first dynode. This leads to delayed undersized pulses.

FDH	There is a non-zero probability that photons get transmitted through the photocathode, imping on the first dynode and initiate the emission of a photoelectron on the first dynode. This effect results in early, undersized pulses referred to as first dynode hits.
ICV	Inner Cryostat Vessel housing the TPC and Skin detectors.
IES	Photoelectrons can backscatter inelastically off the first dynode or the metal structures around the first dynode. This leads to delayed pulses.
LCE	Light collection efficiency in the LZ detector. It is distinguished between scintillation LCE (g_1) and electroluminescence LCE ($g_{1,gas}$).
LRFs	Light response function used by Mercury. See Mercury for more details.
LUX	Large Underground Xenon (LUX) experiment was a two-phase liquid xenon TPC running from 2013-2015 in the Homestake mine, South Dakota. It is the direct predecessor experiment to LZ.
LZap	LZap is the LZ event reconstruction framework.

MDC-2	Mock Data Challenge 2 was a collaboration wide challenge to analyse simulation data representing the first 6 months of LZ data taking.
Mercury	Position reconstruction algorithm previously used in LUX and now being prepared for LZ. Light response functions are used to predict the response of each PMT for interactions at an arbitrary distance from that PMT. The algorithm uses an iterative method to minimise all LRFs at the same time.
NEST	The Noble Liquid Simulation Technique models underlying micro-physics in noble liquids using a semi-empirical collectin of models verified using calibration data from previous experiments.
OCV	Outer Cryostat Vessel housing the ICV.
PLR	Probability Likelihood Ratio method.
PMT	Photomulitplier Tubes are very sensitive light detectors. A photon gets converted to a photoelectron on the photocathode. The photoelectron is subsequently multiplied using a chain of dynodes. The charge is collected and read out from the anode. For a detailed discussion see Chapter 3.

QE	Quantum Efficiency describes the probability that a photon impinging onto a PMT initiates a response in said PMT.
SDC	A photoelectron can miss the first dynode completely or scatter of it at high speed to be directly collected on the second dynode. This results in early undersized pulses.
SPE	Single photoelectron emitted from a PMT photocathode after absorption of a single photon.
SPE resolution	Measure of the width of the SPE peak in the PMT area response spectrum. A Gaussian is fitted to the peak, and the resolution can be calculated as $\frac{\sigma}{\mu}$.
TPC	A time-projection chamber is a type of detector which uses electric fields to allow 3D event localisation. In LZ the TPC is the central part of the detector containing the active xenon volume. A detailed overview is given in Chapter 2.

References

[1] G. Bertone and D. Hooper. A History of Dark Matter. pages 1–88 (2016). URL http://arxiv.org/abs/1605.04909. 1605.04909.

[2] T. E. H. T. Collaboration. First M87 Event Horizon Telescope Results. I. The shadow of the Supermassive Black Hole. *The Astrophysical Journal Letters*, 875(L1):17pp (2019). ISSN 20418213. doi:10.3847/2041-8213/ab0c96. URL https://iopscience.iop.org/article/10.3847/2041-8213/ab0c96.

[3] V. C. Rubin and J. Ford, W. Kent. Rotation of the Andromeda Nebula from a Spectroscopic Survey of Emission Regions. *The Astrophysical Journal*, 159:379 (1970). ISSN 0004-637X. doi:10.1086/150317. URL http://adsabs.harvard.edu/doi/10.1086/150317.

[4] G. Bertone, D. Hooper, and J. Silk. Particle dark matter: Evidence, candidates and constraints. *Physics Reports*, 405(5-6):279–390 (2005). ISSN 03701573. doi:10.1016/j.physrep.2004.08.031.

[5] A. Sorgho, et al. Early observations of the MHONGOOSE galaxies: Getting ready for MeerKAT. *Monthly Notices of the Royal Astronomical Society*, 482(1):1248–1269 (2019). ISSN 13652966. doi:10.1093/mnras/sty2785. arXiv:1810.05467v1.

[6] W. J. G. de Blok, et al. Mass Density Profiles of LSB Galaxies. (2001):1–6 (2001). doi:10.1086/320262. URL http://dx.doi.org/10.1086/320262.0103102.

[7] K. Begeman, A. Broeils, and R. Sanders. Extended rotation curves of spiral galaxies: dark haloes and modified dynamics. *Mon. Not. R. astr. Soc.*, pages 523–537 (1991).

[8] F. Zwicky. On the masses of nebulae and of clusters of nebulae. *The Astrophysical Journal*, 86(3):217–246 (1937).

[9] D. Clowe, et al. A direct empirical proof of the existence of dark matter. *The Astrophysical Journal*, (648):L109–L113 (2006). ISSN 0004-637X. doi:10.1086/508162. URL http://arxiv.org/abs/astro-ph/0608407{%}0Ahttp://dx.doi.org/10.1086/508162. astro-ph/0608407.

[10] Planck Collaboration:, et al. Planck 2018 results. VI. Cosmological parameters. pages 1–71 (2018). arXiv:1807.06209v1.

[11] S. Dodelson. *Modern Cosmology*. Academic Press, San Diego (2003).

[12] P. C. Y. Akrami, et al. Planck 2018 results. I. Overview, and the cosmological legacy of Planck (2018). arXiv:1807.06205v1.

[13] P. Collaboration, et al. Planck 2018 results. I. Overview and the cosmological legacy of Planck (2018). 1807.06205.

[14] C. Baugh. Correlation Function and Power Spectra in Cosmology. In P. Murdin (editor), *Encyclopedia of Astronomy & Astropphysics*. Institute of Physics Publishing.

[15] D. S. Aguado, et al. The Fifteenth Data Release of the Sloan Digital Sky Surveys : First Release of MaNGA- derived Quantities , Data Visualization Tools , and

Stellar Library. *The Astrophysical Journal Supplement Series*, 240(23):25pp (2019). doi:10.3847/1538-4365/aaf651.

[16] C. S. Frenk and S. D. M. White. Dark matter and cosmic structure. *Annalen der Physik*, 524(9-10):507–534 (2012). ISSN 00033804. doi:10.1002/andp.201200212.

[17] J. Navarro, C. S. Frenk, and S. D. M. White. The Structure of Cold Dark Matter Halos (1995). 9508025.

[18] S. D. M. White, C. S. Frenk, and M. Davis. Clustering in a neutrino-dominated universe. *The Astrophysical Journal*, 274(1):1–5 (1983).

[19] S. Dodelson and L. M. Widrow. Sterile neutrinos as dark matter. *Phys. Rev. Lett.*, 72:17–20 (1994). doi:10.1103/PhysRevLett.72.17. URL https://link.aps.org/doi/10.1103/PhysRevLett.72.17.

[20] B. W. Lee and S. Weinberg. Cosmological lower bound on heavy-neutrino masses. *Phys. Rev. Lett.*, 39:165–168 (1977). doi:10.1103/PhysRevLett.39.165. URL https://link.aps.org/doi/10.1103/PhysRevLett.39.165.

[21] G. Jungman, M. Kamionkowski, and K. Griest. Supersymmetric dark matter. *Physics Reports*, 267(5-6):195–373 (1996). ISSN 03701573. doi:10.1016/0370-1573(95)00058-5. URL http://www.sciencedirect.com/science/article/pii/0370157395000585. 9506380.

[22] M. Schmaltz and D. Tucker-Smith. Little Higgs Review. (3):1–44 (2005). doi:10.1146/annurev.nucl.55.090704.151502. URL http://arxiv.org/abs/hep-ph/0502182{%}0Ahttp://dx.doi.org/10.1146/annurev.nucl.55.090704.151502. 0502182.

[23] D. Hooper and S. Profumo. Dark matter and collider phenomenology of universal extra dimensions. *Physics Reports*, 453(2-4):29–115 (2007). ISSN 03701573. doi:10.1016/j.physrep.2007.09.003. 0701197v2.

[24] R. D. Peccei and H. R. Quinn. CP Conservation in the Presence of Pseudoparticles. *Physical Review Lett*, 38(25):1440–1443 (1977).

[25] L. D. Duffy and K. van Bibber. Axions as dark matter particles. *New Journal of Physics*, 11(10):105008 (2009). doi:10.1088/1367-2630/11/10/105008. URL https://doi.org/10.1088%2F1367-2630%2F11%2F10%2F105008.

[26] N. Du, et al. Search for invisible axion dark matter with the axion dark matter experiment. *Phys. Rev. Lett.*, 120:151301 (2018). doi:10.1103/PhysRevLett.120.151301. URL https://link.aps.org/doi/10.1103/PhysRevLett.120.151301.

[27] L. Visinelli and P. Gondolo. Dark matter axions revisited. *Physical Review D*, 80:035024 (2009). doi:10.1103/PhysRevD.80.035024.

[28] D. Jackson Kimball, S. Afach, and D. Aybas. Overview of the Cosmic Axion Spin Precession Experiment (CASPEr) (2018). URL https://arxiv.org/abs/1711.08999.

[29] D. Akerib, et al. First Searches for Axions and Axion-Like Particles with the LUX Experiment. *Phys. Rev. Lett.*, 118 (2017). doi:10.1103/PhysRevLett.118.261301. URL https://arxiv.org/abs/1704.02297.

[30] E. Armengaud, et al. Axion searches with the EDELWEISS-II experiment. *Journal of Cosmology and Astroparticle Physics*, 2013(11):067–067 (2013). doi:10.1088/1475-7516/2013/11/067. URL https://doi.org/10.1088%2F1475-7516%2F2013%2F11%2F067.

[31] Z. Ahmed, et al. Search for axions with the cdms experiment. *Phys. Rev. Lett.*, 103:141802 (2009). doi:10.1103/PhysRevLett.103.141802. URL https://link.aps.org/doi/10.1103/PhysRevLett.103.141802.

[32] R. Ansari. EROS : a Galactic Microlensing Odyssey. (July):1–9 (2004). 0407583v1.

[33] C. Alcock, et al. The MACHO Project: Microlensing Results from 5.7 Years of LMC Observations. *The Astrophysical Journal*, 542:281–307 (2000). 0001272v1.

[34] LIGO Scientific Collaboration and Virgo Collaboration. Astrophysical Implications of the Binary Black-Hole Merger GW150914. 22 (2016). doi:10.3847/2041-8205/818/2/L22. URL http://arxiv.org/abs/1602.03846{%}0Ahttp://dx.doi.org/10.3847/2041-8205/818/2/L22. 1602.03846.

[35] A. Kashlinsky. LIGO gravitational wave detection, primordial black holes and the near-IR cosmic infrared background anisotropies. *The Astrophysical Journal Letters*, 823(2):1–6 (2016). ISSN 2041-8213. doi:10.3847/2041-8205/823/2/L25. URL http://arxiv.org/abs/1605.04023{%}0Ahttp://dx.doi.org/10.3847/2041-8205/823/2/L25. 1605.04023.

[36] K. Freese. Status of Dark Matter in the Universe. In *WSPC*, January 2017, pages 1–32 (2017). ISSN 0218-2718. doi:10.1142/S0218271817300129. URL http://arxiv.org/abs/1701.01840. 1701.01840.

[37] F. Kahlhoefer. Review of LHC dark matter searches. *International Journal of Modern Physics A*, page 1730006 (2017). ISSN 0217-751X. doi:10.1142/S0217751X1730006X. URL http://arxiv.org/abs/1702.02430{%}5Cnhttp://www.worldscientific.com/doi/abs/10.1142/S0217751X1730006X. 1702.02430.

[38] M. Aaboud, et al. Constraints on mediator-based dark matter and scalar dark energy models using $sqrts = 13\,\mathrm{TeV}$ pp collision data collected by the ATLAS detector. *Journal of High Energy Physics*, 2019(5):142 (2019). ISSN 1029-8479. doi:10.1007/JHEP05(2019)142. URL `http://link.springer.com/10.1007/JHEP05(2019)142`.

[39] M. W. Goodman and E. Witten. Detectability of certain dark-matter candidates. *Physical Review D*, 31(12):3059–3063 (1985). ISSN 05562821. doi:10.1103/PhysRevD.31.3059.

[40] A. M. Green. Astrophysical uncertainties on the local dark matter distribution and direct detection experiments. (3):1–10 (2017). `arXiv:1703.10102v2`.

[41] J. D. Lewin and P. F. Smith. Review of mathematics, numerical factors, and corrections for dark matter experiments based on elastic nuclear recoil. *Astroparticle Physics*, 6(1):87–112 (1996). ISSN 09276505. doi:10.1016/S0927-6505(96)00047-3.

[42] C. Savage, et al. Compatibility of DAMA/LIBRA dark matter detection with other searches in light of new galactic rotation velocity measurements. *Journal of Cosmology and Astroparticle Physics*, 2009(9) (2009). ISSN 14757516. doi:10.1088/1475-7516/2009/09/036.

[43] Y. Wu, et al. Uncertainties in Direct Dark Matter Detection in Light of GAIA. 10(3):1–11 (2019). URL `http://arxiv.org/abs/1904.04781`. `1904.04781`.

[44] D. S. Akerib, et al. Calibration, event reconstruction, data analysis and limits calculation for the LUX dark matter experiment. *Physical Review D*, 97(10):102008 (2017). ISSN 24700029. doi:10.1103/PhysRevD.97.102008. URL `http://arxiv.org/abs/1712.05696`. `1712.05696`.

[45] E. Aprile, et al. Dark Matter Search Results from a One Ton-Year Exposure of XENON1T. *Physical Review Letters*, 121(11):1–8 (2018). ISSN 10797114. doi:10.1103/PhysRevLett.121.111302. arXiv:1805.12562v2.

[46] R. Agnese, et al. Results from the Super Cryogenic Dark Matter Search Experiment at Soudan. *Physical Review Letters*, 120(6):61802 (2018). ISSN 10797114. doi:10.1103/PhysRevLett.120.061802. URL https://doi.org/10.1103/PhysRevLett.120.061802.

[47] CRESST Collaboration, et al. First results from the CRESST-III low-mass dark matter program. pages 1–9 (2019). URL http://arxiv.org/abs/1904.00498. 1904.00498.

[48] K. Freese, J. Frieman, and A. Gould. Signal modulation in cold-dark-matter detection. *Physical Review D*, 37(12):3388–3405 (1988). ISSN 05562821. doi:10.1103/PhysRevD.37.3388.

[49] R. Bernabei, et al. Final model independent result of DAMA/LIBRA-phase1. *European Physical Journal C*, 73(12):1–11 (2013). ISSN 14346052. doi:10.1140/epjc/s10052-013-2648-7. arXiv:1308.5109v2.

[50] R. Bernabei, et al. First model independent results from DAMA/LIBRA-phase2. pages 1–28 (2018). URL http://arxiv.org/abs/1805.10486. 1805.10486.

[51] G. Adhikari, et al. Search for a dark matter-induced annual modulation signal in NaI(Tl) with the COSINE-100 experiment. pages 1–5 (2019). URL http://arxiv.org/abs/1903.10098. 1903.10098.

[52] J. Amaré, et al. First results on dark matter annual modulation from ANAIS-112 experiment. pages 1–6 (2019). URL http://arxiv.org/abs/1903.03973. 1903.03973.

[53] P. Montini. Dark matter search with the SABRE experiment. pages 5–8 (2018). URL http://arxiv.org/abs/1807.08073. 1807.08073.

[54] R. Agnese, et al. New results from the search for low-mass weakly interacting massive particles with the cdms low ionization threshold experiment. *Phys. Rev. Lett.*, 116:071301 (2016). doi:10.1103/PhysRevLett.116.071301. URL https://link.aps.org/doi/10.1103/PhysRevLett.116.071301.

[55] V. Chepel and H. Araújo. Liquid noble gas detectors for low energy particle physics. *Journal of Instrumentation*, 8(04):R04001–R04001 (2013). ISSN 1748-0221. doi:10.1088/1748-0221/8/04/R04001. URL http://iopscience.iop.org/1748-0221/8/04/R04001.

[56] P. A. Amaudruz, et al. First Results from the DEAP-3600 Dark Matter Search with Argon at SNOLAB. *Physical Review Letters*, 121(7):1–9 (2018). ISSN 10797114. doi:10.1103/PhysRevLett.121.071801. arXiv:1707.08042v2.

[57] P. Agnes, et al. Darkside-50 532-day dark matter search with low-radioactivity argon. *Phys. Rev. D*, 98:102006 (2018). doi:10.1103/PhysRevD.98.102006. URL https://link.aps.org/doi/10.1103/PhysRevD.98.102006.

[58] C. E. Aalseth, et al. DarkSide-20k: A 20 tonne two-phase LAr TPC for direct dark matter detection at LNGS. *European Physical Journal Plus*, 133(3) (2018). ISSN 21905444. doi:10.1140/epjp/i2018-11973-4.

[59] D. S. Akerib, et al. Results from a Search for Dark Matter in the Complete LUX Exposure. *Phys. Rev. Lett.*, 118:021303 (2017). doi:10.1103/PhysRevLett.118.021303. URL https://link.aps.org/doi/10.1103/PhysRevLett.118.021303.

[60] M. Ibe, et al. Migdal effect in dark matter direct detection experiments. *J. High Energ. Phys.*, 194 (2018). doi:10.1007/JHEP03(2018)194. URL https://link.springer.com/article/10.1007.

[61] C. Kouvaris and J. Pradler. Probing Sub-GeV Dark Matter with Conventional Detectors. *Phys. Rev. Lett.*, 118:031803 (2017). doi:10.1103/PhysRevLett.118.031803. URL https://link.aps.org/doi/10.1103/PhysRevLett.118.031803.

[62] D. S. Akerib, et al. Results of a Search for Sub-GeV Dark Matter Using 2013 LUX Data. *Phys. Rev. Lett.*, 122:131301 (2019). doi:10.1103/PhysRevLett.122.131301. URL https://link.aps.org/doi/10.1103/PhysRevLett.122.131301.

[63] M. J. Dolan, F. Kahlhoefer, and C. McCabe. Directly Detecting Sub-GeV Dark Matter with Electrons from Nuclear Scattering. *Phys. Rev. Lett.*, 121:101801 (2018). doi:10.1103/PhysRevLett.121.101801. URL https://link.aps.org/doi/10.1103/PhysRevLett.121.101801.

[64] C. Amole, et al. Dark Matter Search Results from the PICO-2L C_3F_8 Bubble Chamber. *Phys. Rev. Lett.*, 114:231302 (2015). doi:10.1103/PhysRevLett.114.231302. URL https://link.aps.org/doi/10.1103/PhysRevLett.114.231302.

[65] C. Amole, et al. Dark Matter Search Results from the Complete Exposure of the PICO-60 C$_3$F$_8$ Bubble Chamber. pages 1–9 (2019). URL http://arxiv.org/abs/1902.04031. 1902.04031.

[66] J. B. Battat, et al. Low threshold results and limits from the DRIFT directional dark matter detector. *Astroparticle Physics*, 91:65–74 (2017). ISSN 09276505. doi:10.1016/j.astropartphys.2017.03.007.

[67] CYGNO Collaboration. CYGNO: a CYGNUs Collaboration 1 m^3 Module with Optical Readout for Directional Dark Matter Search. (January):3–8 (2019). URL http://arxiv.org/abs/1901.04190. 1901.04190.

[68] J. Aalbers, et al. DARWIN: towards the ultimate dark matter detector. page 36 (2016). ISSN 14757516. doi:10.1088/1475-7516/2016/11/017. URL http://arxiv.org/abs/1606.07001. 1606.07001.

[69] J. Alexander, et al. Dark Sectors 2016 Workshop: Community Report (2016). URL http://arxiv.org/abs/1608.08632. 1608.08632.

[70] E. Aprile and T. Doke. Liquid xenon detectors for particle physics and astrophysics. *Reviews of Modern Physics*, 82(3):2053–2097 (2010). ISSN 00346861. doi:10.1103/RevModPhys.82.2053. 0910.4956v1.

[71] V. N. Lebedenko, et al. Results from the first science run of the ZEPLIN-III dark matter search experiment. *Physical Review D - Particles, Fields, Gravitation and Cosmology*, 80(5):1–14 (2009). ISSN 15507998. doi:10.1103/PhysRevD.80.052010. 0812.1150.

[72] J. Angle, et al. First Results from the XENON10 Dark Matter Experiment at the Gran Sasso National Laboratory. *Phys. Rev. Lett.*, 100:021303 (2008). doi:10.1103/PhysRevLett.100.021303. URL https://link.aps.org/doi/10.1103/PhysRevLett.100.021303.

[73] E. Aprile, et al. Dark Matter Search Results from a One Tonne Year Exposure of XENON1T. (Dm):1–8 (2018). URL http://arxiv.org/abs/1805.12562. 1805.12562.

[74] X. Cui, et al. Dark Matter Results from 54-Ton-Day Exposure of PandaX-II Experiment. *Phys. Rev. Lett.*, 119:181302 (2017). doi:10.1103/PhysRevLett.

119.181302. URL https://link.aps.org/doi/10.1103/PhysRevLett.119.181302.

[75] LZ Collaboration. LUX-ZEPLIN (LZ) Technical Design Report (2017). URL http://arxiv.org/abs/1703.09144. physics.ins-det/1703.09144.

[76] D. Akimov, et al. Observation of coherent elastic neutrino-nucleus scattering. *Science*, 0990(10.1126):1–11 (2017).

[77] J. Birks. *The theory and practice of scintillation counting*. Pergamon Press, 1^{st} edition (1964). ISBN 9781483156064.

[78] C. E. Dahl. *The physics of background discrimination in liquid xenon, and first results from XENON10 in the hunt for WIMP dark matter*. Ph.D. thesis, Princeton University (2009).

[79] P. Sorensen. Electron train backgrounds in liquid xenon dark matter search detectors are indeed due to thermalization and trapping. pages 1–5 (2017). arXiv:1702.04805v1.

[80] J. Lindhard, et al. Integral equations governing radiation effects. *K. Dan Vidensk Selsk. Mat. Fys. Medd.*, 33(10) (1963).

[81] P. Sorensen and C. E. Dahl. Nuclear recoil energy scale in liquid xenon with application to the direct detection of dark matter. *Phys. Rev. D*, 83:063501 (2011). doi:10.1103/PhysRevD.83.063501. URL https://link.aps.org/doi/10.1103/PhysRevD.83.063501.

[82] D. S. Akerib, et al. Low-energy (0.7-74 keV) nuclear recoul calibration of the LUX dark matter experiment using D-D neutron scattering kinematics. pages 1–24 (2016). ISSN 15502368. doi:10.1103/PhysRevD.93.072009. 1512.03133.

[83] N. Ion, et al. Absolute Scintillation Yields in Liquid Argon and Xenon for Various Particles (2002). doi:10.1143/JJAP.41.1538.

[84] E. Aprile, et al. Observation of anticorrelation between scintillation and ionization for MeV gamma rays in liquid xenon. *Physical Review B*, 76(014115):1–7 (2007). doi:10.1103/PhysRevB.76.014115.

[85] D. S. Akerib, et al. Signal yields, energy resolution, and recombination fluctuations in liquid xenon. pages 1–11 (2016). `arXiv:1610.02076v1`.

[86] D. S. Akerib, et al. Projected WIMP sensitivity of the LUX-ZEPLIN (LZ) dark matter experiment. pages 1–16 (2018). URL `http://arxiv.org/abs/1802.06039`. `1802.06039`.

[87] D. S. Akerib, et al. Identification of radiopure titanium for the LZ dark matter experiment and future rare event searches. *Astroparticle Physics*, 96:1–10 (2017). ISSN 09276505. doi:10.1016/j.astropartphys.2017.09.002. `1702.02646`.

[88] Hamamatsu. R11410 Data Sheet (2011).

[89] F. Liao. *Development of Xenon Level Instrumentation for the LZ Dark Matter Detector*. Ph.D. thesis, University of Oxford (2017).

[90] K. Boast. *A Position-Sensing System for the Top PMT Array in the LUX-ZEPLIN Dark Matter Experiment*. Ph.D. thesis, University of Oxford (2017).

[91] C. Carels. *Search for Dark Matter with the LUXZEPLIN Detector Acoustic Sensor Performance and Detector Response*. Ph.D. thesis, University of Oxford (2018).

[92] T. J. Whitis. *Measurement of time projection chamber optical properties and xenon circulation system development of the LZ experiment*. Ph.D. thesis, Case Western Reserve University (2019).

[93] S. Haselschwardt, et al. A liquid scintillation detector for radioassay of gadolinium-loaded liquid scintillator for the lz outer detector. *Nuclear Instruments and Methods in Physics Research Section A: Accelerators, Spectrometers, Detectors and Associated Equipment*, 937:148 – 163 (2019). ISSN 0168-9002. doi:https://doi.org/10.1016/j.nima.2019.05.055. URL http://www.sciencedirect.com/science/article/pii/S0168900219307119.

[94] E. Druszkiewicz. The data acquisition system for LZ. *Journal of Instrumentation*, 11(02):C02072–C02072 (2016). doi:10.1088/1748-0221/11/02/c02072. URL https://doi.org/10.1088%2F1748-0221%2F11%2F02%2Fc02072.

[95] A. Dobi. *Measurement of the electron recoil band of the LUX dark matter detector with a tritium calibration source*. Ph.D. thesis, University of Maryland (2014).

[96] D. S. Akerib, et al. Tritium calibration of the LUX dark matter experiment. *Physical Review D*, 93(7) (2016). ISSN 24700029. doi:10.1103/PhysRevD.93.072009. 1512.03133.

[97] F. Gray, et al. Cosmic ray muon flux at the Sanford Underground Laboratory at Homestake. *Nuclear Instruments and Methods in Physics Research Section A: Accelerators, Spectrometers, Detectors and Associated Equipment*, 638(1):63 – 66 (2011). ISSN 0168-9002. doi:https://doi.org/10.1016/j.nima.2011.02.032. URL http://www.sciencedirect.com/science/article/pii/S016890021100338X.

[98] L. Reichhart, et al. Measurement and simulation of the muon-induced neutron yield in lead. *Astroparticle Physics*, 47:67 – 76 (2013). ISSN 0927-6505. doi:https://doi.org/10.1016/j.astropartphys.2013.06.002. URL http://www.sciencedirect.com/science/article/pii/S0927650513000972.

[99] E. H. Miller, et al. Constraining radon backgrounds in LZ. *AIP Conference Proceedings*, 1921 (2018). ISSN 15517616. doi:10.1063/1.5018996. 1708.08533.

[100] B. Lenardo, et al. A Global Analysis of Light and Charge Yields in Liquid Xenon. 62(6):3387–3396 (2015).

[101] D. S. Akerib, et al. Position Reconstruction in LUX (2017). URL http://arxiv.org/abs/1710.02752. 1710.02752.

[102] G. Cowan, et al. Asymptotic formulae for likelihood-based tests of new physics. *The European Physical Journal C*, 71(2):1554 (2011). ISSN 1434-6052. doi:10.1140/epjc/s10052-011-1554-0. URL https://doi.org/10.1140/epjc/s10052-011-1554-0.

[103] D. S. Akerib, et al. First searches for axions and axionlike particles with the lux experiment. *Phys. Rev. Lett.*, 118:261301 (2017). doi:10.1103/PhysRevLett.118.261301. URL https://link.aps.org/doi/10.1103/PhysRevLett.118.261301.

[104] R. F. Lang, et al. Supernova neutrino physics with xenon dark matter detectors: A timely perspective. 103009:18 (2016). ISSN 15502368. doi:10.1103/PhysRevD.94.103009. URL http://arxiv.org/abs/1606.09243. 1606.09243.

[105] A. Fieguth, et al. Search for double β-decays of ^{124}Xe with XENON100. *Journal of Physics: Conference Series*, 888(012251) (2017).

[106] E. Aprile, J. Aalbers, and F. Agostini. Observation of two-neutrino double electron capture in $ˆ{124}{ Xe}$ with XENON1T. *Nature*, (568):532–535 (2019). doi:10.1038/s41586-019-1124-4.

[107] K. Lung, et al. Characterization of the Hamamatsu R11410-10 3-in. photomultiplier tube for liquid xenon dark matter direct detection experiments. *Nuclear Instruments and Methods in Physics Research, Section A: Accelerators, Spectrometers, Detectors and Associated Equipment*, 696:32–39 (2012). ISSN 01689002. doi:10.1016/j.nima.2012.08.052. URL http://dx.doi.org/10.1016/j.nima.2012.08.052. 1202.2628.

[108] L. Baudis, A. Behrens, and A. Ferella. Performance of the Hamamatsu R11410 photomultiplier tube in cryogenic xenon environments. *Journal of Instrumentation*, page 16 (2013). ISSN 1748-0221. doi:10.1088/1748-0221/8/04/P04026. URL http://iopscience.iop.org/1748-0221/8/04/P04026. 1303.0226.

[109] A. Lyashenko, et al. Measurement of the absolute Quantum Efficiency of Hamamatsu model R11410-10 photomultiplier tubes at low temperatures down to liquid xenon boiling point. *Journal of Instrumentation*, 9(11):P11021–P11021 (2014). ISSN 1748-0221. doi:10.1088/1748-0221/9/11/P11021. URL http://stacks.iop.org/1748-0221/9/i=11/a=P11021?key=crossref.1a1dae5669aa6dfbcef17e14a34143b0.

[110] L. Baudis, et al. Measurements of the position-dependent photo-detection sensitivity of the Hamamatsu R11410 and R8520 photomultiplier tubes (2015). URL http://arxiv.org/abs/1509.04055. 1509.04055.

[111] P. Barrow, et al. Qualification Tests of the R11410-21 Photomultiplier Tubes for the XENON1T Detector (2016). URL http://arxiv.org/abs/1609.01654. astro-ph.IM/1609.01654.

[112] B. L. Paredes, et al. Response of photomultiplier tubes to xenon scintillation light. *Astroparticle Physics*, 102:56 – 66 (2018). ISSN 0927-6505.

doi:https://doi.org/10.1016/j.astropartphys.2018.04.006. URL http://www.sciencedirect.com/science/article/pii/S0927650518300173.

[113] C. H. Faham, et al. Measurements of wavelength-dependent double photoelectron emission from single photons in VUV-sensitive photomultiplier tubes. *Jinst*, 10(P09010) (2015). ISSN 17480221. doi:10.1088/1748-0221/10/09/P09010. physics.ins-det/1506.08748.

[114] D. Akimov, et al. Performance of Hamamatsu R11410-20 PMTs under intense illumination in a two-phase cryogenic emission detector. *Journal of Instrumentation*, 11(12):P12005–P12005 (2016). ISSN 1748-0221. doi:10.1088/1748-0221/11/12/P12005. URL http://stacks.iop.org/1748-0221/11/i=12/a=P12005?key=crossref.b466c6fa3d94ed476c16a2938328bf8f.

[115] F. Kaether and C. Langbrandtner. Transit time and charge correlations of single photoelectron events in R7081 photomultiplier tubes. *Journal of Instrumentation*, 7(09):P09002–P09002 (2012). ISSN 1748-0221. doi:10.1088/1748-0221/7/09/P09002. URL http://stacks.iop.org/1748-0221/7/i=09/a=P09002?key=crossref.56e89f1635778de509934da9718ce26d. physics.ins-det/1207.0378v1.

[116] I. Fedorko, S. Tokar, and I. Chirikov-Zorin. Simulation of photomultiplier response. In *ATL-TILECAL-99-012*, pages 1–17 (1999). URL http://cds.cern.ch/record/683884.

[117] W. E. Spicer and A. Herrera-Gomez. Modern theory and applications of photocathodes. *Proceedings of SPIE*, 2022(International Symposium on Optics, Imaging and Instrumentation):18–35 (1993). ISSN 0277786X. doi:10.1117/12.158575. URL https://proceedings.spiedigitallibrary.org/proceeding.aspx?doi=10.1117/12.158575.

[118] Hamamatsu Photonics K. K. *Photomultiplier Tubes: Basics and Applications*. Hamamatsu Photonics K. K., third edition (2006). ISBN 9780819463524. doi:10.1117/3.682726.p35. URL papers://a18bb931-cf28-45a2-890e-68a459b787f5/Paper/p342.

[119] A. G. Wright. *The Photomultiplier Handbook*. Oxford University Press, Oxford (2017). ISBN 9780199565092.

[120] P. B. Coates. Photomultiplier collection efficiencies and nonpoissonian pulse height distributions. *Journal of Physics D: Applied Physics*, 6(2):153–163 (1973). ISSN 00223727. doi:10.1088/0022-3727/6/2/303.

[121] T. Takahashi, et al. Emission spectra from Ar-Xe, Ar-Kr, Ar-N2, Ar-CH4, Ar-CO2 and Xe-N2 gas scintillation proportional counters. *Nuclear Instruments and Methods in Physics Research*, 205(3):591–596 (1983). ISSN 0167-5087. doi:10.1016/0167-5087(83)90028-5. URL https://www.sciencedirect.com/science/article/pii/0167508783900285?via{%}3Dihub.

[122] F. Neves, et al. ZE3RA: the ZEPLIN-III Reduction and Analysis package. *Journal of Instrumentation*, 6(11):P11004–P11004 (2011). ISSN 1748-0221. doi:10.1088/1748-0221/6/11/P11004. URL http://stacks.iop.org/1748-0221/6/i=11/a=P11004?key=crossref.99995c76e4a4367139a25d547e7e0620. 1106.0808.

[123] C. Carels, et al. LZUK Milestone and Deliverable Completion Report on DER (2016). Internal Document.

[124] ET Enterprises. Understanding photomultipliers (2011). URL http://www.et-enterprises.com/files/file/Understanding-photomultipliers.pdf.

[125] E. I. Shubnikov and F. M. Subbotin. On the shape of the one-electron pulse from a photoelectro multiplier. *Translated from Pribory i Tekhnika Éksperimenta*, 1(January - February):179–180 (1973).

[126] K. Fujii, et al. High-accuracy measurement of the emission spectrum of liquid xenon in the vacuum ultraviolet region. *Nuclear Instruments and Methods in Physics Research Section A: Accelerators, Spectrometers, Detectors and Associated Equipment*, 795:293 – 297 (2015). ISSN 0168-9002. doi:https://doi.org/10.1016/j.nima.2015.05.065. URL http://www.sciencedirect.com/science/article/pii/S016890021500724X.

[127] HAMAMATSU. R5912 Data Sheet (2000).

[128] X. Bai, et al. Extending light WIMP searches to single scintillation photons in LUX. pages 1–11 (2019). arXiv:1907.06272v1.

[129] D. S. Akerib, et al. Liquid xenon scintillation measurements and pulse shape discrimination in the LUX dark matter detector. *Physical Review D*, 97(11):1–16 (2018). ISSN 24700029. doi:10.1103/PhysRevD.97.112002. 1802.06162.

[130] E. Aprile, et al. First Dark Matter Search Results from the XENON1T Experiment. pages 6–11 (2017). ISSN 0031-9007. doi:10.1103/PhysRevLett.119.181301. URL http://arxiv.org/abs/1705.06655{%}0Ahttp://dx.doi.org/10.1103/PhysRevLett.119.181301. 1705.06655.

[131] B. Bolotovskii. Vavilov Cherenkov radiation : its discovery and application. *Phys.-Usp.*, 62(11):1099–1110 (2009). doi:10.3367/UFNe.0179.200911c.1161.

[132] J. E. Y. Dobson, P. Beltrame, and A. S. J. Murphy. The impact of Cerenkov light generating mechanisms on LZ. Technical report (2014).

[133] B. Gaythe. *Impact of Coincident Backgrounds on the LZ WIMP Dark Matter Search.* MSci Physics Project Report, year = 2019, University College London.

[134] E. B. B. Rebel, et al. High Voltage in Noble Liquids for High Energy Physics. *Jounal of instrumentation*, 9(1748-0221):64 (2014). ISSN 17480221. doi:10.1088/1748-0221/9/08/T08004. URL `http://arxiv.org/abs/1403.3613`.

[135] A. Bondiou, G. Labaune, and J. P. Marque. Electromagnetic radiation associated with the formation of an electric breakdown in air at atmospheric pressure. *Journal of Applied Physics*, 61(2):503–509 (1987). ISSN 00218979. doi:10.1063/1.338250.

[136] C. J. Kim. Electromagnetic Radiation Behavior of Low-Voltage Arcing Fault. *IEEE Transactions on power delivery*, 24(1) (2009).

[137] Z. Jin, et al. Two types of compact UHF antennas for partial discharge measurement. *2008 International Conference on High Voltage Engineering and Application, ICHVE 2008*, pages 616–620 (2008). ISSN 10036520. doi:10.1109/ICHVE.2008.4774011.

[138] M. Kanegami, et al. Waveform analysis of partial discharge current in liquid nitrogen immersed insulation. *Proceedings of Conference on Electrical Insulation and Dielectric Phenomena - CEIDP '96*, 2:529–532 (1996). doi:10.1109/CEIDP.1996.564526. URL `http://ieeexplore.ieee.org/lpdocs/epic03/wrapper.htm?arnumber=564526`.

[139] J. Liu, et al. Study on miniaturized UHF antennas for partial discharge detection in high-voltage electrical equipment. *Sensors (Switzerland)*, 15(11):29434–29451 (2015). ISSN 14248220. doi:10.3390/s151129434.

[140] R. L. Mannino. *Measuring backgrounds from ^{85}Kr and ^{210}Bi to improve the sensitivity of dark matter detectors.* Ph.D. thesis, Texas A&M University (2017).

[141] N. McConkey, et al. Cryogenic CMOS cameras for high voltage monitoring in liquid argon. *Journal of Instrumentation*, 12(03):P03014 (2017). ISSN 17480221. doi:10.1088/1748-0221/12/03/P03014. URL `http://stacks.iop.org/1748-0221/12/i=03/a=P03014`.

[142] M. M. Yaacob, et al. Review on partial discharge detection techniques related to high voltage power equipment using different sensors. *Photonic Sensors*, 4(4):325–337 (2014). ISSN 21907439. doi:10.1007/s13320-014-0146-7.

[143] C. a. Balanis. *Antenna Theory Analysis and Design Third Edition*. John Wiley & Sons, Inc., third edition (2005). ISBN 9786468600.

[144] W. L. Stutzman and G. A. Thiele. *Antenna Theory and Design*. John Wiley & Sons, Inc., Danvers, third edition (2013). ISBN 9780470576649.

[145] J. Dobson. Private correspondence (2018).

[146] P. Scovell. LZ Sensors: Component-level radioactivity (2016). Internal Document.

[147] J. Lin. Report on prototype loop antenna sensor (2014). Internal Document.

[148] A. Aykan. Calibration of circular loop antennas. *IEEE Transactions on Instrumentation and Measurement*, 47(2):446–452 (1998). ISSN 00189456. doi:10.1109/19.744189.

[149] M. Neiman. The principle of reciprocity in antenna theory. *Proceedings of the IRE*, 31(12):666–671 (1943). ISSN 0096-8390. doi:10.1109/JRPROC.1943.233683. URL `http://ieeexplore.ieee.org/xpls/abs{_}all.jsp?arnumber=1694633`.

[150] S. N. Makarov. *Antenna and EM Modeling with MATLAB*. John Wiley & Sons, Inc., New York (2002). ISBN 0-471-21876-6.

[151] V. Solovov, et al. Measurement of the refractive index and attenuation length of liquid xenon for its scintillation light. *Nuclear Instruments and Methods in Physics Research Section A: Accelerators, Spectrometers, Detectors and Associated Equipment*, 516(2):462 – 474 (2004). ISSN 0168-9002. doi:https://doi.org/10.1016/j.nima.2003.08.117. URL `http://www.sciencedirect.com/science/article/pii/S0168900203024331`.

[152] A. Cole. Loop Antenna Screening (2018). Internal Report.

[153] J. Harrison. Loop Antenna Radon Emanation (2019). Internal Report.